UNIVERSITY OF MESSINA

Department of Chemical, Biological, Pharmaceutical and Environmental Sciences

Doctoral Course in
Advanced Catalytic Processes for using Renewable Energy Sources (ACCESS)

Surface passivated zeolites: synthesis and catalytic contribution in de-fossilization strategy

PhD thesis of:

Giorgia Ferrarelli

Supervisor:

Prof. Massimo Migliori

The coordinator of the Doctoral Course:

Prof. Gabriele Centi

Academic Year 2022-2023- XXXVI cycle.

S.S.D. ING-IND 27

To Fede, mommy and daddy

this PhD was the easiest battle we have fought together.

To Marco,

you are the light I follow when I'm in the dark

Thank you for always bringing me home.

I love you.

PREFACE

This PhD work has been performed in the Chemical Engineering, Catalysis and Sustainable Processes Laboratory (CECaSP_Lab) of the University of Calabria (UNICAL) and in collaboration with the Department of Chemical, Biological, Pharmaceutical and Environmental Sciences of the University of Messina (Unime), from November 2020 until now, under the supervision of Professor Massimo Migliori. The research activity included a six-month period abroad at the "Institute of Chemical Technology" of Valencia under the supervision of Prof. Avelino Corma. Some physicochemical characterizations have been performed in collaboration with the Laboratory of Catalysis and Spectroscopy (LCS), CNRS ENSICAEN, University of Caen (France).

I would like to thank my supervisor, Professor Massimo Migliori, for giving me the chance to start this hard, but very motivating journey. Not just for all the things he taught me, but also for believing in me, often more than I do, and always pushing me to be the best I can be.

I want to thank Professor Girolamo Giordano, his experience and advices helped me improve as a researcher.

I'd like to express my deepest gratitude to Professor Avelino Corma for giving me the chance to spend six wonderful, challenging months at ITQ in Valencia.

Furthermore, I must express my gratitude to my colleagues, who have supported me throughout this journey, and who have encouraged and supported me each day. Your contribution has been and will always be precious to me. I love you.

Finally, I can't help but thank my wonderful family for their constant support. I make every choice and do whatever I can to make you proud of me. I love you to the moon and back.

ABSTRACT

In recent years, great interest has been focused on the search for strategies aimed at tuning the structural and acidity properties of zeolites to improve catalytic performances. The acid sites located inside the crystals catalyse reactions exploiting the internal channel shape-selectivity different depending on the zeolitic structure employed. On the contrary, acid sites located on the external surface did not offer the possibility to control the size of molecules involved in reactions. This aspect generally leads to a loss of selectivity towards desired products and to the uncontrolled production of coke. Passivating surface acidity is a promising way to overcome deactivation issues and to enhance zeolites catalytic performances. In the literature, different techniques have been studied with the aim of neutralising external acid sites such as chemical liquid and vapour deposition of tetraethyl orthosilicate. Moreover, other post-synthetic treatments with HNO_3 or with NaOH, deposition of MgO or impregnation with phosphorus have also been investigated. Recently, the synthesis of zeolitic core-shell materials attracted great attention among researchers. Particularly, this technique could be used to passivate external acid sites through the growth of a layer of aluminium-free zeolite, e.g. Silicalite-1, over the surface of a starting acidic zeolite meanwhile preserving the catalytic activity maintaining the accessibility of the internal acid sites. Furthermore, the synthesis of core-shell type catalysts coupling different zeolitic structures could also be useful to enhance their performances in catalytic processes. Zeolite composites synthesis through the integration of shell zeolites with smaller pores and core zeolites with larger pores is a rational strategy. The shell's structure is designed for separation tasks, but it also allows for additional catalytic activities to take place in the core. Meanwhile, the shell could also be used to neutralize the core external acidity, thereby preventing the occurrence of unwanted side reactions.

This PhD work can be divided into two main parts. In the first part of this PhD thesis, the synthesis of zeolite catalysts with different structures, the passivation of their external acid

sites through the employment of different techniques and the characterization of their main properties have been reported. This section in turn includes three steps.

The first step is focused on the employment of the epitaxial growth technique to synthesise a shell of Silicalite-1 over the surface of ZSM-5 zeolites with the aim of neutralizing external acid sites. Firstly, an acidic ZSM-5 core with a high aluminium content (Si/Al ratio equal to 11) has been synthesized and coated with Silicalite-1. Then, a novel strategy for the growth of Silicalite-1 has been proposed; particularly, the coating of Silicalite-1 has been performed using an as-made form core (with the organic template still inside the channels) to prevent the partial blockage of the pores due to the growth of Silicalite-1 crystals. Moreover, ZSM-5 zeolites with different aluminium content have been synthesised and passivated employing the epitaxial growth technique in order to study the effect of acid sites distribution on the properties of resulting composite ZSM-5@Silicalite-1 catalysts.

The second step of this work relates to the synthesis of BEA@Silicalite-1 samples via a steam-assisted crystallization technique.

The third step has been focused on the use of chemical vapour deposition of TEOS to passivate external acid sites of ZSM-5 zeolite (with a Si/Al ratio equal to 25) in order to study the properties of passivated catalysts and to compare them with results obtained using ZSM-5@Silicalite-1 composite materials.

All the obtained catalysts have been characterised by classical analytic techniques such as XRD, porosimetry, TG/DTA, SEM-EDX, NH_3-TPD and FT-IR. The main results are summarized in Chapter 4.

The second part of this PhD thesis mainly focuses on the application of catalysts synthesized for different purposes. External acidity passivation could be useful to prevent the formation of undesired products during reaction and the deactivation of catalysts. For this reason, parent zeolites and passivated samples have been tested for two different catalytic applications. In a period in which accelerating the pathway toward decarbonization and reducing the dependence on fossil fuels became essential for governments, the synthesis of dimethyl-ether and its employment as a chemical intermediate has attracted great attention. For this reason, methanol to DME (MTD) and DME to olefins (DTO) reactions have been

chosen to test synthesised catalysts and to analyse the effect of the passivation via the epitaxial growth of Silicalite-1 over samples catalytic behaviour. Interesting and challenging results, reported in Chapters 5 and 6, have been obtained for both applications.

Finally, also a new application of BEA@Silicalite-1 materials is shown: the synthesis of Zeolite-templated carbons (ZTCs) employing the composite as a scaffold. In this part of the work, the "gate effect" due to the narrower pores of the Silicalite-1 layer coating the BEA surface on ZTCs final properties has been evaluated. Samples have been characterised through XRD, TG/DTG, SEM, FT-IR and Raman Spectroscopy. Obtained ZTC materials have been employed as adsorbents in Carbon Capture and Storage (CCS) processes and interesting differences have been found between samples obtained starting from a simple BEA zeolite and samples obtained from BEA@Silicalite-1 composite materials. The main results of this part of the work are summarized in Chapter 7.

Table of Contents

CHAPTER 1. Zeolites

Since the aim of this thesis work mainly concerned the tuning and passivation of the external acidity of zeolites and the use of the synthesized samples in various catalytic applications, in this chapter an overview of zeolites and their main physicochemical properties has been presented. Particular attention was paid to the description of the MFI and BEA frameworks, employed in this research work.

1.1 Background on zeolites.

The International Union of Pure and Applied Chemistry (IUPAC) has classified porous materials into three primary groups based on their pore size: microporous (d_p < 2 nm), mesoporous (2 ≤ d_p ≤ 50 nm), and macroporous (d_p > 50 nm) materials [1]. Zeolites, a type of porous material, are characterised as low-density, crystalline aluminosilicates with a well-organized microporous structure, featuring an extremely narrow and uniform pore size distribution. This unique property makes zeolites significant members of the microporous materials category. Zeolites exhibit a distinctive three-dimensional structure composed of TO_4 tetrahedra, where T represents a tetravalent or trivalent atom, commonly Si^{4+} or Al^{3+} [2]. These tetrahedra are interconnected by sharing oxygen atoms, forming repeating subunits that contribute to the creation of the crystal lattice. The spatial arrangement of these subunits results in an organized system of cavities and channels. This system possesses well-defined dimensions that vary from one zeolite to another, contributing to the unique characteristics of each zeolitic structure. It's crucial to highlight that when aluminium represents the tetrahedral atom, it creates a partial negative charge due to its trivalent nature and connection to four oxygen atoms. This negative charge is counteracted by the presence of cationic species situated within the lattice voids. The chemical composition of zeolites can be represented by the following general formula:

$$M_{2/n}O \cdot Al_2O_3 \cdot xSiO_2 \cdot yH_2O$$

Where *M* represents the cation, often an alkali metal or alkaline earth metal, *n* is the cation valence charge, *x* can vary from 2 to infinite and *y* represents the number of water molecules incorporated into the zeolite framework.

Zeolites and their structures can be categorized based on various parameters [2]. According to the Si/Al ratio, zeolites can be divided into:

1. **Low Si/Al Ratio Zeolites:** with Si/Al < 2
2. **Intermediate Si/Al Ratio Zeolites:** with 2 < Si/Al < 10
3. **High Si/Al Ratio Zeolites:** with 10 < Si/Al < 100
4. **Zeolites with "Infinite" Si/Al Ratio - "Pure Silica Zeolites":** with a Si/Al ratio equal to ∞, often referred to as "pure silica zeolites."

Each category of zeolite with varying Si/Al ratios may exhibit different properties and applications, and the specific ratio can impact their performance in various industrial and scientific contexts.

Another classification of zeolitic structures is based on the size of the pores and cavities within them, which plays a crucial role in the adsorption of molecules by zeolites. This classification includes:

- **Small-Pore Zeolites:** zeolites with pore openings formed by six, eight, or nine tetrahedra.
- **Medium-Pore Zeolites:** zeolites characterized by pore structures consisting of at least 10 tetrahedra interconnected.
- **Large-Pored Zeolites:** zeolites with pore structures formed by at least 12 tetrahedra connected together.

Lastly, zeolites can be categorized based on the arrangement of the channels that define their structures in space [2]. There are three distinct channel systems:

- **One-dimensional channels:** channels that are arranged in space parallel to each other without any interconnection.
- **Two-dimensional Channels:** channels that extend in space in two directions and have perpendicular interconnections between them.

- **Three-dimensional channels:** channels arranged in all three spatial dimensions and can have elliptical or circular shapes.

Zeolites synthesis involves as the first step the preparation of a mixture that includes all the required reagents. The precursor gel is composed of silicate and aluminate sources, a mineralizer (OH^-/F^-), organic/inorganic structure-directing agents (SDA), and water predominantly used as the solvent [1]. The following step regards the production of zeolitic materials starting from the prepared precursor gel and it is generally carried out at high temperatures and autogenous pressures. This second step could be performed through standard hydrothermal synthesis (HT) or through dry gel conversion techniques (DGC). In the DGC technique, a thoroughly dried gel is positioned on a support within an autoclave that contains a liquid phase, ensuring no direct mixing of the two phases. The liquid phase at the bottom of the support may consist of either an aqueous mixture of organic SDAs, which can later be volatilized to reach the dried zeolite gel (referred to as vapor phase transport or VPT technique), or, for non-volatile organic SDAs, simply pure water to generate the necessary steam for the crystallization of the dry gel, known as the steam-assisted technique (SAC) [1]. Although achieving a thorough and comprehensive understanding of zeolite formation remains an ongoing objective, it is generally described as a multi-step process involving prenucleation, primary nucleation, nuclei growth, and crystal growth. In the prenucleation step, Si and Al sources undergo dissolution/hydrolysis with a consequent condensation process of amorphous oligomeric silicate and aluminate species. Primary nucleation can occur homogeneously or heterogeneously within the solution gel or solid-like materials, respectively. The final step involves crystal growth from small nuclei, potentially accompanied by secondary nucleation.

For zeolites synthesis, different silica sources are employed (such as sodium silicate solution, amorphous precipitated silica, colloidal silica, and tetraethyl-orthosilicate). The choice of silica source significantly impacts crystallization rates and can influence the formation of specific zeolite phases [3]. Aluminum sources, including sodium aluminate and aluminum hydroxide, are also necessary for the synthesis process. A mineralizer agent is utilized to enable the dissolution of the silica source, typically in a basic medium with a

pH range of 8 to 12, using OH^- species. Alternatively, silica mineralization can occur under acidic conditions employing F^- ions [4]. Additionally, the nature of the inorganic cation, employed to balance the zeolitic framework charge, can influence the morphology of zeolite crystals and impact the nucleation period [5]. Structure-directing agents (SDA) are compounds used in the synthesis of zeolites to guide or direct the formation of specific structures during the crystallization process. These agents, such as alkylammonium salts, alkylammonium hydroxide, amines, alcohols, or ethers, play a crucial role in influencing the kinetic and/or thermodynamic aspects of zeolite lattice formation. They contribute to the organization of TO_4 units around organic molecules, directing the growth of the zeolite structure.

Finally, crystallization time and temperature are key factors that strongly influence the zeolite synthesis process [6]. For example, increasing synthesis temperature enhances the rates of nucleation and crystal growth paths. The relative rates of nucleation and crystal growth are crucial in determining the final material characteristics such as the crystals size. After having summarized the fundamental information relating to the structure, classification, and synthesis of zeolites, in the following paragraphs further in-depth information will be presented on MFI and BEA frameworks.

1.2 Materials related to this work.

1.2.1 The MFI framework.

The MFI structure, one of the most extensively studied zeolite topologies, holds great significance in industries like petroleum refining, petrochemicals, and pollution control processes. The MFI framework is built starting from the pentasil unit shown in **Figure 1** [7,8]. The pentasil unit, the composite building unit of the MFI framework, is in turn up of eight linked membered rings also called pentagons (each composed of five T atoms bonded together). Chains of pentasil units are obtained by joining CBUs across corners (**Figure 1**). The connection of adjacent chains results in the formation of sheets within the *b-c* plane.

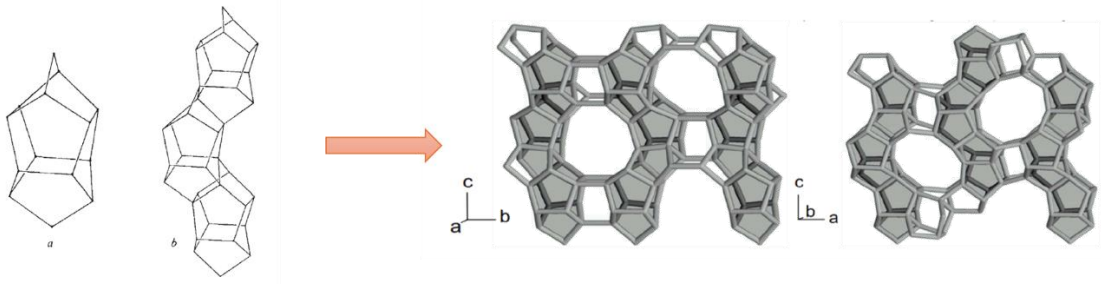

Figure 1: Pentasil unit and chains and sheets it produces [7,8]**.**

These sheets are assembled through mirror planes, leading to the creation of 4 and 6-membered rings. This assembly of sheets gives rise to a three-dimensional framework, establishing a system of two-dimensional 10-membered-ring (10-MR) channels (**Figure 2**):

1. **Channels along the [010] Axis** (axis b in the figure above)**:**
    - These channels follow a linear path parallel to the [010] axis.
    - They are delimited by an elliptical cycle comprising ten tetrahedra.
2. **Zigzag Channels along the [100] Axis** (axis a in the figure above)**:**
    - These channels exhibit a zigzag pattern parallel to the [100] axis.
    - They are delimited by a ring containing ten T atoms.

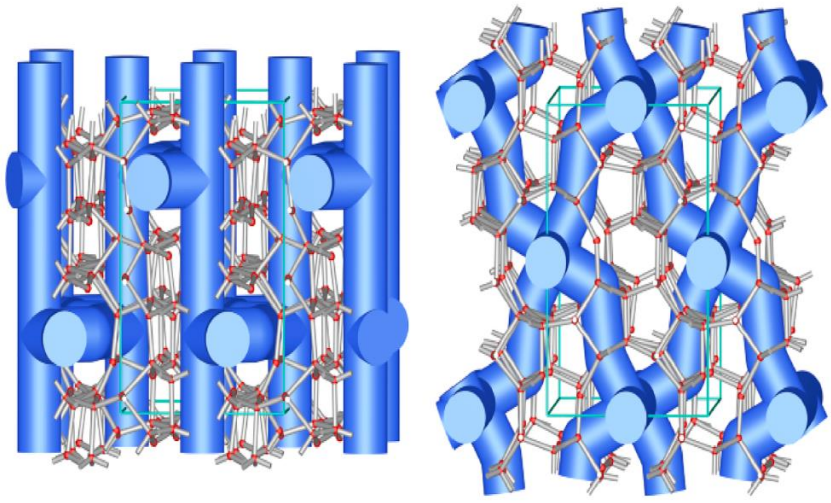

Figure 2: MFI channels [8]**.**

There are several zeolites with MFI structure among which the most commonly used are ZSM-5 and Silicalite-1 also synthesized in this thesis work. ZSM-5 zeolite was first synthesized in 1972, five years after the Beta zeolite was synthesized through the

employment of tetraethylammonium cations. These discoveries marked significant developments, introducing the concept of using organic structuring agents [8]. Silicalite-1, a pure silicious MFI zeolite, was synthesized for the first time in 1978 when Flanigen and his colleagues employed the first time fluoride ion as a mineralizing agent instead of OH^- ions. Silicalite-1 is characterized by a strong hydrophobic nature. This property makes Silicalite-1 well-suited for the recovery of organic compounds from various effluents [8]. ZSM-5 zeolite exhibits exceptional chemical and thermal stability, making it highly durable. It is easily synthesized using low-cost precursors and can have a versatile Si/Al ratio [8]. Additionally, its modulable acidity and shape selectivity render it a versatile catalyst to produce various valuable products. ZSM-5 major commercial application lies in fluidized bed catalytic cracking of heavier crude oil fractions [9]. Beyond catalytic cracking, ZSM-5 is utilized in various processes, including the conversion of methanol to hydrocarbons, olefine, or gasoline, the cyclization of paraffins and light olefins for aromatic hydrocarbon production, xylene isomerization, and the synthesis of chemical industry intermediates [10–13].

1.2.2 The BEA framework.

Zeolite beta stands out as one of the most intricate materials within the zeolite family, holding significant importance. Its structure is an intergrowth of two or three polymorphs: chiral polymorph-A, achiral polymorph-B, and polymorph-C [14,15]. These polymorphs arise from the same centrosymmetric layer shown in **Figure 3**, but they differ based on how these layers are connected. The starting secondary building units are characterized by 16 T-atoms arranged in the plane along two directions (**Figure 3**).

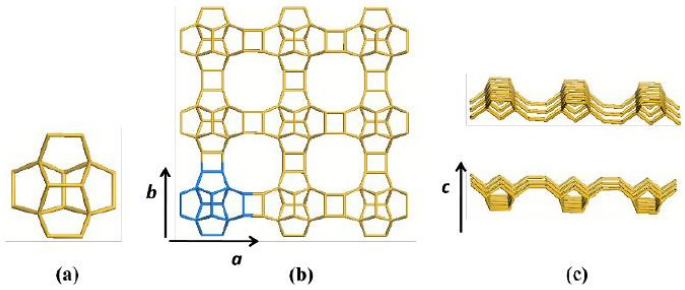

Figure 3: Secondary building units and centrosymmetric layer [15]

The adjacent buildings layer can be associated through a 90° rotation of the topologically identical layer around the c-axis, which is perpendicular to its plane direction as shown in **Figure 4**. Given the tetragonal nature of the layer, the view along the a-axis closely resembles that along the b-axis.

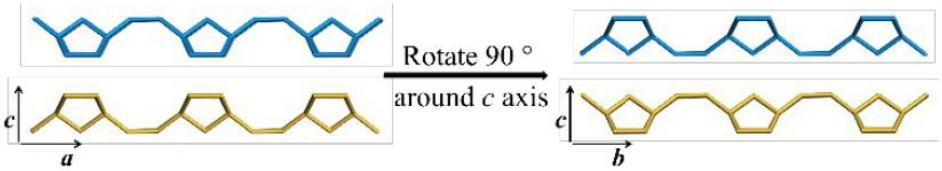

Figure 4: Adjacent building layers [15]**.**

The chemical connectivity between adjacent layers could be ensured by employing three translation modes, that occur either on the a-axis or the b-axis, shown in **Figure 5**:

- No Translation: The upper layer is shifted by 0 periods along the a-axis or b-axis direction relative to the lower layer (**Figure 5a**).
- +1/3 Translation: The upper layer is shifted by a +1/3 period along the a-axis or b-axis direction relative to the lower layer (**Figure 5b**).
- -1/3 Translation: The upper layer is shifted by the -1/3 period along the a-axis or b-axis direction relative to the lower layer (**Figure 5c**).

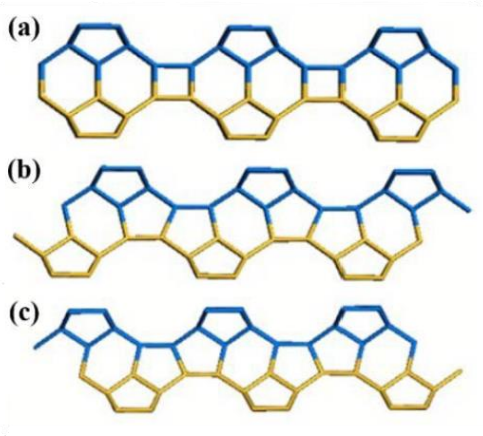

Figure 5: Adjacent building layers connection modes [15].

The periodic connection modes of the interphase layer on the 2D plane (ac plane or bc plane) can be categorized into the following three types:

- Alternating Sequence: In this type (**Figure 6a**), the interphase layers follow the alternating sequence +1/3, -1/3, +1/3, -1/3..., resulting in 12-membered ring channels presenting the ABABAB… type stacking sequences when viewed on the ac (or bc) plane.
- Consecutive Sequence: In this type (**Figure 6b**), the interphase layers follow the consecutive sequence +1/3, +1/3, +1/3… (or -1/3, -1/3, -1/3...), leading to 12-membered ring channels with ABCABC… type stacking sequences when viewed on the ac (or bc) plane.
- No Translation: In this type (**Figure 6c**), the interphase layers arrange without any translation, resulting in 12-membered ring channels presenting the AAA… type stacking sequences when viewed on the ac (or bc) plane.

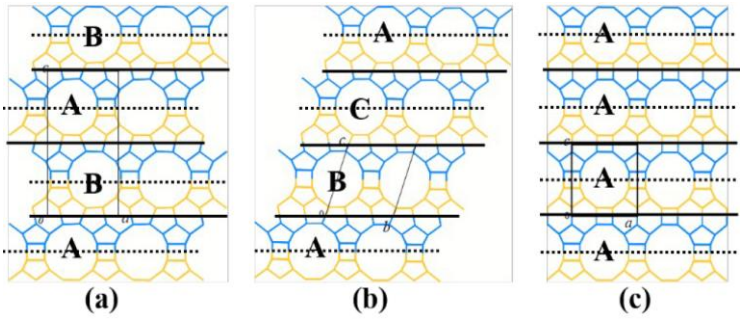

Figure 6: Periodic connection modes of the layers on the 2D plane [15].

Different polymorphs of zeolite beta are obtained based on the stacking configurations of interphase layers on ac and bc planes. These include Polymorph-A, Polymorph-B, Polymorph-C, Polymorph-CH (an ordered intergrowth of Polymorph-A and Polymorph-B), Polymorph-D (an ordered intergrowth of Polymorph-B and Polymorph-C), and Polymorph-E (an ordered intergrowth of Polymorph-A and Polymorph-C). Polymorph-A is formed when the interphase layers follow the alternating sequence on both ac and bc planes. Polymorph-B is formed when the interphase layers follow the consecutive sequence on both the ac and bc planes. Polymorph-C is formed when the interphase layers are linked

without any translation on both the ac and bc planes. Polymorph-A, the chiral variant of zeolite beta, is in great demand for its potential uses in enantioseparation and asymmetric catalysis. Despite its high desirability, achieving the pure form of polymorph-A in zeolite beta remains an elusive goal.

Whatever the polymorph obtained, the channel system obtained is always three-dimensional with 12-ring pores.

Beta zeolite was synthesized for the first time in 1967 using the hydrothermal method and employing silicon gel, aluminum, alkali, and tetraethyl ammonium hydroxide as chemicals [16]. Because of its unique properties such as high Bronsted acidity concentration, high Si/Al ratio, high thermal and hydrothermal stability, and high surface area, beta zeolite has been widely used in petrochemical, fine chemical, and environmental fields. For example, BEA zeolite has been employed in fluid catalytic cracking and for the alkylation of benzene or isobutene [17–19]. In the environmental field, potassium tungstophosphate supported on BEA zeolite has been successfully employed for pesticide removal [20]. Moreover, recently Sn-BEA zeolite and dealuminated BEA zeolites have been used to monitor environmental pollutants using gas sensors. Gas sensors incorporating Sn-BEA and DeAl-BEA zeolites as selective microporous layers have been developed and put through extensive testing. The Sn-BEA-based sensor exhibited notable selectivity for NO_2, while the DeAl-BEA sensor demonstrated selectivity for CO_2 and NO_2, even in the presence of water vapor at room temperature [21].

1.3 Main properties of zeolites.

In this paragraph, the main properties of zeolites will be briefly discussed giving higher attention to shape selectivity and acidity.

High internal surface area and pore volume. Zeolites are characterized by a high specific surface area (>200 m^2/g) and a high pore volume directly linked to their pore architecture. This unique structure enables zeolites to accommodate a variety of species in their frameworks, making them particularly appealing for different industrial uses such as separation and catalysis.

Shape selectivity. The extensive utilization of zeolites in catalysis can be attributed to their remarkable molecular shape-selectivity properties. Shape selectivity in catalysis refers to the ability of a catalyst to exhibit specificity in chemical reactions based on the size and shape of the reacting molecules. In zeolites, shape selectivity arises from the constrained environment of their nanoporous structure. Only molecules that can fit within the defined pore dimensions of the zeolite can access the internal catalytic sites and undergo reactions. In the same way, only molecules capable of exiting the crystal appear in the final product. Synthesizing zeolites with different channel sizes involves modulating their shape-selectivity. Different types of shape-selectivities can be identified depending on the specific aspect of the catalytic process influenced by the channel size within the zeolite structure. This includes scenarios where the entrance of reacting molecules is limited by the channel size, the release of product molecules is constrained, or the formation of transition states is affected. Shape selectivity towards products is, for example, employed in methanol to olefins reaction. Particularly, the employment of SAPO-34 catalysts, with narrow channels (3.8 Å, three-dimensional) allows to obtain as main product ethylene and propylene rather than heavier hydrocarbons. However, the presence of larger cages in the framework of zeolite allows hydrocarbon pool mechanisms to occur [22]. Shape selectivity related to the state of transition occurs when, despite the possibility of various competing reactions, only the intermediate that fits within the size constraints of the zeolite voids is formed. Examples of this type of selectivity include the disproportionation and trans-alkylation of alkyl-aromatic compounds [23]. In the acid-catalyzed trans-alkylation of di-alkylbenzene, a bimolecular reaction occurs where one alkyl group is transferred from one molecule to another. The transition state involves the formation of di-phenylbenzene, which can subsequently dissociate to yield either a 1,2,4 isomer or a 1,3,5 isomer of tri-alkylbenzene, along with mono-alkylbenzene. When mordenite is used as the catalyst, the transition state for the 1,3,5 isomer is hindered due to its size, resulting in a 100% yield of the 1,2,4 isomer [24].

Acidity. Together with shape selectivity, the acidity of zeolites is one of their most important properties as catalysts. Knowing the nature of acid sites, their strength, and their location

within frameworks is fundamental for the following zeolite catalytic applications. As already explained, zeolites are crystalline aluminosilicates with a structure formed by connecting SiO_4 and AlO_4 tetrahedra through shared corner oxygen atoms. The presence of trivalent Al^{3+} species in the framework leads to a net negative charge, which is counteracted by cations like Na^+, K^+, Mg^{2+}, Ca^{2+}, NH^{4+}, or protons (H^+). When the negative charge is compensated by a proton a strong Brønsted acid site is formed [25,26]. A Brønsted acidic proton consists of hydrogen linked to the oxygen atom that connects the tetrahedrally coordinated cations as shown in **Figure 7**. One of the most common approaches employed to obtain Brønsted acid sites involves the exchange between the zeolite counter-cation and the ammonium ion, followed by high-temperature calcination, typically around 550°C. The amount of Bronsted acid sites can be modulated by varying the Si/Al ratio of the zeolite [27]. Moreover, acid site strength can be tuned employing isomorphous substitutions, whether performed during direct synthesis or through post-treatment leading to metallosilicates with zeolite structures where some of the T sites are replaced by a trivalent element other than Al, such as Ga, Fe, In, B, etc. Both theoretical calculations and experimental assessments of acid strength using methods like IR spectroscopy and ammonia TPD consistently demonstrated that acid site strength follows the order: Al(OH)Si > Ga(OH)Si > Fe(OH)Si > In(OH)Si > B(OH)Si [28]. Lewis acid sites in zeolites are electron-deficient sites that can therefore accept electrons during interaction with molecules. In contrast to Brønsted acid sites, the source of Lewis acid sites in zeolites remains a topic of discussion. The uncertainty arises from the various potential Lewis acid sites, attributed to the structural flexibility of aluminum, leading to numerous aluminium species. Methods like steaming, high-temperature calcination, and acid or base leaching can induce Lewis acidic character in aluminum through post-synthesis treatments. These processes typically involve the hydrolysis of framework Si–O–Al bonds, leading to the removal of aluminum from the framework and the creation of 'extra-framework aluminum' (EFAl) species with Lewis acidity [29]. An example is shown in **Figure 7**. Moreover, EFAl exists in several oxide and hydroxide forms, such as $Al(OH)^{2+}$, $Al(OH)^{2+}$, AlOOH, Al_2O_3, and $Al(OH)_3$. Furthermore, studies demonstrated that framework Lewis acid sites arise from framework

dehydroxylation [30] and that Lewis acid sites were also detected on the external surface of extra framework-free zeolites [31]. Busca et al. found strong Lewis acid sites on low-aluminum faujasite H-Y, suggesting that the contribution to Lewis acidity in protonic zeolites may come from both extra-framework species and framework tetrahedral aluminum ions [32]. It is clear that the right tuning of acid site distribution represents a key factor for catalysis applications. It has been demonstrated, for example, that calcination temperature influences acid sites distribution [33]. Moreover, also organic template employed in the synthesis gel can affect the Brønsted/Lewis acidity ratio [34].

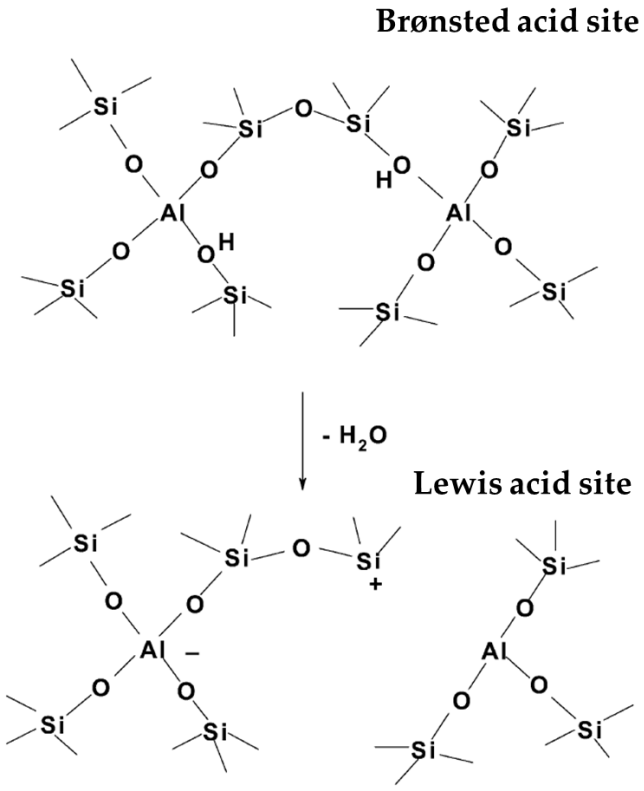

Figure 7: Strong Brønsted acid site and generation of Lewis acid sites via dehydroxylation [35]

Several techniques can be employed to analyze the acidity of zeolites. The quantification of acid sites, including their number and strength, can be achieved through ammonia titration (NH_3-TPD measurements). However, this method cannot distinguish between Brønsted and Lewis acid sites. To address this limitation, other techniques such as FT-IR of adsorbed

probe molecules (e.g., acetonitrile, pyridine, ammonia, and CO) can be utilized. Additionally, NMR analysis (including ^{1}H-, ^{27}Al-, ^{29}Si-, ^{23}Na-NMR) provides a comprehensive understanding of the origin of acid sites in zeolites.

Ion exchange Capacity. Zeolites possess a porous crystalline structure that includes ions, specifically cations which can include H^+, Li^+, Na^+, K^+, Cs^+, Mg^{2+}, Ca^{2+}, or transition metal cations. These cations play a crucial role in neutralizing the negative charge generated when an aluminum atom forms a tetrahedron by binding to four oxygen atoms and they can be easily exchanged. Zeolites, with their ability to exchange ions, find applications in various fields. For instance, zeolite A is employed in water softening, where Na^+ ions in the zeolite structure are exchanged with Ca^{2+} ions from water, effectively removing calcium ions [36].

High Chemical, Mechanical, Thermal, and Hydrothermal stability. In contrast to non-crystalline aluminosilicates, crystalline zeolitic substances have proven to be generally more adept at withstanding the challenging conditions prevalent in numerous industrial catalytic procedures.

Easy Regeneration. Although zeolites can deactivate during reaction because of the formation of coke, they can be easily regenerated through processes that have little to no impact on the original structure (e.g. calcination treatment).

Support for Metal. Zeolites can also be used as support for catalytic metal or metal oxide allowing the production of bifunctional acid-metal catalysts.

CHAPTER 2. Tuning zeolite properties: external acidity passivation

Zeolites, a significant group of crystalline microporous materials, have been synthesized since the 1940s. As already explained, they possess distinct physical and chemical properties that make them ideal for adsorption and catalysis also because of their shape-selectivity. In addition, the possibility to adjust acidity in a controlled structure, coupled with hydrothermal stability, high surface area, and pore volume, promoted the applications of zeolites in petrochemistry, gas separation, and energy applications [37]. Many efforts are still being made to enhance the performance of such materials. In catalysis, current investigations involve two main aspects: structure and acidity tuning. Structural modifications mainly consist of introducing mesoporosity in the internal channels of zeolites or changing the crystal size [38], to reduce mass limitation factors. Acidity modifications concern both techniques used to vary the number and distribution of acid sites [39] and techniques employed for the passivation of external acid sites [40].

The study of acid sites distribution and location, inside or outside the channels, represents a complex topic of great interest [31,41–43]. About this aspect, Busca et al. deeply characterized external and internal sites of H-ZSM5 zeolites (with different Si/Al ratios) via an FT-IR study by employing different molecules as probes. Particularly, they used pivalonitrile and other molecules with a similar critical radius because they cannot enter ZSM-5 channels and consequently are useful to characterize external acidity. Results obtained revealed that ZSM-5 zeolites exhibited the presence of two different types of terminal silanol groups on their external surfaces appearing similar in their OH stretching band but varying in Brønsted acidity. Moreover, the authors stated that external surfaces of ZSM5- zeolites, even in samples with low Al content, possess two types of Lewis acid sites, with higher quantities of stronger external Lewis acid sites in high Al content samples. On the contrary, no proof supporting the presence of bridging Si-(OH)-Al sites on the external surface was found, suggesting the confinement of strong Brønsted acid sites within the pores.

The presence of acid sites in the channels of the zeolitic framework implies the capability to catalyze the reactions by exploiting the fundamental characteristic of shape selectivity. Conversely, the existence of acidic sites on the outer surface of zeolites hinders the use of this characteristic. Therefore, the decrease in selectivity towards the desired products might be linked to the absence of shape selectivity in external acid sites. Acid sites present on the external surface of ZSM-5 zeolite may also prompt extensive coke formation during catalytic reactions. This accumulation could potentially cover or obstruct the surface and pore openings. Consequently, the acid sites within the micropores might lose their efficiency, leading to rapid deactivation.

In this research work great attention was paid to external zeolites acidity passivation techniques. As will be explained in the next paragraphs within the existing methodologies, the epitaxial growth of a layer of Silicalite-1, steam-assisted crystallization (SAC), and chemical liquid deposition of TEOS have been explored. For this reason, an overview of the major passivation techniques studied and used in literature is drawn up in the next paragraphs. In particular, attention was initially paid to the synthesis of core-shell type catalysts and among these to ZSM-5@Silicalite-1 samples obtained through the epitaxial growth technique. Moreover, fundamental information about zeolitic core-shell catalysts composed of a core and a shell with a different framework is provided. Finally, other passivation techniques have been described with particular emphasis on the chemical liquid deposition of TEOS.

2.1 Core-shell type catalysts.

"Core-shell concept" involves materials composed of two distinct parts: an outer shell and an inner core or hollow region [44]. The different properties of core (or hollow region) and shell allow to generate of new desirable characteristics while largely preserving the original properties of each component and results in enhanced features compared to the individual components or their physical blends. As a result, such materials find suitability in various fields like adsorption, catalysis, storage, and biomedical applications [45]. **Figure 8** represents three types of encapsulated structures that can be obtained by combining cores, shells, and hollow regions:

- **Core-Shell Structure**: This type involves a composite nanomaterial where a single nuclear material is uniformly coated by secondary shell material, creating a core-shell connection.
- **Hollow Structure:** Unlike the core-shell structure, the hollow structure lacks a nucleus. It can be synthesized through the treatment of the core-shell structure or by direct synthesis.
- **Yolk-Shell Structure**: This structure represents a core-shell design in which the core and shell are not connected but separated by a hollow region.

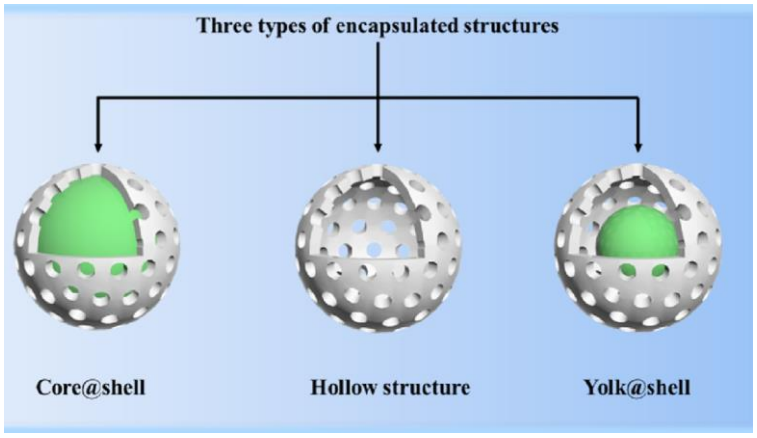

Figure 8: Type of encapsulated materials [44].

Encapsulated catalysts usually consist of a part of zeolite which could be the shell, the core, or both the shell and the core as shown in **Figure 9**.

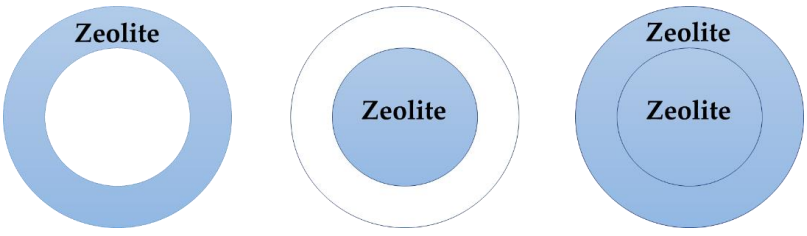

Figure 9: Position of zeolite in zeolitic core-shell catalysts.

Particular attention in this thesis work will be paid to core-shell catalysts. Among these, a further distinction can be made. Depending on the core material, two categories can be counted:

- **Metal-oxide@Zeolite** [46,47], suitable for safeguarding metals from harsh environments.
- **Zeolite@Zeolite** [40,48–52], core–shell suitable for passivating external surface acid sites or achieving a gradient distribution of zeolite acid sites.

Although a discussion of the main uses and synthesis techniques was addressed to all types of core-shell, the greatest attention will be paid to the second category (zeolite@zeolite) since they represent a strategy to achieve the neutralization of the external acid sites, the main aim of the research.

Metal oxides such as Fe, Co, Ni, and Ru serve as catalysts in industrial hydrocarbons production such as light olefins, liquefied petroleum gas, and gasoline. One of the main problems related to these catalysts is their tendency to deactivate because of poisoning, sintering, and agglomeration [53].

Coating metal oxide catalysts surface with zeolitic shells in core-shell configuration improves catalyst stability during thermocatalytic reactions. These structures prevent core material agglomeration, migration, and sintering, thereby maintaining active catalytic sites and enhancing catalytic longevity. Additionally, the regular pore structure of the zeolite shell improves site accessibility, reducing the risk of coking by facilitating the transport of reactants and by-products [44]. Because of their unique characteristics, core-shell catalysts have already been employed in various applications such as Fischer-Tropsch synthesis. Co-based core-shell catalysts were synthesised by Javed et al. using a ZSM-5 zeolite as support for the subsequent incipient-wetness impregnation with cobalt nitrate solution. Then Co-ZSM5 catalyst was encapsulated by a microporous shell of Silicalite-1 employing a hydrothermal synthesis technique [54]. Catalytic tests of direct synthesis of syngas into gasoline range hydrocarbons via FTS were performed and the Co/ZSM-5@Silicalite-1 core-shell catalyst exhibited the highest selectivity (74.7%) for C_5-C_{11} hydrocarbons, with notable lower CO_2 and CH_4 selectivities compared to other zeolite supported Co-based catalysts with no core-shell structure. Moreover, core-shell catalysts exhibited lower deactivation over time and the higher CO conversion proving that the Silicalite-1 layer prevented coke deposition from occurring on the metal phase [54]. In another work,

F_3O_4@Silicalite-1 core-shell catalysts were prepared and the effect of the thickness of the shell on product distribution of Fischer-Tropsch synthesis was evaluated. It was found that the presence of a Silicalite-1 shell increased catalyst stability avoiding its cracking and sintering [55]. Core-shell catalysts have also been used for methane co-aromatization with propane [56]. The core-shell configuration of the Zn/SiO2@ZSM-5 catalyst led to the development of a unique micro-macroporous system. This system facilitated the rapid diffusion of desired products through the intraframework channels, preventing the accumulation of carbon deposits. In brief, the Zn/SiO_2@ZSM-5 catalyst, compared with a traditional Zn/ZSM-5 catalyst, showed superior methane and propane conversion as well as high aromatic selectivity and improved stability [56].

In addition, the design flexibility of core-shell structures allows the integration of two functional materials, enabling multi-stage catalytic performance. Particularly, by employing the spatial confinement effect of the core-shell structure, it is possible to promote specific reaction sequences enhancing conversion rates, product yields, and energy efficiency. Ethanol synthesis from dimethyl ether and syngas is usually performed through a two-step process in which firstly DME is carbonylated to methyl acetate and then the following hydrogenation of methyl acetate produces ethanol and methanol. Employing a core-shell catalyst consisting of a core of Cu/ZnO and a shell of H-MOR zeolite allowed to perform successfully one-step ethanol synthesis from DME and syngas with excellent performances [57].

Core shells consisting of both the core and the shell of different zeolitic materials allow to combine of unique characteristics of different zeolitic structures designing high-quality composites with multiple features. In the next paragraphs, techniques employed to synthesise zeolite@zeolite core-shell catalysts will be discussed.

2.1.1 Passivating zeolite external acidity via the deposition of a layer of Silicalite-1: ZSM-5@Sil-1 catalysts.

Among the various core-shell catalysts of the zeolite@zeolite type, particular attention has been paid in this thesis work to the materials consisting of a ZSM-5 core and a Silicalite-1

shell. Both are made of MFI structure, a shell of Silicalite-1 allows to neutralize acid sites located on the external surface of the ZSM-5 core and meanwhile preserves the catalytic activity not limiting the access of the molecules through the internal acid sites. In the literature, ZSM-5@Silicalite-1 core-shell catalysts have been studied and employed for various applications but they continue to attract the attention of researchers.

ZSM-5@Silicalite-1 catalysts are usually synthesized employing the so-called "in situ" technique. This synthesis method consists of two steps: during the first step the core, eventually pretreated, is immersed in the Silicalite-1 precursor solution and the hydrothermal crystallization of the shell is carried out during the second step [45]. Structural similarities between ZSM-5 and Silicalite-1 zeolites, both characterized by an MFI-type framework, promote the intergrowth of the two zeolitic phases during the hydrothermal synthesis of the shell. On the contrary, the direct growth of a shell with a zeolitic structure different from that of the core is more difficult and challenging but, as explained in the next paragraph, some works in literature have been published regarding the coupling of different zeolitic frameworks. An issue in the formation of core@shell crystals, employing the "in situ" technique, involves the competition between nucleation centers in the bulk gel and those on the core surface, often leading to homogeneous nucleation of shell crystals [45]. Nevertheless, a solution lies in the straightforward separation of core@shell crystals from bulk crystals by employing sedimentation or centrifugation, especially when there's a significant difference in their sizes. To prevent the homogeneous nucleation of Silicalite-1 crystals promoting the epitaxial growth around the core, studies have demonstrated the effectiveness of employing a high H_2O/SiO_2 ratio in the Silicalite-1 precursor solution [58]. A low silica concentration minimizes the heterogeneous nucleation of Silicalite-1 crystal, which is particularly beneficial for achieving uniform shell growth on larger-sized zeolite core crystals (≈3 μm). However, in cases involving smaller zeolite cores (≈400 nm), an excessively high H_2O/SiO_2 ratio in the shell precursor solution may lead to issues like core aggregation and separate nucleation of the shell. Hence, during the preparation of core-shell structures, it is crucial to keep a balanced H_2O/SiO_2 ratio between the core and shell [58]. The precursor solution usually employed for the synthesis of the Silicalite-1 layer consists

of water, an organic template (generally tetrapropylammonium hydroxide), and a silica source commonly represented by TEOS or fumed silica. Furthermore, the addition of ethanol can enhance the crystallization of the zeolite shell but might limit large-scale core-shell catalyst synthesis [37]. In **Table 1** Silicalite-1 precursor solutions and shell crystallization conditions reported in the literature are summarized. Moreover, some information about the core employed is also included.

Table 1: Synthesis conditions of ZSM5@Silicalite-1 catalysts prepared via "in situ" hydrothermal crystallization.

Refs.	type	Core form	Si/Al of the Core	Crystallization of the shell		
				synthesis gel	Time [h]	T [k]
[52]	ZSM5@Sil-1	H-ZSM5	70	0.5 TPAOH: 120 H_2O: 8 EtOH: 2 SiO_2	24	453
[59]	ZSM5@Sil-1	Commercial ZSM5	-	1 SiO_2: 0.09 TPAOH: 16 EtOH: 240 H_2O	24	453
[60]	ZSM5@Sil-1	AS-ZSM5	90	12 SiO_2: 16EtOH: 3.7 TPAOH: 800 H_2O	24	453
[61]	ZSM5@Sil-1	Zn/H-ZSM5	12.5	1TEOS: 0.14 TPAOH: 20 EtOH: 120 H_20	24	453
[62]	ZSM5@Sil-1	Mo/H-ZSM5	15	20 SiO_2: 3TPAOH: 80 EtOH: 1200 H_2O	24	453
[63]	ZSM5@Sil-1	Ga/AS-ZSM5	50	1 SiO_2: x TPAOH: 16 EtOH: 240 H_2O.	24	453
[64]	ZSM5@Sil-1	H-ZSM5	75	Surfactant-directed sol-gel coating	48	453
[65]	ZSM5@Sil-1	Meso-AS-ZSM5	150	Solid-state steam-assisted synthesis	72	453
[66]	ZSM5@Sil-1	Meso-H-ZSM5	50	1 SiO_2: 0.05 TPA_2O: 0.6 Na2O: 10 H_2O	24	443
[67]	ZSM5@Sil-1	Cylinder-shaped H-ZSM5 extruded adding amorphous silica as binder	-	10 SiO_2: TPAOH: 900 H_2O: 40 EtOH	24	443

Refs.	type	Core form	Si/Al of the Core	Crystallization of the shell		
				synthesis gel	Time [h]	T [k]
[68]	ZSM5@Sil-1	-	15	1 SiO_2: 0.3 TPAOH: 120 H_2O: 4 EtOH (Ultra-fast synthesis in a tube reactor)	10 min	463
[69]	ZSM5@Sil-1	Fe-ZSM5 functionalized with PDDA	40	8.3x TPAOH: x SiO_2(TEOS): 230 H_2O	1	473
[51]	ZSM5@Sil-1	H-ZSM5	Various Si/Al ratios	2 SiO_2: 0.5 TPAOH: 8 EtOH:120 H2O	24	453
[50]	ZSM5@Sil-1	H-ZSM5	100	x SiO_2: y TPAOH: z TPABr: 8 EtOH: 120H_2O	24	453
[70]	ZSM5@Sil-1	H-ZSM5	Various Si/Al ratios	1 SiO_2: 0.08 TPAOH: 16 EtOH: 240 H_2O	24	453
[71]	ZSM5@Sil-1	ZSM5 crystals prepared both in fluoride media and conventionally	20	1 SiO_2-0.125 TPABr: 0.9 NH_4F: 33 H_2O	90	453
[72]	ZSM5@Sil-1	Meso-ZSM5	-	17 TEOS: 14 TPAOH: 9500 H_2O	24	373
[73]	ZSM5@Sil-1	ZSM5 treated with an alkaline solution	36	2.29 Na_2O: 1 TPAOH: 15 SiO_2: 2237 H_2O.	24	453
[74]	ZSM5@Sil-1	Calcined ZSM5	80	0.2 TPAOH: 1 TEOS: 250 H_2O	24	448
[75]	ZSM5@Sil-1	Commercial H-ZSM5	216	25 SiO_2: 3 TPAOH: 100 EtOH: 1500 H_2O	24	453

Refs.	type	Core form	Si/Al of the Core	Crystallization of the shell		
				synthesis gel	Time [h]	T [k]
[76]	ZSM5@Sil-1	ZSM5	50	1SiO_2: 0.125 TPABr: 0.9 NH_4F: 33 H_2O	90	453
[48]	ZSM5@Sil-1	Commercial H-ZSM5	38	1 TEOS: 0.25 TPAOH: 80 H_2O	24	453
[77]	ZSM5@Sil-1	NH_4-ZSM5 functionalized with PDDA	70	1 SiO2: 0.5 TPAOH: 8 EtOH: 120 H_2O	2, 4, 8, 16	433

As can be seen from the data in the table, the hydrothermal synthesis of the Silicalite-1 layer is generally performed at 180°C for 24 hours. Moreover, the use of a rotating or tumbling oven is frequent to improve the homogeneity of the core coating [52].

Researchers' efforts are still dedicated to trying to optimize Silicalite-1 coating conditions in order to obtain a homogeneous layer around the core and to avoid the growth of single Silicalite-1 crystals. The presence of inactive Silicalite-1 crystals could drop the efficiency of the catalysts, posing a concern for their catalytic activity. Van Vu et al. reported a substantial increase in crystallized product mass after the coating process during their first studies on ZSM5@Silicalite-1 synthesis. This considerable mass gain, despite the presence of a thin Silicalite-1 layer on the surface of HZSM-5 crystals, was primarily attributed to the process of homogeneous nucleation of Silicalite-1 occurring within the liquid phase. For this reason, they decided to investigate the effect of the variation of molar ratios of silica source and structure directing agent in the Silicalite-1 precursor solution on core-shell morphology [50]. Particularly they employed fumed silica or TEOS as a silica source and TPAOH and/or TPABr as structure-directing agents. In the table below, molar ratios used in the precursor solutions are listed. Researchers measured the mass gain after the coating as the ratio between the mass increase after Silicalite-1 synthesis and the mass of the H-ZSM5 core. From their data in **Table 2**, it is noteworthy that higher molar ratios of TPAOH/silica sources

(A1&A2; T1&T2), lead to a significant increase in mass, primarily attributed to the formation of Silicalite-1 crystals through homogeneous nucleation within the coating solution.

Table 2: Molar ratios employed in Silicalite-1 precursor solutions and mass gain obtained after the coating [50].

Silica source	Sample	Molar ratios x SiO_2:y TPAOH:z TPABr:8 EtOH:120 · H_2O	Coating time	Mass gain [%]
Fumed silica	A1	$x = 2.0, y = 0.12, z = 0$	1	+167
	A2	$x = 2.0, y = 0.12, z = 0.12$	1	+194
	A3	$x = 2.0, y = 0.06, z = 0.06$	1	+88
	A4	$x = 2.0, y = 0.03, z = 0.09$	1	+56
	A5	$x = 1.0, y = 0.12, z = 0$	1	+127
	A6	$x = 0.5, y = 0.12, z = 0$	1	+40
	A7-1	$x = 0.5, y = 0.06, z = 0$	1	+51
	A7-2	$x = 0.5, y = 0.06, z = 0$	2	–
	A8	$x = 0.5, y = 0.03, z = 0$	1	+36
TEOS	T1	$x = 2.0, y = 0.5, z = 0$	1	+180
	T2	$x = 1.5, y = 0.5, z = 0$	1	+151
	T3	$x = 1.0, y = 0.12, z = 0$	1	+120
	T4	$x = 1.0, y = 0.06, z = 0$	1	+71
	T5	$x = 0.5, y = 0.12, z = 0$	1	+65
	T6	$x = 0.5, y = 0.06, z = 0$	1	+44
	T7	$x = 0.5, y = 0.03, z = 0$	1	+35

To obtain ZSM5@Silicalite-1 core-shell catalysts with minimal defects, synthesis procedures in fluoride media of both core and shell have been developed [71,76]. However, the presence of fluoride (F^-) is considered environmentally dangerous and a limiting step for industrial-scale synthesis processes.

Other techniques, different from the commonly used hydrothermal synthesis, to produce ZSM5@Silicalite-1 catalysts have been recently developed. Goodarzi et al. proposed a straightforward solid-state steam-assisted technique aimed at producing a non-acidic ultrathin layer of Silicalite-1 surrounding mesoporous ZSM-5 crystals [65]. The technique used began with pulverizing the as-synthesized mesoporous ZSM-5 in a mortar and drying it overnight to remove moisture. Then sequential impregnation with TPAOH and TEOS in a Teflon beaker, followed by drying and heating in a Teflon-lined stainless-steel autoclave with distilled water to generate steam at 180°C for 72 hours was carried out.

An ultrafast post-synthesis procedure to prepare ZSM-5@Silicalite-1 core-shell catalysts was recently proposed [68]. The process for synthesizing Silicalite-1 involved preparing a solution by combining TEOS, TPAOH, water, and ethanol. After stirring this mixture for 2 hours, the ZSM-5 core was introduced and stirred for an additional hour. Subsequently, the reactants were transferred into a tubular reactor with dimensions of 10 mm outer diameter and 8 mm inner diameter. The mixture was then heated at 190°C for 10 minutes in a pre-heated oil bath.

The synthesis of core-shell ZSM-5@silicalite-1 with a consistent and structured morphology was achieved using a novel tandem synthesis approach. This innovative strategy involved two sequential steps: the incorporation of nearly all aluminum sites through organ template-free synthesis, followed by the crystallization of the remaining silica sites through organ template-oriented synthesis [78]. In **Figure 10** schematic representation of the synthesis method is reported. In the first step, regarding the organ template-free synthesis, chemicals including colloidal silica, $Al_2(SO_4)_3 \cdot 18H_2O$, NaOH, H_2O, and seeds were mixed and stirred at room temperature and then transferred to a stainless-steel autoclave for a dynamic crystallization of 8 hours at 170°C. Subsequently, in the organic template-oriented synthesis phase, a specific quantity of the template agent TPABr was added, and this mixture was then subjected to dynamic crystallization at 170°C for 72 hours.

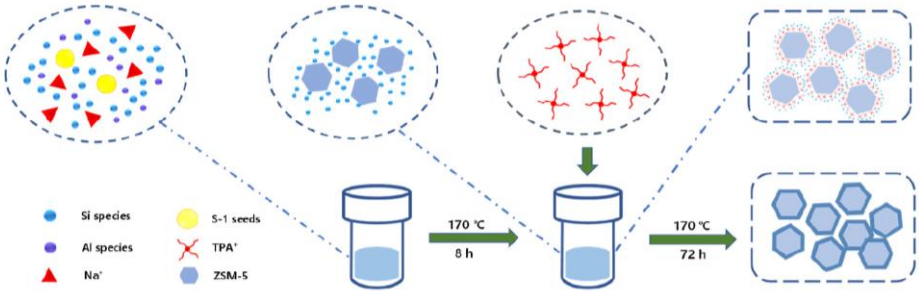

Figure 10: Schematic representation of a new ZSM5@Silicalite-1 synthesis strategy [78].

Several techniques have been employed to fully characterize ZSM5@Silicalite-1 core-shell catalysts in order to demonstrate the growth of the Silicalite-1 shell over the external surface of the starting core and its effect on external acidity. To investigate core-shell catalyst morphology, scanning electron microscopy (SEM), field emission scanning microscopy

(FE-SEM), and transmission electron microscopy (TEM) were successfully employed [52,59,62,68,74]. Van Vu et al. in one of their works employed SEM analysis to observe ZSM5@Silicalite-1 core-shell structures [52]. By using a core with different crystal sizes (5-30 μm) they found that the thickness of the Silicalite-1 layer was less than a few μm and that it did not increase so much after the second cycle of deposition. To obtain a deeper characterization of crystalline structure, FE-SEM and TEM measurements were carried out over small H-ZSM5 crystals coated with Silicalite-1. FE-SEM images of core-shell catalysts revealed small Silicalite-1 crystals (10-150 nm) formed on the H-ZSM-5 crystal (300nm). Silicalite-1 crystals have bigger development along the [001] than in [100] and [010] directions, indicating a preferential crystalline growth rate along the c-axis direction, as shown in **Figure 11a**. This finding was also confirmed by another published study [75]. In this work, authors fixed ZSM-5 crystals over a Cu substrate and performed the coating with Silicalite-1 under hydrothermal conditions studying the growth evolution after fixed time intervals with FE-SEM measurements. The growth rate of the Silicalite-1 crystals was observed to be preferential along the direction of the c-axis of ZSM-5 (**Figure 11b**). FE-SEM measurements performed allowed them to hypnotize a model for Silicalite-1 layer growth over the surface of ZSM-5 crystals (**Figure 11c**). The surfaces of a ZSM-5 crystal, perpendicular to the a and c axes, were found to be coated with thin Silicalite-1 layers and it was observed that the Silicalite-1 layer appeared thicker in the direction of the c-axis after a synthesis period from roughly 6 to 24 hours.

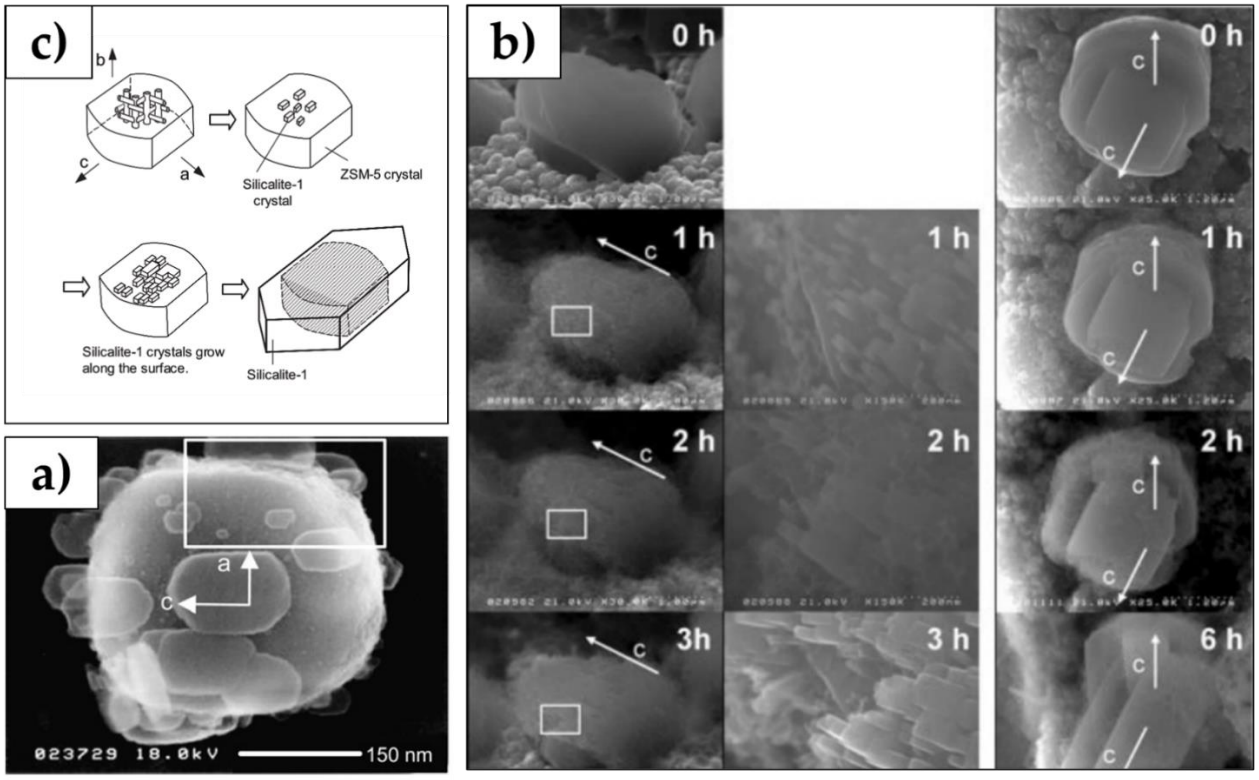

Figure 11: FE-SEM images of ZSM5@Silicalite-1 catalysts obtained by Van Vu et al. [52] **(a) and Miyamoto M. et al.** [75] **(b) and proposed model for Silicalite-1 layer growth over ZSM-5 surface (c)** [75]**.**

Moreover, to demonstrate the success of the coating with Silicalite-1, techniques such as atomic absorption, X-ray photoelectron spectroscopy (XPS), and inductively coupled plasma spectroscopy (ICP) have been employed [62,65,66,79]. The increase of Si/Al ratio or the absence of aluminum on the external surface of ZSM5@Silicalite-1 proved the presence of a layer of pure Silicalite-1.

N_2 adsorption/desorption isotherms have been used to estimate textural properties of ZSM5@Silicalite-1 samples such as BET surface area, micropore area, external surface area, and pore volume. The growth of a layer of Silicalite-1 on a ZSM-5 core allows the creation of interconnections between the two phases which both have an MFI-type structure, allowing on one hand the external surface acidity passivation and on the other not to alter textural properties of the starting sample as it happens when other passivation techniques are used [80]. However, in some published works authors underlined a decrease in micropore volume after the coating with Silicalite-1 [61,81]. Li G. et al. suggested that the reduction of micropores in the core-shell sample was due to the use of tetraethyl

orthosilicate in the hydrothermal synthesis. They noted that during the crystallization process, some of this material was lost, resulting in the formation of an amorphous silica layer on the surface of the initial HZSM-5 zeolite [81].

To evaluate the effect of the coating with Silicalite-1 on the acidity of final core-shell samples, NH_3-TPD and FT-IR analysis have been performed [62,64,65,77,79,81]. Ammonia temperature programmed desorption analysis has been employed to understand how the non-acidic layer of Silicalite-1 influences the total acidity of the final core-shell samples. Moreover, NH_3-TPD analysis results also revealed the amount of weak and strong acid sites before and after the passivation performed by the epitaxial growth of Silicalite-1 crystals. A decrease of both peaks related to weak and strong acid sites was found for ZSM5@Silicalite-1 samples [64,81]. The impact of successive coatings with silicalite-1 on the overall acidity was assessed through NH_3-TPD analysis. Results indicated that the introduction of Silicalite-1 led to a reduction in the total number of acid sites, demonstrating a nearly linear correlation between the amount of acid and the number of Silicalite-1 coatings [62]. Acidity evaluation in terms of Brønsted and Lewis acid site distribution was performed via FT-IR analysis employing different probe molecules. Among these, pyridine has been frequently utilized because it interacts with both internal and external Brønsted and Lewis acid sites. However, to study the external acidity of samples other probe molecules have been chosen.

2,6-ditertbutyl-pyridine (DTBPy) has a diameter of 10.5 Å larger than the pore size of ZSM-5 zeolites and it could easily protonate Brønsted acid sites [61,62]. The band at 1615 cm^{-1} observed in the spectra of adsorbed DTBPy on ZSM-5 relates to the ring vibration mode of the $DTBPyH^+$ ion. Jin Z. et al observed the decrease of this band for ZSM5@Silicalite-1 samples and with the increase of Silicalite-1 loadings (**Figure 12a**). In other works, 2,4,6-collidine was employed to evaluate external acidity [77]. In fact, it is characterized by three methyl groups and possesses a kinetic diameter of 7.4 Å, larger than the pore size of MFI zeolites (measuring 5.5 Å). Consequently, this size disparity restricts the access of collidine exclusively to acid sites located within auxiliary mesopores and the external surfaces of the MFI structure. FT-IR spectra collected after the adsorption of 2,4,6-collidine over ZSM5 zeolites exhibited the presence of two main bands: the band at 1632 cm^{-1} corresponds to

2,4,6-collidine linked Lewis acid sites and the appearance of absorption bands at 1648 cm^{-1} refers to 2,4,6-collidine adsorbed at Brønsted acid sites. Yi D. et al. employed 2,4,6-collidine as a probe to study external acidity evolution as the crystallization time of Silicalite-1 layers increased from 2 to 16 hours (**Figure 12b**). The authors found that the rise in crystallization time resulted in a reduction of the peak areas detected at 1632 and 1648 cm^{-1}. This decline implies a gradual covering of the Brønsted and Lewis acid sites situated on the surface of HZSM-5 crystals by the silicalite-1 shell.

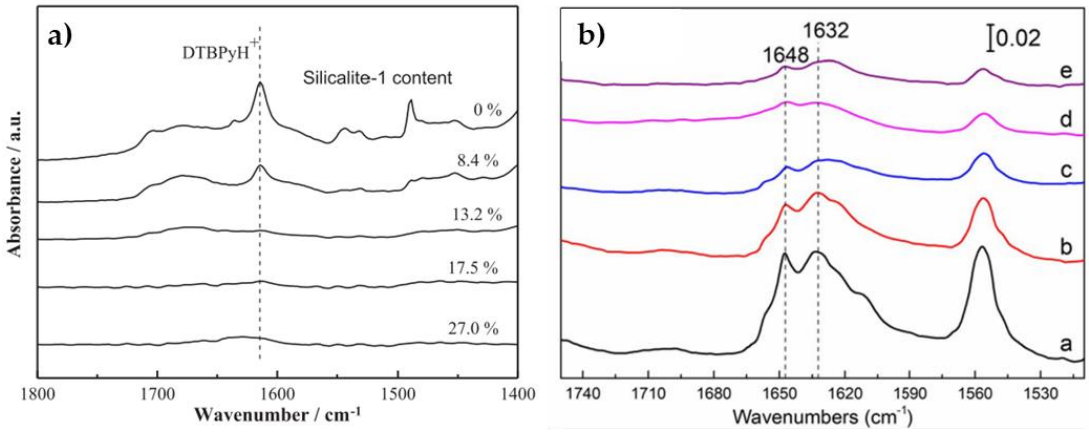

Figure 12: DTBPy [62] **(a) and 2,4,6-collidine** [77] **(b) FTIR spectra obtained for ZSM5@Silicalite-1 catalysts.**

ZSM5@Silicalite-1 core shells have been widely used for various catalytic applications where the neutralization of external acidity could improve catalysts' performances. Among these, para-xylene production via toluene methylation has attracted the attention of researchers in the last years [50–52,74,81,82]. Because of the medium size of its pores, ZSM-5 found widespread use also in p-xylene synthesis via toluene alkylation using methanol. Its pore structure closely matches the size of p-xylene molecules which are formed inside zeolite channels. Nonetheless, once formed, p-xylene molecules swiftly convert into meta- and ortho-isomers on the external surface acid sites of zeolites. To prevent this secondary isomerization process, surface modifications have been implemented, focusing on adjusting the acid properties and pore structure of the zeolites [83]. The epitaxial growth of a Silicalite-1 layer over the external surface of HZSM-5 crystals contributed to reduce the above-mentioned issues. Silicalite-1 shell serves to deactivate the external acid sites of

ZSM-5 and extends the diffusion path for xylenes, without obstructing channels or constricting pore sizes. The elongated diffusion pathways favor higher para-selectivity and shape selectivity, facilitating the conversion of o-xylene and m-xylene into p-xylene and ensuring the release of p-xylene as the primary product from the outer channels. Excellent results and improved catalytic performances have always been obtained. Van Vu. et al. tested uncoated and coated H-ZSM5 in different reaction conditions. ZSM5@Silicalite-1 catalysts tested exhibited remarkable para-selectivity, surpassing 99.9% under various reaction conditions. Moreover, the toluene conversion rates remained constant employing core-shell catalysts, indicating that the Silicalite-1 coating effectively prevented coke formation on the external surface of H-ZSM-5 [51].

Excellent results, in terms of catalyst stability and reduction in coke production, were also obtained by using ZSM5@Silicalite-1 type catalysts in the conversion of methanol to gasoline [66,79].

Catalytic fast pyrolysis of biomass over core-shell ZSM5@Silicalite-1 has also been performed to try to reduce external acidity while preserving the internal one [48]. Results obtained testing the uncoated HZSM-5 and synthesized HZSM-5@silicalite-1 samples indicated noticeable differences in product distributions. The presence of Silicalite-1 coating notably enhanced the production of olefins and BTX (Benzene, Toluene, Xylene), especially promoting the production of BTX. Additionally, the formation of catalyst coke and Polycyclic Aromatic Hydrocarbons (PAHs) was significantly suppressed after applying the Silicalite-1 coating to the HZSM-5 catalyst.

Silicalite-1 layer growth over a ZSM-5 core has been employed to reduce the occurrence of side reactions during the catalytic cracking of hexane [84]. The authors found that by employing core H-ZSM5 zeolite the highest conversion of hexane was obtained together with the highest selectivities of light alkanes and BTX. On the contrary, employing core-shell catalysts allowed to enhance selectivities of light olefins although a slight decrease in hexane conversion was detected. External acid sites of H-ZSM5 zeolite led to the aromatics reaction of hexane and the conversion of light olefins to aromatics and light alkanes through oligomerization, cyclization, aromatization, and hydrogen transfer reactions. On the

contrary, the decrease of external acid sites led to a suppression of the aromatization reaction of hexane, resulting in decreased selectivities of BTX compounds and consequently increased selectivities of olefins. Additionally, the deactivation of active sites on the exterior acted as a protective measure for the formed olefins, preventing further deep reactions. Moreover, it has been demonstrated that the coating of Silicalite-1 on the surface of ZSM-5 zeolite not only passivates external acid sites but also allows for improved hydrothermal stability of catalysts [70,76]. In their work, Miyake K. et al. synthesized ZSM5@Silicalite-1 samples and conducted investigations into the combined effects of steam treatment and NH_3-temperature programmed desorption [70]. Notably, the NH_3-TPD profiles of the core-shells exhibited an unchanged peak area at higher temperatures even after an 8-hour steam treatment unlike what was observed with the uncoated ZSM-5 sample. These findings suggested that Silicalite-1 coatings significantly enhanced hydrothermal stability avoiding the penetration of steam up to the internal Al sites.

2.1.1 Others zeolite@zeolite core-shell catalysts.

The synthesis of core-shell type catalysts coupling two different zeolitic structures for the core and the shell represents an interesting challenge. Creating zeolite composites by combining shell zeolites, which have smaller pore sizes, with core zeolites possessing larger pore sizes, is a rational approach. This combination aims to effectively take advantage of both individual properties in separation and adsorption. Shell structure could be used for separation while enabling further catalytic transformations within the core. Furthermore, the shell, as already explained, could simultaneously passivate the external acidity of the core avoiding the occurrence of side reactions. Recent developments have reported the synthesis of core-shell zeolite-zeolite composites featuring different structural types [85–87]. Valtchev and co-workers prepared different core-shell zeolite-zeolite composites employing a two-step technique: the first step was the adsorption of seeds over the surface of the starting cores treated with a polycation agent and the second step was the hydrothermal synthesis of the shell [86]. Various zeolitic materials were utilized to explore the impact of framework composition and the synthesis conditions of both the core and shell crystals on

the production of these microcomposites. Particularly, all-silica sodalite@zeolite A, zeolite Beta@zeolite A, zeolite X@silicalite-1, ZSM-5@zeolite Beta, and ZSM-5@silicalite-1 combinations were studied. Analyzing the results obtained, the authors were able to assess that the successful formation of core-shell structures occurred in cases where the materials had compatible framework compositions and closely aligned crystallization conditions. It was observed that a wider overlap between the crystallization region (temperature and Si/Al ratio) promoted the composite formation, whilst the stability range less superimposed confirmed a difficulty in obtaining the core-shell structure (**Figure 13**). In other words, a smaller overlapping area indicates greater challenges or difficulty in achieving the stable presence of both phases and the formation of the core-shell structure as a consequence. The formation of a FAU-MFI core-shell structure was unsuccessful because of the lack of overlapping area between their compositions and synthesis conditions (**Figure 13**). Conversely, when dealing with zeolite Beta and ZSM-5, the close similarity in their framework compositions and synthesis conditions led to a notably easier formation of a core-shell material.

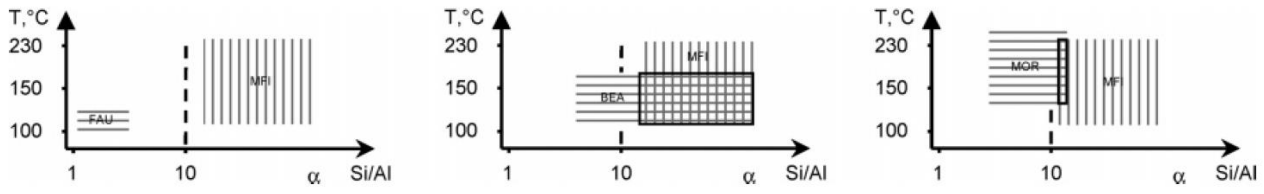

Figure 13: Correlation between the Si/Al ratio and crystallization temperature for various types of zeolite structures: FAU-MFI, MFI-BEA, and MOR-MFI [86].

Recently, to overcome the complex synthesis strategies used which include the seeding stage of the core surface, a new technique for the production of BEA@Silicalite-1 core-shell catalysts has been developed [88]. Particularly, steam-assisted crystallization has been employed for the growth of Silicalite-1 crystals over the surface of the starting BEA zeolite. Firstly, the precursor solution of Silicalite-1 was prepared and heated at 80°C for 4 hours. Subsequently, particles of zeolite Beta were immersed in this Silicalite-1 seed solution, followed by centrifugation and drying at 80°C. Finally, the zeolite Beta particles coated with

Silicalite-1 seeds were transferred onto a Teflon stage within a Teflon-lined stainless-steel autoclave containing 2.0 mL of water at the bottom and heated at 140°C typically for 4 hours. The authors studied the effect of different aspects, such as crystallization time and temperature, on the success of synthesis and on obtained core-shell characteristics. XRD analysis together with SEM micrographs have been employed to demonstrate the success of Silicalite-1 coating over BEA core. Moreover, N_2 adsorption/desorption tests have been used to obtain some interesting information. Beta@Silicalite-1 uncalcined sample revealed a lower amount of volume adsorbed compared to the calcined one; this result demonstrated the successful coating of the core with Silicalite-1 shell that contains TPA^+ inside the pores avoiding N_2 adsorption. In this work, various crystallization times (0, 2, 4, 6, 12, and 24h) were investigated. Characterizations carried out allowed researchers to establish that the optimal crystallization temperature was 4 h. After 4 hours a homogeneous shell with an MFI structure was observed on the surface of the starting BEA zeolite. After 6 or more hours, however, the destruction of the BEA structure was observed and correlated to the corrosive effect of the basic synthesis gel employed. The optimal crystallization temperature was set at 140°C because at lower temperatures the crystallization of silicalite-1 was not complete and, instead, higher temperatures triggered significant erosion due to the alkali present in the dry gel. Finally, the authors demonstrated that even a minimal quantity of aluminum within the core zeolite was necessary to avoid corrosion induced by the crystallization of the shell dry gel at 140°C for 4 hours.

2.1 Other external acidity passivation techniques

To achieve the goal of passivating the external surface of zeolite, responsible for coke formation and the loss of high selectivity during reactions, many other different techniques have been employed. In this paragraph, an overview of the main procedures studied and applied in literature has been presented. Particularly, **Table 3** summarizes the major passivation techniques and the catalytic applications of passivated catalysts.

Table 3: Passivation techniques employed in literature and catalytic applications of passivated catalysts.

Refs.	Zeolite to be passivated	Passivation method employed	Catalytic application
[89]	ZSM-5	Chemical liquid deposition of TEOS	Methanol to Olefins (MTO)
[90]	ZSM-5	Chemical liquid deposition of TEOS (tetraethyl orthosilicate)	-
[80]	ZSM-5	Chemical liquid deposition of TEOS	Toluene disproportionation
[91]	ZSM-5	HNO_3 treatments	Catalytic Cracking of paraffins
[92]	ZSM-5	MgO and 2,4-dimethylquinoline (2,4-DMQ) deposition	Catalytic Fast Pyrolysis of bio-derived furan
[93]	ZSM-5	Functionalization with HDTMA and impregnation with Phosphoric acid	Alkylation of toluene with methanol
[94]	ZSM-5	Impregnation with Phosphorus	Benzene alkylation with methanol
[95]	ZSM-5	Treatments with antimony oxide	Toluene disproportionation
[96]	ZSM-5	Dealumination in oxalic acid solutions and Chemical liquid deposition of TEOS	Isomerization of o-X/ Cracking of TIPB/ Competitive reaction of EB and m-X
[97]	ZSM-5	Desiliconization followed by Chemical liquid deposition of TEOS	Methanol to Aromatics (MTA)
[98]	ZSM-5	Chemical liquid deposition of TPEOS (triphenyl ethoxy silane)	Catalytic cracking of n-decane
[99]	ZSM-22	Alkaline treatment with NaOH	1-Butene Skeletal Isomerization
[100]	MOR	Chemical liquid deposition of TEOS or of 3,5-dimethyl phenyl magnesium bromide (DPB)	Isomerization of o-ethyltoluene

Refs.	Zeolite to be passivated	Passivation method employed	Catalytic application
[101]	ZSM-5	Chemical vapour deposition of TEOS and germanium tetraethoxide	Catalytic Cracking of hexane and of 1,3-di-isopropyl benzene.
[102]	BEA	Chemical liquid deposition of TEOS and trimethylchlorosilane	MPV reduction of 4-tert-butylcyclohexanone
[103]	ZSM-5	Chemical vapour deposition of silicon tetrameth-oxide	Alkylation of toluene with methanol
[104]	SSZ-13	Chemical liquid deposition of TEOS tramethylorthosilicate (TMOS), and tetrabuthylorthosilicate (TBOS)	Ethylene to Propylene
[105]	ZSM-5	Chemical liquid and vapour deposition of TEOS followed by impregnation with MgO	alkylation of ethylbenzene with ethylene

Among the various techniques summarized in **Table 3**, chemical liquid deposition of TEOS has been widely used to passivate the external surface of different zeolites. Usually, the chemical vapor deposition treatment involves mixing/stirring a specific quantity of zeolite with hexane, followed by a heating step. Then tetraethyl orthosilicate is added to the mixture and the silylation proceeds for a fixed time. In the last steps, hexane is removed by evaporation and the sample is finally dried and calcined [90]. Silylation procedures are often repeated more than once to ensure the neutralization of all external acid sites. Post-synthesis modification via chemical vapour deposition of TEOS has also been often employed to passivated external acid sites [101,104] but the key advantage of conducting the reaction in the liquid phase (CLD) as opposed to the gas phase (CVD) lies in its increased adaptability for scaling up in industrial settings to produce larger quantities more easily.
Zheng S. et al studied the mechanism of chemical liquid deposition of TEOS employing H-ZSM5 zeolites and passivating them one or three times [90]. FT-IR measurement

conducted employing pyridine and di-tert-butyl-pyridine (DTBPy) as probes allowed them to propose a silylation mechanism in chemical liquid deposition. Results regarding acid site distribution after silylation treatments showed that the reaction of tetraethyl orthosilicate (TEOS) with Lewis acid sites precedes its reaction with silanol and bridging hydroxyl groups. In fact, after the first deposition cycle, all the accessible Lewis acid sites were passivated instead multicycle silylation was required to further decrease the concentration of silanol and bridging hydroxyl groups. This is attributed to the higher accessibility of TEOS to external surface Lewis acid sites and their probably stronger acidity. The mechanism proposed by the authors is reported in **Figure 14**. During the liquid-phase reaction, tetraethyl orthosilicate (TEOS) undergoes hydrolysis exclusively on Brønsted and Lewis acid sites, forming Si-O-Al bonds. Upon calcination, the remaining ethoxyl groups convert into hydroxyl groups, partially merging with adjacent silanol groups to create Si-O-Si bonds. For this reason, chemical vapour deposition of TEOS caused a decrease of Brønsted and Lewis acid sites, as well as silanol groups within the zeolite.

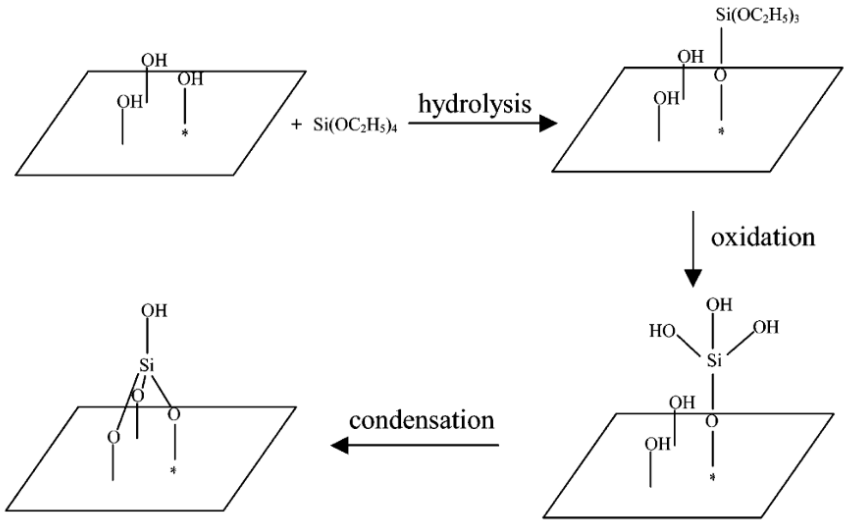

Figure 14: Silylation mechanism

Sample passivated via chemical liquid deposition of TEOS were successfully employed for different catalytic applications. Valtchev et al. employed silylated nanosized ZSM-5 for methanol to olefins reactions reaching higher selectivities versus light olefins. Meanwhile, they noticed that the repetition of the passivation process likely resulted in the narrowing of pore mouths. This narrowing could potentially accelerate the deactivation rate compared

to the original samples [89]. Also in other published works, the decrease of micropore area after the chemical vapour deposition of TEOS has been underlined [96].

Post-synthetic treatments with HNO_3 have been used to remove Al selectively from the external surface of ZSM-5 zeolites reducing consequently the concentration of external acid sites and enhancing catalysts stability during the catalytic cracking of n-hexane [91].

Moreover, it was recently demonstrated that the modification of the external surface of ZSM-5 zeolite using positively charged hexadecyltrimethylammonium resulted in selective deposition of phosphorus on the external surface and pore entrance. This modification led to enhanced para-selectivity in the process of alkylating toluene with methanol [93]. In addition to those already mentioned, other innovative techniques have also been used to passivate external acidity such as the deposition of MgO and 2,4-dimethylquinoline (2,4-DMQ) [92] or of antimony oxide [95]. Although the passivation goal is also achieved with these methods, the significant deposition of amorphous layers on the surface of the starting zeolite causes a decrease in crystallinity and a narrowing of the pore's mouths.

CHAPTER 3. Materials and methods

To comprehensively investigate the effect of surface acidity in different catalytic applications, passivation procedures have been employed to neutralize external acid sites of the starting parent zeolites. Zeolites with different channel systems have been synthesized. Particularly, MFI and BEA zeolites have been prepared and syntheses of MFI zeolites with different content of aluminium were also carried out, to investigate the effect of the Si/Al ratio over acid sites distribution.

Particularly, based on the use of as-made "core" zeolites, a novel strategy to perform the epitaxial growth of Silicalite-1 over the surface of zeolite crystals has been developed. This technique will be fully explained in the following paragraphs.

All the samples investigated during this research project have been synthesized in the laboratory using hydrothermal conditions by the employment of Teflon-lined stainless-steel autoclaves. Before each synthesis a cleaning procedure for the autoclaves was carried out; the first cleaning step was done using nitric acid (68%) to remove traces of organic molecules and the second step was performed using hydrofluoric acid (48%) to remove traces of zeolite crystals eventually left in the autoclaves from the previous synthesis. Finally, distilled water was used to wash autoclaves until a neutral pH value was achieved.

3.1 Synthesis of MFI-type samples.

MFI-type zeolites with Si/Al ratio in the synthesis gel equal to 11, 25, and 50 were synthesized. The synthesis gels were prepared according to the following molar ratios:

$$0.08\ Na_2O - 0.08\ TPABr - 1\ SiO_2 - x\ Al_2O_3 - 20\ H_2O$$

(where x= 0,045-0.01-0.02 to set the Si/Al ratio). The chemicals used for the syntheses were Silica gel 60 (Aldrich), sodium aluminate ($NaAlO_2$, Aldrich), sodium hydroxide (Aldrich), distilled water and tetrapropylammonium bromide (TPABr, VWR Chemicals) as structure directing agent (SDA). The hydrothermal syntheses were conducted in 150 ml PTFE-lined stainless-steel autoclave at 170 °C for 7 days (Si/Al=11), 4 days (Si/Al ratio = 25), and for 3

days (Si/Al ratio = 50). The crystalline phase was separated from the mother liquor, carefully washed with distilled water, and dried at 90 °C overnight. To obtain the zeolites in their acidic form, samples were firstly calcined at 550°C for 8 hours (thermal ramp of 5°C/min, static air), subjected to a double ion exchange with NH_4Cl (1M), and calcined again as previous. MFI catalysts synthesized were named Z11, Z25 and Z50. Different batches of the same MFI samples were synthesized during this research work and used in different applications; syntheses reproducibility was verified and samples with similar properties were always obtained but, where necessary, characterizations of zeolites obtained from different batches have been shown in the following paragraphs.

3.2 Synthesis of BEA-type samples.

A sample with BEA structure and a Si/Al ratio in the synthesis gel equal to 25 was prepared starting from the following synthesis gel:

$$0.10Na_2O - 0.2TEAOH - 1SiO_2 - 0.02Al_2O_3 - 10H_2O$$

Chemicals used were Silica gel 60 (Aldrich), sodium aluminate (NaAlO2, Aldrich), sodium hydroxide (Aldrich), tetraethylammonium hydroxide (TEAOH, Aldrich), and distilled water. The prepared synthesis solution was stirred for 2 hours at room temperature and then transferred into an autoclave left in the oven at 150°C for 6 days. The product was washed carefully with distilled water and dried at 90°C overnight. To reach the acid form, the same procedure described in the previous paragraph was carried out.

3.3 Surface acidity passivation via the epitaxial growth of Silicalite-1: ZSM5@Sil-1 samples.

The epitaxial growth of a thin layer of Silicalite-1 was the first adopted technique to passivate the surface acidity of the parent MFI zeolites. Silicalite-1 synthesis gel was prepared including TEOS (TEOS, Aldrich) as silica source, tetrapropylammonium hydroxide (TPAOH, Aldrich) as structure directing agent, and alkali source, ethanol, and distilled water. The obtained solution was characterized by the following molar ratios:

$$2\ SiO_2 - 0{,}5TPAOH - 8EtOH - 120H_2O$$

ZSM-5 zeolite crystals previously synthesized were then immersed in the Silicalite-1 synthesis gel and mixed for a while. The crystallization of the layer of Silicalite-1 was carried out using a Teflon-linen stainless-steel autoclave under hydrothermal conditions at 180°C for 24 hours in a tumbling oven (**Figure 15**). The solid product obtained was separated from the mother liquor, carefully washed with distilled water, and dried at 90 °C overnight [106].

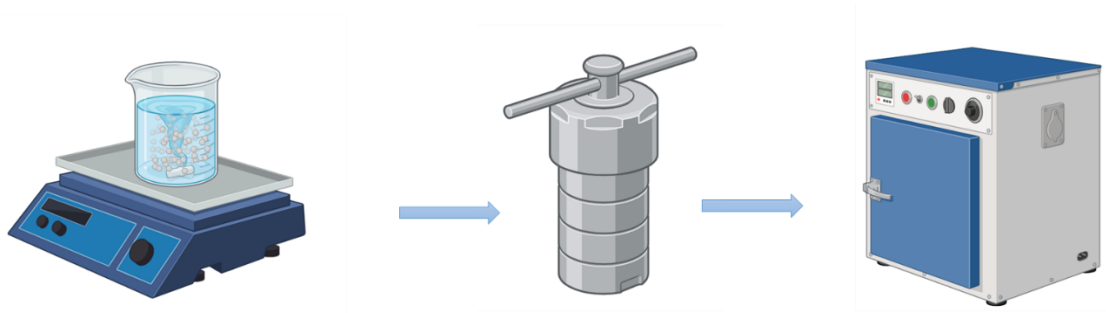

Figure 15: Steps of Silicalite-1 deposition (Created with BioRender.com).

The first efforts of this research work were focused on the coating with Silicalite-1 of a ZSM-5 zeolite with the highest aluminum content possible [107]. Since total acidity value increases with the decrease of the Si/Al ratio (**Chapter 4, paragraph 4.1.7**), the choice of coating a ZSM-5 zeolite with a Si/Al ratio equal to 11 was done to evaluate the probably stronger effect of passivation procedure over surface acidity of the starting catalyst. 5 grams of zeolite in H^+-form were immersed in the Silicalite-1 synthesis gel with a ratio of 0.6 between the mass of zeolite to be passivated and the mass of synthesis gel. Hydrothermal synthesis of the Silicalite-1 layer was then conducted as already explained above. The as-synthetized composite material was then calcined at 550°C for 8 hours (using a thermal ramp of 2°C/min under static air). A part of this sample was used for further characterizations and was labeled as H-Z11_X where X indicated the presence of a single Silicalite-1 layer. To increase the thickness of the layer, the passivation procedure was repeated twice in the same conditions. The sample obtained after the second deposition cycle was named H-Z11_XX (double X indicated the coating with two layers of Silicalite-1).

The following step of the research concerned the idea of improving the technique used for the epitaxial growth of Silicalite-1. Physical properties characterizations results of passivated samples obtained (H-Z11_X and H-Z11_XX) revealed that Silicalite-1 crystals probably grew over the pores mouths of the starting parent zeolite causing a partial blockage of channels (see **paragraph 4.1.6** for detailed discussion). For this reason, the strategy adopted was changed, synthesizing passivated samples using an MFI zeolite with a Si/Al ratio equal to 25 but performing the coating over the synthetised-form core and keeping the procedure using H^+-form core as a reference, to understand if the presence of structure directing agent in the pores of the starting crystals could prevent the partial occlusion found for the previous obtained samples. ZSM-5 zeolite crystals with the organic template still inside the pores (AS-Z25) were then coated with a layer of Silicalite-1 following the same procedure described above and the sample obtained was named AS-Z25_X where AS indicated the core form during the shell deposition. Also in this case, the procedure was repeated twice to promote the growth of a second layer of Silicalite-1 over the small crystals of Silicalite-1 deposited during the first synthesis. For this reason, a part of the AS-Z25_X sample was subjected to the classical procedure to obtain the H+-form, and the rest was passivated again to obtain the AS-Z25_XX sample. The same ZSM-5 zeolite crystals in H^+-form were employed to obtain H-Z25_X and H-Z25_XX samples (H indicating the H^+-form of the core then coated with Silicalite-1). Catalysts were all characterized to deeply investigate the effect of the organic template filling the pores of the starting zeolite on obtained passivated sample properties.

Therefore, after having established which was the best technique for the epitaxial growth of Silicalite-1 (see **Chapter 4** for detailed discussion), the effect of the Si/Al ratio of the parent zeolite on the passivation treatment was then analyzed. For this reason, the MFI zeolite with a Si/Al ratio equal to 50 (Z50) was used and its surface acidity was neutralized by the growth of two thin layers of Silicalite-1. Specifically, the zeolite was covered starting from a core with the organic template agent filling the pores according to the procedure already described. Moreover, the Z11 sample was also subjected to two cycles of passivation starting

from the core with the organic template inside the pores, and sample AS-Z11_XX was obtained.

Finally, to increase the degree of coating, MFI zeolites with a Si/Al ratio equal to 11 and 25 were coated with two layers of Silicalite-1 but doubling the ratio between the grams of the starting as synthetized-form crystals (to be coated) and the grams of Silicalite-1 synthesis gel used (ratio ≅ 1,2). To identify these samples the codes AS-Z25_2XX and AS-Z11_2XX were used. All obtained samples codes and main features are summarized in **Table 4**. Also, in this case, it is useful to underline that samples AS-Z25_2XX, AS-Z11_XX and AS-Z11_2XX were obtained starting respectively from a ZSM-5 zeolite with a Si/Al ratio of 11 and one with a Si/Al ratio equal to 25 different from those used for the other passivated catalysts (H-Z11_X, H-Z11_XX and H-Z25_X, H-Z25_XX, AS-Z25_X and AS-Z25_XX).

The reproducibility of synthesis techniques of both the parent zeolites and of the subsequent layers of Silicalite-1 was verified and the characterizations of specific samples will be shown only if necessary.

Table 4: Synthesised H/AS-ZY_X/XX/2XX samples: where H and AS indicated the H^+-form or the as synthesised-form of the core, Y indicated the Si/Al ratio of the starting core, X and XX indicated the presence

of one or two layers of Silicalite-1 and 2XX indicated the presence of two layers of Silicalite-1 coated employing a double quantity of Silicalite-1 synthesis gel.

Sample code	Passivation treatment	Cycle of Passivation	To be coated crystals/Sil-1 synthesis gel (g/g)
H-Z11	-	-	-
H-Z11_X	Sil-1 epitaxial growth	One	0.6
H-Z11_XX	Sil-1 epitaxial growth	Two	0.6
AS-Z11_XX	Sil-1 epitaxial growth	Two	0.6
H-Z25	-	-	-
H-Z25_X	Sil-1 epitaxial growth	One	0.6
H-Z25_XX	Sil-1 epitaxial growth	Two	0.6
AS-Z25_X	Sil-1 epitaxial growth	One	0.6
AS-Z25_XX	Sil-1 epitaxial growth	Two	0.6
H-Z50	-	-	-
AS-Z50_XX	Sil-1 epitaxial growth	Two	0.6
AS-Z11_2XX	Sil-1 epitaxial growth	Two	1.2
AS-Z25_2XX	Sil-1 epitaxial growth	Two	1.2

3.4 Synthesis of composite BEA@Silicalite-1 via steam-assisted crystallization.

BEA crystals, previously synthesized in as made form as described in Par. 2.2, were used as the core for the Silicalite-1 deposition via Steam Assisted Crystallization (SAC). Silicalite-1 synthesis gel was prepared and heated at 80 °C for 4 h under stirring according to the following molar ratios:

$$1SiO_2 - 0.33TPAOH - 30H_2O$$

2.5 g of the as-made BEA core crystals were then immersed into the Silicalite-1 precursor solution (ratio between the mass of zeolite and the mass of the Sil-1 gel equal to 0.5), stirred to promote the contact between the two phases, centrifuged, and dried at 90°C as shown in **Figure 16** [88].

Figure 16: First steps of BEA@Sil-1 synthesis (Created with BioRender.com).

Once dried, the sample was grounded in a mortar and transferred to a Teflon holder placed in a Teflon-lined stainless-steel autoclave with 5.0 mL water in the bottom. SAC was then conducted at 140°C for 4h (**Figure 17**). The products were rinsed repeatedly with deionized water and dried at 90°C overnight.

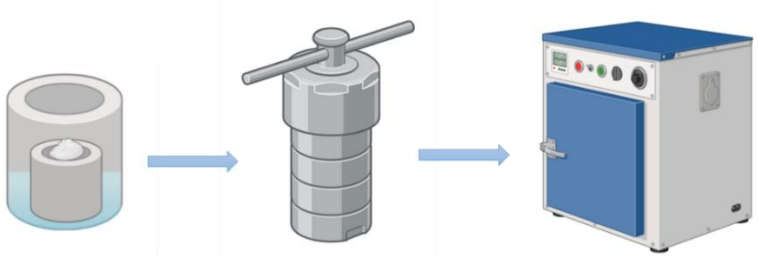

Figure 17: Steam-assisted crystallization (SAC) of BEA@Sil-1 synthesis (Created with BioRender.com).

The sample obtained after the first deposition cycle was named BEA_X. A part of this catalyst was calcined in air at 550°C for 8 h, ion-exchanged, and then calcined again to obtain the H^+-form, instead, the remaining part was used to repeat the coating procedure in order to increase Silicalite-1 layer thickness. The catalyst obtained from the second Silicalite-1 coating, labeled BEA_XX was then processed to obtain the H^+-form. Samples obtained and used for further investigation are summarized in **Table 5.**

Table 5: Parent BEA-type zeolite and composite BEA@Sil-1 samples obtained via steam-assisted crystallization.

Sample code	Post synthesis treatment	Cycles of Passivation	To be coated crystals/Sil-1 synthesis gel (g/g)
BEA	-	-	-
BEA_X	SAC of Sil-1	One	0.5
BEA_XX	SAC of Sil-1	Two	0.5

3.5 Surface passivation of ZSM-5 zeolites via chemical liquid deposition of TEOS.

MFI zeolites with a Si/Al ratio equal to 11 and 25 were also subjected to a treatment of surface passivation through chemical liquid deposition (CLD) using tetraethylorthosilicate (TEOS) [89]. 1 g of calcined zeolite was mixed under vigorous stirring with 25 mL of hexane and heated at 60°C under reflux. Then, 0,15 mL of TEOS was added and the solution was stirred for another hour. Finally, hexane was removed using a rotavapor by evaporation. The treated sample was then dried at 90°C and then calcined at 550°C. Surface silylation was repeated three times. Sample obtained after the surface treatments are summarized in **Table 6** and named H-Z11_S and H-Z25_S where S indicated the passivation via surface silylation carried out.

Table 6: Samples obtained via chemical liquid deposition of TEOS over the surface of MFI zeolites.

Sample code	Passivation treatment	Cycle of Passivation
H-Z11_S	CLD of TEOS	Three
H-Z25_S	CLD of TEOS	Three

3.6 Catalysts Characterizations.

All the examined catalysts have been characterized utilizing various techniques. These include X-ray diffraction (XRD), porosimetric analysis, chemical analysis, thermogravimetric/differential thermal analysis (TG/DTA), scanning electron microscopy (SEM), and energy dispersive X-ray analysis (EDX). Some of them were also characterized by transmission electron microscopy (TEM). Acidity characterization of catalysts was carried out employing thermal programmed desorption analysis of pre-absorbed ammonia (NH_3-TPD) and Fourier transform infrared spectroscopy (FT-IR).

3.6.1 XRD

Powder X-ray diffraction is a widely used technique employed to analyze the crystalline phases within solid materials, utilizing Bragg's equation as a fundamental principle [108]. When applied to zeolite powders, this analysis enables the examination of crystallization evolution, material purity, and the determination of sample crystal size. By utilizing this technique, a spectrum is generated through X-ray diffraction within the atomic lattice space. Particularly, the diffraction pattern consists of a series of peaks obtained by varying the incidence angle (2θ) of the X-ray beam. Comparing this pattern with published references facilitates the identification of the obtained phase(s). Furthermore, analyzing peak intensity and shape allows the extraction of information regarding sample crystallinity. The XRD patterns of the investigated catalysts were obtained using Miniflex (Rigaku, Japan) at a scanning rate of 0.05°/min (from 5° to 40°).

3.6.2 Porosimetric analysis

Structural properties of the samples are estimated by means of a 77 K nitrogen adsorption/desorption isotherm in a range of relative pressure 0 – 99 P/P°. For this purpose, the Micromeritics ASAP 2020 porosimeter was used. The specific surface area has been estimated employing the BET model while external area, micropore area, and micropore volume have been calculated using the t-plot method [109].

3.6.3 Chemical analysis

To determine the chemical composition in terms of aluminum and silicon in the samples, we employed atomic absorption spectroscopy (GBC 932 AA), a technique commonly used for quantitative analysis. In this method, the sample is exposed to radiation of a specific wavelength within the UV/visible region, causing its intensity to decrease due to absorption effects. This decrease correlates with the concentration of the element in the sample. Before conducting the measurement, the zeolite undergoes dissolution in hydrofluoric acid (HF) with a concentration of 40% and nitric acid (HNO_3) with a concentration of 65%. This dissolution process is followed by dilution to ensure that the sample's concentration aligns with the calibration range of the instrument used for analysis.

3.6.4 TG/DTA

Thermogravimetric (TG) and differential thermal (DT) analysis have been conducted to estimate the quantity of organic Structure-Directing Agents (SDA) confined within the channels of the synthesized material determining their combustion temperature and to assess the quantity of coke deposited during the reaction. Analyses were performed employing a DSC-SDT 650 instrument and heating the sample from ambient temperature to 850 °C (heating ramp of 5°C/min) under air flow (100 ml/min).

3.6.5 SEM/EDX

Scanning Electron Microscopy (SEM) using the Phenom Pro G6 instrument from ThermoFisher Scientific was employed to examine the catalysts' morphology. SEM images were captured at various magnifications subsequent to sputter-coating the samples with

gold. Additionally, to estimate the Si/Al ratio, Energy-Dispersive X-ray (EDX) analyses were conducted employing different voltages.

3.6.6 TEM

Some of the synthesized samples were characterized by employing Transmission Electron Microscopy (TEM) in collaboration with Professor Svetlana Mintova of the "Laboratoire Catalyse et Spectrochimie (LCS)" (Caen, France). Analyses were conducted using a JEOL F200 transmission electron microscope operated at 200 kV equipped with a Gatan RIO16 camera and a JEOL Centurio EDS detector.

3.6.7 NH_3-TPD

Temperature-programmed desorption of ammonia (TPD) is a straightforward and consistent method employed to assess both the quantity and strength of acid sites present within zeolites. The procedure involves initially adsorbing ammonia onto the sample, followed by its desorption using a controlled thermal ramp. The desorbed ammonia molecules are then detected using either Thermal Conductivity Detectors (TCD) or Mass Spectrometry (MS) detectors. The quantification of acid sites involves estimating the quantity of desorbed ammonia, while the determination of their strength is derived from analyzing the temperatures at which desorption peaks occur. The analyses have been conducted employing a TPDR0 1100 instrument. Firstly, about 100 mg of dry catalysts are placed within a quartz tubular reactor, positioned between two layers of quartz wool. The reactor is then placed in one of the two ovens of the TPDR0 to start the pretreatment of the sample which consists of 4 steps:

- Drying: Subjecting the sample to drying at 300°C in a helium flow of 20 mL/min for 30 minutes, followed by cooling to 150°C and maintaining this temperature for 5 minutes.
- Adsorption: Introducing ammonia at 150°C using a diluted ammonia stream (NH_3/He, 10% v/v) with a flow rate of 20 mL/min for 120 minutes to allow ammonia adsorption onto the sample.

- Removal: Purging the sample with helium flow at 20 mL/min for 90 minutes to eliminate physically adsorbed ammonia.
- Cooling: Cooling the sample down to 100°C.

The analysis involves the desorption of ammonia previously adsorbed on the sample. The sample is heated in a helium stream at a flow rate of 20 cm3/min, starting from 100°C and gradually increasing to 700°C at a heating rate of 10°C/min. Subsequently, the catalyst is maintained at the maximum temperature for two hours. The output current from the reactor is then examined using a Thermal Conductivity Detector (TCD) for analysis. Experimental data are analyzed using software (PeakFit 4.12) to obtain the deconvolution of peaks and the quantification of peaks area attributable to the ammonia adsorbed on the sample through the use of a calibration line.

3.6.8 FT-IR

The analysis of zeolite acidity involves various techniques, with FT-IR analysis of adsorbed probe molecules being a key method. This technique allows the discrimination between Brønsted and Lewis acid sites on solid catalysts like zeolites. By adsorbing specific probe molecules and analyzing the resulting FT-IR spectra, the interaction between zeolite active sites and the probe molecules can be studied. This interaction induces changes in energy absorption in the infrared region, enabling the identification of the type of active acid sites.

FT-IR measurements were carried out using a Nicolet iS 10 instrument equipped with a DTGS detector. Before analysis, samples were compressed into wafers (P=3 ton) of approximately 25 mg and pre-treated at 400°C under vacuum (10^{-5} torr). Room temperature FT-IR spectra were then recorded under vacuum to assess silanol group characteristics in the zeolite materials. To delve deeper into Brønsted and Lewis acidity, d3-acetonitrile was employed as a probe molecule. The adsorption of d_3-acetonitrile involved exposing sample wafers to the probe at 298 K, followed by evacuation for 1 hour at the same temperature before FT-IR measurements. Total acid site numbers were determined using the Lambert-Beer law, integrating the area of protonated species bands. The equation employed is $A= \varepsilon N \varrho$ where A is the integrated area, ε is the molar extinction coefficient ($cm \cdot mmol^{-1}$),

N is the concentration of the vibrating species (mmol·g^{-1}), and ϱ is the density of the disk (mass/area ratio of the pellet, mg·cm^{-2}). For d_3-acetonitrile, molar extinction coefficients of ε=2.05 cm·μmol^{-1} for Brønsted acid sites, ε=3.6 cm·μmol^{-1} for Lewis sites were used [110]. Integrated area A of peaks relating to Brønsted and Lewis acid sites was calculated by performing a deconvolution using the software Peakfit. Particularly, Gaussian curves were employed to identify both Lewis and Bronsted acid sites. Other two Gaussian curves have been added, when necessary, to identify terminal Si-OH groups (2275-2280 cm^{-1}) and d_3-acetonitrile physisorbed on the catalysts (2265 cm^{-1}) always maximizing the correspondence between the curves of Brønsted and Lewis acid sites obtained through fitting and the experimental peaks. All FT-IR spectra were normalized concerning the disc density.

3.5.9 Solid-state NMR MAS.

Some samples were characterized by solid-state NMR analysis in collaboration with Dr. Eddy Dib of the "Laboratoire Catalyse et Spectrochimie (LCS)" (Caen, France). Solid-state NMR spectra were obtained using a 500 MHz (11.7 Tesla) Avance III HD spectrometer. A 4.0 mm OD probe head was used for ^{29}Si and ^{27}Al NMR spectra, while a 1.9 mm OD probe head was employed for ^{1}H NMR spectra. The 4.0 mm rotors were spun at 12 kHz, and the 1.9 mm rotors were spun at 40 kHz. A one-pulse experiment was conducted for each nucleus, with flip angles of π/3, π/6, and π/2, and radiofrequency powers of approximately 38, 33, and 114 kHz. Recycle delays were set at 20, 1, and 10 seconds for ^{29}Si, ^{27}Al, and 1H spectra, respectively. The number of scans for recording ^{29}Si, ^{27}Al, and 1H spectra were 256, 1024, and 64, respectively.

3.5.6 Spent catalysts: soluble coke analysis.

Soluble coke species deposited after catalytic tests were detected employing a GC-MS system (Agilent 7820 A) equipped with an HP-5 MS column (30 m x 0.250 mm x 0.25 μm). During the analysis, a helium flow of 1 NmL/min was used, and the temperature was increased from 40 to 300°C with a thermal ramp of 5°C/min. Before the analysis, spent zeolites were first dissolved in an HF aqueous solution (40%), and then dichloromethane

was used to extract the coke species. Particularly, 10 mg of zeolite was mixed with 200 µl of HF solution and sonicated for 15 minutes until the solid completely dissolved. Following this, 1000 µl of CH_2Cl_2 (dichloromethane) were added. After stirring vigorously for 2 minutes, the mixture was left undisturbed for an hour to allow the extraction of the organic phase. Then, 1 µL of the extracted solution was injected into the gas chromatograph with a 4-minute solvent delay. The molecules detected were identified by comparing their mass spectra with the NIST98 database library.

CHAPTER 4. Physicochemical properties of investigated catalysts.

4.1 ZSM5@Sil-1

4.1.1 XRD.

XRD patterns are reported in **Figure A1-A6** in **Appendix A** for all parent zeolites and ZSM-5@Sil-1 prepared samples and it demonstrated the crystallinity and purity of the zeolitic phases. To discuss the effect of the deposition of Silicalite-1 over the structure of the starting ZSM-5 zeolites, **Figure 18** shows XRD patterns of Z25, H-Z25_X, H-Z25_XX, AS-Z25_X and AS-Z25_XX samples in as-synthesised form before the cycles of calcination and ion-exchange. For each catalyst, a crystallographic pattern typical of an MFI structure has been detected corresponding to the reference one published on http://www.iza-online.org/. It is dutiful reminding that H-ZSM5_25_X and H-ZSM5_25_XX catalysts were obtained by coating a calcined ZSM-5 core and, for this reason, XRD spectra referred to a sample possessing an acid core and an uncalcined shell of Silicalite-1. Thus, the intensity of the peak at 2θ=7,9 increased and that of the peak at 2θ=23,1 decreased for these catalysts if compared with the signal of the samples AS, i.e. synthetised on the as-made core. No loss of crystallinity was detected for passivated samples and, for this reason, the deposition of amorphous silica on the core surface can be neglected.

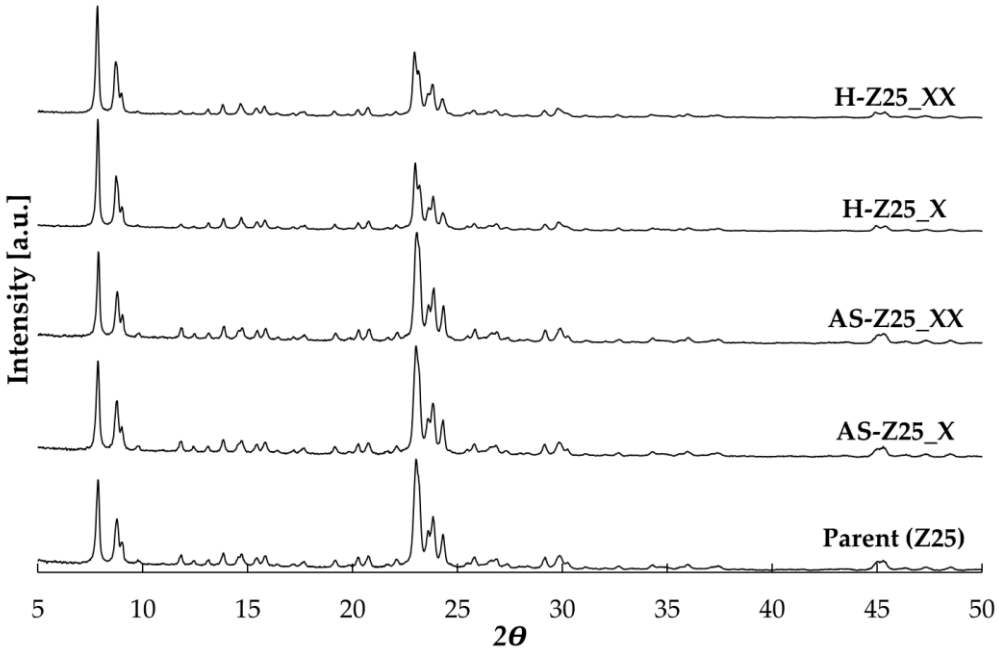

Figure 18: XRD patterns of Z25 and passivated Z25@Sil-1 catalysts.

4.1.2 SEM-EDX analysis.

Figure 19 shows SEM micrographs of ZSM-5 parent zeolites with different Si/Al ratios. All catalysts exhibited a morphology already observed in literature for ZSM-5 zeolites [27]. All investigated samples appeared as 5-20 μm sized round-shaped agglomerates of small crystals of about 1 μm. On the external agglomerated surface, small crystals are observed for the Z25 and Z50 samples, which is reasonably the origin of the higher external surface area obtained for these samples (**paragraph 4.1.6**).

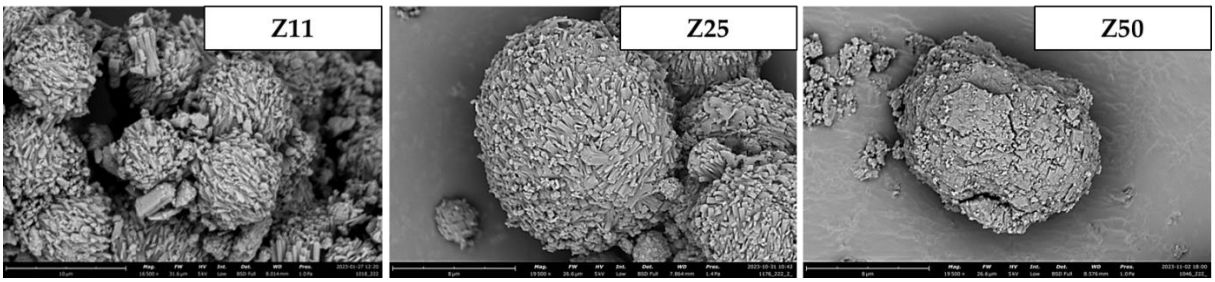

Figure 19: SEM micrographs of parent zeolites.

In **Figure 20**, SEM micrographs of the Z25 sample and passivated catalysts obtained via the epitaxial growth of Silicalite-1 (H-Z25_X, H-Z25_XX, AS-Z25_X, and AS-Z25_XX) are shown

to understand if the coating with Silicalite-1 modified samples morphology. It is clear that no evident differences can be highlighted between the morphology of the parent zeolite and passivated samples using this technique. Probably, the lack of clear differences could be related to Silicalite-1 crystals morphology, which is similar if compared to ZSM-5 zeolite, to Silicalite-1 low crystals size, and the thin thickness of the deposited layer. In fact, the coating of Silicalite-1 was performed at 180 °C for 24 hours as reported in **Chapter 3** and low synthesis times influence the rate of nucleation and the crystals size [111]. Moreover, nucleation of Silicalite-1 occurred over the surface of ZSM-5 crystals and, without doubt, their small size influenced this growth process; Silicalite-1 crystals grown after the coating can never be larger than the starting to be coated ones unless homogeneous nucleation occurred. Only a slight difference between samples coated starting from a core with the organic template inside the pores and catalysts obtained passivating an H^+-form core needs to be emphasized: a much-smoothed form of crystallites was detected for AS-Z25 samples while the crystallites of H-Z25 samples exhibited a more definite and sharper form.

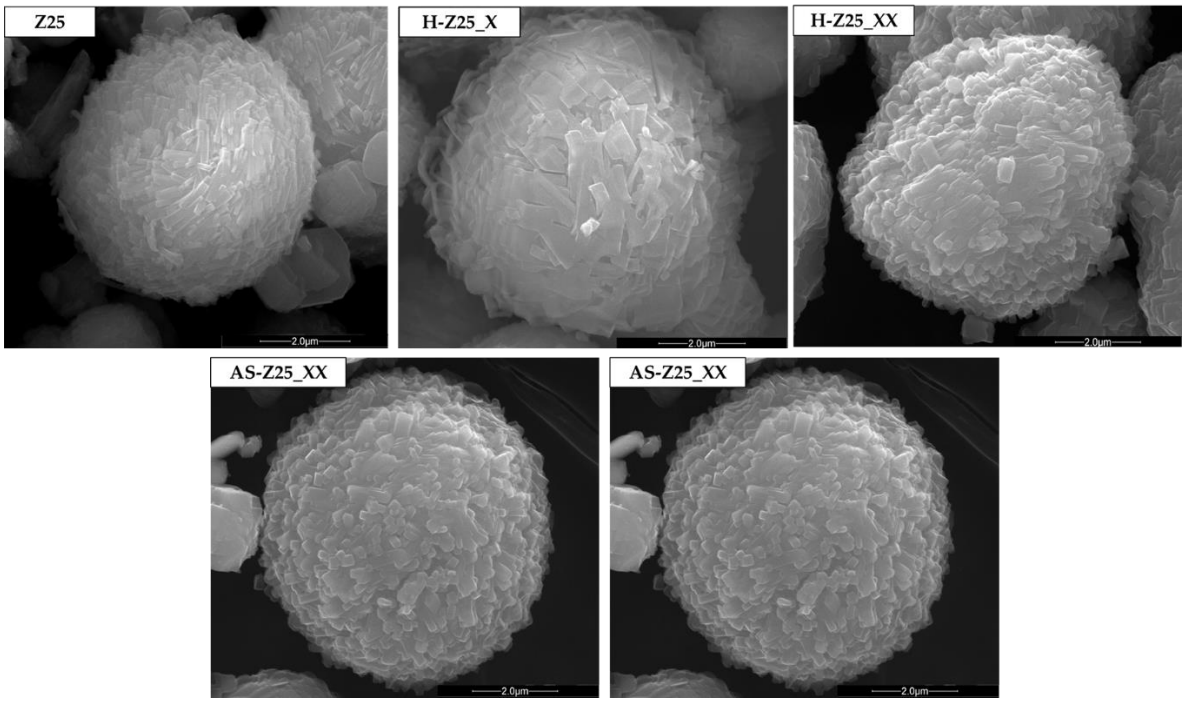

Figure 20: SEM micrographs of Z25 parent zeolite and H-Z25 (X and XX) and AS-Z25 (X and XX) passivated samples.

The impact of increasing the ratio between the mass of crystals to be covered and the mass of Silicalite-1 gel used was investigated as explained in Chapter 3. **Figure 21** shows SEM micrographs of samples passivated employing a greater quantity of Silicalite-1 gel. Particularly, **Figure 21** presents H-Z11_2XX and H-Z25_2XX crystals micrographies at different magnifications (higher magnifications used for micrographies on the left). Results demonstrated that increasing the quantity of Silicalite-1 synthesis gel employed during the passivation treatment, allowed the growth of small crystallites of Silicalite-1 with the typical prismatic shape of about 800-900 μm over the surface of the starting ZSM-5 crystallites agglomerates. Moreover, despite the higher quantity of Silicalite-1 synthesis gel employed during passivation treatments, the presence of homogeneous nucleation of Silicalite-1 crystals was not significantly observed. SEM images of the other passivated samples are reported in **Figures A10-A11** in Appendix A.

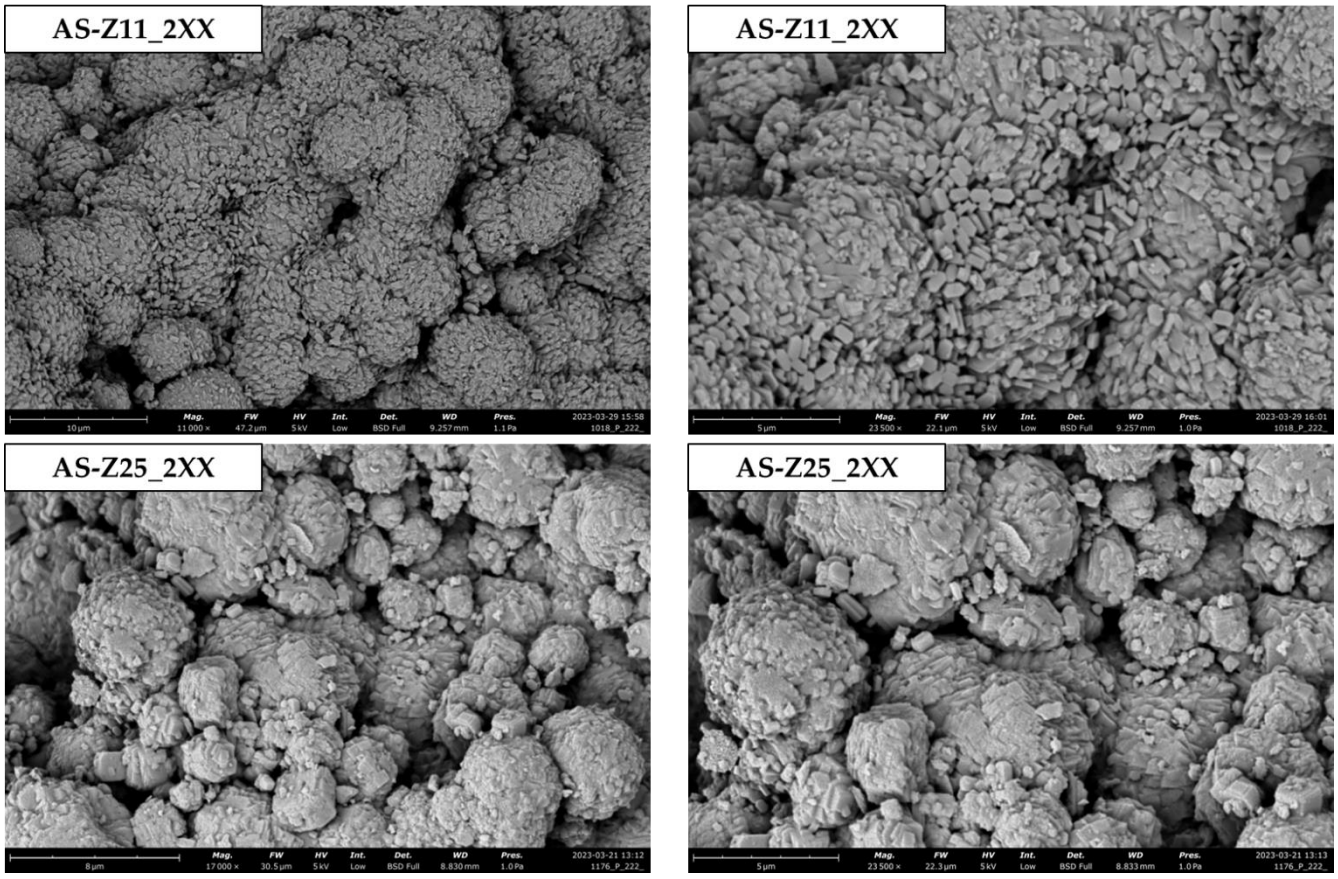

Figure 21: SEM micrographs of AS-Z11_2XX and AS-Z25_2XX passivated samples.

To estimate the Si/Al ratio of catalysts synthetised EDX analysis at different voltages (5 and 15 kV) were performed. In **Table 7**, results obtained for parent zeolites (Z11, Z25, and Z50) are summarized. Si/Al ratio decreased for each investigated sample when EDX measurements were conducted at 15 kV rather than at 5 kV. Particularly a decrease of about 27%, 16%, and 17% was detected for Z11, Z25, and Z50 respectively. This trend confirmed that the quantity of aluminum contained in the internal channels of zeolites is always higher than the one located on the external surface.

Table 7: EDX measurement results for parent zeolites.

Sample Code	Si/Al [mol/mol] [5 kV]	Si/Al [mol/mol] [15 kV]
Z11	9.2	6.7
Z25	23.7	19.9
Z50	36.6	30.1

Moreover, EDX measurements at different voltages were also used to check the Silicalite-1 coating, verifying if the Si/Al external surface ratio changed after the passivation treatment of samples. Analyses were carried out using a voltage of 5 kV on a large number of different points and crystals of the same sample and results are reported in terms of the distribution of the Si/Al ratio in the population analyzed. Particularly, the crystals with a Si/Al ratio lower than 9, between 9 and 15, between 15 and 25, between 25 and 100 and finally greater than 100 were counted. Then the percentage of the various groups concerning the total was calculated and finally, the cumulative function was constructed. **Figure 22** shows cumulative functions obtained employing EDX results at 5kV of Z25 parent zeolite, the passivated sample obtained coating the as-made core of the starting zeolite with two layers of Silicalite-1 (AS-Z25_XX), and the coated sample synthesized employing the same procedure but doubling the quantity of Silicalite-1 synthesis gel employed during the treatments. Results demonstrated that parent zeolite (Z25) was characterized by a higher number of crystals with a lower Si/Al ratio. For example, it was calculated that half of the

crystals of the parent zeolite had a Si/Al ratio lower than 25 while only 20% of the analyzed crystals of the AS-Z25_XX sample exhibited a Si/Al ratio lower than 25. Moreover, it is clear that with the increasing of the quantity of Silicalite-1 synthesis gel employed for coating the parent zeolite, a decrease of crystals that exhibited a lower Si/Al value was detected. The value of 500 on x-axe was used to indicate an infinite Si/Al ratio.

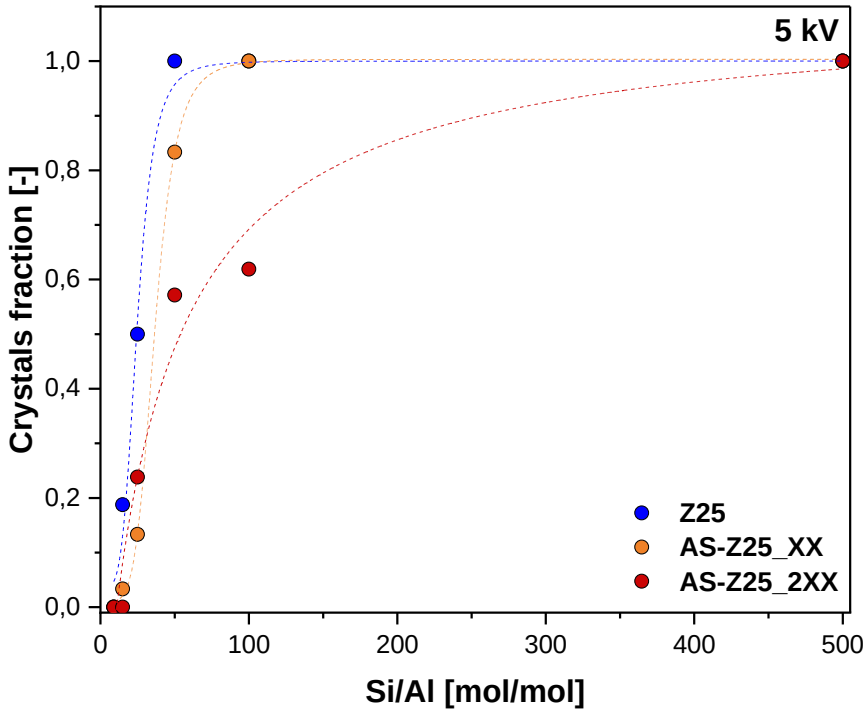

Figure 22: Cumulative functions of Z25, AS-Z25_XX, and AS-Z25_2XX samples obtained via EDX measurements at 5kV.

Figure 23 shows cumulative functions of Z25, AS-Z25_XX, and AS-Z25_2XX calculated employing EDX measurements results obtained at 15kV. It is clear that, in this case, no differences were detected between parent zeolite and passivated catalysts. This result confirmed that the rise in the Si/Al resulted from the growth of Silicalite-1 over the external surface of the catalysts as when the voltage used for analysis increased, and the X-ray penetrated deeper into the crystals, the difference detected between coated and non-coated samples was undetectable.

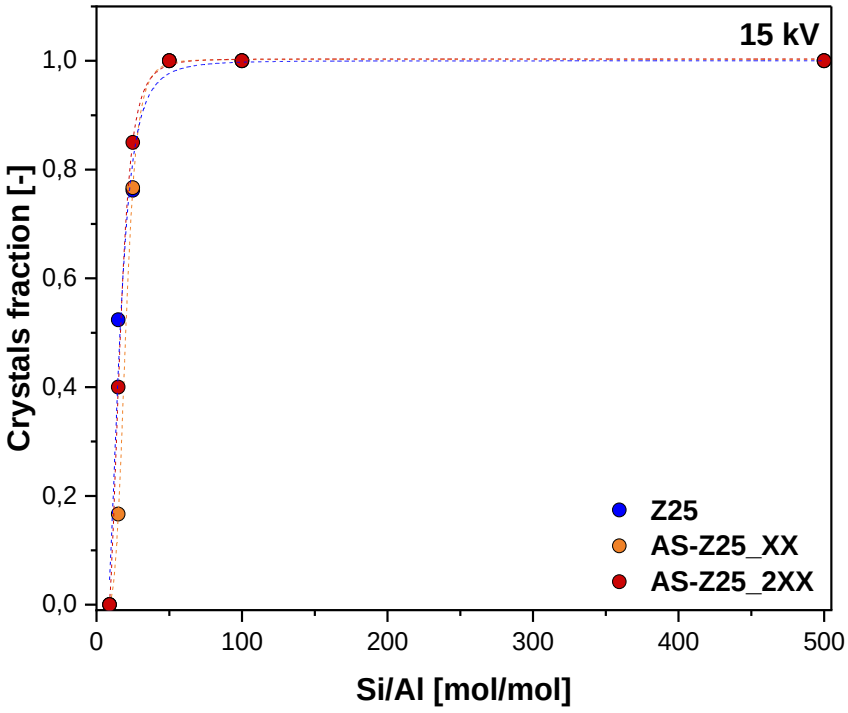

Figure 23: Cumulative functions of Z25, AS-Z25_XX, and AS-Z25_2XX samples obtained via EDX measurements at 15kV.

The same trend was also found for Z11 and Z50 zeolites with their corresponding passivated samples and results are reported in **Appendix A (Figure A12-A13).**

4.1.3 TEM analyses.

TEM micrographs of samples Z11, H-Z11_X, and H-Z11_XX are reported in **Figures 24, 25, and 26** and represent direct evidence of the success of Silicalite-1 deposition with the epitaxial growth technique employed during this research work.

Figure 24 reports parent Z11 micrographs and reveals the presence of agglomerates consisting of smaller crystals of 100 nm (**Figure 24a**) and of bigger crystals characterized by a thickness greater than 200 nm and a length greater than 1 μm. Furthermore, the sedges of Z11 crystals were well-defined and smooth without any detectable coating.

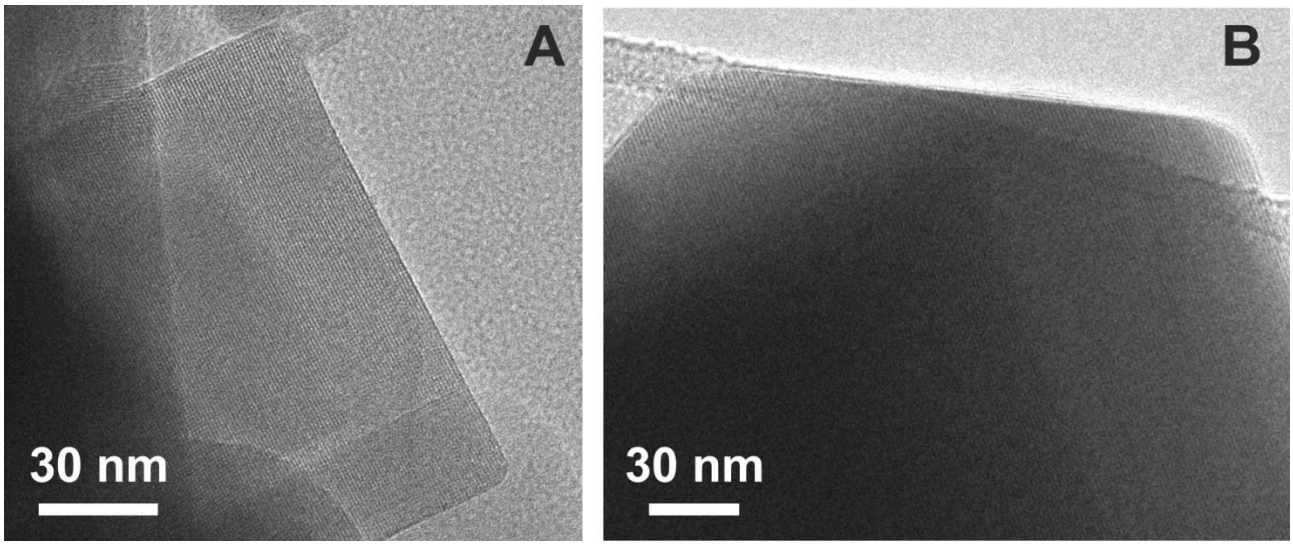

Figure 24: TEM pictures of parent Z11 showing two crystals at the same magnification, M=30 nm

In **Figure 25**, H-Z11_X micrographs at different magnifications are reported. After the first passivation step, it was possible to observe a thin layer of Silicalite-1 grown over the external surface of the starting crystallites, not completely ordered and probably partially amorphous.

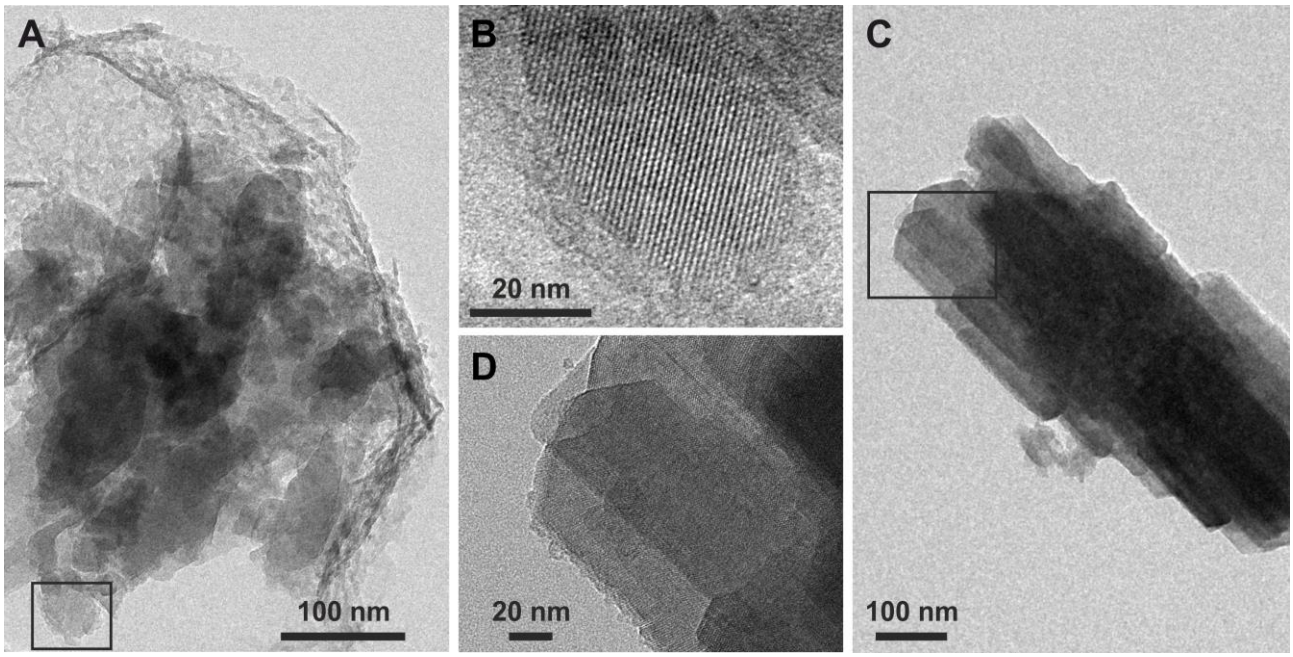

Figure 25: TEM images of H-Z11_X passivated sample showing partially covered crystals at different magnifications, M= 100 nm (A and C) and 20 nm (B and D)

After the second passivation step, a thin layer covering the starting crystals was detectable and visible and within this layer crystalline domains typical of an MFI structure were recognizable. Moreover, chemical analysis performed at different points of the sample, as shown in **Figure 26 (C and D)**, demonstrated that the aluminum signal was almost undetectable in the layer covering the starting zeolite. On the contrary, the silicon signal increased when the analysis was performed on the external surface coated with small crystallites (C) if compared with that detected in the internal part of the ZSM-5 crystal (D).

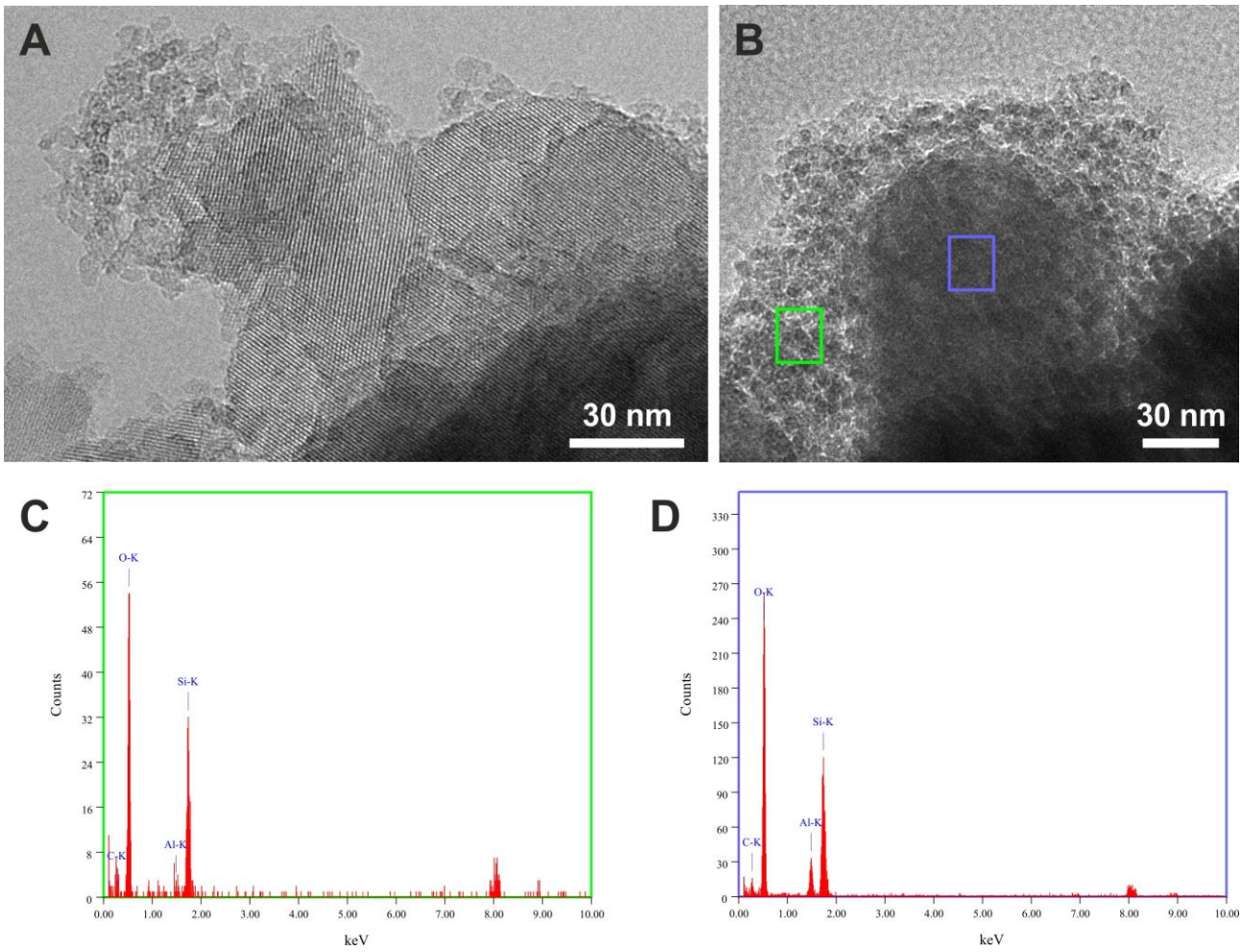

Figure 26: TEM pictures of sample H-11_XX coated twice with Silicalite-1 showing the multi-silicalite-1 layer grown over the starting zeolite (A and B), M=30. Chemical analyses in different points of the crystal are shown (C and D).

4.1.4 Chemical analysis: AAS results.

Si/Al ratios measured by atomic absorption analysis (AAS) technique for parent zeolites (Z11, Z25, and Z25) well agreed with the starting ratio adopted for the crystallization. Furthermore, in **Table 8** results obtained for samples passivated with Silicalite-1 are

reported. Silicon content increased with the depositions of Silicalite-1 and these results, obtained for all passivated catalysts, represent further indirect evidence of the success of the employed technique.

Si/Al ratio increase detected for samples AS-Z25_X and AS-Z25_XX obtained coating an as synthetized-form core, was greater than that found for samples H-Z25_X and H-Z25_XX, obtained passivating a H^+-form core, if compared with the starting parent Z25 zeolite confirming the better shell growth efficiency when as-made form core is employed.

Furthermore, starting from the theoretical cell composition of an MFI zeolite ($H_nAl_nSi_{96-n}O_{192}$) and knowing the Si/Al ratios of both passivated and non-passivated samples (Z11, ZS25, and ZS50), it was possible to calculate the weight percentage of the synthesized Silicalite-1 layer [106] and results are reported in **Table 8**. It is evident that the quantity of Silicalite-1 layer coated over the starting ZSM-5 samples was very low as the goal of treatment was to passivate the external acidity trying not to modify the properties of the parent zeolite acid core.

Table 8: AAS measurement results for all investigated samples.

Sample Code	Si/Al $_{bulk}$ (mol/mol)	% wt of Silicalite-1 deposited
Z11	15.4	-
H-Z11_X	17.6	5.9
H-Z11_XX	27.1	25
Z25	27.6	-
H-Z25_X	28.6	1.7
H-Z25_XX	30.2	4.1
AS-Z25_X	29.3	2.5
AS-Z25_XX	31.5	6.0
Z50	44	-
AS-Z50_XX	52	7.7

4.1.5 TGA analysis

In this paragraph, results obtained via the thermogravimetric analyses of samples are summarised. Particularly, all the profiles reported below refer to analyses carried out employing samples in the as-synthetised form before any calcination and ion-exchange treatment and using an air flow of 100 ml/min as described in **Chapter 3.**

Figure 27 shows a comparison between parent Z25 zeolite and samples H-Z25_X (**Figure 27a**) and H-Z5_XX (**Figure 27b**) synthetized passivating the external surface of the starting zeolitic core in H^+-form, already calcined and without the organic template inside the pores. Observing the DTG profiles, for the parent zeolite (blue profiles in the pictures) three main peaks were detected: the first one around 100°C refers to the evaporation of water from the zeolitic framework; the second one at about 460°C indicates the combustion of the organic template used for the synthesis of MFI zeolite (tetrapropylammonium bromide); the last one at about 630°C probably deals silanol dehydration that usually occurs at temperatures higher than 550°C [112]. Profiles obtained for H-Z25_X and H-Z25_XX samples (red lines in **Figure 27a and 27b**) show four main peaks. The first one, at about 80°C refers to water evaporation, the second one at 220°C, not found for the parent zeolite, still is due to water trapped in the starting hydrophilic ZSM-5 core and which therefore came out at higher temperatures. Furthermore, the porosimetric analyses, described in the next paragraph, revealed that the Silicalite-1 crystals grown on a core with empty pores caused a decrease in the volume of the micropores, probably due to the partial blockage of the channels. For this reason, the higher temperature outflow of water trapped in the zeolite channels, which produced the peak at 200°C, could be attributed to this partial occlusion. For H-Z25_X and H-Z25_XX samples the peak of organic combustion (at about 456°C) is wider and lower in intensity than in the case of Z25. Since the starting core was in calcined form, the combustion peak of the organic refers only to the TPA^+ derived from tetrapropylammonium hydroxide used to synthesize the thin layer of the Silicalite-1 layer. The same evidences were found for the sample covered by a double layer of Silicalite-1 (H-Z25_XX) as the second layer deposition starts on the calcined H-Z25_X sample (free from organic template). By calculating the weight loss corresponding to the exothermic combustion peak of the organic

it was possible to estimate the quantity of SDA present on the sample after the epitaxial growth of Silicalite-1. For both H-Z25_X and H-Z25_XX samples, the amount of TPA^+ found after the passivation treatment corresponded to 1% by weight of the sample mass.

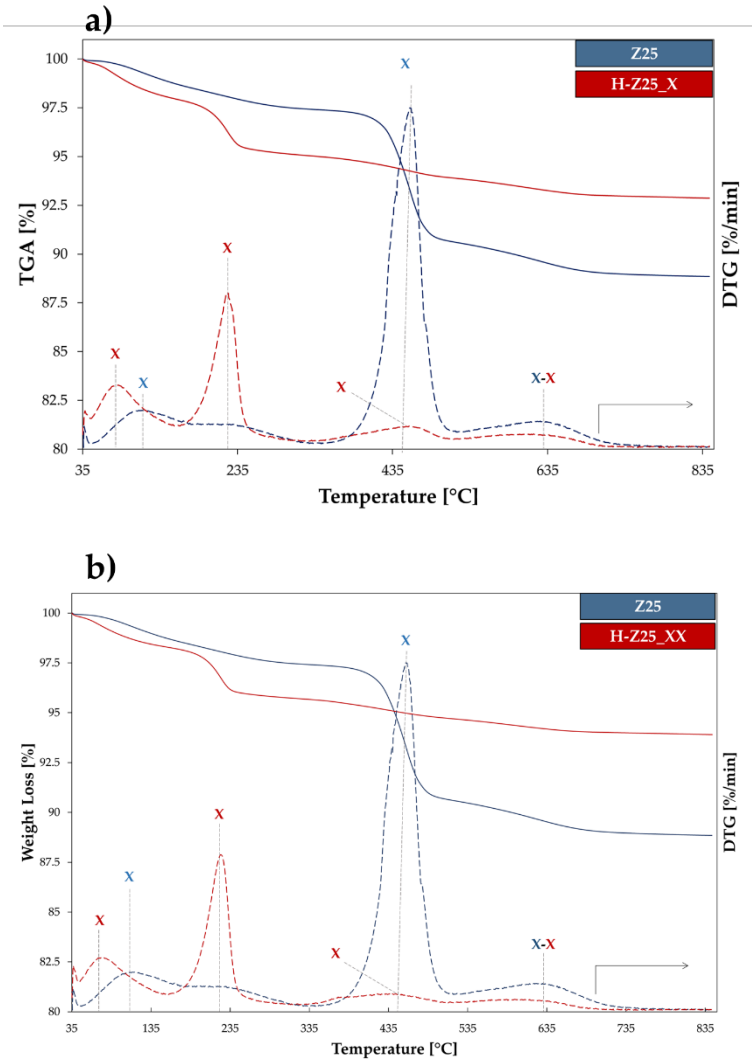

Figure 27: TGA/DTG profiles of Z25 parent zeolite compared with H-Z25_X (a) and H-Z25_XX (b).

Figures 28a and 28b show comparisons between TGA/DTG results of parent Z25 zeolite and those obtained for passivated AS-Z25_X and AS-Z25_XX samples. In this case profiles trend is the same showing only the three main peaks already described above for the Z25. From this evidence is clear that the use of an As-made core during passivation determines a different final material. In fact, for AS-Z25_X and AS-Z25_XX samples peaks found at 460°C refer to the combustion of the organic template of the starting core (tetrapropylammonium bromide) that was passivated without any prior calcination step and, being the amount of

the core organic much higher than the amount of SDA used for the synthesis of Silicalite-1, it was difficult to detect the peak related to the combustion of TPA^+ derived from tetrapropylammonium hydroxide, especially after the first passivation step (AS-Z25_X sample). AS-Z25_XX sample was obtained by covering the already coated sample (AS-Z25_X) a second time with Silicalite-1 without subjecting it to a treatment of calcination but using it with the channels shield by SDA. For this reason, results relating to the double deposition step silicalite-1 layered catalyst show an exothermic peak around 375°C (as a shoulder of the main one) which identifies the combustion of the organic contained in the first and second layer of Silicalite-1.

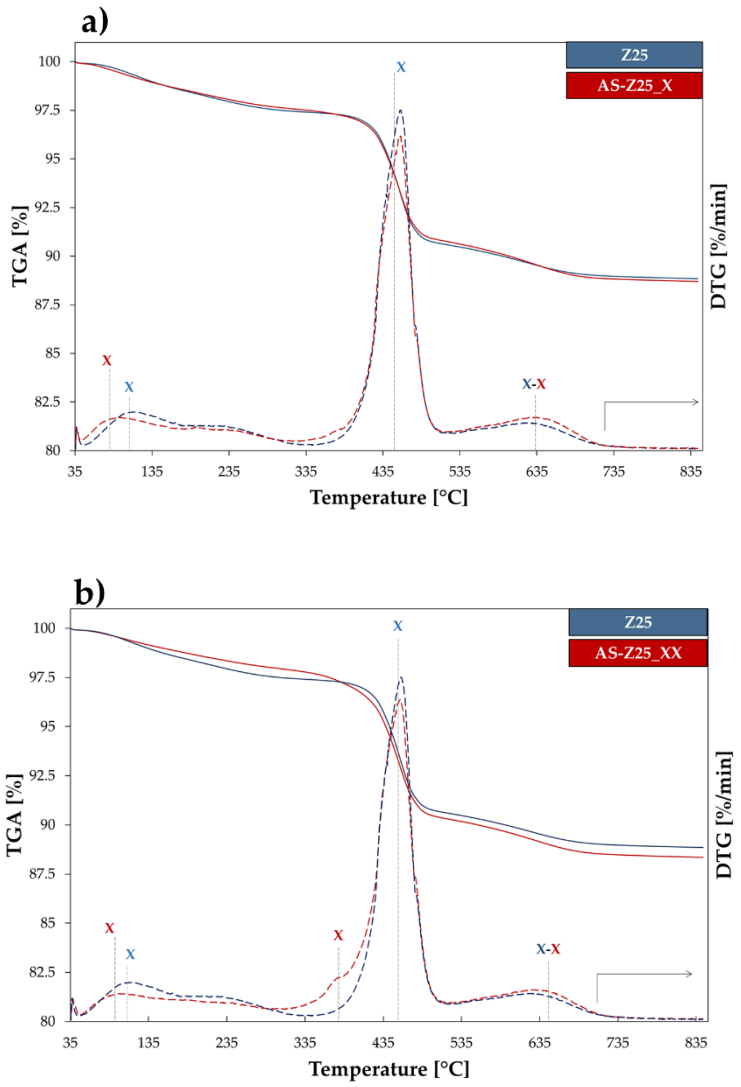

Figure 28: TGA/DTG profiles of Z25 parent zeolite compared with AS-Z25_X (a) and AS-Z25_XX (b).

Figure 29 shows a TGA/DTG comparison between Z25 parent zeolite and passivated sample AS-Z25_2XX obtained by coating the starting surface of MFI zeolite with two layers of Silicalite-1 but using a double amount of Silicalite-1 synthesis gel for each step of passivation. In this case, the peak around 370°C is visible and well-defined and certainly is related to the combustion of tetrapropylammonium hydroxide used in the Silicalite-1 synthesis gel.

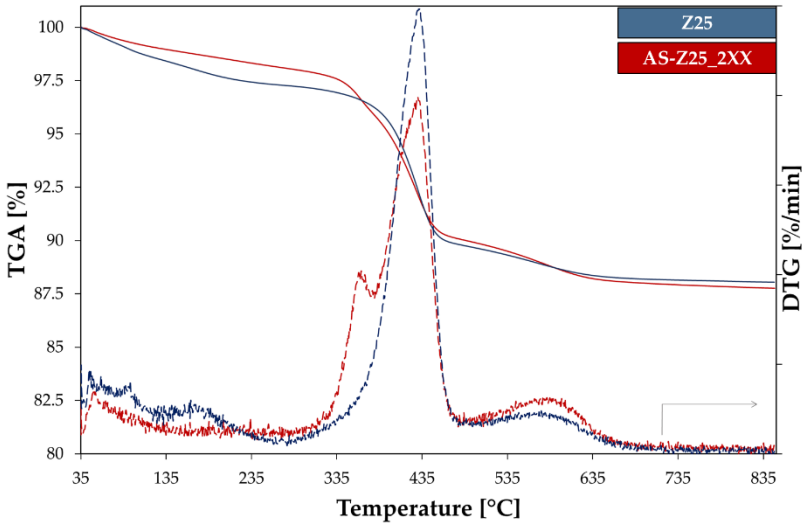

Figure 29: TGA/DTG profiles of Z25 parent zeolite compared with AS-Z25_2XX sample.

To confirm the temperature assignment of the peaks, differential thermal analyses (DTA) were performed (in the same conditions as TGA analyses) for samples Z25 and AS-Z25_2XX. Furthermore, DTA analysis was also carried out for a Silicalite-1 non calcined zeolite synthetized using the same gel employed for the passivation treatments (**Figure 30)**. The silicalite-1 catalyst profile showed an exothermic peak at around 390°C relating to the combustion of TPA^+ derived from tetrapropylammonium hydroxide. Contrariwise, Z25 zeolite was characterized by an exothermic peak at around 440°C related to TPA^+ combustion. Passivated sample (AS-Z25_XX) DTA profile revealed the presence of two main exothermic peaks because of the presence of Silicalite-1 (passivating layer) over a ZSM-5 zeolite (core) and organic template inside the channels (TPA^+ resulting from both TPABr and TPAOH) interacted differently with the two zeolitic phases. Observing **Figure 30** it is clear that a shift of both exothermic peaks versus lower temperatures was detected

for the passivated sample (AS-Z25_XX). To understand if the cause of this shift could be related to the interactions between the two zeolitic phases (ZSM-5 and Silicalite-1) a mechanical mixture of Z25 and Silicalite-1, both in as-made form, was prepared and DTA analysis was performed. Particularly, two mechanical mixtures were prepared: the first one with a content of about 10% of Silicalite-1 and the second one increasing this content to 20%. **Figure 30** reports DTA profiles of mechanical mixtures and reveals that the shift of exothermic peaks observed for AS-Z25_XX samples was not detected. This result represents an indirect proof of the deposition of Silicalite-1 because it demonstrates that the passivated sample obtained, composed of two zeolitic phases (ZSM-5 and Silicalite-1) interacting with each other, differs from a mechanical mixture of the same two zeolites.

TGA/DTG analysis results of ZS11 and Z50 parent zeolites and corresponding passivated samples showed the same trend already described and are reported in **Appendix A** (Figure A7-A9).

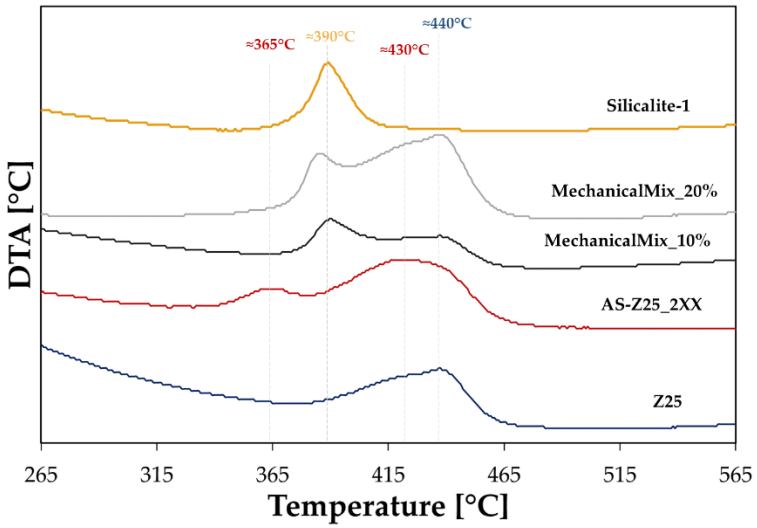

Figure 30: DTA profiles in the organic combustion temperature range of Z25, Silicalite-1, AS-Z25_2XX passivated sample, and mechanical mixtures (composed respectively by the 10% and 20% by weight of Silicalite-1).

4.1.6 Porosimetric results.

Adsorption isotherms of N_2 at 77K of all investigated samples are reported in **Figure A14-A19** in **Appendix A**. All samples were characterized in terms of a superficial specific area (B.E.T), micropore area (M.A., estimated by t-plot method), external area (E.A.,

estimated by t-plot method), micropore volume (M.V., estimated by t-plot method) and total pore volume (P.V.). All catalysts exhibited mixed type I/IV isotherms with H_4 hysteresis at about P/P_0 typical of aggregated microporous crystals with textural mesopores [113]. Moreover, the more pronounced uptake of nitrogen detected at low P/P_0 was associated with the filling of the zeolites micropores. Textural properties calculated by analyzing adsorption isotherms are reported in **Table 9**. Parent zeolites exhibited similar textural properties except for the external surface area that was lower for the ZS11 catalyst. These results agree with the SEM micrographs discussion in **Paragraph 4.1.2**. In fact, Z25 and Z50 samples exhibited the presence of small crystals on the external surface of bigger crystals agglomerates, and this could be reasonably the cause of the higher external surface area values found. The results obtained are similar to other MFI zeolites reported elsewhere [114]. The BET surface area of sample H-Z11_X decreased by 14% if compared with the starting parent zeolite (Z11). Micropore area and external surface area also decreased after the deposition on the first shell of Silicalite-1. These values increased again after the deposition of the second layer of Silicalite-1 (H-Z11_XX). The worsening of textural properties (i.e. BET surface area and micropore area) for sample H-Z11_X can also be identified observing the downward translation of its N_2 adsorption/desorption isotherm (**Figure A14**). To understand the reason of this trend found after the growth of the first layer of Silicalite-1, the idea of coating a core with the pores closed by the presence of the organic template agent was followed. **Table 9** reports results obtained for the starting Z25 zeolite and of passivated samples synthesized covering the Z25 core in as synthetized-form (AS-Z25_X and AS-Z25_XX) and in H^+-form (H-Z25_X and H-Z25_XX). The effect of the form of the core (acidic or as made) over the physical properties of the resulting passivated catalyst is evident. Sample H-Z25_X exhibited the same trend found for H-Z11_X compared with their respective non-coated starting zeolites. In fact, a decrease of 15% was found for the BET surface area of the H-Z25_X catalyst assuming as reference the parent Z25 zeolite. This finding could be explained by hypothesizing that a thin layer of Silicalite-1 was grown into the empty pores of the starting zeolite after the first deposition step. Contrariwise, the slight increase of these properties in the sample H-Z25_XX was explained by the regrowth of

Silicalite-1 over the first synthesized shell. A similar trend was observed for the microporous area (S_{micro}) and external surface area (S_{ext}). This trend was not detected for the AS-Z25_X sample in which the starting zeolite was covered in as-synthesized form because of the presence of organic template filling core channels and preventing pores blockage. Inversely, micropore volume values (V_{micro}) of AS-Z25_X and AS-Z25_XX samples were higher compared with the parent zeolite (Z25) demonstrating the growth of the Silicalite-1 layer over the core surface and not in the internal channels.

The results obtained for the other passivated samples demonstrated that the properties of the starting zeolite have always been preserved. For the sake of completeness, textural properties of the other two parent zeolites with Si/Al ratios equal to 11 and 25 (Z11_2 and Z25_2) were also reported in this case because passivated samples AS-Z11_XX and AS-Z11_2XX were synthetized starting from Z11_2 batch and AS-Z25_2XX catalysts were obtained coating Z25_2 zeolite.

Table 9: Textural properties of investigated catalysts.

Catalyst	S_{bet}[a] (m^2/g)	S_{micro}[b] (m^2/g)	S_{ext}[b] (m^2/g)	V_p[c] (cm^3/g)	V_{micro}[b] (cm^3/g)
Z11	**404**	310	94	0.21	0.12
H-Z11_X	**349**	267	80	0.17	0.10
H-Z11_XX	**389**	293	96	0.20	0.11
Z11_2	**389**	296	93	0.20	0.117
AS-Z11_XX	**385**	292	92	0.18	0.115
Z25	**420**	290	130	0.23	0.117
AS-Z25_X	**423**	308	115	0.21	0.123
AS-Z25_XX	**428**	308	121	0.21	0.122
H-Z25_X	**389**	245	143	0.20	0.100
H-Z25_XX	**421**	257	164	0.22	0.105
Z50	**424**	212	212	0.15	0.09
AS-Z50_XX	**424**	212	213	0.15	0.09
Z25_2	**409**	264	145	0.24	0.107
AS-Z25_2XX	**442**	294	148	0.22	0.119
AS-Z11_2XX	**391**	280	110	0.19	0.112

[a]Calculated by the multipoint BET method in the Rouquerol p/p^0 range; [b]Calculated by the t-plot method; [c]Calculated at p/p^0 0.95

4.1.7 NH_3-TPD analysis

NH_3-TPD measurements were employed to estimate the amount and the strength of acid sites of samples synthesized. Moreover, this technique was used to evaluate the effect of post-synthesis passivation treatment on the total acidity of the coated sample and the ratio between strong and weak acid sites. In **Figure 31.** NH_3-TPD profiles of parent zeolites (Z11, Z25, and Z50) are reported. Each catalyst exhibited the typical profile of an MFI zeolite with two main desorption peaks: the first one, at low temperatures, related to the interaction of ammonia with weak acid sites, and the second one, at higher temperatures, related to strong acid sites [115]. **Figure 31** showed that for Z11 parent zeolite a higher peak at temperatures lower than the others was detected proving the high amount of weak acid sites. Although NH_3-TPD analyses do not allow us to distinguish between Brønsted and Lewis acid sites, in literature the desorption peak at low temperatures is either related to the presence of Lewis acid sites or extra framework aluminum oxide/hydroxide species [116,117].

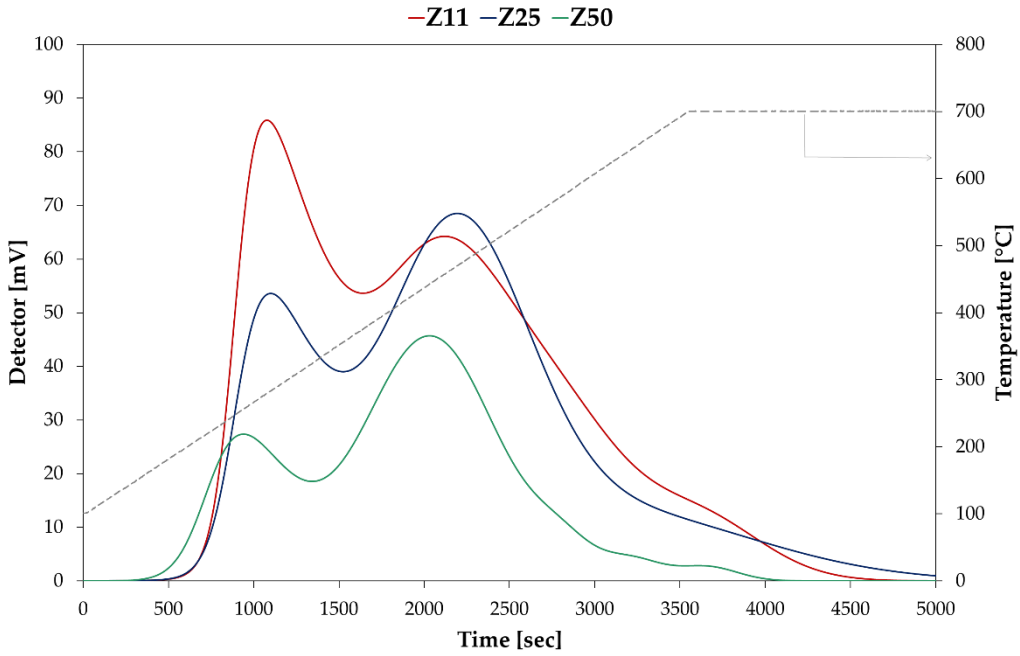

Figure 31: NH_3-TPD profiles of parent zeolites.

To discuss the effect of the passivation procedure over acidity properties of samples, in **Figure 32 (a,b)** profiles of the starting parent zeolite (Z25) and of layered samples obtained coating the core in as-made form (AS-Z25_X and AS_Z25_XX, **Figure 32a**) and in H^+-form (H-Z25_X and H-Z25_XX, **Figure 32b**) are shown. NH_3-TPD profiles obtained for the other investigated samples are reported in **Appendix B (Figure B1-B3)**. **Figure 32** shows that also passivated samples exhibited an MFI typical NH_3-TPD profiles with two main desorption peaks. Results obtained demonstrated that passivating the core in H^+-form caused a stronger decrease of total acidity already from the first deposition cycle. Moreover, ammonia maximum desorption temperatures did not change after the growth of Silicalite-1, both for AS-Z25 and H-Z25 samples. For this reason, it can be concluded that epitaxial growth of Silicalite-1 did not strongly affect the strength of acid sites.

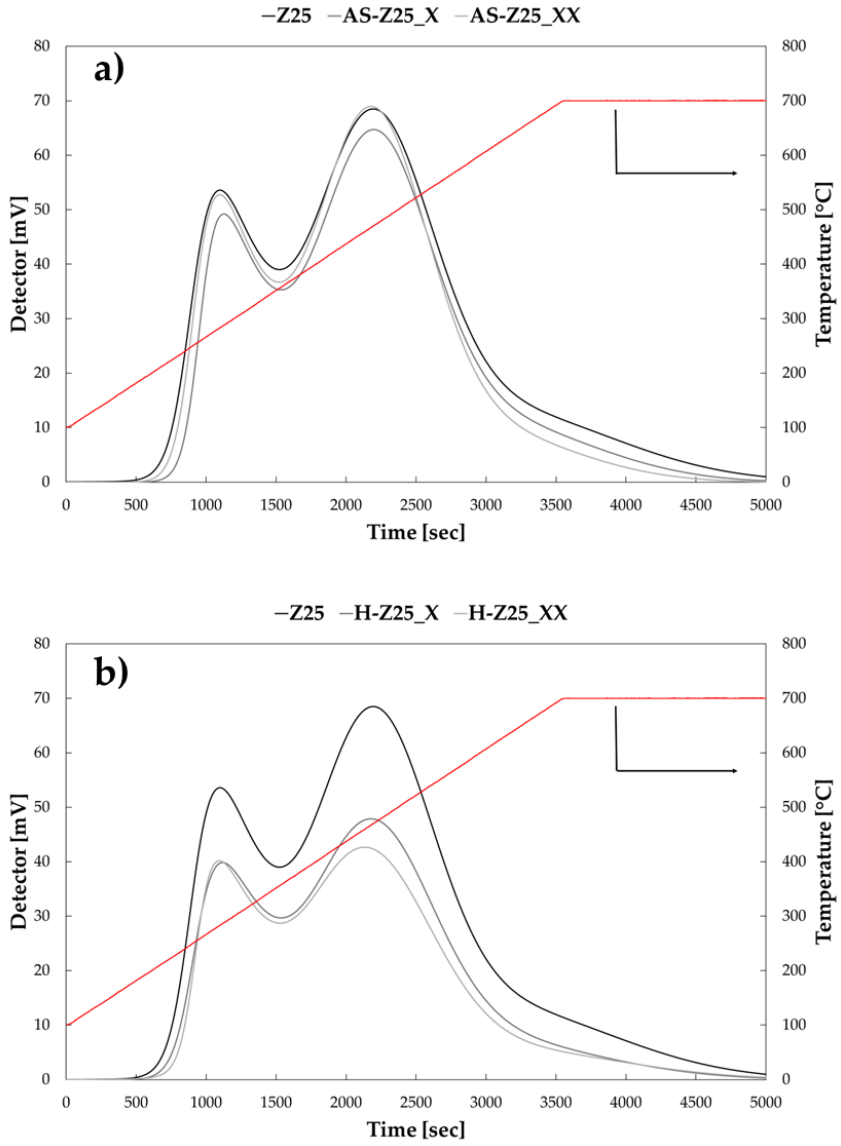

Figure 32: NH_3-TPD profiles of Z25 parent zeolite compared with H-Z25_X and H-Z25_XX (a) and with AS-Z25_X and AS-Z5_XX (b).

Table 10 summarizes the quantitative results of all investigated samples obtained through the peaks deconvolutions. It is useful to underline that samples of NH_3-TPD profiles also exhibited the presence of peaks at temperatures higher than 550°C. These peaks are usually associated with silanol dehydroxylation [112] and to quantify the total acidity of samples, the ones at temperatures higher than 550°C were considered only for the curve deconvolution, not accounted for the total acidity.

For sample H-Z11_X total acidity a decrease of about 25% was detected if compared with the starting parent Z11 zeolite. The second deposition of Silicalite-1 did not cause a strong decrease in total acidity and on the contrary, a slight increase of this value was found.

Similarly, H-Z25_X and H-Z25_XX passivated catalysts exhibited a lower value of total acidity than the starting Z25 parent zeolite. Particularly a decrease of 28% and 33% was detected respectively. In both cases (Z11 and Z25 and correspondingly passivated H-Z samples) the decrease in total acidity was less pronounced after the second growth of Silicalite-1 than the first one. This trend confirms the hypothesis that covering a core with empty pores causes a partial occlusion of the same due to the growing Silicalite-1 at the pores' mouth. For this reason, the strong decrease in total acidity obtained after the first coating is probably not due to a real decrease but is caused by the inability of ammonia to reach the acid sites. On the contrary, the total acidity of AS-Z25_X and AS-Z25_XX catalysts measured via NH_3-TPD analysis decreased only by 6% and 10% respectively if compared to the parent Z25 zeolite. This was due to the presence of the organic template agent which, by protecting the zeolite channels, allowed passivation of only the superficial acid sites pursuing the initial goal of the treatment. The purpose was to neutralize external acid sites without strongly modifying the properties of the catalysts and without decreasing the number of active acid sites for catalysis. AS-Z50_XX sample, synthesized coating with Silicalite-1 and ZSM-5 with a Si/Al ratio of 50, showed an acidity value 7% lower than the parent zeolite (Z50). As the Si/Al ratio increased, the decrease in total acidity obtained after the growth of the Silicalite-1 layer decreased and this trend will also be confirmed by the results of the FT-IR analyses reported in the following paragraph.

Table 10: Quantitative data obtained from NH_3-TPD analysis of investigated samples.

SAMPLE	Weak acid sites (W) (μmol g_{cat}^{-1})	Strong acid sites (S) (μmol g_{cat}^{-1})	W + S (μmol g_{cat}^{-1})	S/W
Z11	259 (290 °C)	424 (456 °C)	683	1.6
H-Z11_X	207 (280°C)	299 (445°C)	506	1.4
H-Z11_XX	195 (290°C)	324 (450°C)	519	1.7
AS-Z11_XX	176 (290°C)	436 (460°C)	611	1.7
Z25	155 (280 °C)	478 (470 °C)	633	3.1
H-Z25_X	116 (280 °C)	342 (460 °C)	458	3.0
H-Z25_XX	98 (290 °C)	317 (470 °C)	415	3.2
AS-Z25_X	141 (290 °C)	454 (465 °C)	595	3.2
AS-Z25_XX	150 (290 °C)	418 (465 °C)	568	2.8
Z50	90 (250 °C)	250 (440 °C)	340	2.8
AS-Z50_XX	78 (250 °C)	238 (440 °C)	316	3.0

[a] From NH_3-TPD profiles: weak sites NH_3 desorption range 100–300 °C, strong sites NH_3 desorption above 300 °C. Values into brackets are desorption temperature peaks (°C);

4.1.8 FT-IR

In this paragraph, the main results obtained from performing FT-IR analysis of samples are reported. Particularly FT-IR spectra were collected before and after D_3-acetonitrile adsorption. **Figure 33** shows spectra of parent zeolites in the OH-stretching region acquired at room temperature after a pre-treatment at 400°C for 2 hours under vacuum and before the adsorption of the probe. A band at 3745 cm^{-1} was detected for each sample related to the presence of silanols group located at the external surface of catalysts [43,118]. A small band

at about 3735 cm^{-1} was detected for Z25 zeolite and it could be attributed to the presence of internal silanols groups located within micropores [118]. Each catalyst exhibited a band at 3610 cm^{-1} corresponding to the acidic bridging Si-(OH)-Al groups. Although quantitative analysis is not possible in this region, the intensity of this band could be correlated with various factors such as the Si/Al ratio in the synthesis gel or the crystals size. The Z11 sample exhibited a lower intensity band at 3610 cm^{-1} despite the higher aluminum content in the synthesis gel. Moreover, a band at 3665 cm^{-1} was found in the spectra of the Z11 sample associated with the presence of extra-framework Al-OH species [41].

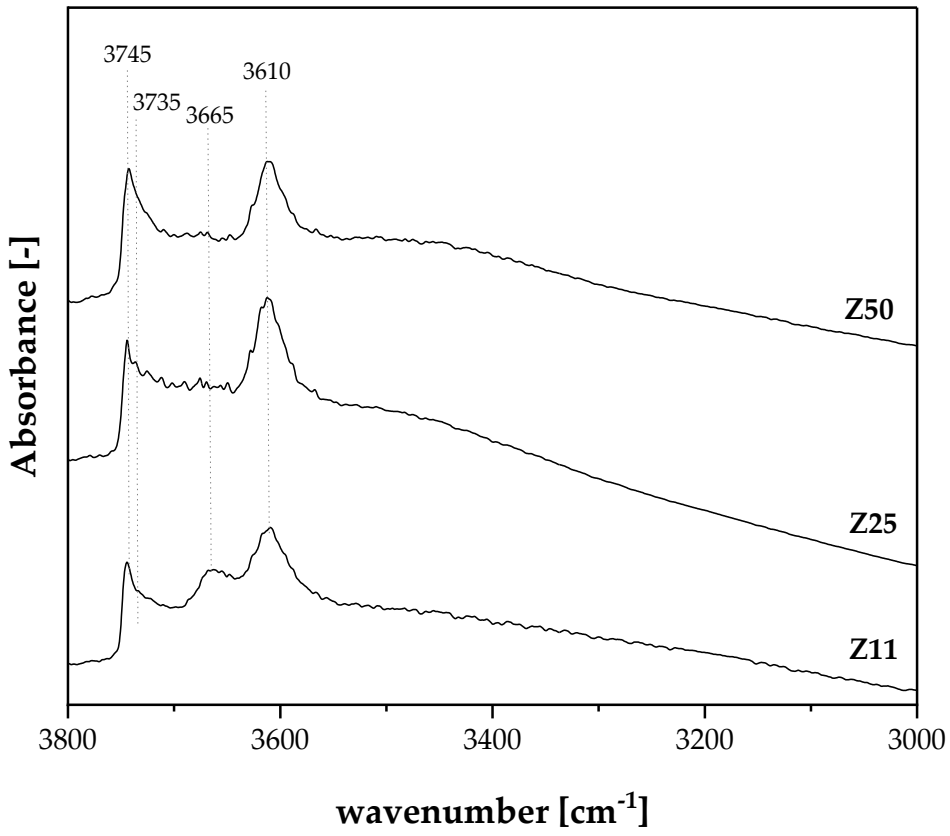

Figure 33: FT-IR spectra in the OH stretching region before the adsorption of d_3-acetonitrile of parent zeolites.

To make a comparison between passivated and non-passivated samples, **Figure 34** shows spectra of Z25 parent zeolites and coated samples in the OH region obtained before the adsorption of d_3-acetonitrile. Particularly, results of both samples obtained coating an H^+-form core (H-Z25_X and H-Z25_XX) and an as synthesized-form core (AS-Z25_X and AS-Z25_XX) are reported. A slight decrease of the band at 3610 cm^{-1} was detected for all

catalysts passivated with one or two layers of Silicalite-1. Moreover, an increase of the band at 3665 cm^{-1}, associated with extra-framework Al-OH species, was found for samples H-Z25_X and H-Z25_XX. This result demonstrates that coating a calcined zeolite with empty pores through the growth of Silicalite-1, carried out by hydrothermal synthesis, probably causes an escape of aluminum from the zeolitic framework and then an increase of the Al-OH extra-framework species.

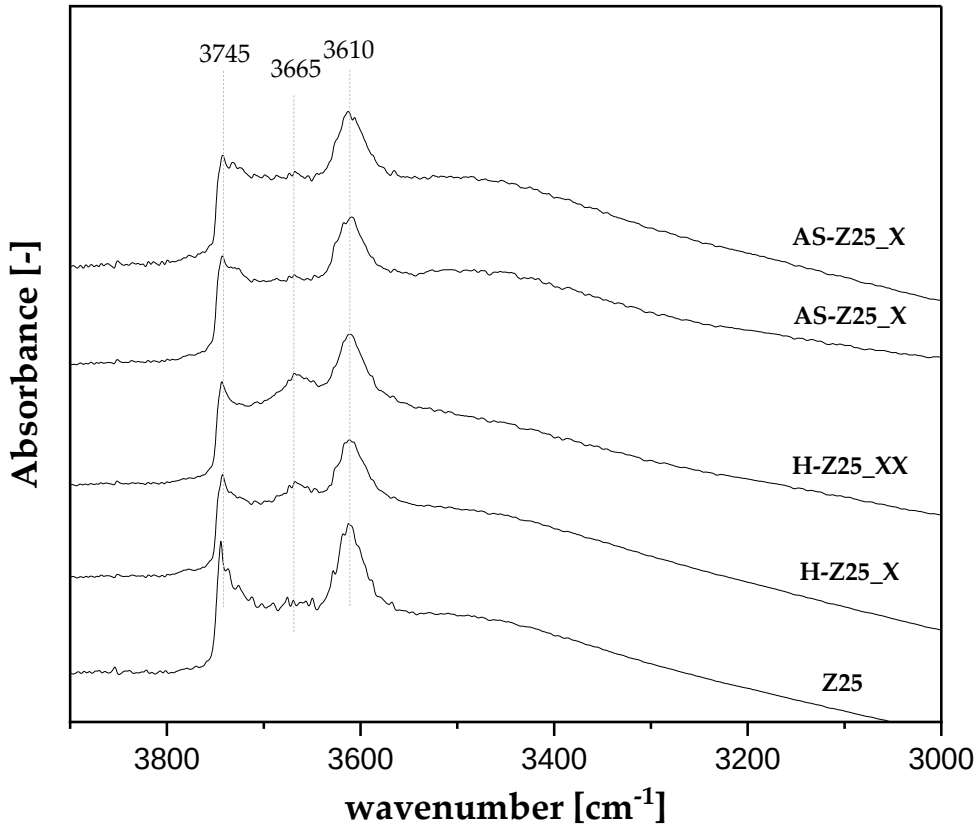

Figure 34: FT-IR spectra in the OH stretching region before the adsorption of d_3-acetonitrile of parent zeolite (Z25) and passivated samples (H-Z25 and AS-Z25).

In **Figure 35**, spectra obtained after the interaction of analyzed parent zeolites (Z11, Z25, and Z50) with d_3-acetonitrile are reported in the wavenumber range 2400-2200 cm^{-1}. Three main peaks are detected as usual: the first one at 2320 cm^{-1} related to d_3-acetonitrile reacting with Lewis acid sites, the second one at 2290 cm^{-1} referred to Brønsted acid sites linked to the probe, and the third one at 2275 cm^{-1} indicating the presence of terminal silanols group reacting with d_3-acetonitrile [110].

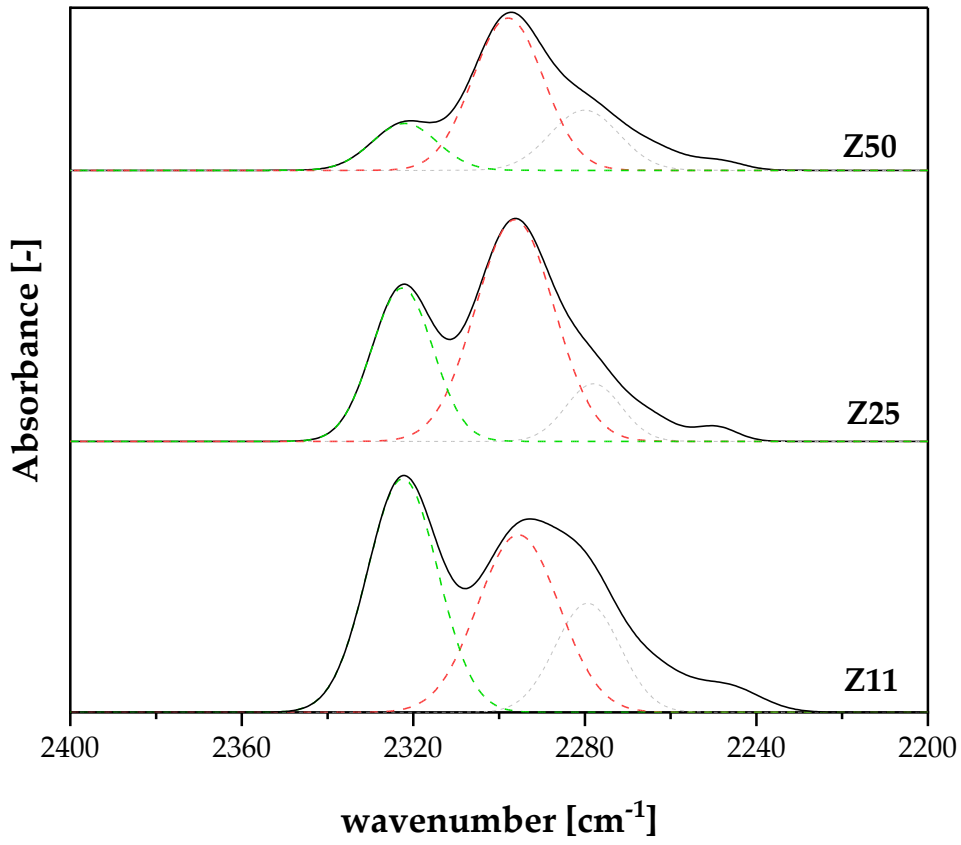

Figure 35: FT-IR spectra of parent zeolites in the LAS/BAS region (d3-acetonitrile probe) after evacuation at room temperature.

Figure 36 (a,b) compares spectra of passivated samples and the starting parent zeolite (Z25) interacting with d3-acetonitrile. Particularly spectra collected for Z25 and corresponding coated samples are shown to underline the main differences found; spectra collected for all the other investigated samples are reported in the 2400-2200 cm^{-1} range in **Appendix B (FigureB5-B9)**. Results shown in **Figure 36** confirmed NH_3-TPD results already discussed as coating the core in H^+-form had a stronger effect over the total acidity of the starting zeolite. Particularly, when the core was passivated in acidic form a decrease of the band intensity related to both Brønsted and Lewis acid sites was detected. On the contrary, when the starting zeolite was coated with the organic template inside the pores the higher decrease detected was for the band linked to Lewis acid sites; instead, only a slight decrease of the band at 2290 cm^{-1} was found.

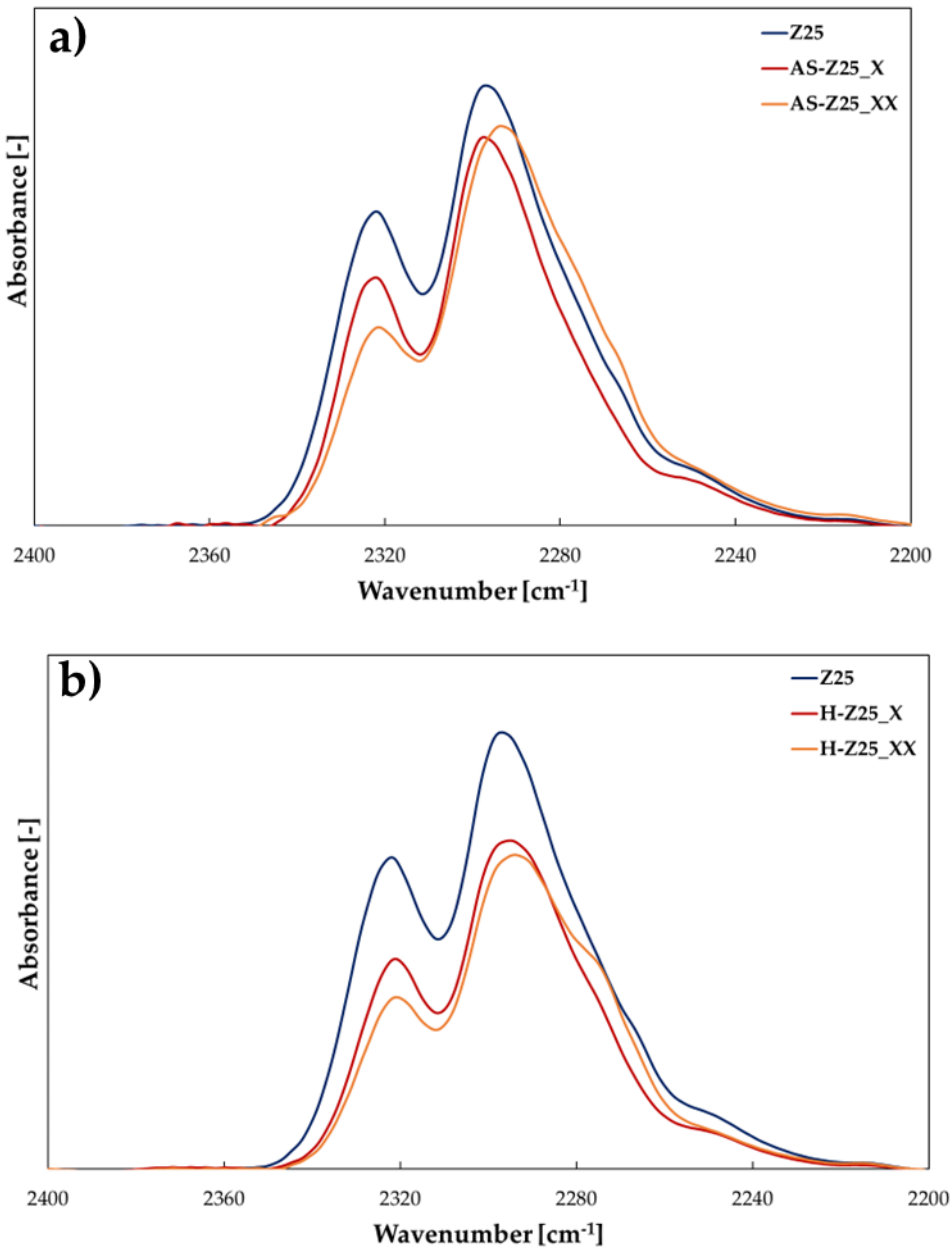

Figure 36: FT-IR spectra in the LAS/BAS region (d3-acetonitrile probe) after evacuation at room temperature of parent zeolite (Z25) compared to AS-Z25 passivated samples (a) and H-Z25 passivated samples (b).

Quantitative results obtained via the deconvolution of peaks related to Brønsted and Lewis acid sites for all investigated samples are reported in **Table 11**. Comparing parent zeolites, the effect of the Si/Al ratio on the total acidity appeared clear: with the increase of the Si/Al ratio, total acidity decreased. However, the different quantity of aluminum in the synthesis gel, only a difference of about 6% between Brønsted acid sites was found between Z11 and Z25 samples. On the contrary, Z11 catalysts exhibited a quantity of Lewis acid sites about 40% higher than the Z25 sample probably due to the presence of Al extra-framework

species. Moreover, the ratio between Brønsted and Lewis acid sites increased with the increase of the Si/Al ratio.

Results summarized in **Table 11** revealed that the effect of the passivation procedure depends on the form of the core. In the case of AS-Z25_X and AS-Z25_XX, only a decrease of Lewis acid sites was detected of about 26% and 28% respectively if compared with the parent Z25 zeolite. Contrariwise, a strong reduction of both Brønsted and Lewis acid sites was found for H-Z25 catalysts. Whatever the technique of passivation used, the reduction of acidity detected was more evident after the first deposition of Silicalite-1 than after the second cycle of passivation.

It is also useful to analyze how the Si/Al ratio influenced the success of the passivation method in terms of a decrease in total acidity value. Comparing parent zeolites (Z11, Z25, and Z50) with the respectively passivated samples (AS-Z11_X, AS-Z25_XX, and AS-Z50_XX) the effect of the Si/Al ratio was detectable. In the case of AS-Z11_XX and AS-Z25_XX coated samples, a decrease of about 10% in total acidity was found if compared with the parent zeolites. On the contrary, although the increase was found in the Si/Al ratio after the passivation process (highlighted in **Paragraph 4.1.4**), no significant differences were detected between the acidity of Z50 and AS-Z50_XX samples. It appeared clear that the passivation procedure over the parent zeolites with a Si/Al ratio equal to 11 and 25 influenced more Lewis acid sites as already explained. This evidence agrees with results already reported by Busca et al. [42] according to which since no bridging Si-(OH)-Al sites were found on the external surface of ZSM-5, the presence of strong Bronsted acid sites is limited to the internal channels of zeolites. Besides, in the same work, it was found that two types of Lewis acid sites exist on the surface of ZSM-5: Lewis acid sites bonded to tetrahedrally or trigonally coordinated Al^{3+} cations and Lewis acid sites with incompletely coordinated octahedral Al^{3+} cations, due to extra framework alumina species. The first ones are stronger, and they are much more abundant in samples with a higher Al content [42]. As showed in **Table 11**, Z50 already exhibited a much lower number of Lewis acid sites than Z25 and Z11. Consequently, a smaller number of strong Lewis acid sites already exist on the surface of ZSM5 zeolite with a Si/Al ratio equal to 50. It is probably for this reason that the

growth of Silicalite-1 (AS-Z50_XX) over the starting catalyst (Z50) did not strongly affect Lewis acidity.

Quantitative results obtained for AS-Z25_2XX and AS-Z11_2XX demonstrated that employing a higher quantity of Silicalite-1 synthesis gel during passivation procedure, caused a greater decrease of total acidity. Comparing passivated samples (AS-Z25_2XX and AS-Z11_2XX) with the starting parent zeolites also in this case a greater effect of passivation procedure over Lewis acid sites rather than over Brønsted acid sites detected. Furthermore, quantitative results summarized in **Table 11** demonstrated that, after the coating with Silicalite-1, the ratio between Brønsted and Lewis acid sites always increased as a consequence of the stronger effect of the passivation procedure over Lewis acid sites.

Table 11: Brønsted and Lewis acid sites distribution of the catalysts via FT-IR measurements.

SAMPLE	Brønsted Acid Sites[a] (BAS) (μmol g_{cat}^{-1})	Lewis Acid Sites (LAS)[b] (μmol g_{cat}^{-1})	BAS+LAS (μmol g_{cat}^{-1})	BAS/LAS
Z11	436	214	650	2.0
AS-Z11_XX	420	170	590	2.5
Z25	411	155	566	2.7
H-Z25_X	298	114	412	2.6
H-Z25_XX	271	97	368	2.8
AS-Z25_X	399	115	514	3.5
AS-Z25_XX	395	112	507	3.5
Z50	270	49	319	5.5
AS-Z50_XX	276	46	322	6.0
AS-Z25_2XX	356	90	446	3.9
AS-Z11_2XX	406	149	556	2.7

[a] Brønsted acid sites (IMEC= 2.05 cm/μmol, [110])

[b] Lewis acid sites (IMEC= 3.6 cm/μmol, [110])

To assess the strength of the acid sites and to deeply investigate the effect of the epitaxial growth of Silicalite-1, FT-IR spectra CD_3CN after desorption at different temperatures were performed and results are reported in **Figure 37 (a, b, c, d)** in terms of the fraction of covered sites, referred to the sites measured at 25°C (assumed to be completely covered). Desorption spectra are reported in **Appendix B (Figure B9)**. A significant reduction of Brønsted acid sites was found already at 150°C for all investigated catalysts. Only a residual adsorbed fraction below 20% remained at 400°C. On the contrary, the decrease of Lewis acid sites was less strong, and at 400°C a fraction of about 50% remained adsorbed. This trend confirmed that Lewis acid sites are stronger than Brønsted acid sites also after the deposition of Silicalite-1. After the deposition of Silicalite-1 over the core in as synthetised-form, a decrease in the strength of Brønsted acid sites was found. In fact, at 150°C a decrease of covered Brønsted acid sites more pronounced for AS-Z25_X and AS-Z25_XX was detected if compared with the starting parent zeolite. This trend was not observed for Lewis acid sites as the curves obtained are always similar. For, what concerns H-Z25_X and H-Z25_XX catalysts, the behavior found was more incoherent. Brønsted acid sites strength increased after the first deposition cycle as a higher fraction of covered sites was found at 150°C for the H-Z25_X sample. The fraction of covered Brønsted acid sites decreased at 150°C for the sample passivated with two layers of Silicalite-1 but it was higher at 200°C, 300°C and 400°C if compared with the parent Z25 sample (**Figure 37b**). For what concerns Lewis acid sites (**Figure 37d**), the double coating of the core in acidic form caused a weakening of the Lewis acid sites. These results confirmed the idea according to which coating a core with the organic template inside the pores allowed to obtain passivated catalyst with a tidier structure and with properties close to that of the starting zeolite. In fact, only a small difference of about 60 μmol/g was detected between Z25 and AS-Z25_XX samples related to the neutralization of external acid sites while the total acidity value was preserved. Moreover, reducing the strength of Brønsted acid sites could be useful in catalytic applications where mainly Brønsted acid sites cause coke formation and catalysts deactivation [119].

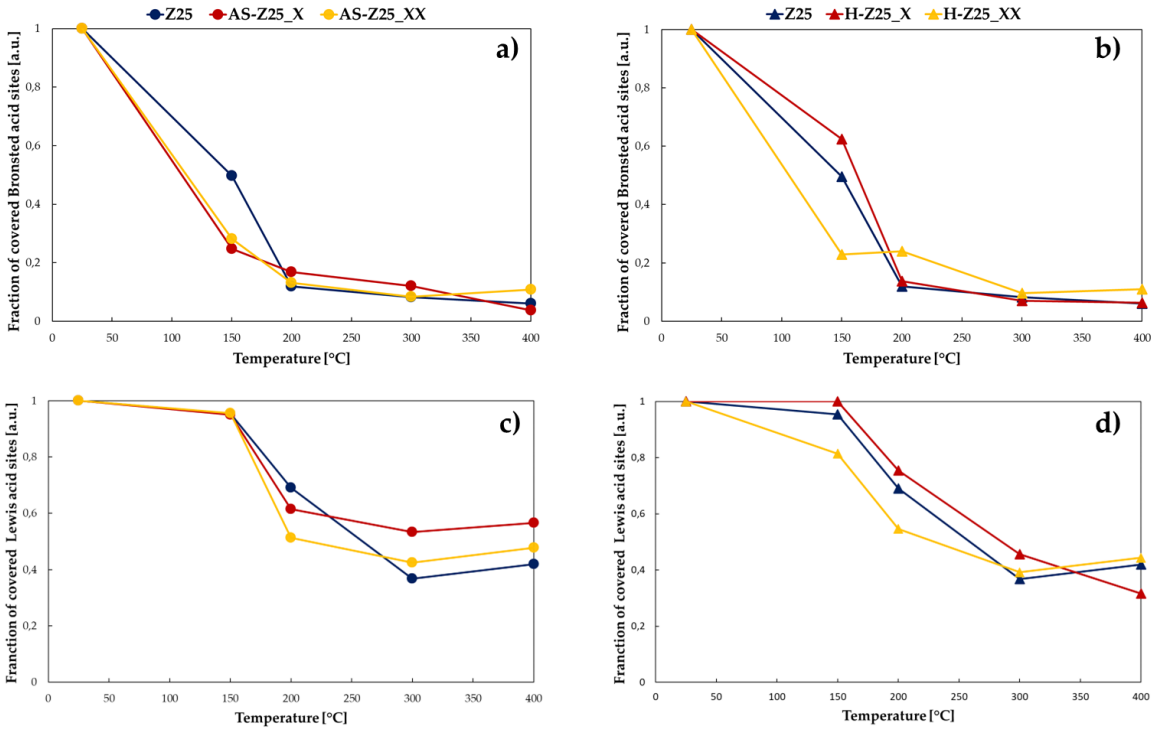

Figure 37: Fraction of covered Brønsted (a and b) and Lewis acid sites as a function of the desorption temperature.

4.1.9 Solid-state NMR MAS.

In **Figure 38** ^{29}Si NMR spectra of Z25 parent zeolite and passivated H-Z25_XX and AS-Z25_XX are reported. Parent zeolite and coated catalyst obtained starting from an as synthetised-form core (AS-Z25_XX) exhibited the same Si local environment. On the contrary, a slight broadening in the Q^4 region was detected for the H-Z25_XX sample. Al NMR spectra also reported in **Figure 38** show the same trend: Z25 and AS-Z25_XX samples exhibited the same Al environment while a slight distortion was observed for the H-Z25_XX catalyst. High-resolution ^{1}H-NMR spectra were also acquired and are shown in **Figure 38.** The peak at 3.7 ppm, related to isolated Bronsted acid sites, decreased by 40% for sample H-Z25_XX if compared with the parent zeolite. On the contrary, only a slight decrease of 4% was found for sample AS-Z25_XX. These results are in line with d3-acetonitrile FT-IR quantitative results already explained in **paragraph 4.1.8**. Furthermore, broad bands were detected at high chemical shifts (above 5.8 ppm) for the AS-Z25_XX sample probably related

to the formation of some nests due to the links between Silicalite-1 and the starting parent ZSM-5.

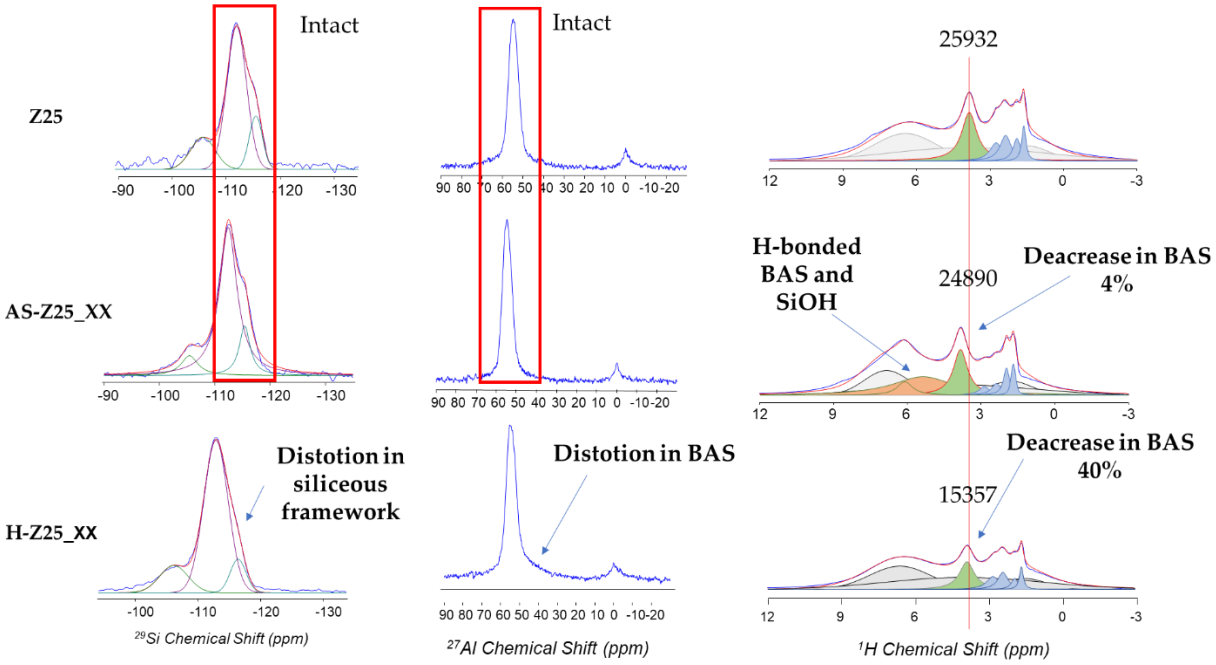

Figure 38: NMR spectra (Si-NMR, Al-NMR, and H-NMR) of parent zeolite (Z25) and passivated samples (AS-Z25_XX and H-Z25_XX)

4.2 BEA@Sil-1

4.2.1 XRD.

Figure 39 shows XRD patterns of investigated BEA-type samples before (BEA) and after (BEA_X and BEA_XX) the Silicalite-1 deposition. Moreover, to underline the growth of the MFI structure over the starting BEA zeolite, the Silicalite-1 pattern was also reported in **Figure 39.** BEA catalyst exhibited a crystallographic pattern typical of BEA-type zeolite with characteristic peaks at 2θ=7.6 and 2θ=22.4 according to the reference pattern published on http://www.iza-online.org/. BEA_X and BEA_XX samples pattern also showed the classic BEA pattern with the addition of typical MFI peaks at 2θ values of 7.9°, 8.8° and 23.1°. Moreover, MFI-type peaks intensity increased with the increasing of steam-assisted crystallization procedures carried out. No trace of amorphous silica was observed in any sample.

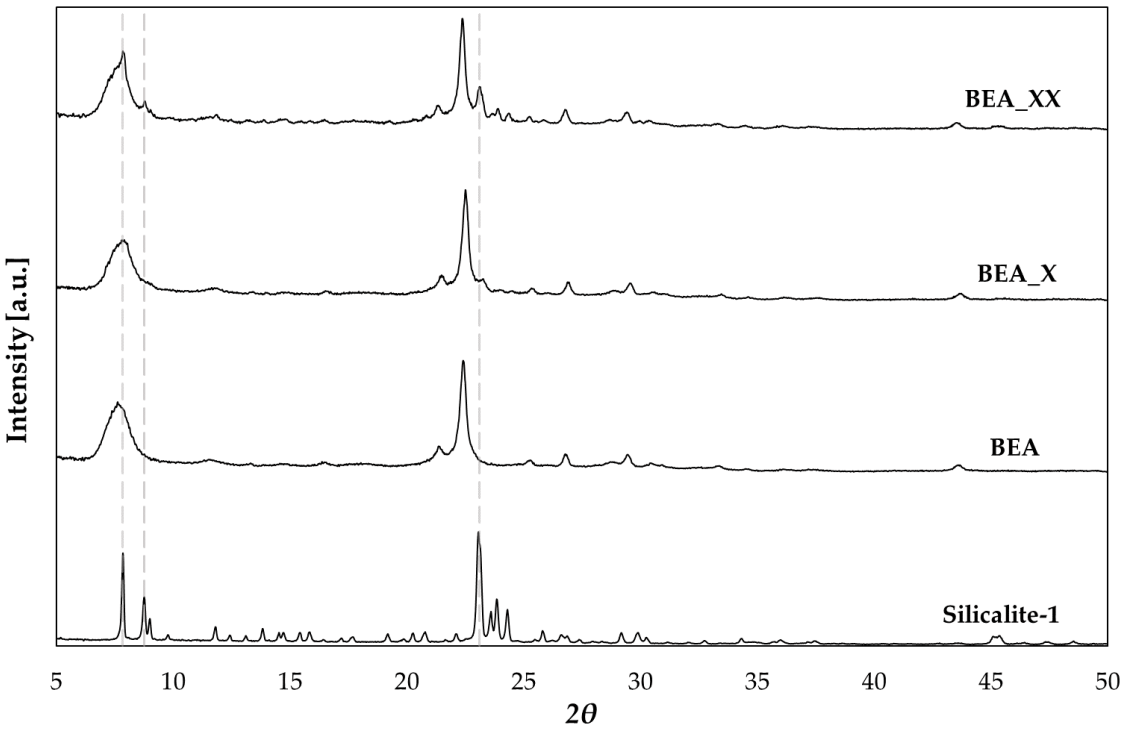

Figure 39: XRD spectra of investigated samples.

4.2.2 SEM-EDX.

Figure 40 shows samples crystals morphology observed by means of scanning electron microscopy. Both BEA and coated samples (BEA, BEA_X and BEA_XX) consisted of crystals with a size of 100-200 nm and with a flattened spheroid shape. Although the presence of Silicalite-1 crystals grown over the surface of the starting zeolite was impossible to be detected with this technique, SEM micrographs of BEA_X and BEA_XX did not demonstrate the presence of two distinct phases (BEA and MFI) and, for this reason, homogeneous nucleation of Silicalite-1 can be denied.

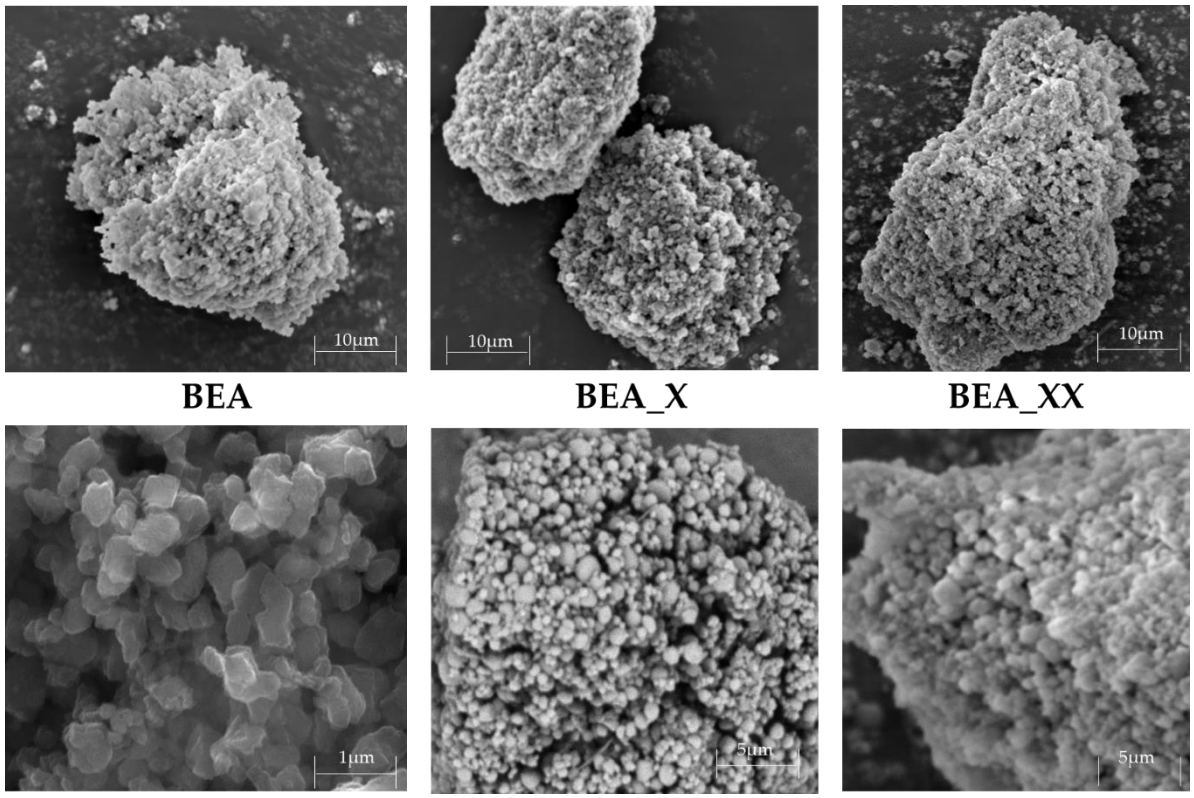

Figure 40: SEM micrographs of BEA, BEA_X and BEA_XX samples at different magnifications.

EDX measurements for BEA parent zeolite and coated BEA_XX sample were performed at different voltage to evaluate the Si/Al ratio (**Table 12**). The Si/Al ratio obtained for parent zeolite was higher than the one employed in the synthesis gel (equal to 25). A decrease in the Si/Al ratio was detected for the BEA@Sil-1 sample and demonstrated that a thin layer of Silicalite-1 grew over the external surface of parent zeolite. For both investigated catalysts, an increase in Si/Al was found with the increasing of voltage employed during EDX measurements proving that the quantity of aluminium is higher in the internal channels rather than on the external surface.

Table 12: EDX measurements results of investigated catalysts.

Sample Code	Si/Al [mol/mol] [5 kV]	Si/Al [mol/mol] [7 kV]	Si/Al [mol/mol] [10 kV]
BEA	11.1	10.2	10.2
BEA_XX	13.2	12.1	12.0

4.2.3 Porosimetric results.

N_2 adsorption/desorption isotherms of BEA, BEA_X and BEA_XX catalysts are shown in **Appendix A (Figure A20).** The main physical properties of catalysts are summarized in **Table 13**.

Table 13: Textural properties of investigated catalysts.

Catalyst	S_{BET}[a] (m^2/g)	S_{micro}[b] (m^2/g)	S_{ext}[b] (m^2/g)	V_p[c] (cm^3/g)	V_{micro}[b] (cm^3/g)
BEA	**576**	428	148	0.37	0.170
BEA_X	**662**	449	212	0.40	0.180
BEA_XX	**616**	442	174	0.37	0.177

[a]Calculated by the multipoint BET method in the Rouquerol p/p^0 range; [b]Calculated by the t-plot method; [c]Calculated at p/p^0 0.95

As shown in **Table 13**, no evident changes were detected between parent zeolite and coated samples micropore area values and this result demonstrated that the growth of Silicalite-1 over the external surface of BEA-type zeolite did not cause any occlusion of pores.

4.2.4 Acidity evaluation: NH_3-TPD and FT-IR.

NH_3-TPD profiles, normalized by the weight of the analysed sample, of parent zeolite and coated catalysts are shown in **Figure 41**. Each catalyst exhibited the typical profile of a BEA-type zeolite with two main peaks: the first one at lower temperatures related to weak acid sites and the second one at higher temperatures linked to the presence of strong acid sites[120]. A decrease in total acid sites appeared clear after each deposition step.

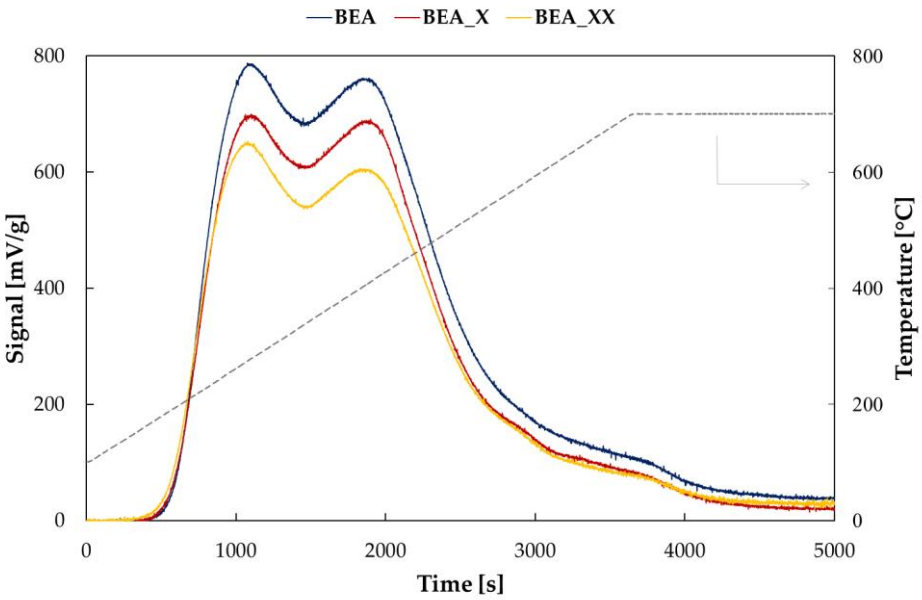

Figure 41: NH_3-TPD profiles of BEA parent zeolite and coated samples (BEA_X and BEA_XX).

Quantitative results obtained via peaks deconvolution are summarized in **Table 14**. Total acidity values confirmed the decreasing trend exhibited after each deposition treatment. Moreover, both weak and strong acid sites decreased for BEA_X and BEA_XX samples if compared with the parent zeolite and the ratio between weak and strong acid sites did not change significantly after the coating with Silicalite-1. Although the reduction in total acidity, maximum desorption temperatures remained unchanged for BEA, BEA_X and BEA_XX samples.

Table 14: Acidity of parent zeolite and coated samples: NH3-TPD analysis and FT-IR d3-acetonitrile.

Catalyst	NH_3-TPD (μmol/g_{cat})			D-Ac FT-IR (μmol/g_{cat})		
	Weak [a]	Strong [a]	**Total**	B [c]	L [c]	**Total**
BEA	250 (280)	421 (405)	**671**	518	214	**731**
BEA_X	243 (280)	368 (405)	**611**	429	202	**631**
BEA_XX	239 (280)	356 (405)	**595**	358	170	**528**

[a] From NH3-TPD profiles: weak sites ammonia desorption range 100–300 °C, strong sites ammonia desorption above 300 °C.
Values in parenthesis are desorption temperature peaks (°C);
[b] B: Bronsted acid sites ($IMEC_B$= 2.05 cm/μmol); L: Lewis acid sites ($IMEC_L$= 3.6 cm/μmol)

Figure 42 shows FT-IR spectra of investigated samples after d3-acetonitrile adsorption in the wavenumber range 2400-2200 cm^{-1}. Three main peaks were detected as usual: the first one at 2320 cm^{-1} related to d3-acetonitrile reacting with Lewis acid sites, the second one at 2290 cm^{-1} linked to Brønsted acid sites linked to the probe and the third one at 2275 cm^{-1} indicating the presence of terminal silanols group reacting with d3-acetonitrile. A decrease of both Brønsted and Lewis acid sites was detected after each step of Silicalite-1 deposition as confirmed by quantitative results summarised in **Table 14**.

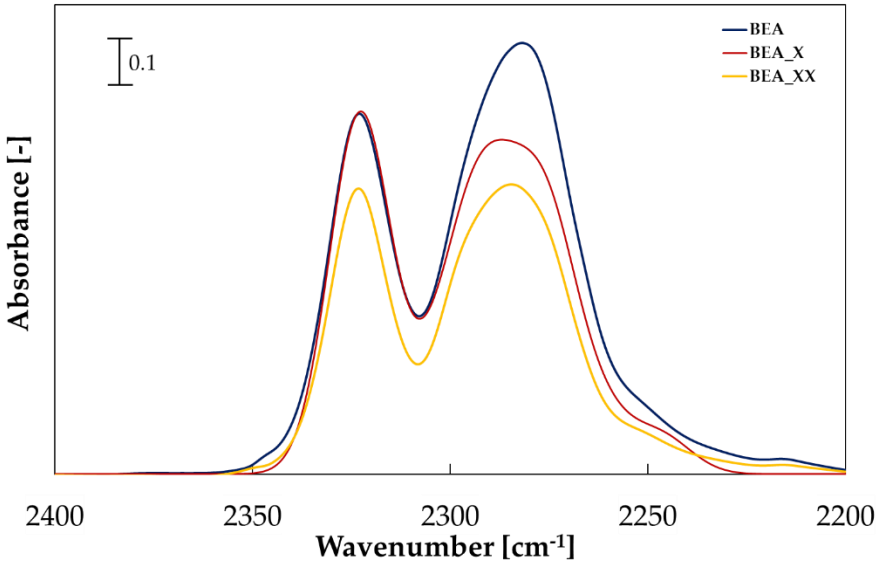

Figure 42: FT-IR d3-acetonitrile spectra of parent zeolite (BEA) and coated samples (BEA_X and BEA_XX).

4.3 ZSM-5 passivated via CLD of TEOS.

4.3.1 XRD

XRD spectra of parent Z11 and Z25 zeolites and samples treated with chemical vapour deposition of TEOS are reported in **Appendix A (Figure A5-A6).** It is clear that passivation carried out with chemical vapour deposition of TEOS caused neither a substantial loss in crystallinity nor the appearance of a new crystalline phase.

4.3.2 SEM-EDX

SEM micrographs of parent zeolites and their passivated counterparts are reported in **Figure 43**. Chemical vapour deposition of TEOS did not affect the morphology of the sample as no evident differences were detected for treated samples if compared with the starting parent zeolites except for the presence of very few amorphous silica traces deposited over the starting crystals agglomerates.

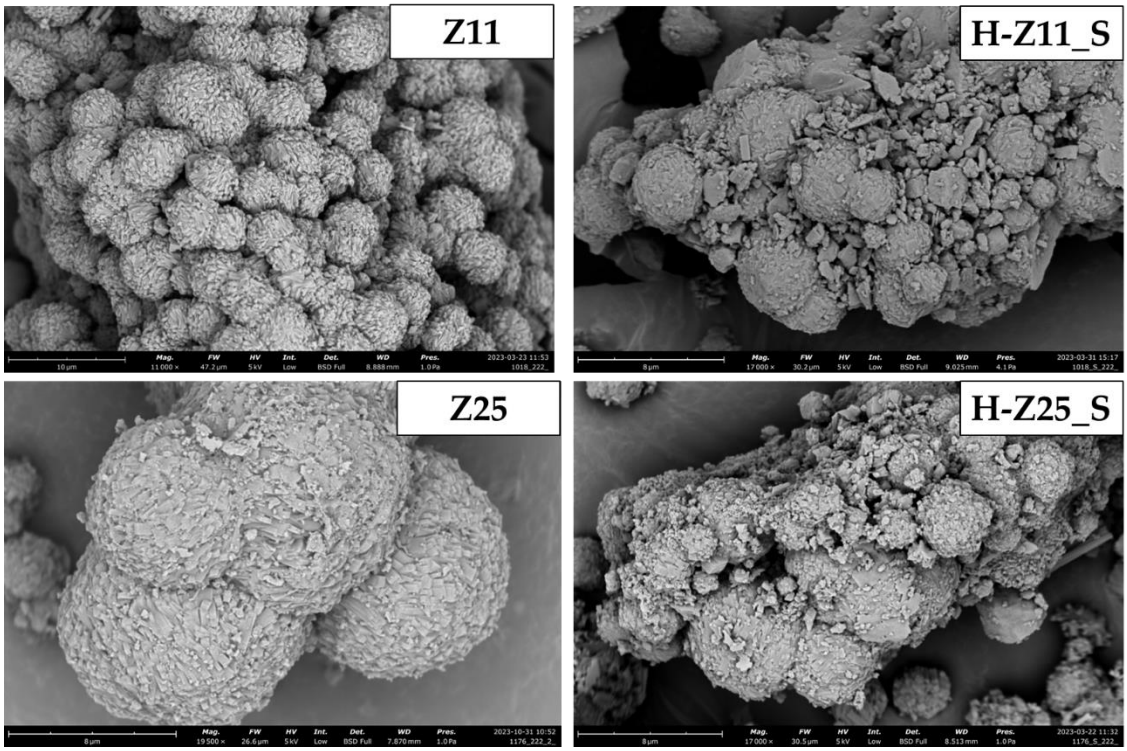

Figure 43: SEM micrographs of parent zeolites (Z11 and Z25) and passivated samples (H-Z11_S and H-Z25_S).

EDX measurements were performed for all investigated catalysts at 5 and 15 kV in order to estimate the Si/Al ratio and results are reported in **Table 15**. For the H-Z11_S sample, a slight increase in the Si/Al ratio was detected both at 5kV and 15kV. This trend was not found for the H-Z25_S catalyst which exhibited the same Si/Al ratio of the parent zeolite at 5kV and a higher Si/Al ratio at 15kV. Results agree with characterization data already reported in the literature demonstrating that no substantial differences in the Si/Al ratios were detected after a treatment of CLD of TEOS over ZSM-5 zeolites [96].

Table 15: EDX measurement results (at 5kV and 15kV) of investigated samples.

Sample Code	Si/Al [mol/mol] [5 kV]	Si/Al [mol/mol] [15 kV]
Z11	9.2	6.7
H-Z11_S	11.6	8.5
Z25	23.7	19.9
H-Z25_S	23.6	16.6

4.3.3 Porosimetric results.

The main textural properties of catalysts are summarized in **Table 16**. Chemical vapour deposition of TEOS caused a decrease in BET surface area and micropores area (higher for AS-Z11_S concerning the starting Z11 parent zeolite) concerning the starting zeolites probably due to a partial blockage of channels. This result agrees with data already published in the literature about the chemical vapour deposition of TEOS [96]. N_2 adsorption/desorption isotherms are reported in **Appendix A (Figure A21-A22).**

Table 16: Textural properties of investigated catalysts.

Catalyst	S_{bet}[a] (m^2/g)	S_{micro}[b] (m^2/g)	S_{ext}[b] (m^2/g)	V_p[c] (cm^3/g)	V_{micro}[b] (cm^3/g)
Z11	389	296	93	0.200	0.117
AS-Z11_S	350	230	121	0.20	0.092
Z25	409	264	145	0.24	0.107
AS-Z25_S	367	257	113	0.19	0.102

[a]Calculated by the multipoint BET method in the Rouquerol p/p^0 range; [b]Calculated by the t-plot method; [c]Calculated at p/p^0 0.95

4.3.4 Acidity evaluation: FT-IR.

Acidity distribution evaluation was performed via FT-IR analysis employing d_3-acetonitrile as a probe. **Figure 44 (a, b)** reports FT-IR spectra of investigated samples in the wavenumber range 2400-2200 cm^{-1}.

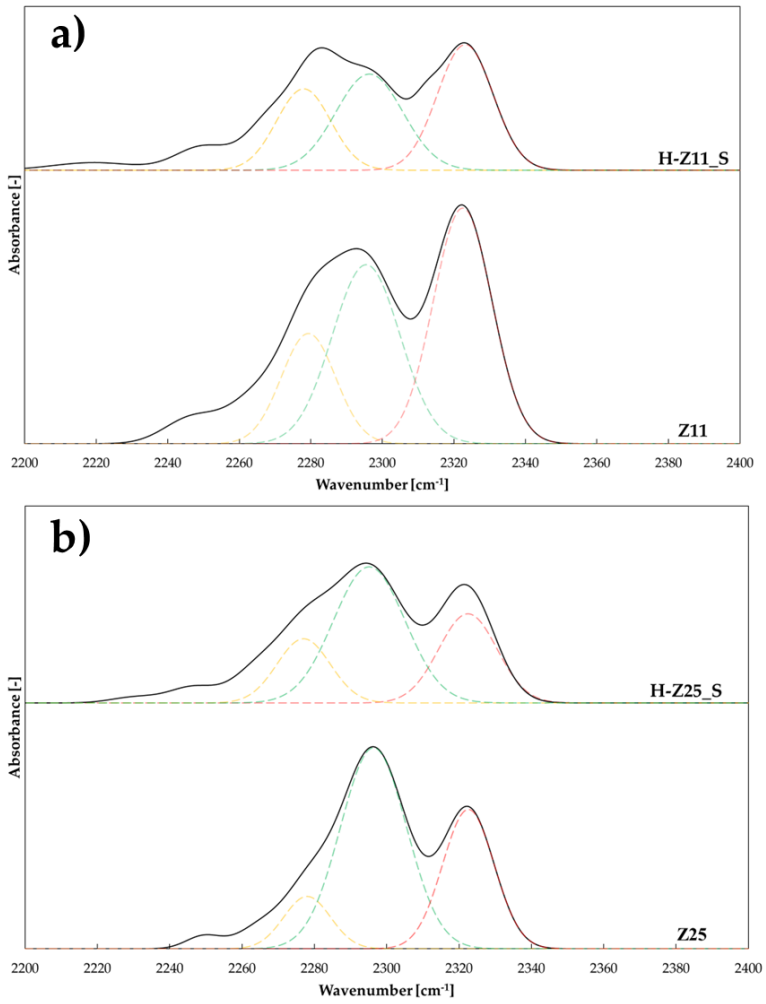

Figure 44: FT-IR spectra after d3-acetonitrile adsorption of Z11 and its passivated counterpart (a) and of Z25 and its passivated counterpart

Three main peaks were detected as usual: the first one at 2320 cm^{-1} related to d_3-acetonitrile reacting with Lewis acid sites, the second one at 2290 cm^{-1} linked to Brønsted acid sites linked to the probe and the third one at 2275 cm^{-1} indicating the presence of terminal silanols group reacting with d_3-acetonitrile. From the deconvolution of the peaks related to Brønsted and Lewis acid sites quantitative results have been obtained and results are summarized in **Table 17**.

Table 17: Acid sites distribution of parent zeolites and passivated samples

SAMPLE	Brønsted Acid Sites[a] (BAS) (μmol g_{cat}^{-1})	Lewis Acid Sites (LAS)[b] (μmol g_{cat}^{-1})	BAS+LAS (μmol g_{cat}^{-1})	BAS/LAS
Z11	380	246	626	1.5
AS-Z11_S	202	133	334	1.5
Z25	423	146	570	2.9
AS-Z25_S	335	124	459	2.7

[a] Brønsted acid sites (IMEC= 2.05 cm/μmol)

[b] Lewis acid sites (IMEC= 3.6 cm/μmol)

A strong decrease in both Bronsted and Lewis sites was found for AS-Z11_S and AS-Z25_S samples if compared with the starting untreated parent zeolites. The ratio between Bronsted and Lewis acid sites remained unchanged after the chemical deposition of TEOS. These findings did not agree with another work published by Valtchev et al. where a decrease of only Bronsted acid sites was found after the treatment [89]. The reduction of Lewis acid sites detected could be related to the fact that starting parent zeolites (Z11 and Z25) were characterised by a high number of Lewis acid sites (higher than that exhibited by zeolites studied by Valtchev et al.) and part of these acid sites were neutralized during the deposition steps.

CHAPTER 5. Methanol dehydration to DME.

Research efforts dedicated to the investigation of methanol dehydration reaction to dimethyl ether could be divided into two different parts. The first part of the work concerned the employment of high aluminum content H-ZSM5 zeolites (Si/Al ratio in the synthesis gel equal to 11) then passivated using the technique of Silicalite-1 epitaxial growth and tested in a bench-scale packed bed reactor operated at 160–240 °C under atmospheric pressure. The development of the innovative passivation technique via Silicalite-1 deposition over a starting ZSM-5 zeolite (Si/Al ratio equal to 25) with the organic template still filling the channels was the central point of the second part of the research work. To understand the effect of passivation treatment used over catalytic performances, passivated samples obtained coating the ZSM-5 zeolite in synthesized form and H^+-form were tested in a methanol dehydration reaction. Furthermore, parent zeolites (Z11, Z25, and Z50) were tested as references, also to assess the effect of the Si/Al ratio on methanol conversion and DME selectivity.

5.1 State of art: Methanol conversion to DME.

Nowadays, because of global warming and environmental pollution, the world community is looking for sustainable and renewable energy sources. This critical situation is attracting governments' and scientists' interest. Particularly, greenhouse gas emissions continue to increase; although the growth rate was higher in the first decade of this century (2.6%), from 2012 to 2019 greenhouse gas emissions grew at an average rate of 1.1% [121]. Furthermore, 2019 was the second warmest year in the last 140 years with an increase in global land and ocean surface temperatures of 0.95°C. The International Energy Agency (IEA) produced a detailed report about CO_2 emissions and showed that although a decrease was registered because of the pandemic situation in 2020, the rapid recovery of the world economy in 2021 caused a rebound of CO_2 emissions of more than 6% (**Figure 45**) [122]. In 2022 CO_2 emissions grew by 0.9% reaching the new high of 36.8 Gt.

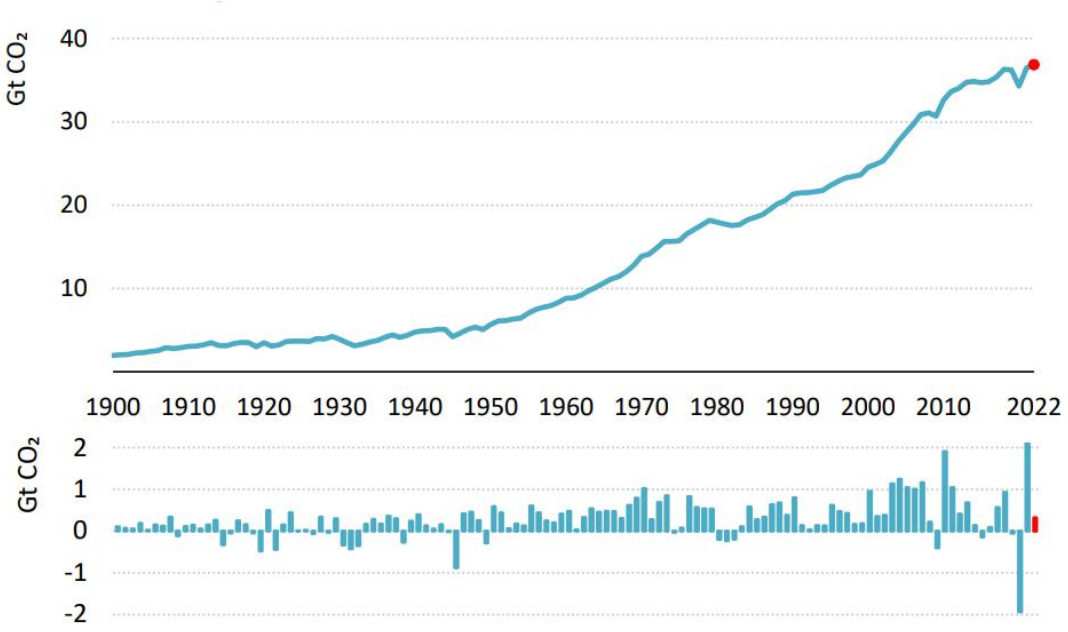

Figure 45: Worldwide CO_2 emissions from energy combustion and industrial processes and their annual change during the years 1900-2022 [122].

In this context, it is dutiful to underline that the transportation sector causes much of the air pollution and it still depends on fossil fuel. It was estimated that 21% of global CO_2 emissions in 2021 originated from the transportation sector [122]. Meanwhile, energy demand is strongly increasing because of the continued growth of the world population, industrialization and fast-growing emerging economies development (e.g. India). In fact, global energy consumption growth increased in 2022 by 2.1% and although it halved in 2021, it remained higher than the average 2010-2019 rate (1.4%/year) [123]. Furthermore, geopolitical tensions caused a great increase in energy prices especially in Europe. For all these reasons, to accelerate the pathway toward decarbonization and to reduce the dependence on fossil fuels became essential for governments. In this regard, a big effort has been made in these years for the implementation of clean and renewable energy sources such as solar, wind, geothermal, CO_2, biomass, and biofuels. As already explained, global energy consumption has increased dramatically in recent years but with it so the renewable energy consumption (**Figure 46**). It has been expected that by 2050 renewable energy consumption will increase and will reach about 247 exajoules (almost 6 times higher than the consumption in 2000) [124].

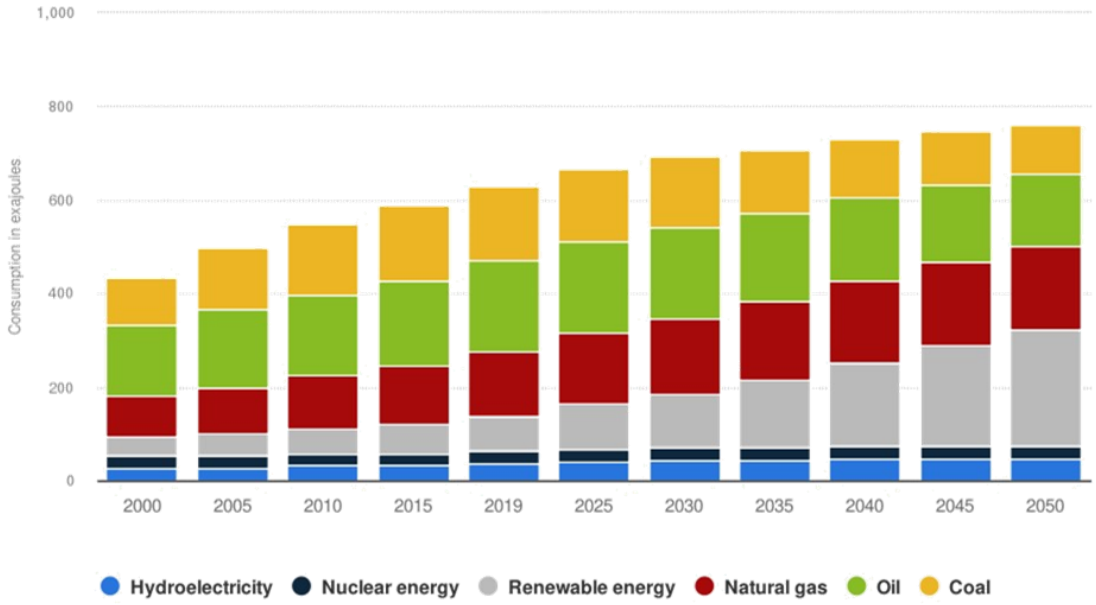

Figure 46: Energy consumption worldwide from 2000 to 2019, with a forecast until 2050, by energy source (in exajoules) [124].

Among the rising alternative fuels, dimethyl ether (DME) seems to be the one with the largest potential impact on society, produced from biomass-derived syngas or non-biogenic CO_2 it could replace conventional fossil-based fuels. DME is the simplest ether with no C-C bonds. The absence of C-C bonds in the DME structure allows to obtain combustion emissions with a lower quantity of NOx, PM, and SOx if compared with traditional diesel emissions [125]. DME is an organic compound, but it is non-carcinogenic, non-teratogenic, non-mutagenic, and non-toxic. It is gaseous under standard atmospheric conditions of 0.1 MPa and 298 K but it can be easily condensed with a pressure of 0.5 MPa. For this reason, it could be stored and transported in pressurized tanks in liquid form. DME characteristics are close to that of liquefied petroleum gas (LGP) and nowadays blends of DME and LGP are already handled using the existing infrastructures employed for LGP. DME can also be used to replace diesel fuel in compression-ignition engines because of its characteristics. Its higher content of oxygen promotes the occurrence of combustion without the production of soot. If compared with diesel fuel, DME is characterized by a lower boiling point at atmospheric pressure (248.1 K), and for this reason, it evaporates rapidly when it is injected into the engine cylinder. Moreover, DME is characterized by a relatively high cetane number between 55 and 60 and its auto-ignition temperature is approximately the same as diesel

fuel (350°C). The reduction of polluting emissions represents one of the advantages linked to the use of DME [126]. On the other hand, some disadvantages have also been identified. First of all, DME exhibits a lower combustion enthalpy if compared with diesel fuel (27.6 J/kg and 42.5 J7kg respectively). For this reason, a larger amount of injected volume and a longer injection period are needed for DME to get the same amount of energy obtained with a lower quantity of diesel fuel. Moreover, some other disadvantages are linked to the necessity of making some changes in engine configuration to substitute diesel fuel with DME. In fact, DME is characterized by a lower viscosity that makes necessary the employ of special gaskets to avoid leak of material from the storage tanks. DME modulus of elasticity is lower than diesel fuel one and this implies a higher DME compressibility and a greater compression work of the fuel pump [126].

It is well known that employing diesel-fueled compression ignition (CI) engines rather than gasoline-fueled spark ignition (SI) engines offers some advantages (like fuel economy and higher predictable life) but also some disadvantages linked to the production of higher quantity of harmful pollutants such as nitrogen oxide (NOx), particular matter (PM), hydrocarbon compounds (HC), carbon monoxide (CO) and sulfur oxides (SOx). Studies conducted by Park et al. demonstrated that emissions of HC and CO were lower if DME was used as fuel instead of diesel [127]. Moreover, DME fuel does not contain sulfur and thus SOx-free exhausted gas is obtained when it is used. As already mentioned, the higher content of oxygen in DME leads to better combustion performances reducing the formation of C-C bonds responsible for soot emissions. Results already published in the literature proved that employing DME particulate yield obtained (0.026%) was always lower than the value reached with both diesel and bio-diesel fuels (0.51%) [128]. Well-to-wheels analysis (WTW) conducted, consisting of a well-to-tank (WTT) and tank-to-wheels analysis (TTW) suggested DME as one of the best alternatives for several vehicles technologies with a WTW efficiency (calculated as the ratio between the energy of the fuel and the total energy consumption of all the steps from feedstock recovery to fuel distribution) comparable with liquefied petroleum gas and compressed natural gas [126]. DME also represents a suitable chemical intermediate for olefins and synthetic gasoline production. In most cases, DME

can be employed in all the processes in which methanol is used as a reactant because it is an intermediate of most of the reactions involving methanol. For example, DME could be employed to produce light olefins and gasoline replacing methanol in MTO (methanol to olefins) and MTG (methanol to gasoline) processes. Substituting methanol with DME allows them to perform a more sustainable process starting from a non-toxic compound. Industrially, the MTG reaction is performed at around 400°C at a pressure of 20-30 atm employing HZSM-5 as a catalyst. Instead, to increase the production of olefins higher temperatures are required and SAPO-34 is usually employed as a catalyst for the reaction [129]. DTO reaction has been widely discussed in **Chapter 6**.

Nowadays, growing attentions are developing on hydrogen production as it can be considered the energy carrier of the future because of its high energy content per unit of mass and because it could be employed in fuel cells to produce electricity with a very low quantity of pollutant emissions [130,131]. DME can also be used as a hydrogen source because high-quality syngas can be produced through DME steam reforming [132,133].

Lastly, dimethyl ether is also a candidate to be used as fuel for power generation in gas turbines because of the low emissions of particulate matter, NOx, and CO during its combustion due to the simplicity of its short carbon chain. DME heat value is lower than that of conventional diesel fuel and, for this reason, modifications of the fuel supply system, injection system, and combustion system of the gas turbine are needed to employ it as an alternative fuel [134].

Dimethyl ether can be produced via indirect and direct synthesis processes as shown in **Figure 47**. In the direct route, methanol synthesis and dehydration reactions are performed in one step while in the indirect route, two steps are required [135,136]. The starting point of both direct and indirect routes is syngas, a mixture of carbon monoxide and hydrogen, that can be produced from different feedstocks such as natural gas, coal, oil residues but also biomass [137,138]. Particularly, syngas can be produced via steam reforming of natural gas but also from biomass gasification or biogas (CH_4 and CO_2) dry reforming [125]. If the starting feedstock employed to produce syngas is not fossil-derived, DME can be considered a sustainable and renewable product.

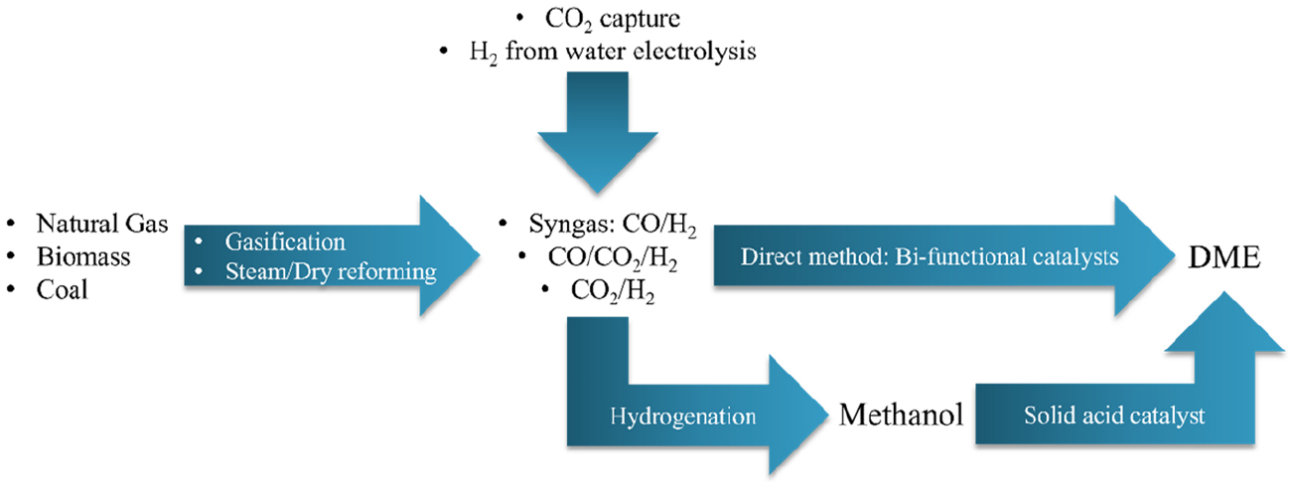

Figure 47: DME production via direct and indirect methods [125].

The indirect process is the traditional way to produce DME and it consists of two main steps: methanol synthesis from syngas employing Cu/Zn-based catalysts and methanol subsequent dehydration to DME using an acid catalyst. Methanol produced after the first step should be purified from unreacted gas and water. Similarly, to obtain the desired DME purity, DME from methanol dehydration should be separated from water and unreacted methanol [136].

Methanol is produced via the hydrogenation reaction of carbon oxides. Industrially this reaction is conducted at high pressure (50-100 bar) and in a temperature range of 200-300°C [139]. $Cu/ZnO/Al_2O_3$ (CZA) is the catalyst commonly used for methanol synthesis from syngas. Cu represents the active sites, ZnO is a textural promoter because it improves Cu dispersion and prevents its agglomeration while Al_2O_3 is a structural promoter needed to stabilize Cu and ZnO avoiding sintering. Although CZA is a state-of-the-art catalyst for methanol production, many works to study how to improve its catalytic performance are still being published. Liu et al. prepared some copper/zirconia catalysts using three different methods: deposition-precipitation, co-precipitation, and simple impregnation [140]. Results demonstrated that ultra-fine particles obtained via the deposition-precipitation method allowed to obtain a higher catalytic activity. In another work, authors studied the effect of calcination temperature over $CuO/ZnO/ZrO_2$ catalyst, and they demonstrated that copper dispersion decreased with the increase of calcination temperature. They identified the

catalyst calcined at 400°C as the one that exhibited the best catalytic performances [141]. A lot of efforts have been dedicated to analyzing the effect of adding a promoter on catalysts properties. Sloczynski et al. prepared Cu/Zn/Zr catalyst adding Mg and Mn as promoters. Researchers defined a factor combining adsorptive properties and catalytic activity of catalysts and demonstrated that this factor increased in this order: CuZnZr < CuZnZrMg < CuZnZrMn [142]. In another work, ZrO_2-doped CuZnO catalysts have been synthesized using a successive precipitation method and tested in the reaction of CO_2 conversion to methanol. Doped catalysts showed a higher CO_2 conversion if compared to CuZnO one because copper active species had better dispersion when Zr was added [143]. Furthermore, palladium incorporation in Cu-Zn based catalysts has been explored and, also in this case, adding a promoter allowed to achievement of better catalytic performance in terms of methanol yield found [144].

The second step of indirect DME synthesis is methanol dehydration reaction:

$$2CH_3OH \leftrightarrow CH_3OCH_3 + H_2O$$

It is an exothermic reversible reaction (- $\widetilde{\Delta H}_r^0\,(298\,K) = 23.5\,kJ/mol$) without moles variation and for this reason pressure does not influence equilibrium conversion while low temperatures have a thermodynamic positive effect. Methanol dehydration is an acid-catalysed reaction and, depending on the catalyst employed, it could be performed both in vapor and liquid phase (temperature range: 100-300°C and pressure up to 20 bar). γ-Al_2O_3 is the most common catalyst used for methanol dehydration reactions because of its weak and medium-strength Lewis acid sites [136]. Even if γ-Al_2O_3 exhibits a high selectivity versus DME also at reaction temperatures up to 400°C, its activity is not so high at low reaction temperatures. In fact, a temperature of 250-270°C is necessary to increase methanol conversion [145]. Furthermore, γ-Al_2O_3 presents a hydrophilic character and, for this reason, water produced in the dehydration reaction can reduce its acidity and also adsorb on its surface instead of methanol [136]. Lots of studies have been conducted to modify γ-Al_2O_3 properties such as increasing its acidity or decreasing its hydrophilicity. Meanwhile, other catalysts have been studied and tested for the reaction of methanol dehydration and among these zeolites. The most studied zeolite is HZSM-5 characterised by both Brønsted and

Lewis acid sites. Unlike γ-Al_2O_3, this zeolite does not deactivate due to the water produced and thanks to its stronger acid sites it shows higher activity even at lower temperatures [146]. The presence of strong acid sites causes the shift of the reaction versus the production of by-products leading to the formation of coke; in fact, DME is an intermediate for the production of olefins as well explained in the following Chapter. For this reason, lots of efforts have been dedicated to tune zeolites' acidity properties decreasing the total acidity, or modifying acid sites strength and distribution [147]. Neutralizing external acid sites of zeolites could also be a route to inhibit coke formation as already elucidated in **Chapter 2** and it has been the technique employed to tune properties of ZSM-5 catalysts synthetised for this research work and employed for DME synthesis. Zeolites structure represents a key factor to inhibit successive undesired reactions. It has been demonstrated that 3D-framework BEA-type zeolite exhibited a higher conversion of methanol but, with its larger pores, led to the formation of a greater amount of coke. 2D-framework FER-type zeolites with its small pores exhibited the best catalytic performance in terms of DME selectivity and lowest coke formation if compared with MFI-type and BEA-type zeolites [114]. In **Figure 48** the scheme of process for indirect DME synthesis is reported. It usually consists of two distillation columns: the first one for DME purification and the second one to separate methanol from water and to recycle the alcohol to the reactor [148].

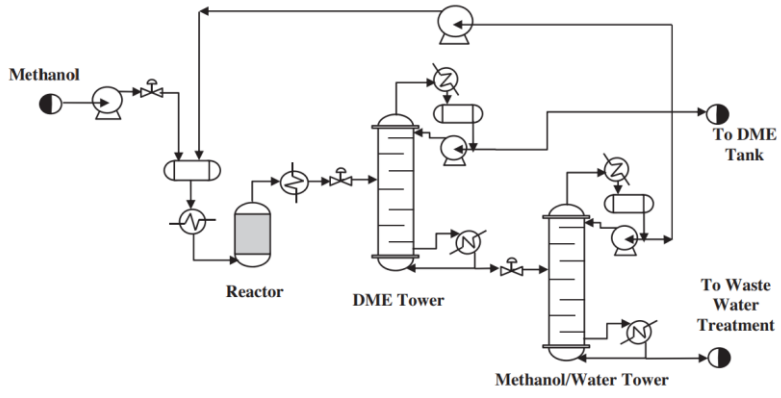

Figure 48: Scheme of indirect DME synthesis process [148].

DME direct routes are characterized by fewer chemical units because only one reactor is needed to produce DME directly from syngas and because no purification units are required for unreacted CO_2 and syngas as in the indirect process [125].

In **Table 18**, reactions involved in the direct synthesis process are listed: reaction (c) is the synthesis of methanol from syngas, reaction (d) is the dehydration reaction of methanol to DME, and reaction (e) is the water-gas shift reaction. When reaction (e) does not take place, the overall process is described by reaction (b); on the contrary, when water-gas-shift occurs, reaction (a) represents the overall process [149].

Table 18: Reactions involved in DME direct synthesis [149].

	Reaction	Reaction heat (kJ/mol)
(a)	$3CO+3H_2 \rightarrow CH_3OCH_3+CO_2$	-246
(b)	$2CO+4H_2 \rightarrow CH_3OCH_3+H_2O$	-205
(c)	$2CO+4H_2 \rightarrow 2CH_3OH$	-182
(d)	$2CH_3OH \rightarrow CH_3OCH_3+H_2O$	-23
(e)	$CO+H_2O \rightarrow CO_2+H_2$	-41

Methanol conversion is the most equilibrium restricted and as it is exothermic and occurs with a decrease in the number of moles, it is favored at low reaction temperatures and high pressures. The effect of reaction temperature on syngas equilibrium conversion for DME direct synthesis and methanol synthesis has been calculated and for both reactions, the negative effect of increasing the temperature has been demonstrated. Moreover, results showed that DME direct synthesis allowed to obtain a higher syngas equilibrium conversion than that obtained for methanol synthesis [149]. Catalysts used for DME direct synthesis need to combine two catalytic functions: a metallic function to produce methanol from syngas and an acid function for the reaction of methanol dehydration to DME. The commonly employed catalyst for DME direct synthesis is a redox/acid bifunctional catalyst operating at the same conditions as methanol synthesis (250-280°C and 5-10 MPa). Particularly, the catalyst for DME direct synthesis is a combination of the CZA catalyst described above and an acid catalyst such as zeolites or γ-Al_2O_3. Methods used to combine acid and metallic functions influence the activity of the final catalyst. First of all, to obtain a hybrid catalyst the mechanical mixture of the metallic and acid functions can be prepared and subsequently pelletized [136]. However, many other techniques can be employed such

as co-precipitation, sol-gel, and impregnation. In this case, many parameters have to be considered affecting the final properties of hybrid catalysts. For example, in a published work the effect of copper source has been clarified demonstrating that employing copper acetate rather than copper nitrate or chloride allowed to preserve acidity properties of the final bi-functional catalyst [150]. Also, the effect of calcination temperature has been studied identifying the best one at 623 K (for 2 hours) to obtain the greatest dispersion of small copper particles [151]. Ordomsky et al. demonstrated that acid sites on the external surface of zeolite employed promoted copper sintering, and, for this reason, the neutralization of these acid sites could be a promising route to improve catalyst stability [152]. The passivation of external acid sites is the key topic of this thesis and proves to be a fundamental aspect in several fields of application including the use of zeolites with neutralized external surfaces in the synthesis of hybrid catalysts in which contact between acid sites and metal function is avoided. In the last years, the use of core-shell type catalysts attracted great interest [153–155]. There are many advantages to the use of core-shell catalysts. First of all, since the core is generally the metallic phase and the shell is the acidic phase, methanol produced in the core passes through the shell and the water produced by the dehydration reaction does not encounter the metallic phase causing its deactivation. Moreover, the unfavorable synergistic effect due to the close contact between small particles of both functions is minimized by employing core-shell catalysts. For example, in an already published work, the comparison between a core-shell type hybrid catalyst (CuO-ZnO-ZrO_2@SAPO-11) and the physical mixture counterpart has been investigated testing them in the direct conversion of CO and CO_2 to DME. Results demonstrated that core-shell catalyst allowed to obtain a higher CO_x conversion and higher stability during time-on-stream tests [153].

In **Figure 49**, a scheme of direct DME synthesis process is reported [148]. In this case, only a reactor is employed and products of the direct DME synthesis are firstly treated in an adsorption column with water to separate the gas phase (H_2, N_2, CO, CO_2, and CH_4), partially recycled to the reactor, to liquid phase (DME, methanol and water). As in the direct

process, two distillation columns are required to obtain DME in the desired purity and to separate methanol from water.

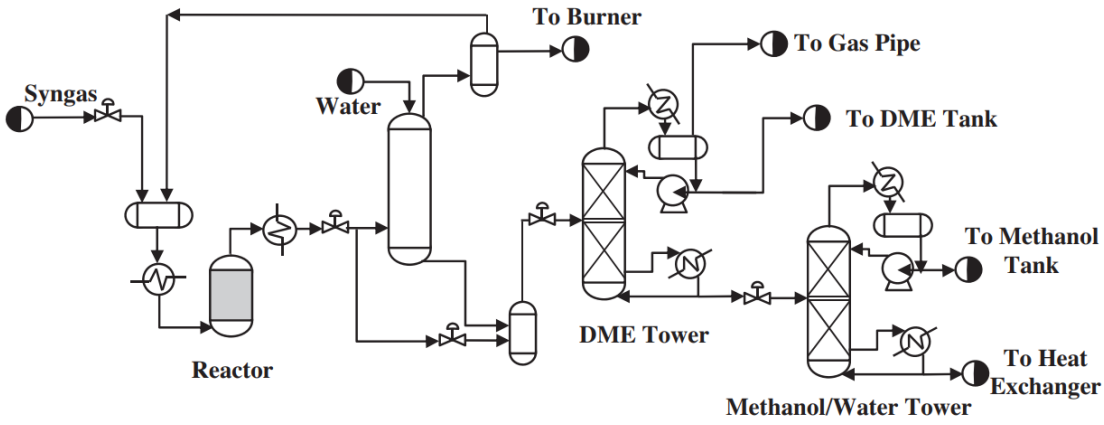

Figure 49: Scheme of direct DME synthesis process [148].

In our work, methanol to DME reactions have been investigated. Particularly, the effect of acid site distribution over methanol conversion has been first explored. Furthermore, passivated catalyst obtained coating starting ZSM-5 zeolites with a layer of Silicalite-1 were tested to evaluate the impact of external acid sites neutralization over catalysts performances in terms of stability and coke formation.

5.2 MTD catalytic tests.

Firstly, catalytic results obtained testing parent zeolites will be discussed to understand the effect of Si/Al ratio and thus of different acid sites distribution over catalyst behavior in terms of methanol conversion, DME selectivity, and in terms of stability, and deactivation. Particularly, catalytic tests were conducted in the temperature range of 140-240°C using a bench scale system operating at atmospheric pressure. 70 mg of each parent zeolite in the form of pellets (300-500 μm) were loaded in a U-shaped quartz-packed bed reactor (ID = 15 mm, L=40 mm) and pretreated at 240°C for two hours to remove adsorbed water. A nitrogen flow (60 STP mL/min) was bubbled through liquid methanol kept in a thermostatic bath (Julabo F12-ED). The methanol molar fraction in the feed stream was controlled by varying the temperature of the bath. Particularly, an initial methanol vapor fraction of 0,06 was fixed and tests were conducted by using a weigh hourly space velocity (WHSV) of about 5 g_{MeOH}

(g_{cat} h)$^{-1}$. Products stream was analyzed by using GC (Agilent 7890 A) equipped with a specific column (J&W 125-1032) and a FID detector using helium as carrier. Methanol conversion and DME selectivity have been calculated using the following equations:

$$Methanol\ conversion = \frac{converted\ MethOH\ (gmol \cdot min^{-1})}{feed\ MethOH\ (gmol \cdot min^{-1})} \quad \textbf{(1)}$$

$$DME\ selectivity = \frac{2\ DME\ outstream\ (gmol \cdot min^{-1})}{converted\ MethOH\ (gmol \cdot min^{-1})} \quad \textbf{(2)}$$

In **Figure 50** methanol conversion obtained by testing parent zeolites at different temperatures is reported. At each reaction temperature investigated, methanol conversion was coherent with the total acidity trend (**paragraph 4.1.8**). The Z11 sample was characterized by the same total acidity as the Z25 sample but exhibited a higher number of Lewis acid sites. For this reason, it could be stated that both Lewis and Brønsted acid sites are responsible for methanol conversion.

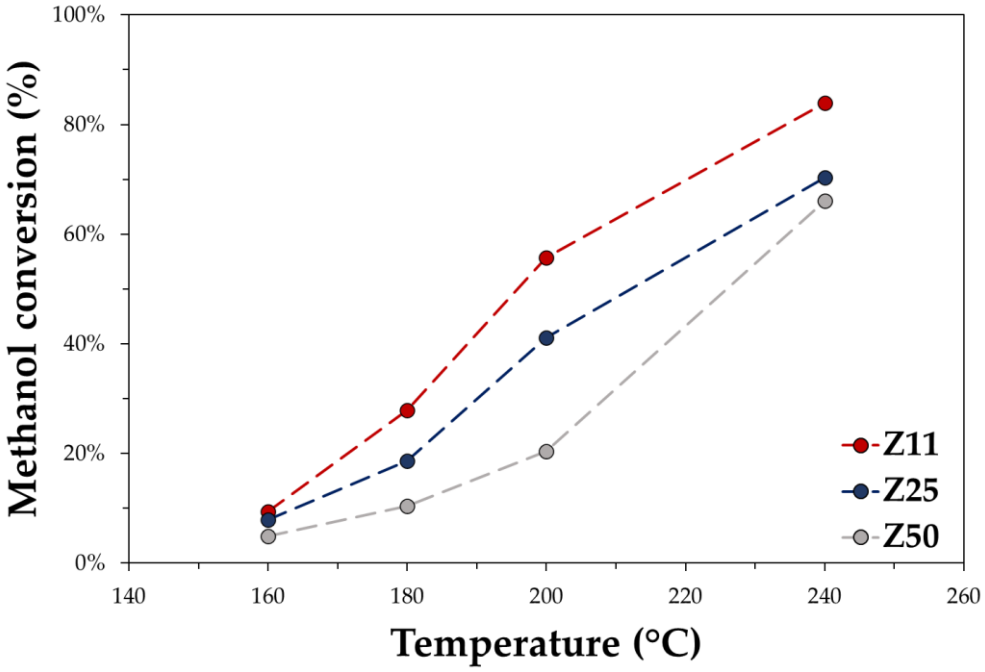

Figure 50: Methanol conversion over Z11, Z25 and Z50 samples.

Turnover frequency calculations were performed using the following equation:

$$TOF\ (h^{-1}) = \frac{SV \cdot x}{A} \quad \textbf{(3)}$$

where SV is the space-time velocity of methanol ($mmol_{MeOH} \cdot h^{-1} \cdot g_{cat}^{-1}$), x is the conversion and A is the sum of Brønsted and Lewis acid sites. TOF results obtained at 200°C are reported in **Figure 51**. Particularly, data obtained are reported as a function of the ratio between Lewis acid sites and Brønsted acid sites. An increased trend of turnover frequency was found with the increasing of Lewis acid sites also related to the presence of extra-framework aluminum species.

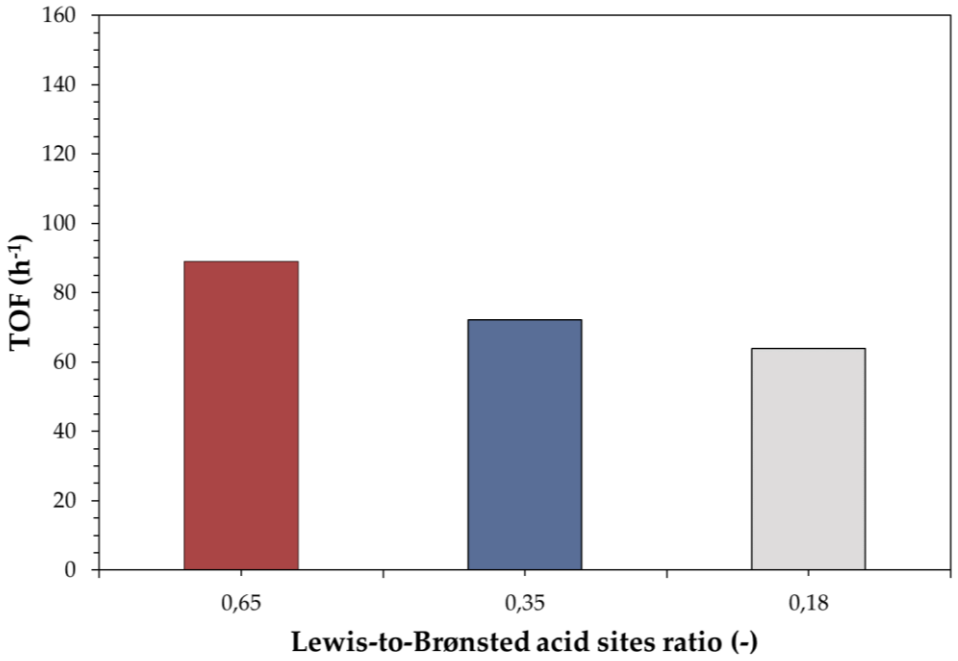

Figure 51: Methanol TOF as a function of LAS/BAS ratio at a reaction temperature of 200°C.

To compare parent ZSM-5 zeolites and passivated samples obtained employing the epitaxial growth technique other additional MTD tests were conducted. Catalysts employed in the first part of this research work are summarized in **Table 19**. Z11 zeolites and coated samples synthetized starting from an H^+-form were employed to assess the effect of neutralization of external acid sites over the catalytic behavior of catalysts. In this case, 140 mg of catalyst was loaded in the reactor, and the weigh hourly space velocity (WHSV) was fixed to a value of about 2.3 h^{-1}.

Table 19: Samples tested.

Code	Core theoretical Si/Al ratio	Surface acidity passivation via Epitaxial growth of Silicalite-1
Z11	11	-
H-Z11_X	11	1 layer of Silicalite-1
H-Z11_XX	11	2 layers of Silicalite-1

Figure 52 shows results obtained in terms of methanol conversion and dimethyl ether selectivity for Z11 and passivated catalysts (H-Z11_X and H-Z11_XX).

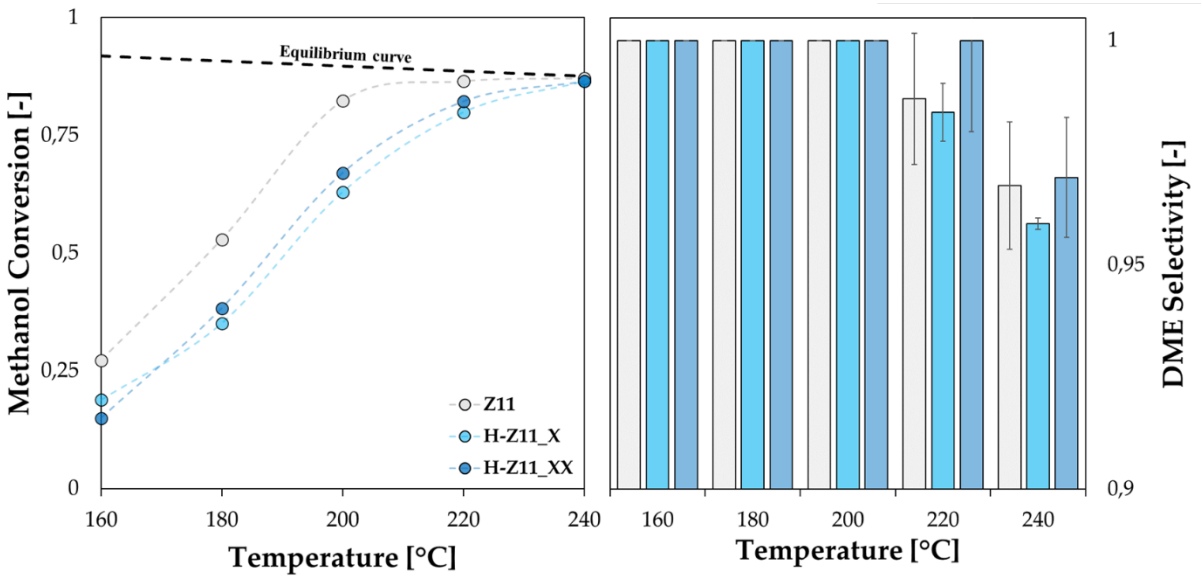

Figure 52: Methanol conversion (left) and DME selectivity (right) of parent Z11 and passivated samples (H-Z11_X and H-Z11_XX).

For each investigated catalyst, methanol conversion increased with the increasing of reaction temperature reaching the equilibrium conversion at 240°C. Z11 parent zeolite exhibited the highest value of conversion at any reaction temperature below 240°C. This result was attributed to the parent zeolite acidity value that was greater if compared with passivated catalysts (**paragraph 4.1.7**) [156]. Although H-Z11_X acidity was higher than the double-step silicalite-1 layered sample (H-Z11_XX), methanol conversion reached using this catalyst was slightly lower. This finding could be attributed to H-Z11_X textural properties as the decrease in micropore volume found for this catalyst (**paragraphs 4.1.3 and 4.1.6**) was related to reduced channel accessibility due to the growth of a partially amorphous layer over the pore mouth of the starting core. No differences were detected in DME selectivity between tested samples at lower reaction temperatures. However, at higher temperatures (220°C and 240°C) where the deactivation of catalysts is usually more pronounced [157,158], H-Z25_XX exhibited the highest DME selectivity (98.4% and 96,9% respectively). This higher value of DME selectivity could be associated with a lower catalyst deactivation due to the neutralization of its external acid sites where the lack of special restrictions causes

coke formation [119]. On the contrary, employing H-Z11_X catalysts a decrease in DME selectivity was detected. Also, in this case, the textural properties of the H-Z11_X sample must be considered. Although the H-Z11_X sample displayed a lower acidity, the amorphous layer grown over its surface could be the cause of an increase in pore tortuosity. This led to an enhanced residence time of produced DME inside the channels causing its conversion versus light olefins in the presence of active acid sites. To prove this hypothesis light olefin production was evaluated and results for all investigated samples at each reaction temperature are reported in **Figure 53** in terms of C_2-C_3 area detected.

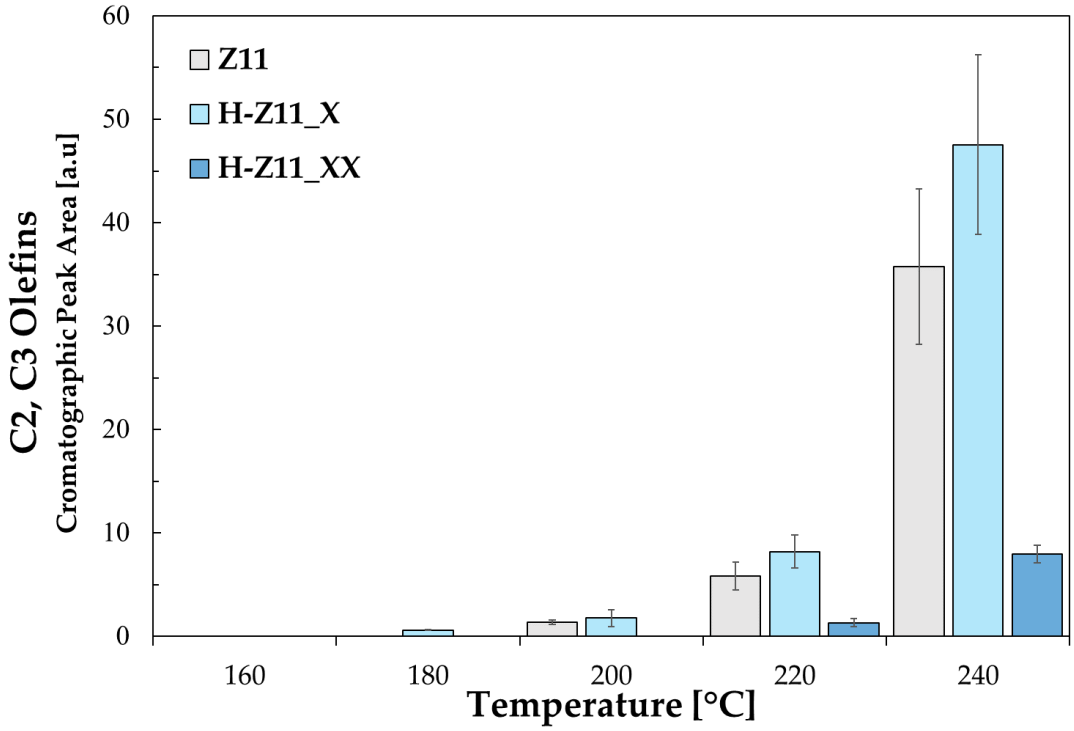

Figure 53: Olefin formation on investigated catalysts at each reaction temperature.

As expected, light olefins production was undetectable at lower reaction temperatures for each investigated catalyst [159]. It appeared clear that employing H-Z11_X led to a higher production of C_2-C_3 byproducts, and this result confirmed the assumption explained above about DME blockage and conversion inside the channels of the catalyst coated once with a layer of Silicalite-1. Furthermore, reduced acidity of H-Z11_XX catalysts led to a decrease of light olefins produced if compared to both parent zeolite (Z11) and H-Z11_X samples showing at this temperature the same methanol conversion.

The amount of coke deposited over on the spent catalysts after catalytic tests (about 5 hours of reaction) was measured by TGA analysis. Spent catalysts were treated under air flow until 850°C and the weight loss in the range 250-850°C was measured and associated to the quantity of coke species formed. TGA/DTG profiles in the range of 200-850°C of parent zeolite and coated spent catalysts are reported in **Figure 54**. DTG curves contained two main peaks: the first one (323°C-335°C) was probably linked to light coke species produced during the reaction and the second one (546°C-556°C) was associated with heavier coke species.

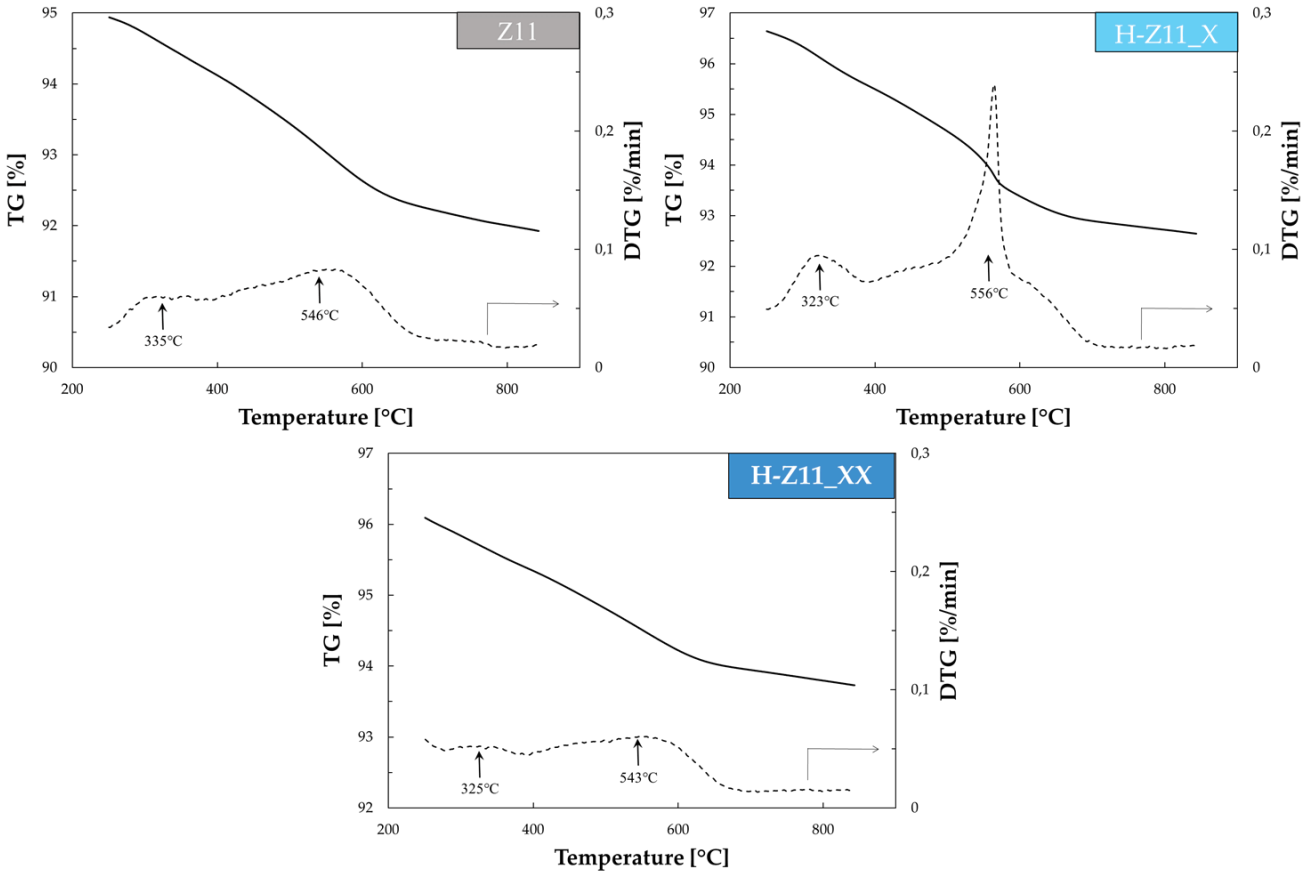

Figure 54: TGA/DTG profiles of spent catalysts.

TGA results were employed to calculate the amount of coke formed per gram of catalyst and the amount of coke deposited per gram of DME produced at the end of catalytic tests (after 5 hours of reaction) and data obtained are summarized in the histograms of **Figure 55**. It is clear that the H-Z11_X sample exhibited a higher amount of coke deposited and this

result could be attributed to its worst textural properties and particularly to the presence of a thin amorphous layer on the surface of this catalyst which probably led to a faster deactivation (**paragraph 4.1.3**). On the contrary, H-Z11_XX spent catalyst was characterized by the lowest amount of coke species trapped inside its channels and on its surface. Although the conversion reached at high reaction temperatures employing parent zeolite and coated catalyst (H-Z11_XX) was almost equal, the passivated catalyst showed better performances in terms of coke species formed. This trend means that the H-Z11_XX sample deactivated slowly thanks to the decrease of external surface acidity that generally leads to the formation of coke species during reactions [89].

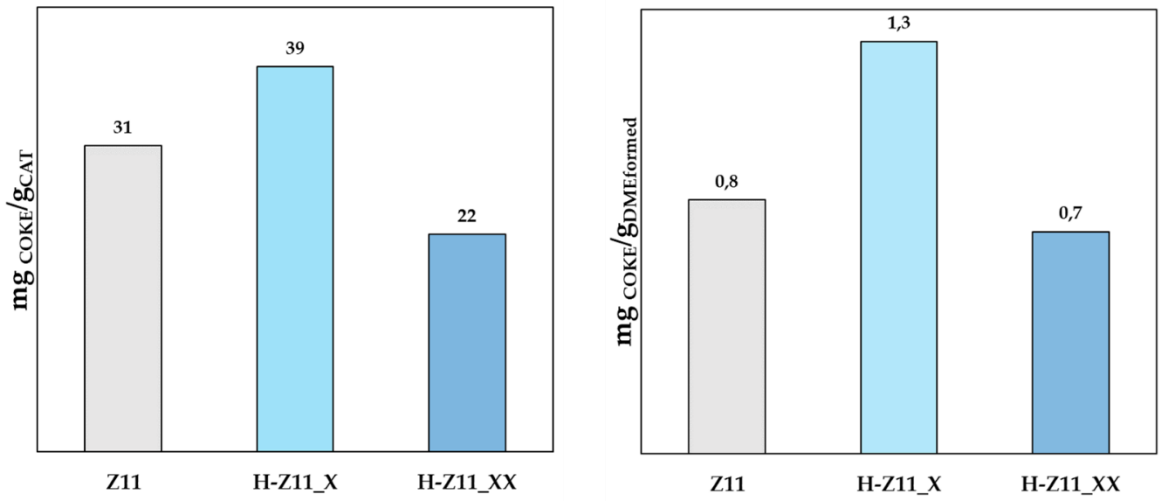

Figure 55: Coke formations on spent catalysts.

Moreover, qualitative analysis of soluble coke species was performed employing gas chromatography-mass spectrometry (GC-MS) dissolving spent zeolites in HF and using dichloromethane to extract soluble coke species. Chromatograms obtained are shown in **Figure 56**. The presence of poly-substituted benzenes was detected, and this result is in agreement with findings already published in the literature about coke species formed during MTD reaction over ZSM-5 zeolites [160]. Tetramethyl-benzene was detected only from the analysis on H-Z11-X sample probably because it was formed inside the channels of zeolite and remained trapped inside because of the presence of the amorphous layer partially blocking the pores. Pentamethyl-benzene and hexamethyl-benzene were also

found in the coke analyses of each tested catalyst. The peak area associated with this compound refers to the quantity detected, and it appeared clear that the H-Z11_XX catalyst exhibited the lower content of this coke species generally formed on the external surface of ZSM-5 zeolites [160]. Moreover, this result agreed well with TGA quantitative results demonstrating that neutralizing eternal surface acid sites of the starting zeolite allowed to obtain a more stable catalyst which deactivated slower because of the lower coke formation on its external surface.

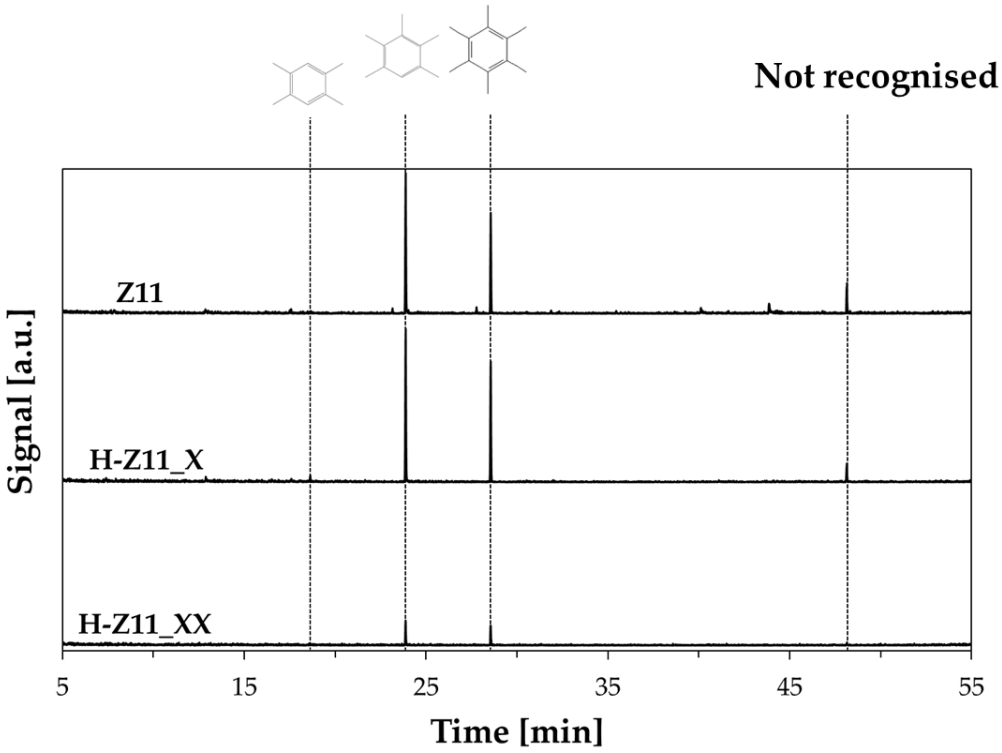

Figure 56: GC-MS chromatogram of spent catalysts.

In the second part of this research work, efforts were dedicated to the development of a novelty technique to grow Silicalite-1 over the external surface of the starting ZSM-5 zeolite. The idea was to cover the starting core with the organic template still inside the channels to protect pores from clogging found for samples coated in H^+-form. For this reason, Z25 zeolite (with a Si/Al ratio in the synthesis gel equal to 25) was passivated starting from a as synthetised-form (AS_Z25_X and AS_Z25_XX) and from H^+-form (H_Z25_X and H_Z25_XX) as described in **Chapter 3**. Samples obtained summarized in **Table 20**, after

characterizations, were tested in the reaction of methanol to dimethyl ether in order to study the effect of passivation technique employed on catalytic performances.

Table 20: Investigated samples.

Code	Core theoretical Si/Al ratio	Surface acidity passivation via Epitaxial growth of Silicalite-1
Z25	25	-
H-Z25_X	25	1 layer of Silicalite-1
H-Z25_XX	25	2 layers of Silicalite-1
AS-Z25_X	25	1 layer of Silicalite-1
AS-Z25_XX	25	2 layers of Silicalite-1

The initial activity of catalysts was evaluated through catalytic tests in the range of 180°C-240°C. Also in this case, 140 mg of catalyst was loaded in the reactor and pretreated at 240°C for 2 hours. Nitrogen was used as carrier gas and methanol molar fraction was kept at 0.06 for all tests. Catalytic test results are reported in **Figure 57** in terms of methanol conversion and DME selectivity. Parent zeolite and passivated catalysts exhibited the same methanol conversion trend that increased with the increase of reaction temperature. Moreover, at low reaction temperatures, it is clear the effect of reduced acidity of coated samples that showed a lower methanol conversion value. This difference was not detected at 240°C where the conversion of all catalysts approached the equilibrium one. No evident differences were detected between catalysts in terms of DME selectivity reached.

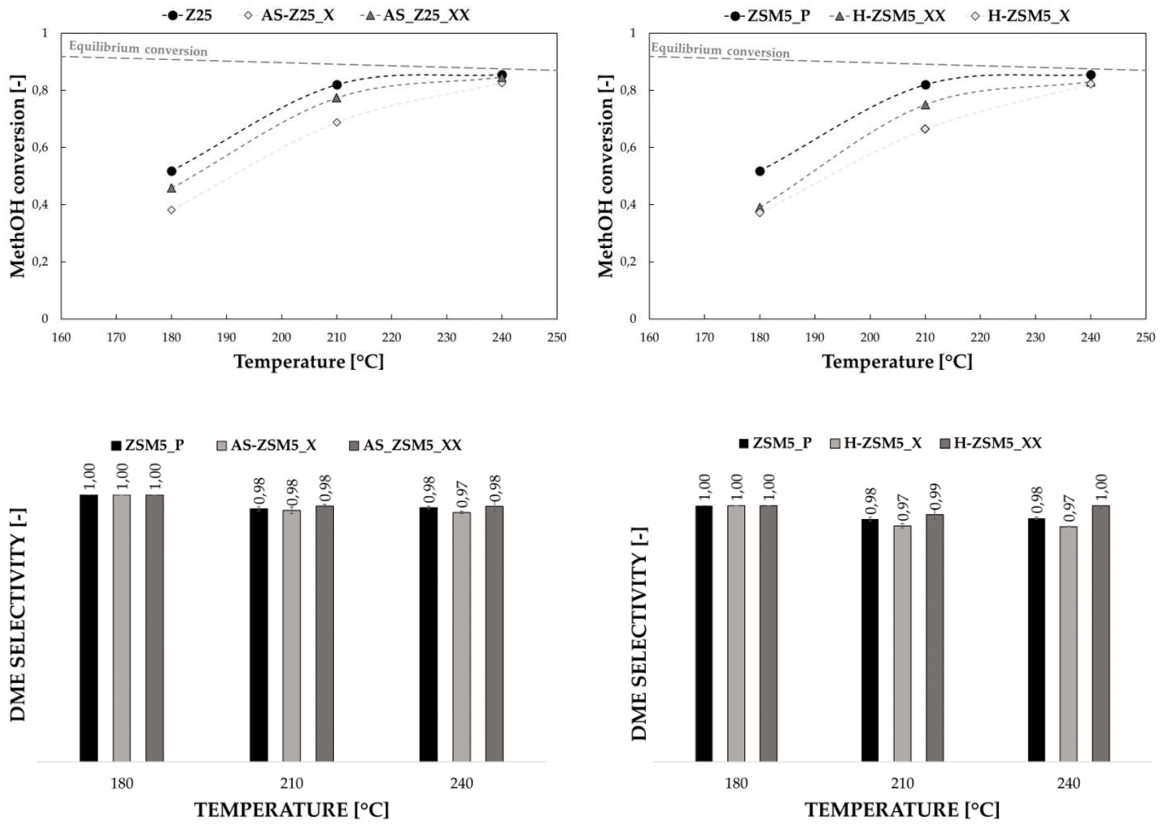

Figure 57: Catalysts' initial activity in MTD reaction (180°C-240°C).

To study catalysts' stability and their tendency to deactivate, time on stream (TOS) tests of 70 hours at 240°C were performed. Results in terms of methanol conversion profiles during the entire time on stream tests are shown in **Figure 58**. It appeared clear that the initial methanol conversion reached employing parent zeolite was higher if compared with values obtained testing AS-Z25_X and AS-Z25_XX passivated catalyst. Parent zeolite exhibited an initial methanol conversion value of about 86% at the beginning of time on stream test but after 70 hours of reaction, it decreased to a value of 84%. On the contrary, employing AS-Z25_X and AS-Z25_XX samples allowed us to obtain a lower initial methanol conversion value (about 84%) but constant for the entire time on stream tests. This trend demonstrated that passivated AS-Z25 catalysts did not deactivate during the time on stream tests of 70 hours and that the neutralization of external acid sites improved catalyst stability already from the first deposition cycle. Moreover, DME selectivity on average values was calculated for each sample, and data are summarized in **Table 21**. Employing parent zeolite, a DME selectivity of 93% was reached on average but this value increased to 96% and 97% when

testing AS-Z25_X and AS-Z25_XX respectively. In the case of H-Z25_X and H-Z25_XX samples, a different trend was observed. H-Z25_X sample rapidly deactivated with a drop in methanol conversion value after 5 hours of reaction. This result was in agreement with the already shown results of the first part of the research work on MTD. H-Z11_X sample also exhibited the worst catalytic performances if compared to the starting parent zeolite (Z11). Also in this case, testing sample obtained coating the H^+-form core of the starting parent zeolite (Z25) led to the worst catalytic performance and this finding could be attributed to its lower value of micropore area and volume (**paragraph 4.1.6**). On the contrary, the H-Z25_XX catalyst exhibited a trend similar to those observed for AS-Z25 coated samples.

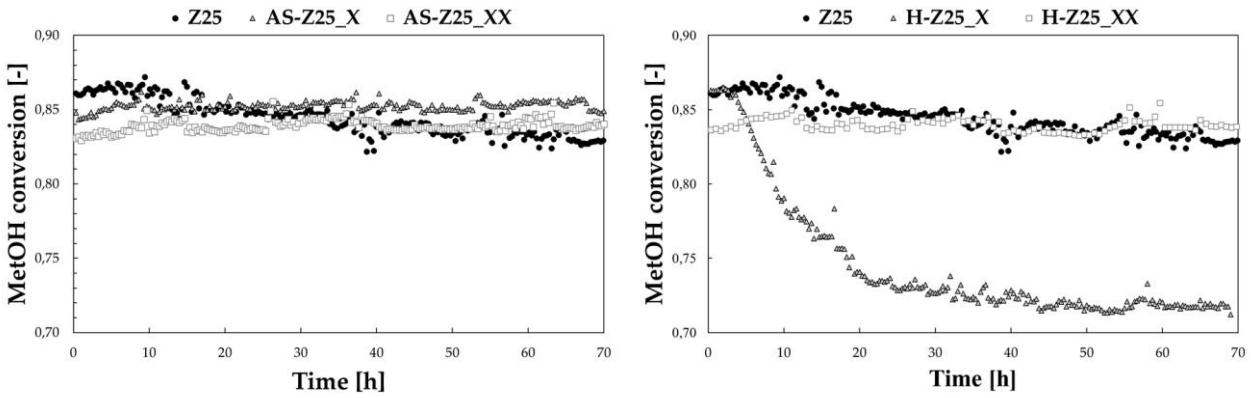

Figure 58: Time on stream tests of parent zeolite and passivated samples (T=240°C, atmospheric pressure, methanol fraction=0.06, N_2 carrier gas).

The amount and type of coke species deposited over spent catalysts after time on stream tests were evaluated through TG analyses and GC-MS analysis respectively. TG analyses were conducted from 25°C to 850°C in air flow and TG/DTG profiles obtained are shown in **Figure 59**. Weight loss detected between 200°C and 850°C indicated the presence of coke species on spent catalysts. DTG profiles of AS-Z25 coated samples exhibited three main peaks: two peaks in the temperature range of 200°C-350°C and a wider peak at 445°C. H-Z25_XX spent catalyst exhibited the same trend observed for AS-Z25_X and AS-Z25_XX samples with a more pronounced peak at 305°C and the same secondary peak detected at

around 444°C. On the contrary, the H-Z25_X sample revealed a profile different from all the other catalysts with the presence of two main peaks at higher temperatures (333°C and 516°C).

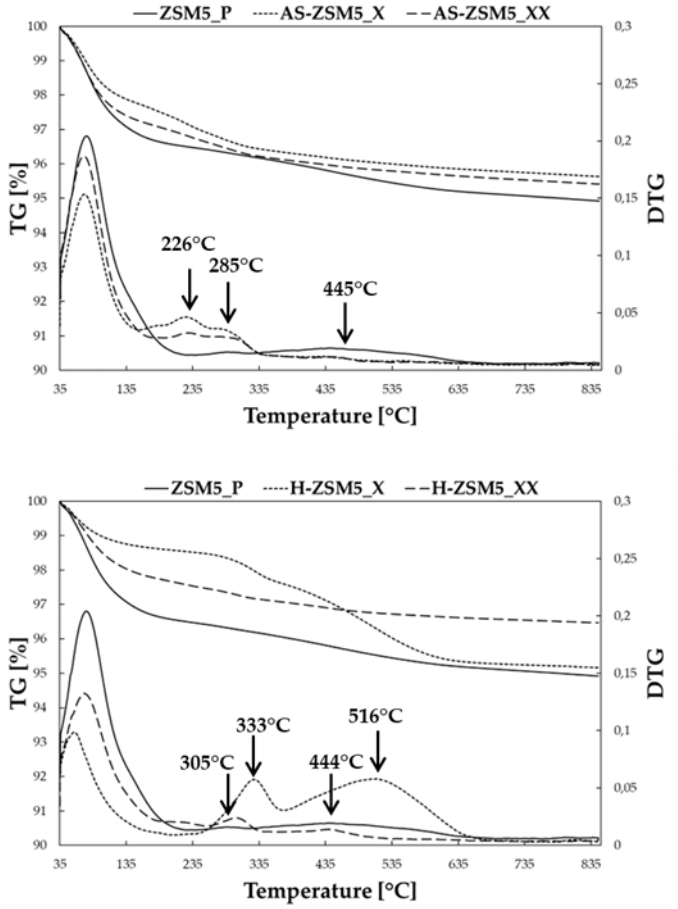

Figure 59: TG and DTG profiles of spent catalysts.

The weight loss detected was used to calculate the amount of coke formed. Particularly the weight losses detected between 200°C and 350°C were associated with coke species that decompose at low temperatures (CLT) while weight losses between 350°C and 850°C were attributed to coke that decompose at high temperatures (CHT). Quantitative results are reported in **Table 21** in terms of milligrams of coke formed per gram of catalyst. AS-Z25_X sample exhibited an increase in the total amount of coke formed concerning the parent zeolite (Z25) but a different distribution of species formed was detected. In fact, a greater quantity of C_{LT} was found together with a decrease in C_{HT}. H-Z25_X catalyst with the worst microporosity and catalytic performance, showed a significant increase of both C_{LT} and C_{HT}

concerning the parent zeolite. On the contrary, whatever the coating procedure used, samples coated with a double layer of Silicalite-1 (AS-Z25_XX and H-Z25_XX) exhibited a lower amount of coke species produced during the time on stream tests. Analyzing coke relative distribution (**Table 21**), it appeared clear that catalysts coated with two layers of Silicalite-1 showed the formation of similar coke species (about 50% of C_{LT} and 50% of C_{HT}). On the contrary, H-Z25_X coke species distribution was like that of parent zeolite (more than 70% of C_{HT}) with a significantly higher amount of coke produced per gram of catalyst (about 35 mg/g_{cat}). This finding proved the formation of different coke species depending on the different acid sites distribution and external acidity.

Table 21: Quantitative analysis of coke formed on spent catalysts after 70 h time on stream tests.

Catalyst	Methanol Conversion* [-]	DME selectivity* [-]	C_{LT}[a] (mg/g_{Cat})	C_{HT}[a] (mg/g_{cat})	(C_{LT}+ C_{HT})[a] (mg/g_{cat})
Z25	0.84	0.93	4.50 (28%)	11.94 (72%)	16.44
AS-Z25_X	0.85	0.96	10.09 (57%)	7.64 (43%)	17.73
AS-Z25_XX	0.84	0.97	7.99 (51%)	7.55 (48%)	15.54
H-Z25_X	0.75	0.86	8.09 (24%)	26.59 (76%)	34.68
H-Z25_XX	0.84	0.96	5.42 (46%)	6.46 (54%)	11.88

* Calculated as an arithmetical average over the entire period of reaction

[a] Calculated from TGA weight loss. Data in brackets are relative distributions of CLT and CHT.

Coke species formed on spent catalysts were analyzed by GC-MS analysis after zeolite dissolution in HF followed by an organic phase extraction using dichloromethane [38]. The effect of external acidity found with quantitative evaluations done via TG analyses was also confirmed by GC-MS analysis results reported in **Figure 60**. Chromatogram of all catalysts

revealed the presence of only poly-substituted benzenes among soluble coke species which is common at low temperatures [160]. Moreover, the effect of the deposition of one and also two layers of Silicalite-1 appeared clear. In fact, Z25 and AS-Z25_X chromatograms showed the presence of pentamethyl and hexamethyl benzene but also of 1,4 dimethyl-2 ethyl benzene that with ethylic branches cannot access the channels of MFI zeolites and be formed on the external surface because of the presence of external acid sites. On the contrary, although the second cycle of passivation seemed not to improve catalytic activity in terms of methanol conversion and DME selectivity reached, AS-Z25_XX exhibited the presence of only pentamethyl benzene with a very lower abundance concerning the other investigated catalysts. H-Z25_X also showed in this case the worst performances in terms of coke species formed and abundance while an improvement in catalyst efficiency was found after the second deposition of Silicalite-1 (H-Z25_XX).

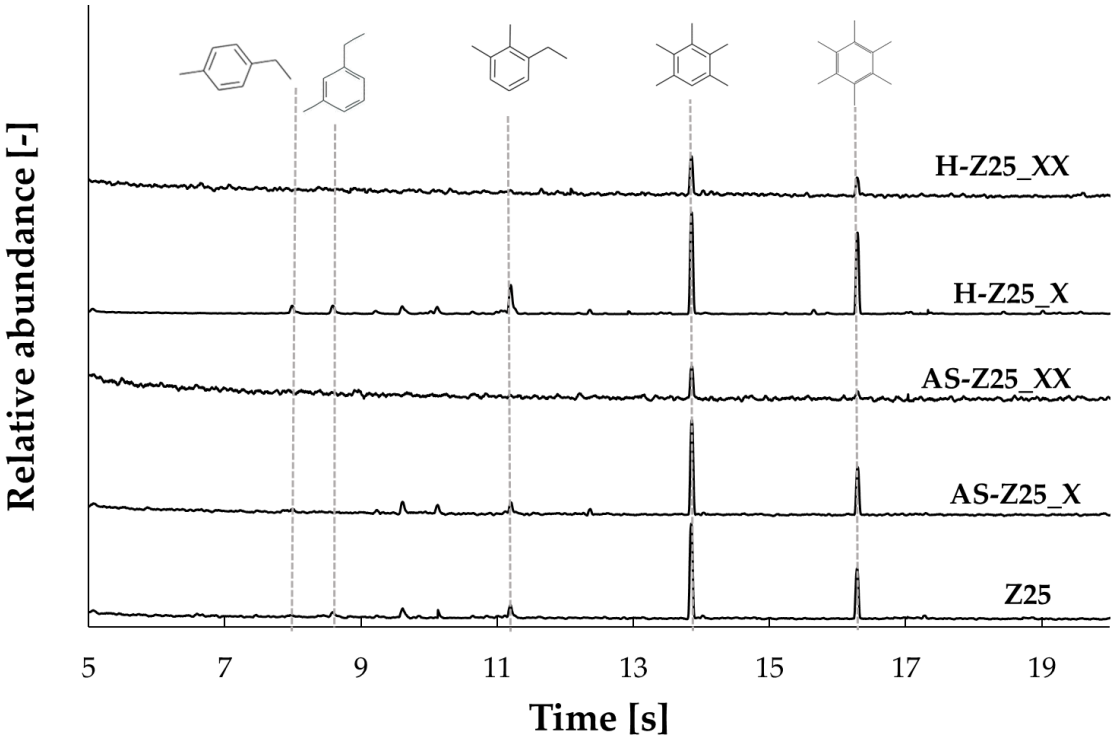

Figure 60: GC-MS analysis of spent investigated catalysts.

5.3 Conclusions.

In the first part of this work, catalysts obtained by passivating the external surface acidity of high aluminum-content ZSM-5 zeolite (Si/Al=11) were employed in the reaction of methanol dehydration to produce dimethyl ether. If compared with Z11 parent zeolite, catalytic performances of the sample obtained coating the H-Z11 core with a single Silicalite-1 layer (H-Z11_X) got worse. H-Z11_X catalyst exhibited a lower methanol conversion and DME selectivity and a higher amount of coke deposited concerning uncovered ZSM-5. The responsibility for these worse catalytic performances was attributed to the growth of a thin amorphous layer after the first coating with Silicalite-1. The deposition of the second Silicalite-1 layer positively influences catalyst behavior. H-Z11_XX catalyst exhibited improved DME selectivity and a lower quantity of coke deposited on its surface.

Since characterizations and catalytic results carried out employing passivated samples obtained coating the starting zeolite in acidic form showed that Silicalite-1 also grew in the empty pores of the core strongly affecting final catalysts properties, a novel technique for passivating external acid sites was developed. Particularly, a parent zeolite with a Si/Al ratio equal to 25 was passivated employing the epitaxial growth technique of Silicalite-1 but coating the starting core both with and without the organic template inside the channels. Textural analysis and acid site characterizations proved that coating the zeolite in a synthetised-form gave significant improvements in final catalysts properties. Samples obtained (H-Z25_X and XX and AS-Z25_X and XX) were also tested in the reaction of methanol dehydration to DME. Catalytic results demonstrated that AS-Z25 samples exhibited methanol conversion and DME selectivity values close to that of parent zeolite but tended to form less quantity of coke and to deactivate slowly. On the contrary, the H-Z25_X sample, because of its textural properties, showed the worst performance in terms of deactivation and coke deposited on its surface while the H-Z25_XX behavior was close to that of AS-Z25 catalysts.

CHAPTER 6. Catalytic applications: Dimethyl ether conversion to Olefins.

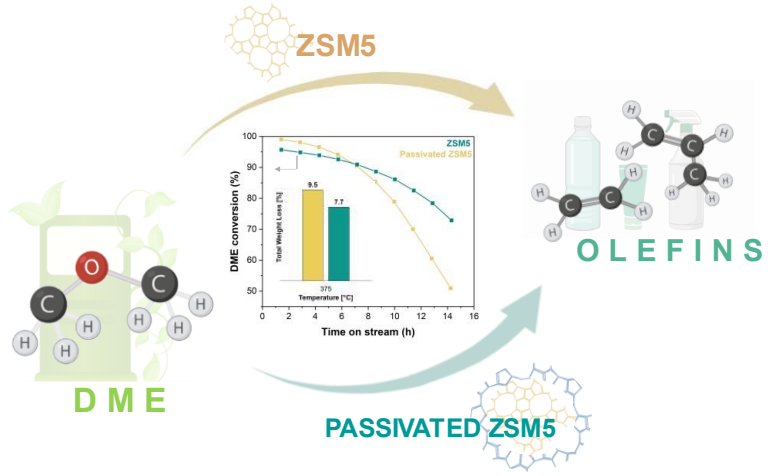

Figure 61: Graphical Abstract

This part of the research work, summarized in **Figure 61**, was dedicated to the employment of ZSM-5 zeolites with different Si/Al ratios and of their passivated counterparts in the reaction of dimethyl ether to olefins. Particularly, two ZSM-5 zeolites with a Si/Al ratio equal to 25 and 50 were synthesized according to the procedure described in Chapter 3 (**paragraph 3.1**). Then, the technique of the epitaxial growth of Silicalite-1 (**paragraph 3.3**) was employed to study the effect of surface passivation on the catalytic behavior of samples in terms of stability and coke production for the reaction of dimethyl ether conversion to olefins. The catalysts used are summarized in the Table below.

Table 1: Investigated samples.

Code	Core theoretical Si/Al ratio	Surface acidity passivation via Epitaxial growth of Silicalite-1
Z25	25	-
AS-Z25_XX	25	2 layers of Silicalite-1
Z50	50	-
AS-Z50_XX	50	2 layers of Silicalite-1

Samples were tested at different reaction temperatures between 300°C and 375°C to understand the effect of the different acid site distributions and the passivation procedure on catalysts performances. Analysis revealed that within hydrocarbons, propylene was the product obtained in greater amounts although methanol was also detected as a result of the dehydration reaction of DME. Dimethyl ether conversion increased with the increasing of reaction temperature but samples with higher acidity showed faster deactivation, especially at 375°C. Catalysts characterized by a Si/Al ratio equal to 50 were more stable although they exhibited higher selectivity versus methanol and lower initial activity, especially at lower reaction temperatures.

6.1 State of art: Dimethyl ether conversion to olefins.

Light olefins like propylene and ethylene are fundamental intermediates for the petroleum industry. Ethylene represents one of the chemicals mostly produced in the world and, because of its high number of applications, its production is frequently employed to analyze the performances of the whole chemical industry [161]. Ethylene is mainly used to produce polyethylene, ethylene oxide, ethanol, ethylbenzene, *etc*. Industries of transportation, packaging, textile, construction, and many others employ ethylene-based products. Propylene is used to produce polypropylene, the most useful polymer because of its chemical and mechanical properties, and to obtain acrylonitrile, propylene oxide, *etc*. In **Figure 62** the main uses of light olefins as platform molecules in the chemical industry are summarized.

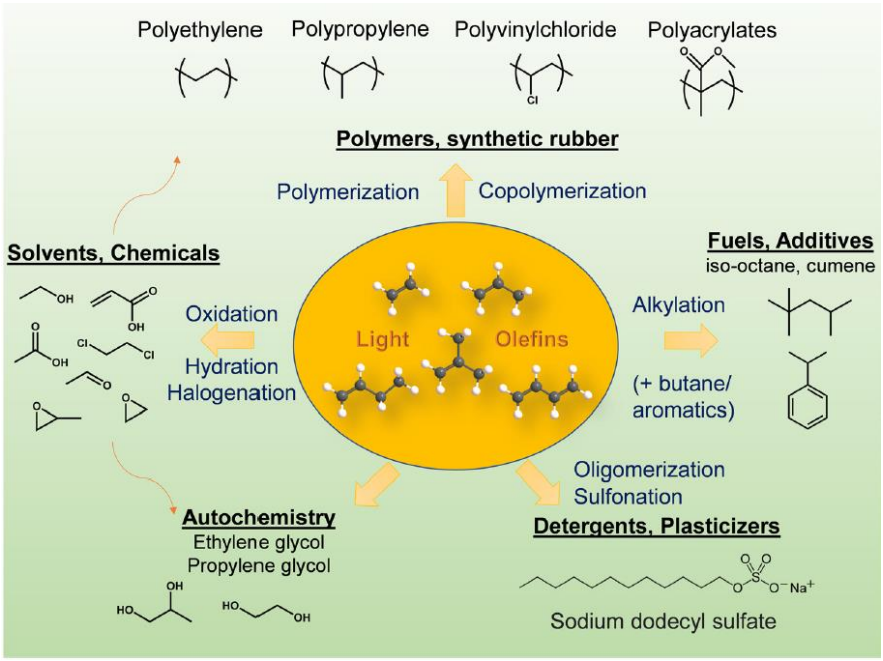

Figure 62: Light olefins employment like platform molecules [161]

Light olefins are traditionally produced by the stream cracking of petroleum hydrocarbons including ethane, naphtha, and gas oil since also propane and other hydrocarbons could be employed as feedstocks [162]. Regardless of the feedstock used, the yield of propylene achieved by steam crackers is always low and new technologies have been developed for years to enhance the productivity of propylene such as the "Olefins Conversion Technologies" developed by ABB Lummus 6 [162]. Because of their employment in different applications, global consumption of ethylene and propylene is always high. Ethylene and propylene global demand were about 168 and 110 million tons in 2018 and data demonstrate that light olefins global demand is increasing year by year [163,164]. Besides this increasing trend, greenhouse gas emissions are getting higher and higher and with them the climate change problems. In a "post-oil" society the need to employ alternative carbon sources arises and for this reason, olefin production will depend more and more on other sustainable pathways and the employ of renewable energy sources. In 2019 hydropower, solar, wind, geothermal, tide/wave/ocean, biofuels, and waste were employed to produce 26% of global electricity (**Figure 63**) [165]. During the last decades, renewable electricity generation showed a continuously increasing trend, and in **Figure 63** pie charts demonstrate changes that occurred between 1973 and 2019 in the sources used to produce the world's electricity. Electricity produced employing renewable sources passed from ≈ 1300 to ≈ 7000

TWh between 1973 and 2019. In this context, storage technologies, and among these chemical storage, play a fundamental role in the framework of Power-to-X technologies to transform the surplus renewable electricity.

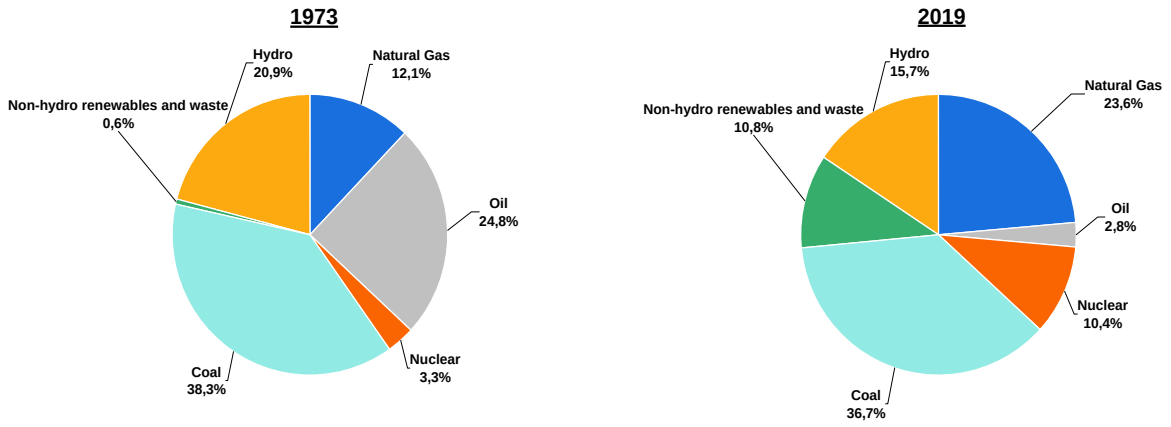

Figure 63: Share of world electricity generation by source in 1973 and 2019

Power-to-X process is simplified in **Figure 64**: electricity produced through the employment of renewable energy sources is converted into hydrogen via water/steam electrolysis. Then hydrogen could react with captured carbon dioxide allowing to obtain different products according to the reaction conditions and catalysts used. Recently CO_2 and CO have been used as raw materials for the synthesis of fuels and chemicals and among these light olefins. Three main synthesis paths are followed: direct hydrogenation of CO_2 to olefins employing a hybrid catalyst, synthesis of methanol or dimethyl ether (DME) followed by the reaction of methanol or DME to olefins (MTO/DTO) using an acid catalyst, and the Fisher-Tropsch synthesis with CO and CO_2 [166]. Producing light olefins through the reaction between captured CO_2 and green H_2 or from methanol or DME, already produced by the reaction between green H_2 and stored CO_2, means following a sustainable pathway and contributing to the chemical storage of renewable electricity.

In literature, great efforts have been made over the years to study the production of light olefins through catalytic dehydration of methanol [4-6] or dimethyl ether.

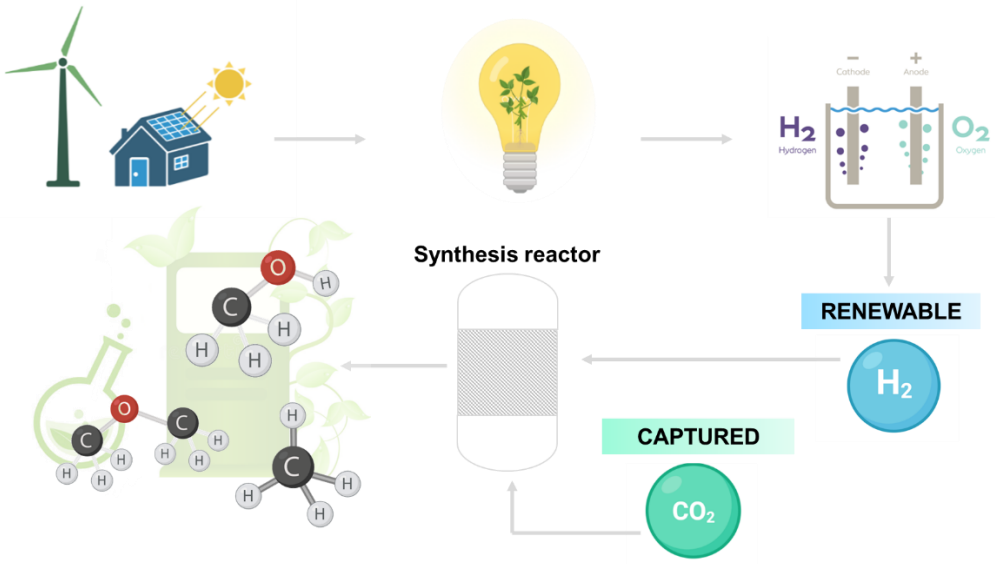

Figure 64: Power-to-X scheme

The employment of DME instead of methanol as feedstock for olefins production could be advantageous for some reasons. DME could be produced directly from syngas through a thermodynamically favored one-stage process instead of a two-step process involving methanol production followed by DME synthesis via methanol dehydration [170]. The one-step DME synthesis also allows valorizing syngas with a lower H_2/CO ratio [171]. Moreover, DME is considered the most reactive intermediate in the synthesis of olefins from syngas; DME is characterized by a higher proton affinity than methanol and by a high ability to react with reaction intermediates leading to the formation of propylene. For these reasons employing DME allows to achieve a faster formation rate of olefins in comparison with that obtained with methanol.

In the last years, several works in literature have been focused on the study of dimethyl ether conversion to olefins. SAPO-type zeolites have been mostly investigated, as they have been generally used as industrial catalysts in the MTO process. Hirota et al. studied the effect of crystal size distribution on the deactivation of catalysts [172]. Particularly, they compared a SAPO-34 nanocrystals zeolite (crystal size: 75 nm) and a SAPO-34 with a crystal size of 800 nm highlighting that SAPO-34 nanocrystals exhibited a higher activity both for MTO and DTO reactions. Authors attributed the better lifetime of nanocrystals zeolites to their lower diffusion length; for crystals with a higher size, the hydrocarbons' residence time is longer, and aromatics, that cannot escape from the pores, could polymerize giving rise to

products that cause zeolite pores blocking and then catalyst deactivation. Instead, inside small crystals, olefins produced easily diffuse out; C_2 and C_3 already out of the crystals cannot re-enter because their diffusivity is lower compared with that of methanol and DME [172]. Manipulating nanocrystals into hierarchical structures has been a successful way to obtain higher activities and better selectivities in MTO/DTO processes. In literature, different methods have been used to prepare hierarchical zeolites; particularly, Cui et al. employed a facile one-step hydrothermal synthesis using polyethylene glycol (PEG) as mesopore generating agent to produce hierarchical SAPO-34 [173]. The larger pores obtained allowed to improve reactants and products diffusion within the catalyst channels and to promote not only the activity of the catalyst but also the selectivity to olefins [173]. In an already published work, researchers analyzed the effect of the presence of a binder on the activity of the SAPO-34 catalyst [174]. They prepared a SAPO-34/ZrO_2 composite catalyst adding different ZrO_2 contents to the synthesis gel of SAPO-34 zeolite. They obtained well-formed SAPO-34 crystals despite the presence of the binder inside the synthesis gel. Moreover, SAPO-34/ ZrO_2 composite catalysts provided a higher selectivity to olefins and exhibited a higher lifetime if compared with the performances shown by other catalysts used in DTO processes. The authors stated that the binder filling the spaces between SAPO-34 crystals allowed to provide new diffusion paths for reactants and products versus the internal active sites of the zeolite. Instead, a free SAPO-34 zeolite is characterized by a pure microporous structure with many active sites on the external surface. For this reason, at the beginning of the reaction, a lot of intermediates will be formed close to each other on the external surface of the zeolite. One of the intermediates of the reaction is hexamethylbenzene which can polymerize to poly-aromatic or poly-alkyl aromatic species causing pores blockage and catalyst-fast deactivation [174]. A kinetic mechanism for coke formation during dimethyl ether conversion to olefins has already been studied obtaining a kinetic equation that correlates the rate of coke formation with DME partial pressure, reaction temperature, and coke content inside the catalyst employed [175]. Zhao et al. studied the performances of AEI/CHA intergrowth zeolites and the effect of phase composition on the reaction of dimethyl ether to olefins [176]. Particularly they

synthetised SAPO zeolites with different SAPO-18/SAPO-34 ratios mixing two different organic templates: diethylamine (DEA) and N, N''-diisopropylethylamine (DIEA). Although all SAPO catalysts exhibited more or less the same DME conversion and products distribution, authors were able to establish that the presence of a higher quantity of the slightly wider AEI cages led to a higher formation of propylene and butene while the presence of the narrower CHA cages led to a preferential production of ethylene. Zhang et al. employed mechanochemical bead-milling and a subsequent porogen-assisted recrystallization over SAPO-34 crystals derived from inexpensive morpholine obtaining nanocrystalline particles that exhibited enhanced stability and better propylene selectivity [177]. It is clear that the whole literature devoted to the study of SAPO zeolites employment in the reaction of dimethyl ether to olefins asserts that these catalysts deactivated very fast making continuous regeneration cycles necessary and exhibited higher selectivities versus olefins with an ethylene to propylene ratio always higher if compared with other zeolite structures.

Furthermore, in the open literature, several works have been reported regarding the testing of H-ZSM5 zeolites in the DTO process. Cordero-Lanzac et al. employed a catalyst prepared agglomerating H-ZSM5 crystals with a mesoporous matrix of γ-Al_2O_3. Authors concluded that the presence of γ-Al_2O_3 mesoporous matrix allowed to reduce of the deactivation of catalyst due to coke species formed over the mouth of zeolite channels favoring the deposition of the carbonaceous structures on the mesoporous surface of the matrix [178]. Pérez-Uriarte et al. compared SAPO type and H-ZSM5 zeolites performances [179]. Particularly, they synthesized the catalysts agglomerating zeolites crystals (H-ZSM5, SAPO-34, and SAPO-18) with bentonite and alpha-alumina. Authors obtained higher selectivities versus light olefins, especially propylene, with H-ZSM5-based catalysts if compared with SAPO-based catalysts and with other silicoaluminophosphate based catalysts employed in the same reaction conditions. In another work, the same authors investigated the effect of the acidity of HZSM-5 and of the binder employed to agglomerate zeolite crystals [180]. Specifically, they employed HZSM-5 zeolites with SiO_2/Al_2O_3 ratios equal to 30, 80, and 280 and bentonite or boehmite as binders. H-ZSM5 zeolite with a lower content of aluminum

favored the production of ethylene, propylene, and butenes while decreasing the selectivities to light paraffins, aromatics, and C_{5+} aliphatic fraction. Moreover, although a decrease in DME conversion was detected using H-ZSM5 zeolite with SiO_2/Al_2O_3 ratio equal to 280, the deactivation of catalyst was significantly reduced as the lower acidity allowed to slow down the rate of coke precursors condensation reactions. Finally, they obtained a more active catalyst using boehmite to agglomerate zeolite crystals. In the open literature, a kinetic model for DTO reaction over an H-ZSM5 zeolite has already been proposed [171]as well as deactivation kinetics [181]. Chen et al. proposed a novel strategy to synthesize nano-sized hierarchical ZSM-5 zeolite through consecutive freezing and vacuum cycles without the use of a hierarchization agent and, employing this catalyst, they obtained improved stability and higher propylene production [182]. The effect of the addition of promoters like La, Ca, and Mg to HZSM-5 has also been investigated [183,184]. Authors demonstrated that the addition of Ca and La species caused changes in the distribution of acid sites of zeolite promoting the formation of weak Brønsted acid sites and new Lewis acid sites; moreover, Ca and La species also promoted the formation of some basic sites on the H-ZSM5 framework. Ca-enriched HZSM-5, because of its higher density of weak and medium acid sites, allowed us to obtain the highest selectivity versus light olefins.

Recently, also other structures have been investigated for the DTO process such as MCM-68 [185], MOR [186,187], and EU-1 [188–190].

In our work, the effect of acidity distribution over H-ZSM5 zeolites has been investigated for the reaction of dimethyl ether to olefins. Moreover, the epitaxial growth of Silicalite-1 over the surface of the starting H-ZSM5 zeolites has been performed to assess the effect of surface acidity passivation over catalysts activity and stability. The effect of external surface acid sites neutralization over coke formation and catalysts deactivation have been deeply studied.

6.2. DTO experimental tests.

Time-on-stream tests of about 14 hours at different reaction temperatures have been performed for all the investigated catalysts. Particularly, DTO tests were performed using a

bench-scale system with precise control of flow rate, temperature (up to 500°C), and pressure (up to 30 bar). A catalytic bed (50 mg) was placed in a 4 mm quartz reactor within a pressure-resistant stainless steel jacket, heated by an electric oven. A sealed thermocouple monitored and controlled the operating temperature inside the reactor. Before testing, each sample underwent pretreatment at 380°C for 2 hours under a nitrogen flow. Operating conditions included a pressure of 2 bar, and the inlet flow rate was adjusted to achieve a space-time of 1 g_{cat}·h/mol_C, using a 3 vol-% DME in the N_2 mixture. Catalytic behavior was assessed at four temperature values (300, 325, 350, and 375°C), with a fresh catalyst sample for each test. Products stream was analyzed using a chromatograph with two columns (HP-5 and HP-PLOT/Q) for separating non-condensable gases and light hydrocarbons, a thermal conductivity detector (TCD), and a flame ionization detector (FID). DME conversion (ζ_{DME}), yield (η_i), and selectivity (σ_i) for the i-th product were calculated employing the following equations:

$$\zeta_{DME} = \frac{\dot{n}_{DME,in} - \dot{n}_{DME,out}}{\dot{n}_{DME,in}} \quad \textbf{(4)}$$

$$\eta_i = \frac{\dot{n}_{C,i,out}}{\dot{n}_{C,in}} = \frac{N_{C,i} \cdot \dot{n}_{i,out}}{2 \cdot \dot{n}_{DME,in}} \quad \textbf{(5)}$$

$$\sigma_i = \frac{\dot{n}_{C,i,out}}{\dot{n}_{C,conv}} = \frac{N_{C,i} \cdot \dot{n}_{i,out}}{2 \cdot \left(\dot{n}_{DME,in} - \dot{n}_{DME,out}\right)} \quad \textbf{(6)}$$

Where $\dot{n}_{DME,in}$ and $\dot{n}_{DME,out}$ represent the inlet and outlet DME molar flow rates, $\dot{n}_{i,out}$ is the molar flow rate of the i-th product and $N_{C,i}$ is the number of carbon atoms in the i-produced species.

Figure 65 shows DME conversion and cumulative products distribution obtained at 300 °C, 325 °C, 350 °C and 375 °C employing Z25 parent zeolite as catalyst. DME initial conversion (calculated after 1.5 hours) was equal to 21% at 325 °C and increased with the increase of reaction temperature (≅ 99% at 375 °C) because of a kinetic effect. Moreover, the DME conversion value exhibited a decreasing trend with time, especially at higher reaction temperatures. At 375 °C, DME initial conversion was about 99% and it dropped to a value of 51 % after about 14 hours of reaction. This detected trend was probably due to coke

formation and consequently to catalyst deactivation which is more marked at high temperatures.

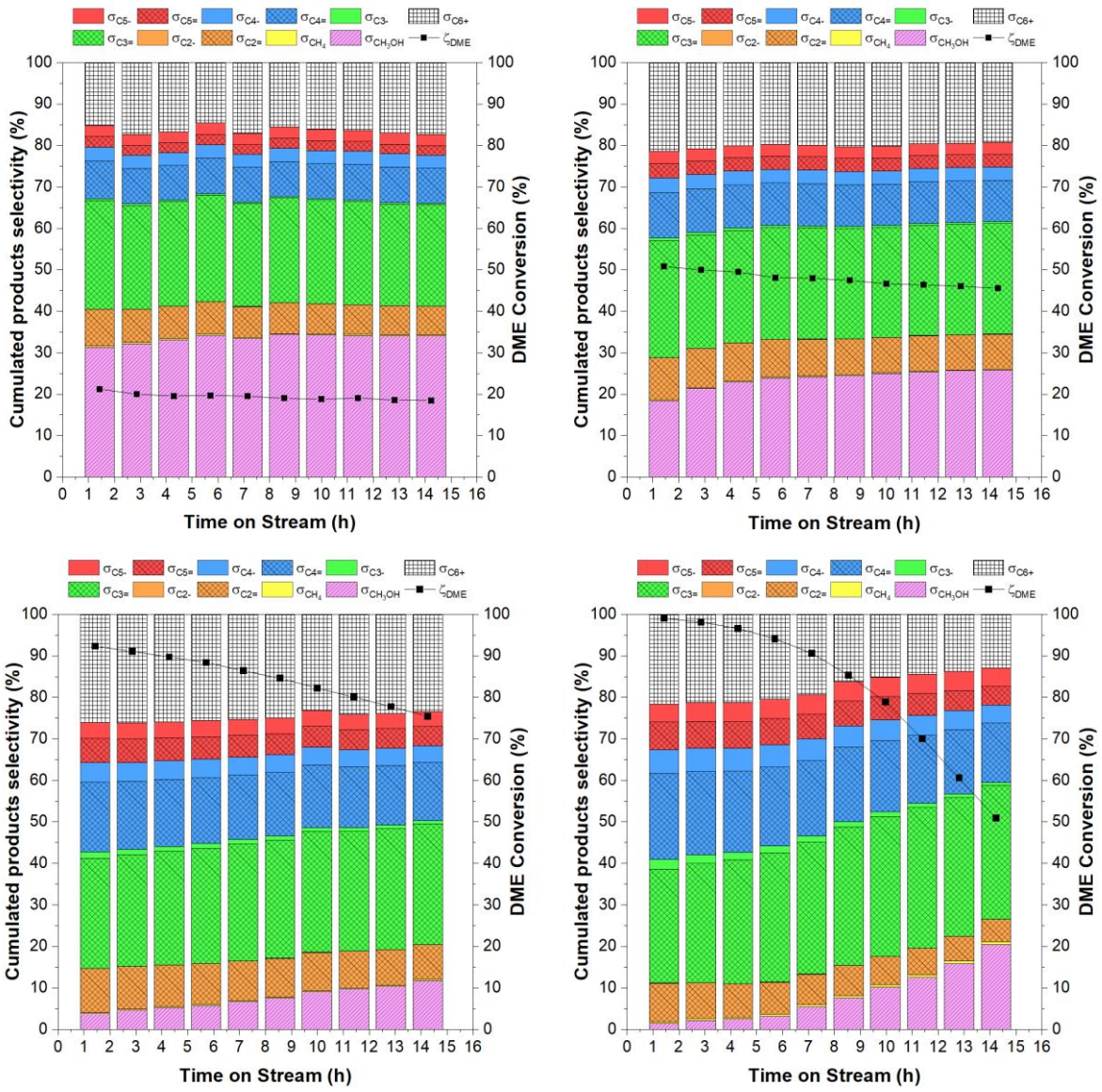

Figure 65: Product distribution (colored bars) and DME conversion (black line) over time on stream for Z25 sample at 300 °C (a), 325 °C (b), 350 °C (c), and 375 °C (d). Olefins selectivity in the range C_2-C_5 is represented with bars having a double diagonal texture.

Results obtained employing Z50 are summarized in **Figure 66**. It appeared clear that the Z50 catalyst exhibited a higher stability, even at higher reaction temperatures. In fact, only a slight decrease in DME conversion value was detected during TOS tests although the initial DME conversion values (at 1.5 hours) were lower at 350°C and 375°C if compared with the Z25 sample. This trend agreed with other literature findings reporting a higher catalyst

deactivation rate when a catalyst with a higher acid strength and a higher acid sites density was employed [191].

Reaction pathways leading to the formation of hydrocarbons have been far studied in literature especially when methanol was used as reactant. For what concerns H-ZSM5 zeolites, findings based on transient $^{12}C/^{13}C$ switching experiments demonstrated that when an H-ZSM5 was used as a catalyst, a modified hydrocarbon-pool mechanism was the predominant source of ethylene. On the contrary, it was proved that propylene and higher alkenes were mostly produced from methylation and cracking reactions of akenes [192]. A dual cycle hydrocarbon-pool mechanism has been accepted to explain how olefins, paraffins, and aromatics are formed during MTO [193]. Ethylene and polymethyl benzenes are mainly formed from methylation and dealkylation reactions involving lower methylbenzene (aromatic-based cycle). Propylene, butenes, and heavier olefins are produced through consecutive methylation and cracking reactions involving olefin (alkenes cycle). The two cycles of the dual-cycle mechanism are interconnected because through H-transfer and cyclization reactions olefins are converted into paraffins and aromatic. For what concerns products distribution, it must be specified that all the species with a carbon number equal or higher than 6 (including paraffins, olefins, and aromatics such as toluene, xylenes, and polymethyl benzenes) have been involved in the group named C_{6+}. Within the products also methanol (pink bar) has been detected in a significant amount and its production could be attributed to the DME hydration reaction which occurs employing water produced from DTO reaction pathways [115]. Moreover, methanol production is higher at lower reaction temperatures; in fact, methanol selectivity, calculated at about 1.5 hours of reaction, was 31 % at 300 °C, 18 % at 325 °C, 4 % at 350 and 1 % at 375 °C. This trend could be explained by knowing that methanol also participates in the reaction pathways leading to the production of hydrocarbons and its conversion increased with the increasing of reaction temperature. Furthermore, an increasing trend of methanol selectivity was observed especially at temperatures higher than 325 °C. Since the increase in methanol selectivity was found together with a DME conversion decrease, it could be related to catalyst deactivation due to the formation on its surface of heavy coke species that, causing

the partial occlusion of zeolite pores, prevented the formation of hydrocarbons thought the "hydrocarbon pool" mechanism [194]. Pores clogging caused a decrease in available acid sites of zeolites strongly influencing reaction pathways leading to the production of hydrocarbons rather than of methanol. At higher reaction temperatures (350°C and 375°C) initial methanol selectivity detected employing ZSM5_25 was always lower if compared with ZSM5_50. However, because of ZSM5_25 faster deactivation, this trend was reversed during the time on stream tests.

Within hydrocarbons produced, propylene selectivity was the highest at each investigated reaction temperature. This result is in accordance with already published works in literature in which H-ZSM5 zeolites are used as catalysts for DTO reaction [38-40]. The ratio between ethylene and propylene remained below 1 for the entire time on stream test at each tested temperature. Furthermore, ethylene and butene selectivity decreased with time and this trend was clear, especially at 350°C and 375°C. This decreasing trend, detected together with the decreasing of DME conversion, suggested that catalyst deactivation had a higher effect over reaction pathways leading to the formation of ethylene (aromatic-based cycle) and the formation of butene (probably mostly produced from the methylation of propylene).

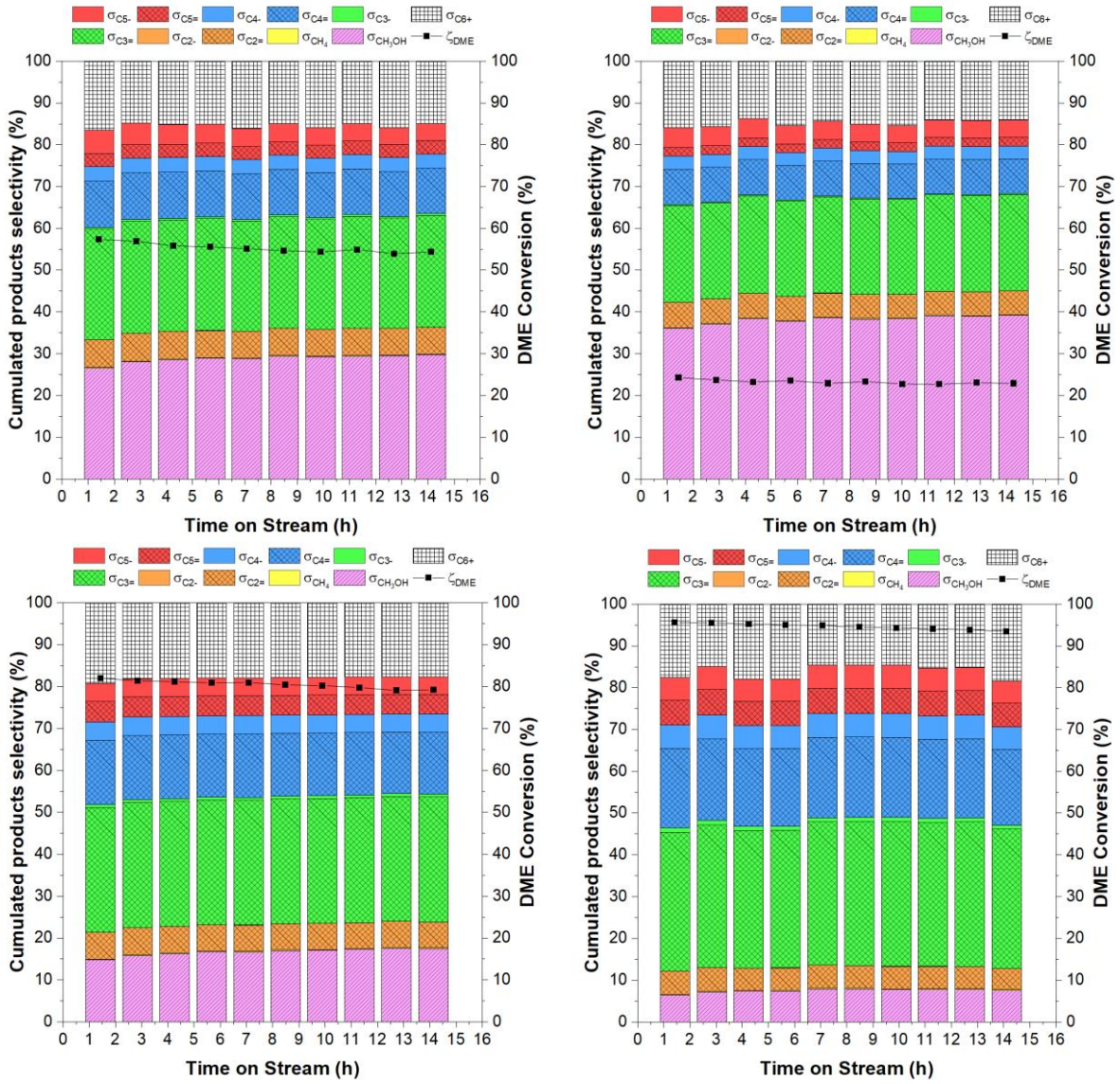

Figure 66: Product distribution (colored bars) and DME conversion (black line) over time on stream for Z50 sample at 300 °C (a), 325 °C (b), 350 °C (c), and 375 °C (d). Olefins selectivity in the range C_2-C_5 is represented with bars having a double diagonal texture.

To elucidate the effect of surface passivation, **Figure 67** reports DME conversion over Z25 and AS-Z25_XX (**Figure 67_a**) and over Z50 and AS-Z50_XX (**Figure 67_b**) obtained at 375°C. The effect of passivation was unmistakable for ZSM-5 zeolite with a Si/Al ratio equal to 25 and negligible for ZSM-5 zeolite with a Si/Al ratio equal to 50. This result could have been predicted because, for the Z25 sample, a faster deactivation was detected. In fact, many works in the literature reported the formation of graphitic coke on the surface of MFI zeolites when catalysts were employed at temperatures higher than 350°C [192]. For this reason, the coating with Silicalite-1 of the Z25 sample, neutralizing the effect of surface acid

sites mainly responsible for coke production, allowed preserving catalyst activity for a longer time (PAS_25). In the case of the Z50 sample, good stability was found even without the growth of Silicalite-1, probably linked to the lower acidity of the zeolitic core surface. Moreover, the concentration of acid sites was lower for the Z50 catalyst and, therefore, it is quite impossible to appreciate the impact of the growth of Silicalite-1 over its surface.

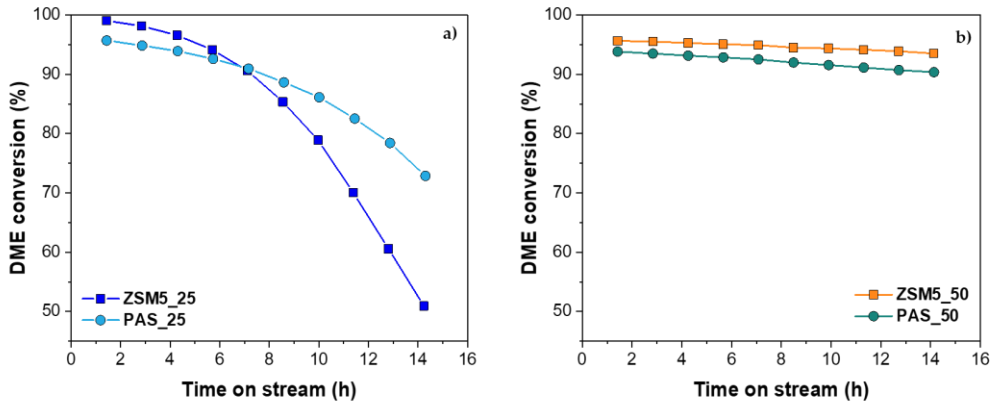

Figure 67: DME conversion at 375°C for Z25 and AS-Z25_XX (a) and for Z50 and AS-Z50_XX (b)

In **Table 22** the average of the sum of the selectivities of C_2-C_4 olefins (ethylene, propylene, and butenes) is reported for all the investigated samples at each reaction temperature. Data obtained at low reaction temperatures (300°C and 325°C) where catalysts did not deactivate, showed a clear trend with the acidity of the investigated sample: the higher the acidity the greater the selectivity of light olefins. This conclusion cannot be drawn for higher reaction temperatures where an evident trend related to acidity was not found.

At high reaction temperatures (350 °C and 375°C) stronger deactivation led to a decrease in ethylene, butenes, and heavier hydrocarbons (C_{6+}) selectivities together with the increase of methanol selectivity and with a drop in DME conversion (especially for Z25 and AS-Z25_XX samples). This could be explained by the hypothesis according to which coke production and consequently catalyst deactivation had a stronger effect on the aromatic-based cycle responsible for producing ethylene and part of C_{6+} compounds. Moreover, butenes are mainly produced from propylene methylation or heavier olefin cracking. The decrease with

time of butene selectivity, together with a detected increase of propylene, could be related to a stronger effect of deactivation over the reaction of propylene methylation to butenes.

Table 22: Average light olefins selectivity ($C_{2=}$-$C_{4=}$) during TOS for each tested catalyst at different reaction temperatures.

	C_2-C_4 olefins selectivity			
	300 °C	**325 °C**	**350 °C**	**375 °C**
ZSM5_25	43.0 %	47.6 %	53.7 %	57.7 %
PAS_25	41.0 %	47.4 %	52.3 %	55.8 %
ZSM5_50	39.0 %	45.6 %	52.0 %	58.6 %
PAS_50	38.2 %	43.0 %	53.5 %	59.6 %

As already mentioned, propylene was the hydrocarbon produced in the highest quantity for all the investigated catalysts. To acquire more information about the quantity of propylene obtained its productivity has been evaluated through yield (**Eq. 5**) and its specific productivity (moles of propylene per hour per kg of catalyst) for all the investigated samples at 375°C. Propylene yield and specific productivity were calculated using product composition obtained after 1.5 hours of reaction when the catalyst performance was not altered by deactivation. Furthermore, to obtain an integral production (per unit of catalyst load) for the tested samples, the propylene flow rate was integrated over the entire time-on-stream. These results are reported in **Table 23**. Propylene productivity was higher for samples with a lower acidity probably because of a higher selectivity exhibited by these samples. Integral propylene production values demonstrated that C_3 olefin productivity increased with the increase of the Si/Al ratio of the investigated sample. Z50 and AS-Z50_XX allowed to obtain the higher production of propylene per g of catalyst, and this could be related to their reduced deactivation at 375°C.

Table 23: C_3H_6 yield, specific productivity, and integral production values at 375 °C for all investigated catalysts.

	C_3H_6 yield	C_3H_6 specific productivity ($mol_{C3H6} \cdot kg_{cat}^{-1} \cdot h^{-1}$)	C_3H_6 integral production ($g_{C3H6}\ g_{cat}^{-1}$)
Z25	27.2 %	91	53
AS-Z25_XX	26.4 %	88	55
Z50	32.0 %	107	64
AS-Z50_XX	34.0 %	113	67

The olefin share was calculated as the ratio between the olefin amount and the totality of the hydrocarbons produced with the same number of C atoms for hydrocarbon classes between C_2 and C_5. For example, for C_2 class the olefin share was calculated as the ratio between ethylene flow rate and the sum of ethylene plus ethane flow rates. This calculation was done for all the investigated samples at each reaction temperature but in **Figure 68** results obtained at 375°C are shown. Particularly, **Figure 68** presents the olefin share (left y axe) and the grouped C_2-C_5 olefin share (right y axe, light blue bars) obtained as an average of the olefin share of each class. The olefin share increased with the decrease in the number of C atoms. Particularly, C_2 olefin share was always close to 100% because almost no ethane was detected. Although **Figure 68** shows results obtained at 375°C, described trends were found at each reaction temperature for all tested samples. The increase of the olefin share with the decreasing of C atom numbers could be explained using the theory according to which paraffins are mainly produced from olefin hydrogen transfer reactions. As this step involves two olefins, lighter paraffins like C_2H_6 and C_3H_8 are not easily formed, while the production of alkanes from C_4 is higher. [192]. C_3 olefin share increased during the time on stream tests of samples that exhibited a higher deactivation (Z25 and AS-Z25_XX at 375°C). Moreover, C_5 class olefin share showed a decreasing trend for Z25 and AS-Z25_XX. This finding could be related to the reduction in butenes selectivity and consequently the reduction of their methylation reactions that, among the other pathways, leads to the production of pentenes.

Besides, C_2-C_5 olefin share calculations (light blue bar in **Figure 68**) demonstrated that during the entire time on stream test, the ratio between C_2-C_5 olefins produced and the total amount of C_2-C_5 hydrocarbons was always above 80%.

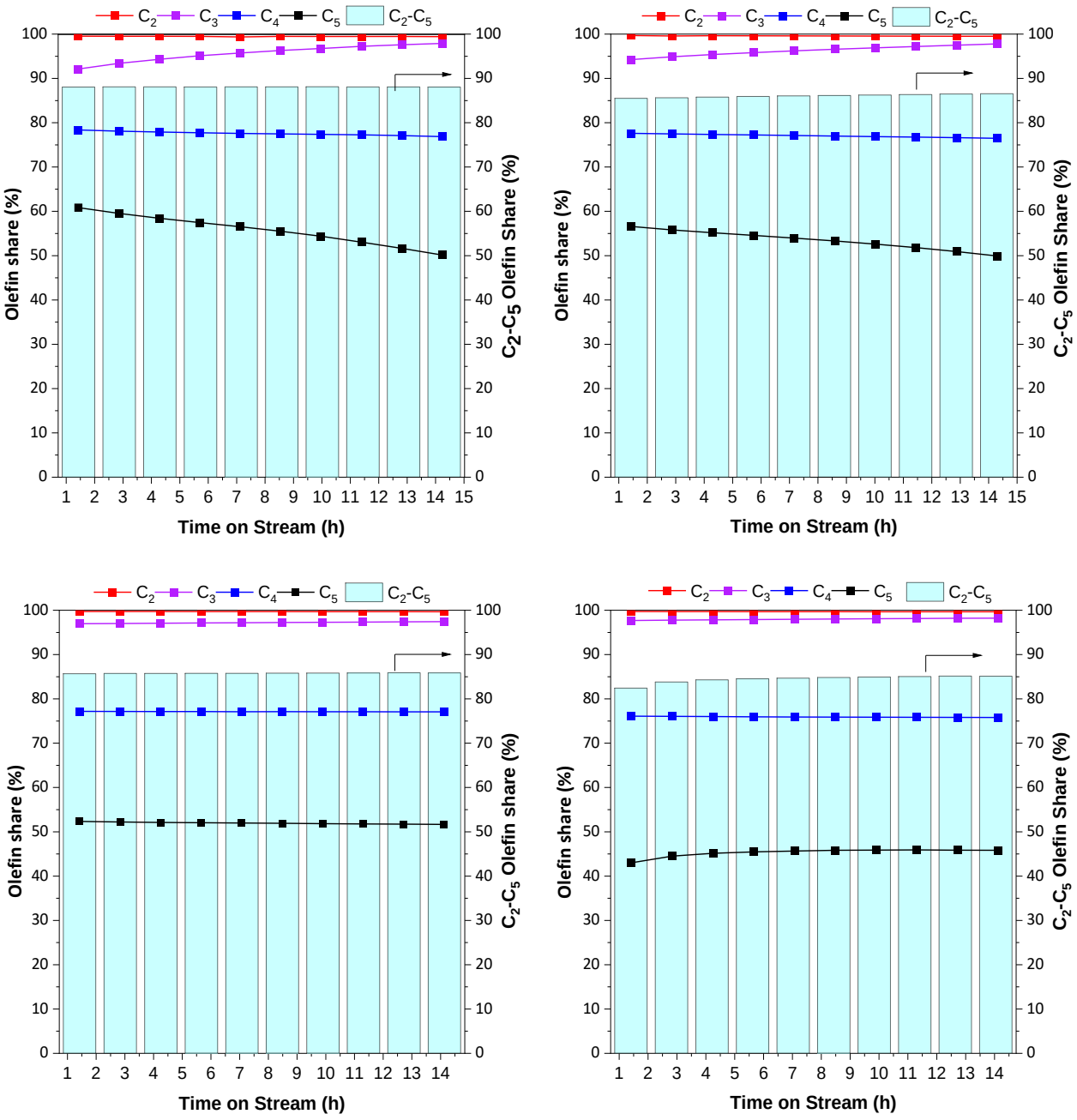

Figure 68: Olefin shares for hydrocarbon classes between C_2 and C_5 at 375 °C for Z25 (a), AS-Z25_XX (b), Z50 (c), and AS-Z50_XX (d).

The dataset obtained from all the TOS carried out demonstrated that the ethylene to propylene ratio was always lower than 1 and confirmed findings of the already published literature when MFI zeolites are used as catalysts for the MTO or DTO reaction. Moreover,

the number of light olefins produced during TOS was always higher than heavier compounds (C_{6+}) and this conclusion leads to the hypothesis according to which alkene cycle is favored when an MFI structure is used to perform DTO tests. Moreover, deactivation, observed for samples with high acidity, had a stronger effect over the aromatic cycle of the hydrocarbon pool causing a decrease in ethylene selectivity. Light olefin selectivity increased with temperature, but deactivation observed at 350°C and 375°C caused a drop in DME conversion and an increase in methanol selectivity probably because also methanol conversion to hydrocarbons was influenced by coke production.

6.3 Characterization of spent catalysts and coke analysis.

Thermogravimetric analyses were performed to characterize spent catalysts. Particularly, as already done in Chapter 5, percentage weight loss in the range of 150-850°C has been estimated and employed to evaluate the quantity of coke produced during the time on stream tests. Results for all reaction temperatures are reported in **Figure 69 (a, b)**. An increasing trend of the weight loss with reaction temperature, and then of the quantity of coke produced, was found for each investigated catalyst. Z25 and AS-Z25_XX samples exhibited almost the same weight loss for all temperatures below 375°C. At 375°C, where the deactivation of catalysts was stronger, the effect of the passivation procedure of Z25 sample was clear as the amount of coke estimated for AS-Z25_XX spent catalyst was about 20% lower if compared with the parent zeolite. However, the growth of Silicalite-1 did not improve performances in terms of coke produced by the Z50 sample. Furthermore, samples characterized by lower acidity values led to a lower formation of coke species as a consequence of their slight deactivation.

Table 24: Coke production refers to the total amount of dimethyl ether converted during the entire TOS test.

Formed coke (mg coke · $g_{dme\ converted}^{-1}$)				
	300 °C	**325 °C**	**350 °C**	**375 °C**
Z25	0.84	0.29	0.23	0.35
AS-Z25_XX	0.85	0.31	0.23	0.26
Z50	0.44	0.15	0.12	0.11
AS-Z50_XX	0.69	0.26	0.17	0.16

Combining results obtained from TGA analyses and the total amount of DME converted during the entire time on stream test, milligrams of coke produced per gram of DME converted were calculated and data are summarized in **Table 24**. For samples Z50 and AS-Z50_XXthe amount of produced coke decreased with temperature because of the higher DME conversion. For Z25 and AS-Z25_XX catalysts, the decreasing trend inverted at 375°C probably because the great coke production was not compensated by the higher conversion. For all investigated temperatures, samples with a Si/Al ratio equal to 50 were allowed to obtain a lower specific coke production.

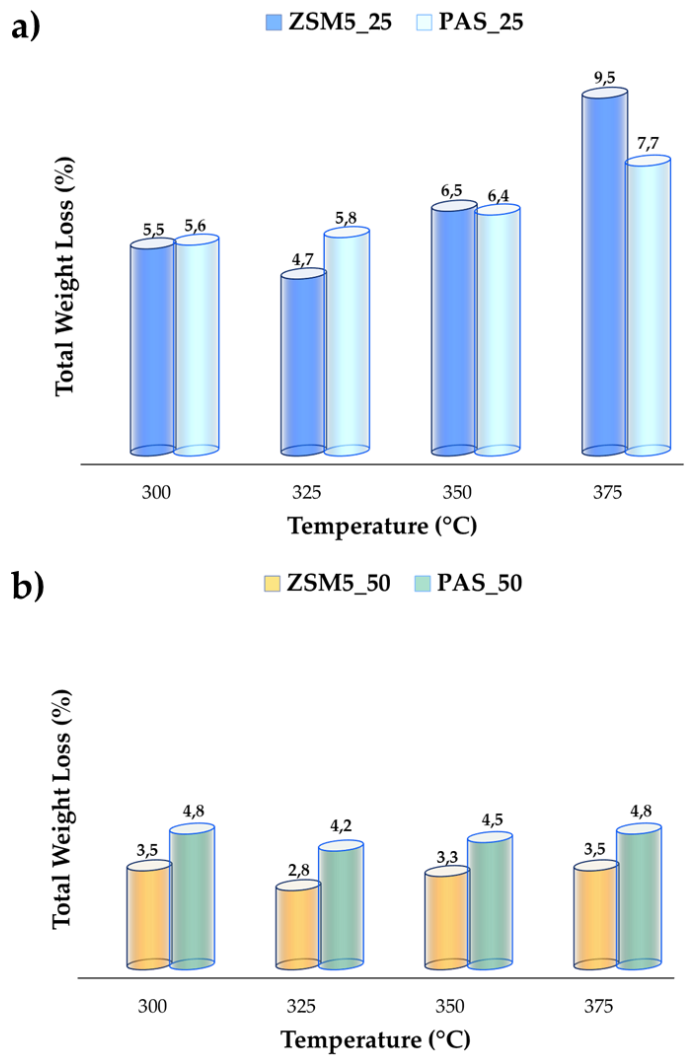

Figure 69: Coke amount estimated at all reaction temperatures for (a) Z25 and AS-Z25_XX and (b) Z50 and AS-Z50_XX.

Figure 70 (a, b, c, d) shows DTA analysis profiles for all tested catalysts at each reaction temperature. Observing profiles obtained for Z25 and AS-Z25_XX spent catalyst tested at low temperature (below 350°C) three main peaks can be identified: the first one at around 100°C is endothermic and referred to the water trapped inside the pores of the catalysts, the second (≈ 270°C) and the third (≈540°C) peaks are exothermic and related to coke species combustion. The exothermic peak detected at higher reaction temperatures could be associated with the presence of heavier coke species [192]. When the reaction temperature was above 350°C, the exothermic peak observed at lower temperatures ≈270°C) shifted towards higher temperatures (≈370°C), and the exothermic peak at 540°C started to be

higher and definite. This trend, instead, was not so clear for Z50 and AS-Z50_XXprobably because of the lesser quantity of coke produced.

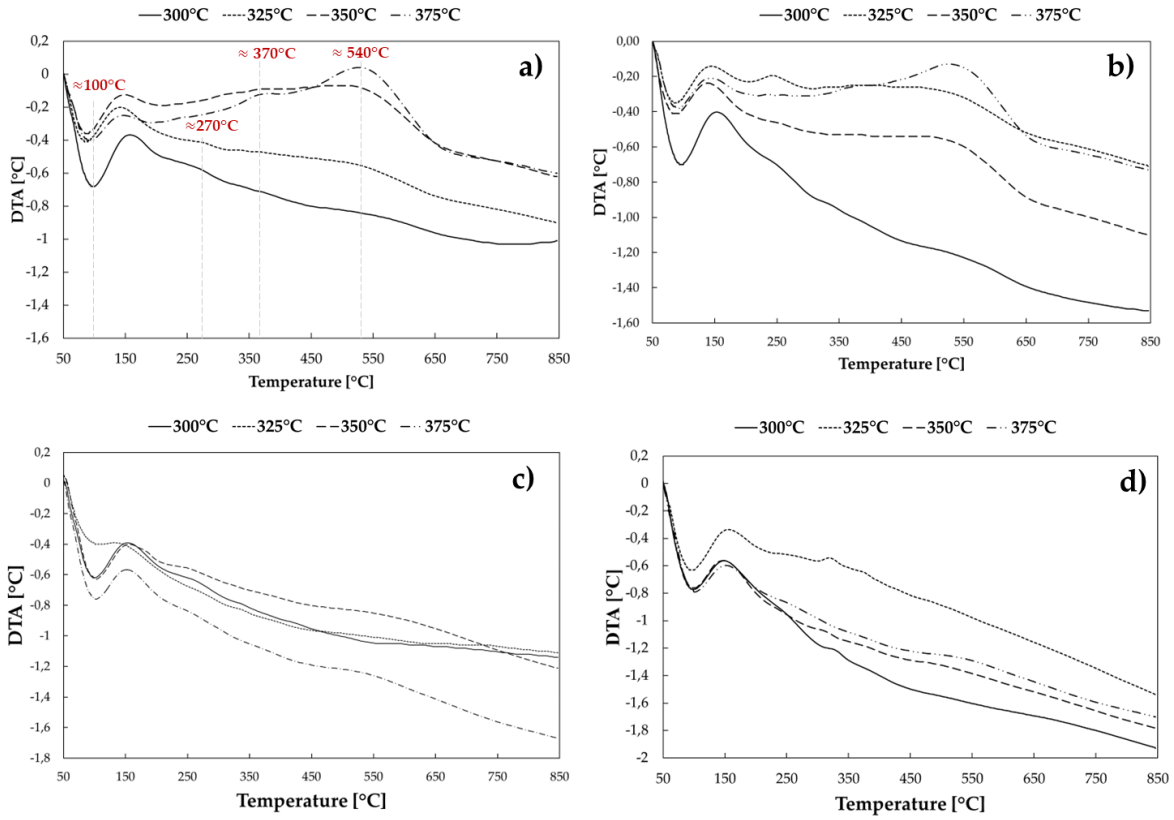

Figure 70: Differential thermal analysis results for: (a) Z25 (b) AS-Z25_XX (c) Z50 and (d) AS-Z25_XX.

GC-MS analysis of soluble coke extracted from spent catalysts using dichloromethane were performed and results are reported in **Figure 71**. The only species trapped inside the spent catalysts and detected during the analyses were pentamethyl and hexamethylbenzene at each reaction temperature. Probably tracks of other coke precursor species were trapped inside the spent sample but, because of their very low quantity, it was not possible to detect them. A decreasing trend with temperature of the intensity of the two peaks related to pentamethyl benzene and hexamethylbenzene was found for all samples. This result confirmed the hypothesis according to which at higher reaction temperatures stronger deactivation of catalysts was caused by the formation of big coke compounds not soluble in CH_2Cl_2 and probably formed on the surface of the catalysts.

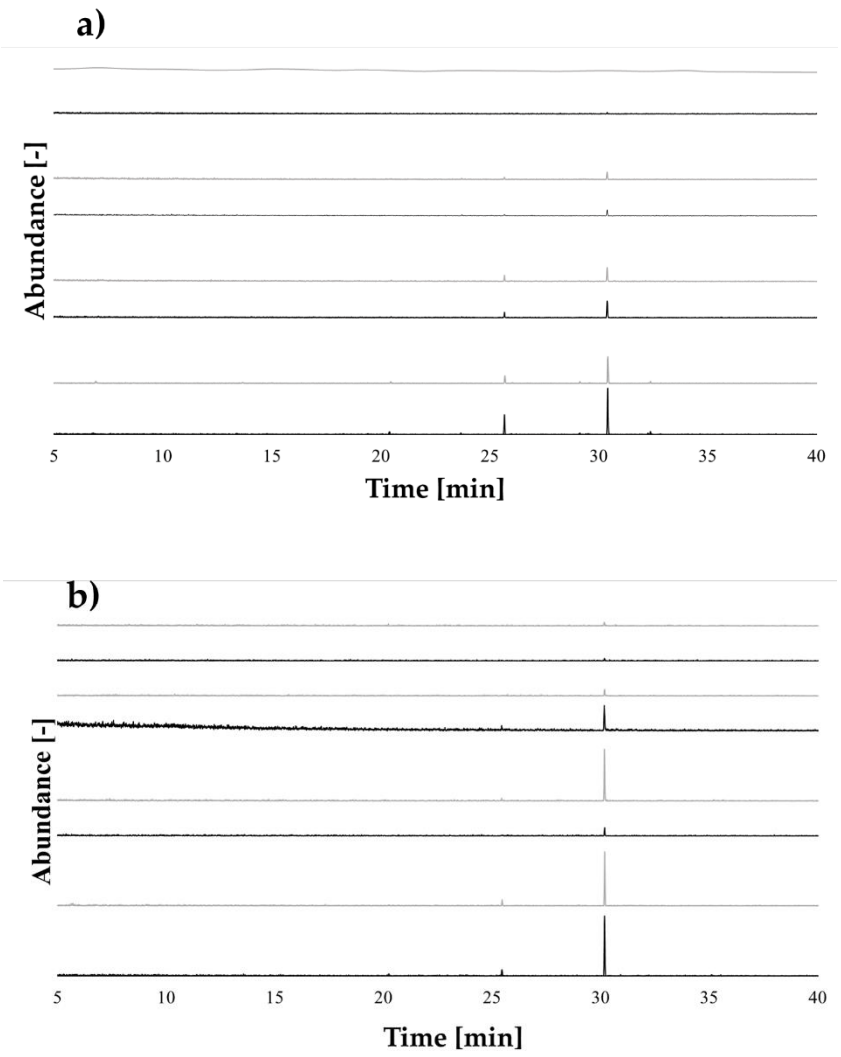

Figure 71: GC-MS analysis results of coke species confined in the framework of (a) Z25 (black line) and AS-Z25_XX (grey line) and (b) Z50 (black line) and AS-Z50_XX (grey line) at each investigated temperature.

In order to understand how catalyst acidity distribution changed after a time on-stream test of 14 hours, AS-Z25_XX spent catalyst (tested at 350°C) was regenerated via TGA under an air flow of 100 ml/min, and acidity was then assessed through d3-acetonitrile FT-IR analysis. Particularly, the AS-Z25_XX catalyst was heated employing a thermal ramp of 5°C/min under air flow until 650°C (temperature at which no further weight loss was detected) and kept at this temperature for 1 hour. TGA analysis results of this regeneration step are reported in **Figure 72**.

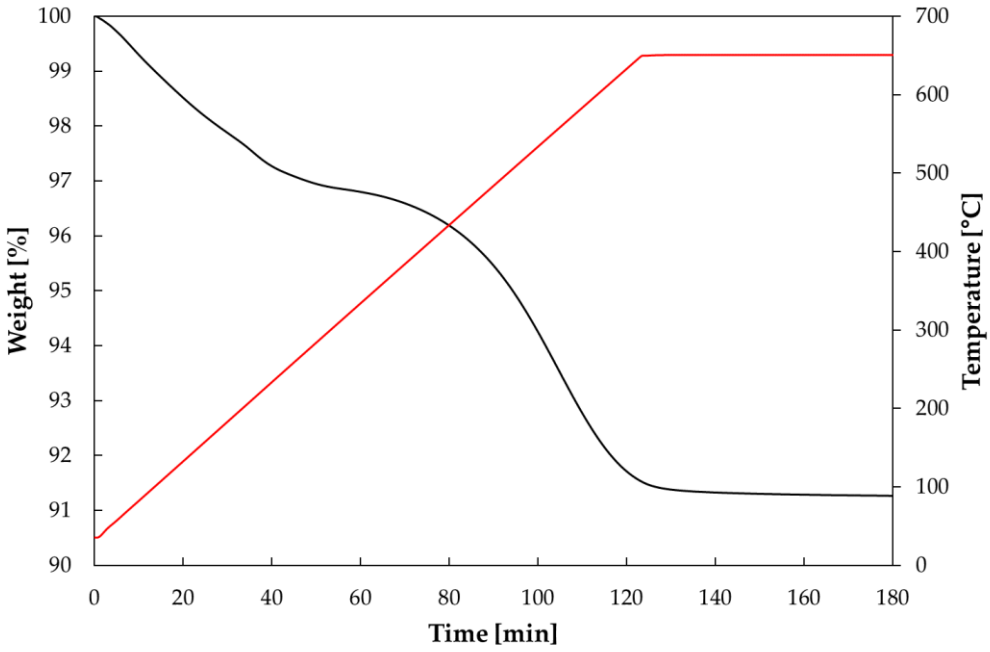

Figure 72: Regeneration via TGA of AS-Z25_XX spent catalyst.

A comparison between the acidity distribution of fresh and regenerated AS-Z25_XX samples is reported in **Table 25**. Only a slight decrease of Brønsted acid sites was detected after the regeneration cycle and this could be related to high temperatures reached during the regeneration that probably led to silanols dehydroxylation (usually found at temperatures above 550°C). The lack of the band at 2275 cm^{-1} (usually associated with external silanols linked to d3-acetonitrile) for the regenerated sample (**Figure 73**) is further proof that silanols dehydroxylation occurred [112].

Table 25: Acid sites distribution of the AS-Z25_XX fresh and regenerated samples evaluated through d_3-acetonitrile FT-IR measurements.

SAMPLE	BAS ($\mu mol\ g_{cat}^{-1}$)	LAS ($\mu mol\ g_{cat}^{-1}$)	BAS+LAS ($\mu mol\ g_{cat}^{-1}$)
Fresh	387	76	**463**
Regenerated	326	81	**411**

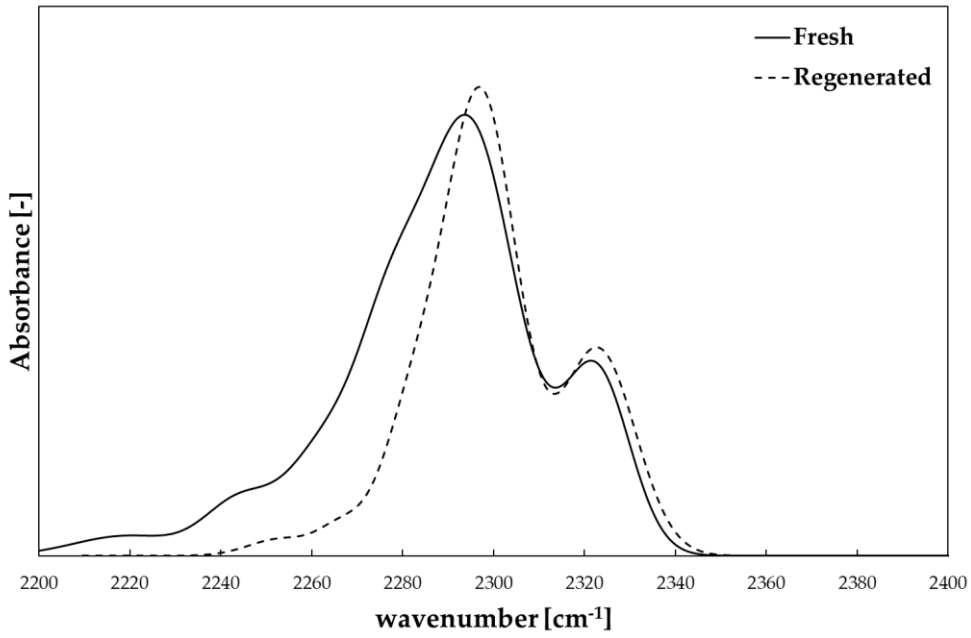

Figure 73: FT-IR spectra of fresh and regenerated sample (AS-Z25_XX) after d_3-acetonitrile adsorption

6.4 Conclusions.

In this part of the research work the role of acidity and the effect of surface acid sites passivation for dimethyl ether conversion to olefins were deeply studied. To reach this goal two MFI zeolites with a Si/Al ratio equal to 25 and 50 were synthesized. Moreover, the surface acidity of these parent zeolites was neutralized through the coating with a layer of Silicalite-1 obtained via the employment of the epitaxial growth technique. Characterization of samples shown in **Chapter 4**, confirmed that the passivation process occurred with success. Catalysts were tested for the reaction of dimethyl ether conversion to olefins during the time on stream tests of about 14 hours at four different reaction temperatures: 300 °C, 325°C, 350°C, and 375°C. Light olefins (i.e., ethylene, propylene, and butenes) selectivity reached were always above 60% for all catalysts and for each investigated temperature. Methanol was always detected within products, especially at low reaction temperatures as an effect of the DME hydration reaction, and methanol selectivity increased when the catalyst employed started to deactivate. Propylene was the product obtained in higher amounts at each reaction temperature tested and during the entire time on stream tests confirming the hypothesis according to which the alkene-based cycle is predominant when

an MFI zeolite is employed as a catalyst for MTO or DTO processes. DME conversion reached at a space-time of 1 g_{cat}·h·mol_C^{-1} with MFI-type zeolites synthesized is higher than the values reported for other zeolite catalysts like SAPO-34. The coating with Silicalite-1 of the ZSM5 zeolite with a Si/Al ratio equal to 25 allowed to enhance catalyst stability, especially at higher reaction temperatures. Moreover, the amount of coke detected for AS-Z25_XX spent catalyst at 375°C was lower if compared to Z25. These results confirmed the idea according to strong deactivation, which occurred at higher reaction temperatures, was caused by the formation of heavy coke compounds on the surface of zeolites that occluded pores and made zeolite active sites inaccessible. Z50 sample, because of its lower acidity, showed higher stability even at higher reaction temperatures but also lower initial activity and higher production of methanol (especially at 300°C and 325°C). Contrary to the results obtained for Z25 zeolite, the passivation procedure did not improve Z50 catalytic performances in terms of stability and coke formation.

CHAPTER 7. Synthesis of Zeolite Templated Carbon (ZTC) over Beta@Silicalite-1 zeolites

BEA parent zeolite and BEA@Silicalite-1 composite materials have been employed as matrices for the subsequent synthesis of microporous carbon materials known as zeolite-templated carbons (ZTC). The effect of the Silicalite-1 layer over the properties of obtained ZTCs such as framework order and crystallinity and oxygen content have been evaluated. Moreover, ZTCs synthesized were also employed for CO_2 adsorption at different temperatures.

7.1 Zeolite templated carbons: state of the art.

ZTCs, or zeolite-templated carbons, are innovative structured microporous carbon materials synthesized by utilizing zeolite as a sacrificial template. Unlike mesoporous carbons, produced starting from mesoporous silica materials, ZTCs are composed ideally of curved, single-layer sp^2 graphene frameworks. This structure led to unique properties such as well-developer microporosity (≈ 1.7 cm^3/g) and exceptionally high surface area (≈ 4000 m^2/g) [198]. ZTCs exhibit favorable compatibility with chemical modifications, enabling the expansion of their functionality through processes such as heteroatom doping or the incorporation of active species by introducing additional compounds [199]. Moreover, ZTCs are characterized by chemical stability both in acid and in basic environments, hydrophobicity, and also good electrical and thermal conductivities. Thanks to these distinctive characteristics, ZTCs find applications in diverse fields such as hydrogen storage, methane storage, CO_2 capture, liquid-phase adsorption, catalysts, electrochemical capacitors, batteries, and fuel cells but also as catalyst support [200–208]. **Figure 74** illustrates a standard schematic representation of the synthesis process for ZTCs. Employing zeolites as matrices, the synthesis process involves chemical impregnation or deposition and leads to the production of a composite material in which carbon molecules are loaded inside the channels of zeolite. Through the removal of the zeolite, a negative replica is obtained, resulting in the formation of a ZTC.

Carbon introduction into zeolite channels can be performed following three main methods [199]:

- Impregnation-carbonization method
- Chemical vapour deposition (CVD)
- Two-steps method

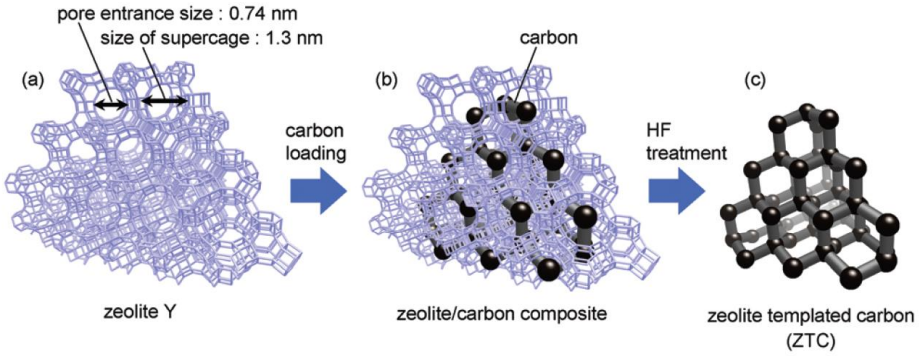

Figure 74: ZTCs synthesis process [199].

The impregnation-carbonization method involves the insertion of organic monomers into zeolite channels, leading to the formation of a polymer/zeolite composite when increasing the temperature. In fact, zeolites active sites allow the conversion of various organic compounds into polymers and subsequently into carbonaceous substances. Monomer introduction can occur through vapor or liquid phases. Different compounds have been investigated for the liquid phase method such as pyrene, and acetonitrile but the most employed is furfuryl alcohol (FA) chosen for its ease of introduction into zeolite micropores under vacuum conditions. After the introduction of FA inside zeolites channels any excess of carbon precursor outside the zeolite is eliminated using a solvent with a larger molecular size than the zeolite's pore entrances. Following this, the impregnated zeolite undergoes carbonization under N_2 flow within a temperature range of 700-900 °C to stabilize the framework.

Chemical vapour deposition is another employed method to synthesise ZTCs samples. ZTCs synthesized by CVD replicate the zeolitic network topology, displaying an ordered

periodic structure with distinct reflections and minimal amorphous carbon. In a typical synthesis, zeolite undergoes an initial treatment under an inert gas, like N_2, at temperatures between 500-700 °C to eliminate impurities. Subsequently, a carbon source is introduced at high temperatures at different times. Common carbon precursors for CVD include ethylene, propylene, butylene, acetonitrile, and methane. Finally, the two-step method involves firstly impregnation-carbonization method and then chemical vapour deposition.

After the carbon introduction, the resulting zeolite/ZTC composite materials are commonly purified using hydrofluoric acid (HF) to dissolve the zeolite matrix and extract the carbon phase. However, HF is toxic, prompting recent efforts to explore safer dissolution methods, such as using lower HF concentrations or alternative reagents like NaOH. While NaOH is effective for high-silica zeolites, it faces challenges with high aluminum-content zeolites. Despite safety concerns, NaOH treatment introduces oxygen-functional groups on ZTC surfaces, altering their electrical characteristics.

Three categories have been identified to classify ZTC materials according to the degree of a replica of the obtained zeolite: Type I, Type II, and Type-III [199].

Type-I ZTCs consist primarily of a well-ordered framework replicated from the zeolite template. Type-II ZTCs are a mix of Type-I structures and additional carbonaceous components formed outside or within the zeolite template. Type-III ZTCs lack or rarely contain the Type-I structure, though some researchers use the term "ZTC" for such disordered materials. Usually, the impregnation-carbonization method employed for the synthesis allows to produce of Type-III ZTCs.

The Si/Al ratio of the zeolite employed for the synthesis of ZTC material is a crucial factor influencing carbon replica in zeolites. Highly acidic zeolites (Si/Al < 20) promote amorphous carbon formation, leading to ZTC Type-II or Type-III. Similarly, low-acid zeolites (Si/Al > 50) result in amorphous carbon due to insufficient acidity to catalyze the polymerization reactions. Optimal conditions for carbon replica require the employment of zeolites with a Si/Al ratio around 20-30. Moreover, the choice of zeolite cation type significantly influences the carbon replica. The H-form leads to direct polymerization with no deposition of carbon on the zeolite surface, while the Na-form is preferred for producing ZTC Type-I with high

surface area. Other alkali metals like K, Ca, and Li also serve as effective scaffolds for ZTC synthesis, with variations in cation forms impacting the properties of the resulting carbon structures.

As already explained before, because of their exceptional properties ZTCs find applications in different fields. They have been a focal point in research as potential electrode materials for supercapacitors [209]. In catalysis, ZTCs have demonstrated promising results in various reactions, such as methanation of carbon monoxide and selective oxidation of furfural to 2-furoic acid [210]. Hydrogen storage is critical for clean energy, and the method of adsorption in porous solids, particularly carbon materials, is noteworthy. Recent research underscores that ZTCs exhibit the most significant hydrogen uptake capacity among porous materials. Considering hydrogen's viability as an eco-friendly alternative to fossil fuels, it is imperative to explore materials like ZTCs, where properties can be adjusted during synthesis to enhance adsorption [211]. Moreover, ZTCs have been widely used both for CO_2 storage and for electrocatalytic reduction. In this research work ZTCs synthetised have been investigated for CO_2 adsorption at different temperatures.

7.1 ZTC synthesis procedure.

ZTC samples were produced using the Chemical Vapour Deposition (CVD) technique, with Ethylene serving as the carbon precursor [212]. The synthesis occurred in a horizontal quartz reactor placed within a laboratory-scale furnace, as depicted in **Figure 75**. In a standard synthesis, 1.50 g of Na-zeolite was placed in the reactor vessel, loaded into the quartz reactor tube, and positioned inside the furnace. To energize the reactor, the zeolite was heated from room temperature to 700°C at a rate of 20°C/min under a nitrogen flow of 455 mL/min for 1 hour. Following this step, a mixture of nitrogen and ethylene (0.03 mol of ethylene, total flow of 515 mL/min) was introduced for 3 hours to induce carbon deposition. After the carbon deposition process, the system was cooled under nitrogen flow for 1 hour.

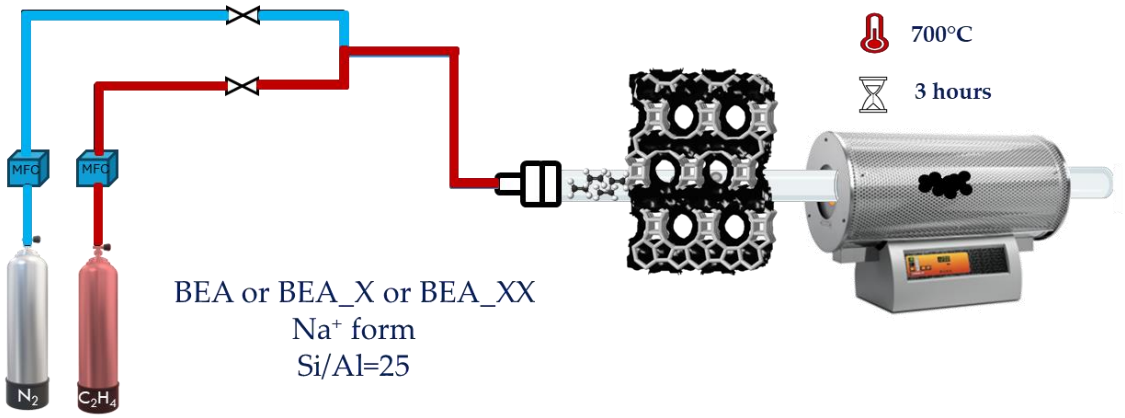

Figure 75: ZTCs synthesis set-up

ZTCs obtained and the corresponding zeolitic matrices employed for the synthesis are summarized in **Table 26**.

Table 26: ZTCs obtained.

Sample code	Zeolite Employed	Synthesis Method
ZTC	BEA	Ethylene CVD
ZTC_X	BEA_X	Ethylene CVD
ZTC_XX	BEA_XX	Ethylene CVD

After the synthesis, samples were subjected to a purification treatment in order to obtain the complete dissolution of the carbon matrix. Purification procedure consisted of two steps:

1. A polyethylene bottle containing 1 g of composite material (zeolite/ZTC) was subjected to stirring with 40 mL of HF (27 M) at room temperature for 12 hours. Following the treatment, the samples were filtered, washed with copious amounts of distilled water, and dried overnight at 90°C.
2. After drying, the ZTC was mixed with HCl (22 M; 40 mL/g) under stirring at room temperature for 6 hours. Similar to the first step, after the treatment, the samples were filtered, washed thoroughly with distilled water, and dried overnight at 90°C.

7.2 ZTC Characterizations.

The ZTCs produced were characterized employing X-Ray Powder Diffraction (XRD), Nitrogen Physisorption at 77 K, Thermogravimetric Analysis (TGA/DTA), Fourier Transform Infrared Spectroscopy (FT-IR), Raman Spectroscopy, and Scanning Electron Microscopy (SEM).

Instruments and methodologies applied for the characterizations were the same as those previously described for zeolitic catalysts (**Chapter 3**). The only differences concern TGA analyses, FT-IR measurements, and Raman spectroscopy that have been employed only to characterize ZTCs. TGA analyses were performed using a nitrogen flow of 100 ml/min and heating the sample (about 10 mg) from room temperature to 800°C (thermal ramp of 5°C/min).

FT-IR measurements were performed by diluting ZTC samples in KBr (0.2 wt.%) and compressing the physical mixture of ZTC and KBr into a self-supporting wafer (13 mm diameter) using a hydraulic press (10 ton). Before the analysis, samples were dehydrated at 105°C for 1 hour and then examined at room temperature in the range of 4000-400 cm^{-1} with an optical resolution of 4 cm^{-1}. In a typical ZTC spectrum (between 1160 and 3600 cm^{-1}) it is possible to identify several adsorption bands that can be attributed to the different functional groups located within the ZTC structure. In this research work, peaks detected in ZTC spectra were deconvoluted and attributed to the functional groups as described in **Table 27** [213]. In this way, a semiquantitative analysis of functional groups was obtained and used to understand differences between ZTCs synthesized starting from a BEA or a BEA@Silicalite-1 zeolite. It is dutiful underline that some "filling" peaks (P1, P5, P6, and P7) have been added to the deconvolution to realise a better fitting.

Table 27: FT-IR peaks attribution [213].

Peak number	Lower Bound (cm^{-1})	Upper Bound (cm^{-1})	Probable assignment	Attribution
P1	1040	1120	**ν (C–OH)**	**C-OH**
P2	1120	1170	**ν (C–O–C);**	**epoxy (–C–O–C–);**
P3	1180	1215	**ν_{as} (C–O–C)**	**epoxy (–C–O–C–)**
P4	1250	1290	**ν (C–O)**	**epoxy (–C–O–C–)**
P5	1320	1360	**δ/β (O–H or C–OH)**	**OH from alcohol**
P6	1430	1450	**δ_{as}/γ (C–H)**	**C-C sp^3**
P7	1450	1530	**ν (C=C)**	**C=C sp^2**
P8	1580	1610	**ν (C=C)**	**C=C**
P9	1630	1660	**ν (C=C)**	**C=C**
P10	1705	1715	**ν (C=O)**	**Ketones or –COOH**
P11	1760	1790	ν (C=O)	**Aldehyde (–CH=O)**

Raman spectroscopy was employed to analyse ZTC (Zeolite-templated carbon) samples, with the primary goal of examining vibrational modes and identifying key bands, specifically the D and G bands which are indicative of structural and bonding characteristics. The investigation employed a DXR TM 3xi Raman Imaging Microscope from Thermo Scientific, equipped with a 900 lines/mm diffraction grating.

7.2.1 Characterization results.

XRD patterns of ZTC samples and BEA parent zeolite are shown in **Figure 76** to make comparisons. BEA_X and BEA_XX patterns have been already discussed in **Chapter 3 (Paragraph 4.2.1)**. ZTCs exhibited two peaks around 2θ =7° and 2θ =15° in the same position as the main peaks of Na-Bea zeolite which correspond to the crystal planes of (201) and (202) respectively [214]. The presence of graphite, usually related to a peak around 2θ=26, can be

denied. No peaks related to MFI structure of Silicalite-1 was detected for ZTC_X and ZTC_XX samples. The layer of Silicalite-1 grown over the BEA surface was very thin and peaks related to MFI structure were not very intense even in Bea@Silicalite-1 starting zeolites (see Chapter 4, paragraph 4.2.1). Therefore, if any characteristic peak of Silicalite-1 was preserved, it might overlap with those of BEA.

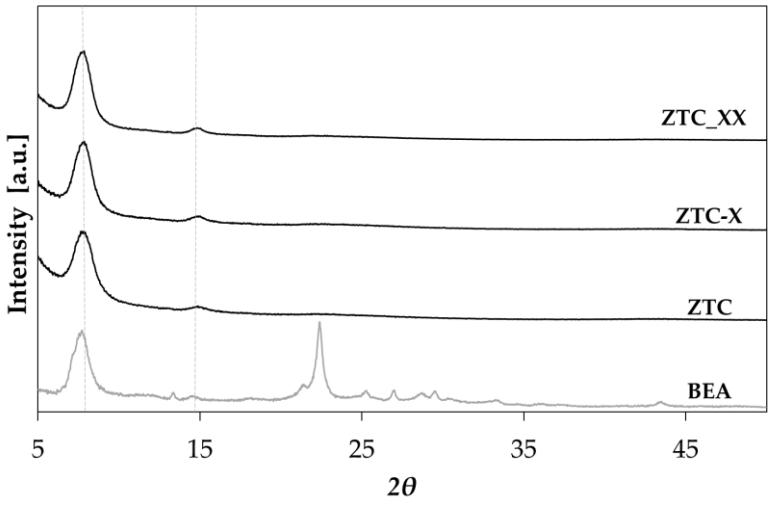

Figure 76: XRD patterns of BEA zeolite and ZTC samples.

N_2 adsorption isotherms of ZTCs are shown in **Figure 77**. Each sample exhibited the typical I/IV isotherm of micro-mesoporous materials. The high quantity of N_2 adsorbed for values of P/P0 < 0.1 suggested the high quantity of micropores contained in the materials. BET surface area, micropore area, and volume values have been evaluated and summarized in **Table 28**. BET surface area decreased when BEA_X and BEA_XX were employed as scaffolds if compared with ZTC obtained starting from the parent BEA zeolite. Conversely, micropore volume and micropore area showed an increasing trend. The ratio between micropore area and total surface area was also calculated and shown in **Table 28**. This ratio also increased for ZTC_X and ZTC_XX samples.

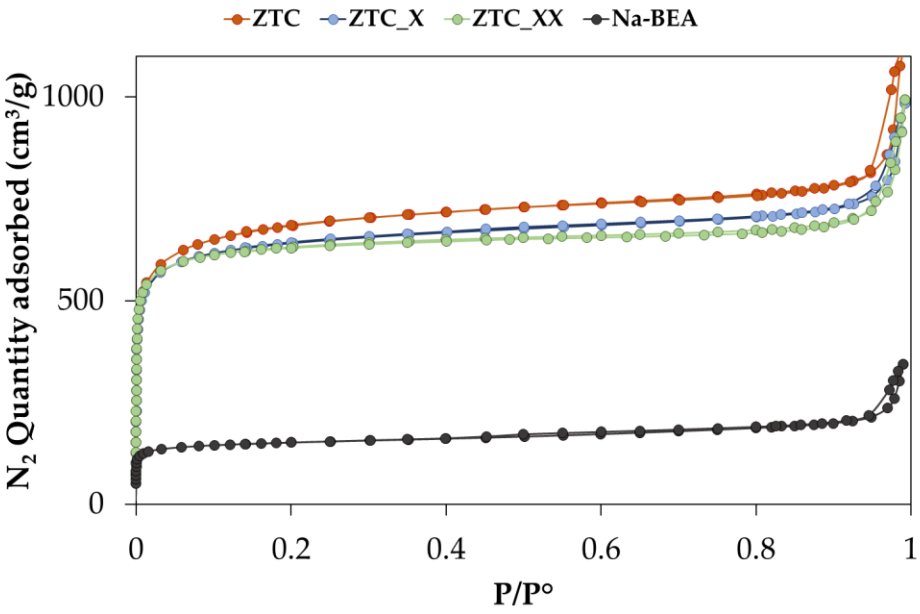

Figure 77: N_2 adsorption/desorption isotherms

Table 28: Porosimetric results.

Sample	B.E.T.[a] (m^2/g)	Micropore Area[b] (m^2/g)	Micropore Volume[b] (cm^3/g)	Micropore area/B.E.T.
ZTC	2334	1595	0.73	0.68
ZTC_X	2176	1639	0.75	0.75
ZTC_XX	2132	1712	0.79	0.80

[a] *calculated by the multipoint BET method in the Rouquerol p/p0 range;*

[b] *calculated by the t-plot method;*

In **Figure 78**, SEM micrographs of ZTC samples are shown. Each ZTC exhibited the same morphology as the starting BEA zeolite. However, as noted for the BEA@Silicalite-1 zeolites, the low presence of Silicalite-1 made it challenging to discern two distinct phases.

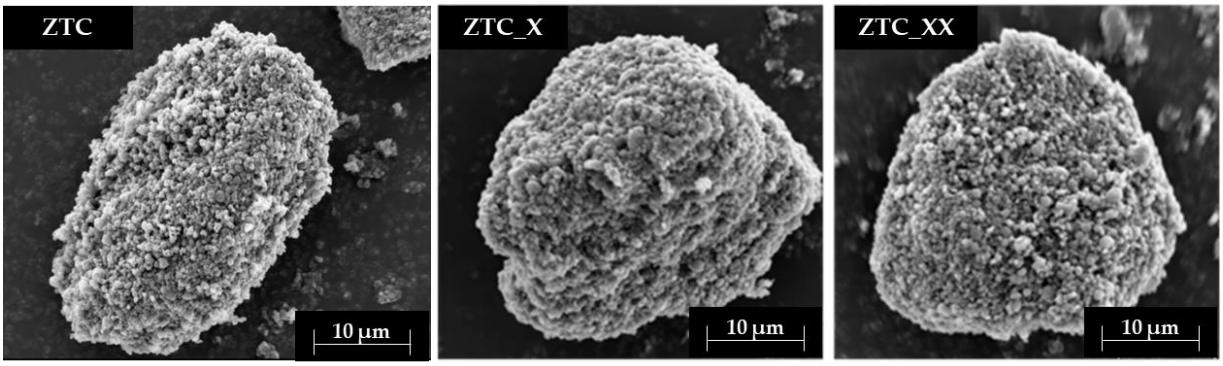

Figure 78: SEM micrographs of ZTCs samples.

N_2-DTG profiles are also shown in **Figure 79** to underline some differences between the ZTC reference sample and ZTC_X and ZTC_XX. DTG profiles give information about various types of oxygenated functional groups present in ZTC samples. For the ZTC reference sample, two broad peaks were detected at around 270°C and 330°C attributed to the presence of acids or anhydrides [215]. Moreover, a symmetrical but wide peak between 500°C and 800°C was detected. This peak probably indicated the overlap of various peaks linked to different functional groups such as lactones (450°C-500°C) or ethers and phenols (500-800°C). ZTC_X sample exhibited the presence of another peak at 430°C probably due to the higher presence of acid anhydride on the ZTC external surface. Instead, peaks at 330°C and 430°C were not detected in the ZTC_XX DTG profile. Both ZTC_X and ZTC_XX showed the presence of a shoulder at 570°C relater to a higher presence of lactones functional groups. N_2-DTG results demonstrated that the different matrix used in the synthesis influences the functional groups of the final material.

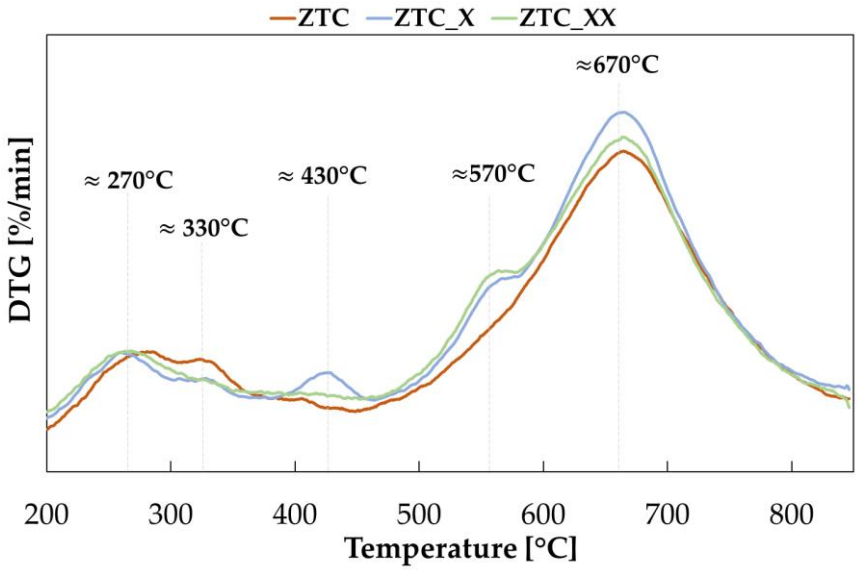

Figure 79: DTG profiles of investigated samples.

In **Figure 80**, FT-IR spectra of analyzed samples are shown in the range 500-3500 cm^{-1}.

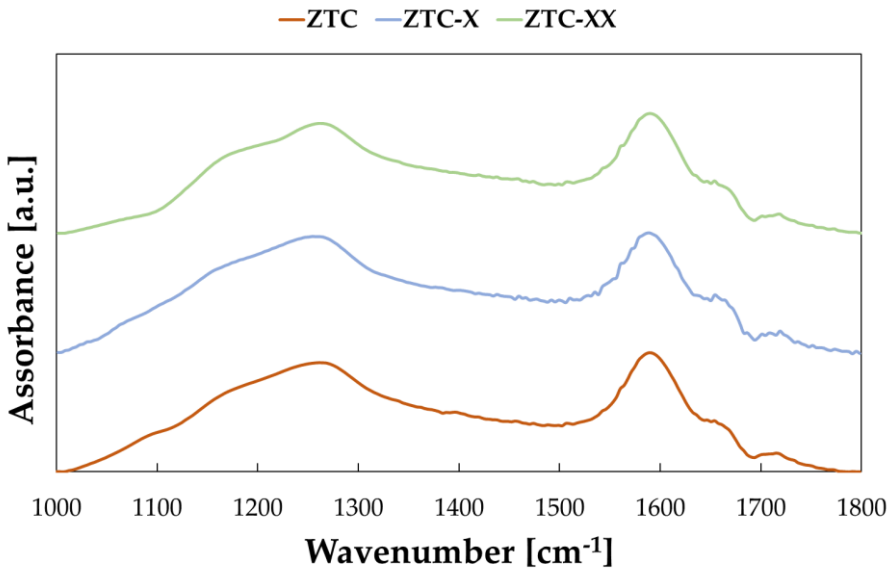

Figure 80: FT-IR spectra in 1000-1800 cm^{-1} region

Instead, in **Figure 81** deconvolutions made in the range 1000-1800 cm^{-1} are reported to obtain a semiquantitative analysis of the amount of carbon-oxygen functional groups present in the materials. Particular, areas related to the C=O bond (1755 and 1718 cm^{-1}), C=C (1645 and 1590 cm^{-1}), and the overlapping of the C-O-R bond (1279, 1200, and 1123 cm^{-1}) have been

evaluated. Then the ratios C-O-R/C=C and C=O/C=C were calculated, and the results are summarized in **Table 29**. A decrease in the C-O-R/C=C ratio between ZTC parent and ZTC_X and ZTC_XX samples was found while the C=O/C=C ratio remained almost unchanged.

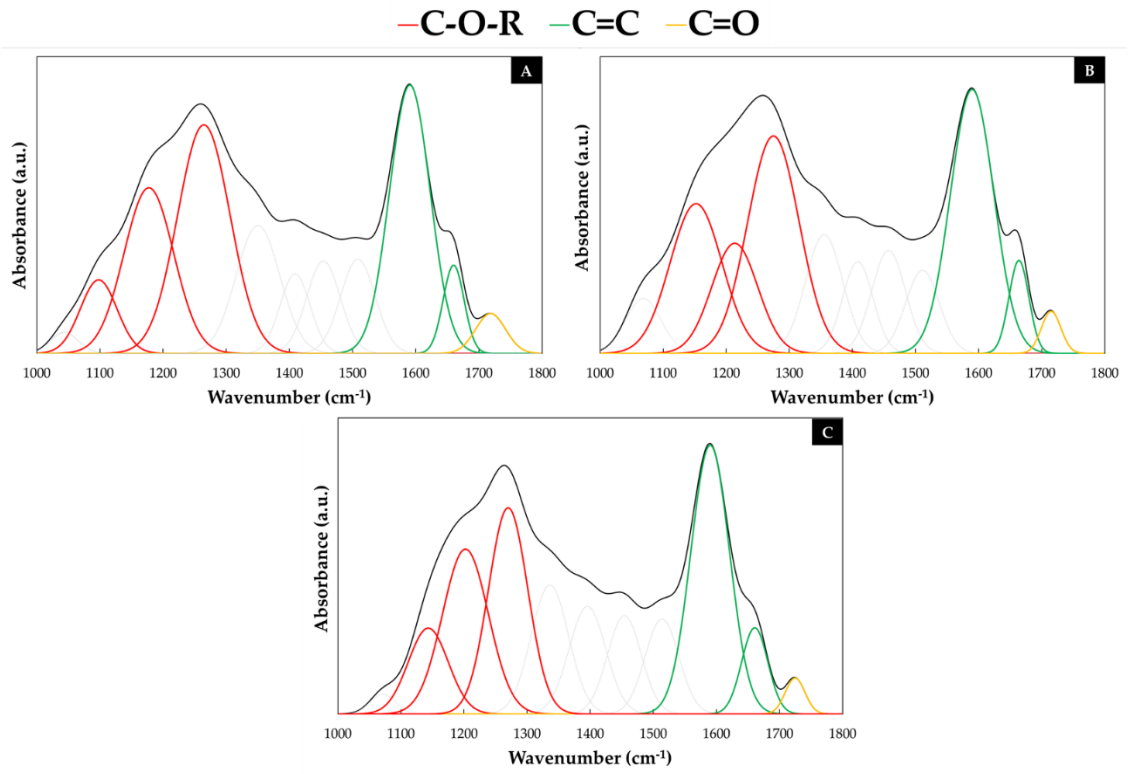

Figure 81: FT-IR deconvolution of A) ZTC parent, B) ZTC_X, and C) ZTC_XX.

Raman spectra obtained for the three samples (**Figure 82**) exhibited the two characteristic bands of carbon materials: the first one around 1600 cm^{-1} referred to the vibrational E2g mode observed in graphene-like structures of sp^2 bonded carbons (G band) and the second one around 1360 cm^{-1} related to framework disorder (D band) [216,217].

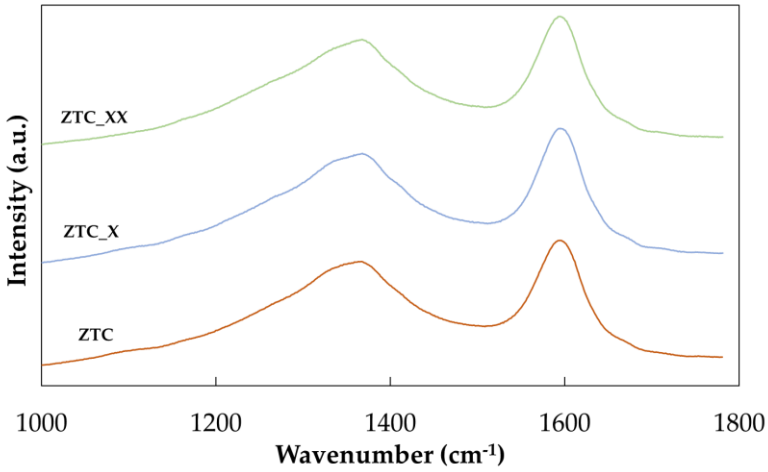

Figure 82: Raman spectra of investigated ZTCs.

Deconvolution of spectra has been carried out (**Figure 83**) and allowed identification of three additional Lorentzian curves: D′ (≈ 1610 cm^{-1}) characteristic of "graphene-like" layers or sp^2 nanostructures, D″ (≈ 1480 cm^{-1}) which intensity is inversely proportional to sample crystallinity, D* (≈ 1290 cm^{-1}) which represents the vibration of carbon sp^3 restricted by oxygen-containing groups [218].

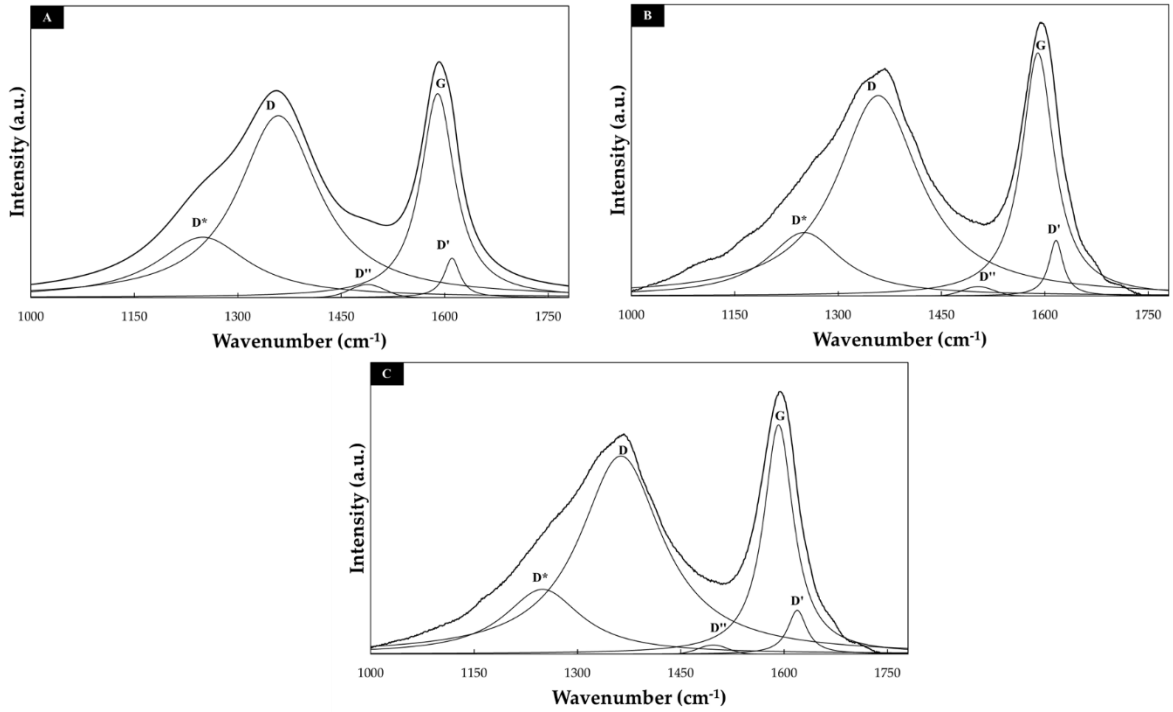

Figure 83: Raman peak deconvolution of A) ZTC parent, B) ZTC_X, and C) ZTC_XX.

Results obtained are summarized in **Table 29** as the ratios between D bands and G band intensity. In fact, in other works already published in literature it was demonstrated that the I_D/I_G ratio indicates structure ordering/disordering, $I_{D''}/I_G$ refers to crystallinity recovery from the amorphous phase, I_{D^*}/I_G is related to structure defectivity, and $I_{D'}/I_G$ is an index of the presence of sp^2 carbons [219].

A gradual decrease of I_D/I_G was detected with the increase of Silicalite-1 layers over the surface of the starting BEA matrix. This decrease could be related to an increase in the structural order of the material due to the "gate effect" promoted by Sicalite-1 coating over the BEA surface. Moreover, the $I_{D'}/I_G$ ratio increased for the ZTC_X sample and decreased again for the ZTC_XX sample. The increase of this ratio indicated a corresponding increase of sample defectivity probably due to the incomplete crystallization of Silicalite-1 after the first deposition cycle over the BEA zeolite. The decreasing trend found for $I_{D''}/I_G$ also demonstrated a reduction of the amorphous phase in ZTC samples obtained starting from a BEA@Silicalite-1 matrix.

Table 29: FT-IR and Raman data obtained.

ZTC Sample	FT-IR area ratio		Raman intensity ratio			
	C-O-R/C=C	C=O/C=C	I_D/I_G	$I_{D''}/I_G$	I_{D^*}/I_G	$I_{D'}/I_G$
ZTC	1.81 ± 0.01	0.08 ± 0.01	0.89	0.06	0.30	0.19
ZTC_X	1.76 ± 0.07	0.07 ± 0.01	0.87	0.04	0.26	0.23
ZTC_XX	1.55 ± 0.02	0.07 ± 0.01	0.83	0.04	0.26	0.19

7.3 CO_2 adsorption on ZTCs.

CO_2 adsorption/desorption measurements were conducted using a customized Sievert-type apparatus known as the f-PcT (volumetric) employing ZTC, ZTC_X, and ZTC_XX samples.

CO_2 isotherms were carried out for three temperature values (5°C, 25°C, and 40°C) in a pressure range between 0-15 bar. Moreover, after the third deposition cycle, ZTCs employed were treated at 200°C for 12 hours to remove CO_2 reversibly adsorbed. After this treatment, the three deposition cycles were repeated. **Figure 84** shows CO_2 isotherms obtained by testing each ZTC sample at each temperature investigated. As it is possible to observe CO_2 uptake increased with the increasing of pressure. Contrariwise, the increasing of temperature hurt ZTC performances in terms of CO_2 adsorbed.

No evident differences between CO_2 isotherms obtained before and after the treatment at 200°C were detected for each ZTC employed.

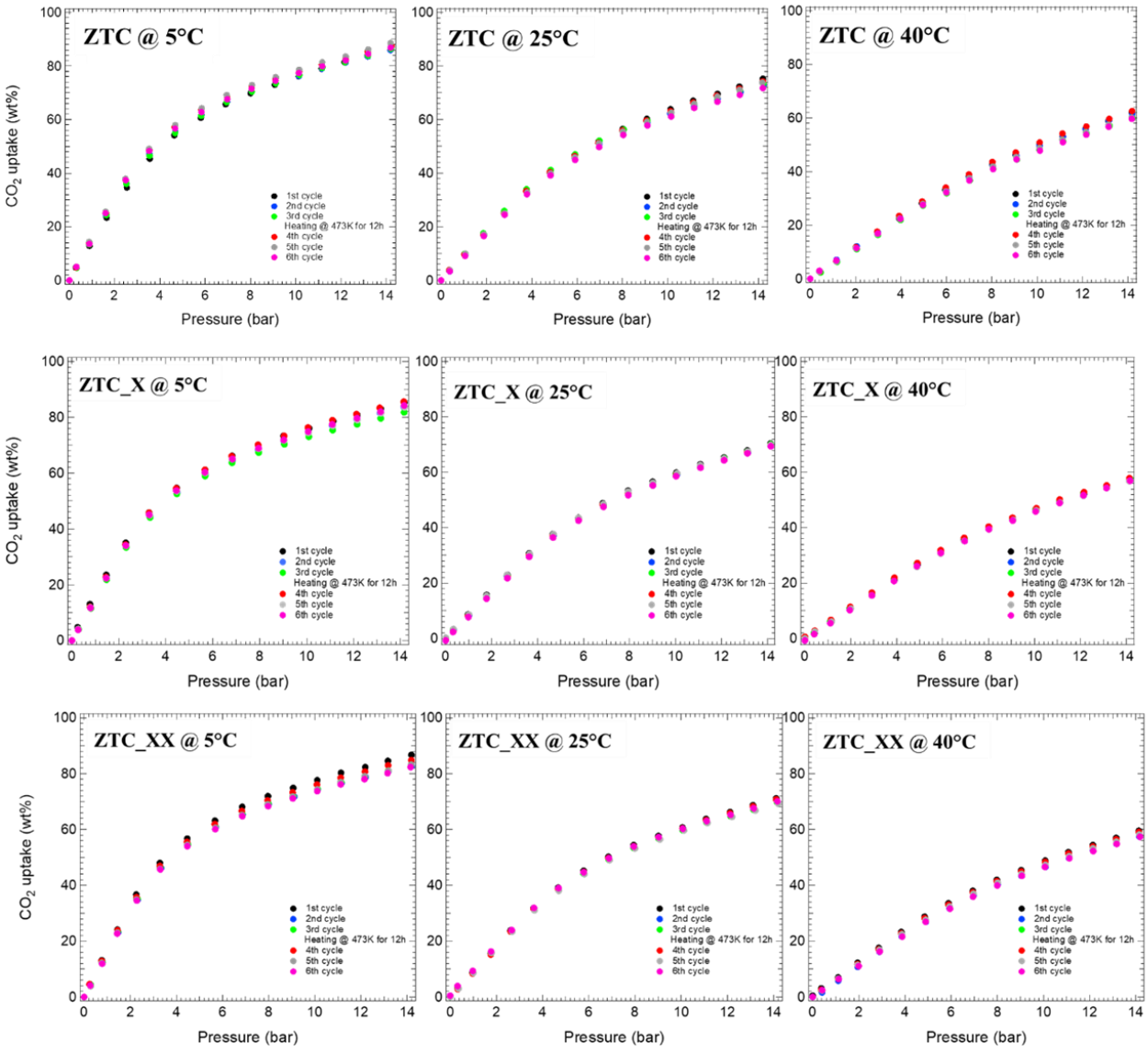

Figure 84: CO_2 multiple adsorption isotherms obtained employing ZTCs at different temperatures and in a pressure range of 0-15 bar.

In **Table 30**, the maximum value of CO_2 uptake (P=15 bar) is reported (in terms of percentage and of mmol of CO_2 per gram of ZTC) for each sample and the three investigated temperatures. As it is possible to observe, no evident differences were found between tested ZTC. Results obtained appear promising if compared with other carbon-based materials already tested in CO_2 adsorption such as graphene oxide [220].

Table 30: Maximum CO_2 uptake reached employing ZTCs.

Sample	5 °C		25°C		40°C	
	CO_2 uptake (wt%)	CO_2 uptake (mmol/g)	CO_2 uptake (wt%)	CO_2 uptake (mmol/g)	CO_2 uptake (wt%)	CO_2 uptake (mmol/g)
ZTC	89.8	20.41	87.8	19.95	59.3	13.41
ZTC_X	78.3	17.79	69.2	15.72	43.3	11.20
ZTC_XX	89.5	20.84	79.4	16.45	60	13.73

To fully characterize ZTCs behavior in CO_2 adsorption, adsorption enthalpy was estimated. After a fitting done employing the Toth Method, low-pressure values, around CO_2 uptake of 0.0011% were identified and employed to obtain a curve ln (P) versus 1/T. Finally, the Clausius-Clapeyron equation was employed to calculate the adsorption enthalpy. The results obtained are shown in **Figure 85**. Adsorption enthalpy increased from a value of 25.6 kJ/mol of the ZTC parent sample to 31.4 kJ/mol of the ZTC_X and ZTC_XX samples. Since adsorption enthalpy provides information about the interaction between CO_2 and the surface of carbon materials, it is possible to conclude that ZTC_X and ZTC_XX exhibited a higher affinity with carbon dioxide. This finding could be related to the presence of Silicalite-1 grown over the surface of the starting BEA zeolites that allows to obtain of a more ordered material.

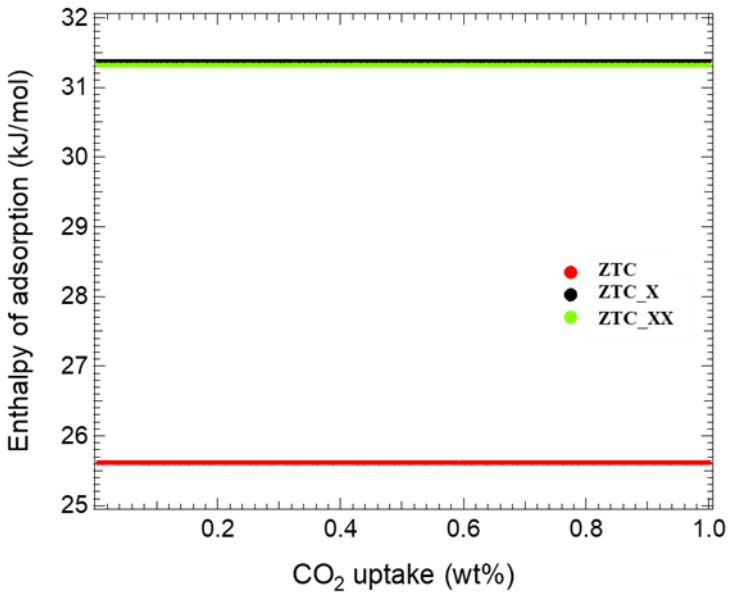

Figure 85: Enthalpy of adsorption calculated for ZTCs investigated.

7.4 Conclusions.

In this part of the research work, BEA parent zeolite and BEA@Silicalite-1 composite materials have been employed as matrices to synthesize ZTC samples. In particular, the "gate effect" due to the narrower pores of the Silicalite-1 layer coating the BEA surface on ZTCs final properties has been evaluated. FT-IR measurements demonstrated that ZTCs synthesized starting from BEA@Silicalite-1 samples were characterized by a lower number of C=O groups compared with ZTC parent. Moreover, Raman spectroscopy revealed that ZTC_XX was characterized by a higher structural order and a lower amorphous phase if compared to ZTC synthesized starting from BEA zeolite. No evident differences were found between ZTCs performances in terms of CO_2 adsorption although adsorption enthalpy calculated for ZTC_X and ZTC_XX was significantly higher than that obtained for ZTC sample demonstrating their better affinity with carbon dioxide.

Conclusions

This PhD work aimed to study different techniques of passivation of external acidity of zeolites with particular attention versus the epitaxial growth of Silicalite-1. The fundamental goal was not only to apply procedures already employed in the literature but also to try to optimize the technique. Moreover, the effect of the passivation of external acidity of zeolite catalysts over their properties and over their behavior in different applications was assessed. A summary of the main results is reported below.

The study of acid sites distribution and location within zeolites framework represents a topic of great interest among researchers. The presence of acid sites within the channels of zeolitic structures allows for the catalysis of reactions, leveraging the inherent feature of shape selectivity. On the other hand, acidic sites located on the external surface of zeolites can hinder the utilization of this property. Thus, a reduction in selectivity towards the desired products may be associated with the lack of shape selectivity at external acid sites. Acidic sites on the outer surface of zeolites could also lead to significant coke production during catalytic processes. For these reasons, various techniques have been proposed to neutralize acid sites located on the external surface of zeolites. Among these, chemical liquid and vapour deposition of TEOS have been widely used; Moreover, other techniques such as post-synthetic treatments with HNO_3 or with NaOH, deposition of MgO, or impregnation with phosphorus have also been investigated. The synthesis of zeolitic core-shell type catalysts characterized by an acidic core and an aluminium-free shell of Silicalite-1 represents an interesting alternative to neutralize external acid sites and this technique has been employed and improved in this PhD thesis. Among the methods used to grow the shell of Silicalite-1 over the surface of a starting zeolite, hydrothermal synthesis, and steam-assisted crystallization have been deeply described and then employed for the synthesis of catalysts employed in this work.

In this work, parent zeolites with different structures have been synthesized (MFI and BEA). Particularly, ZSM-5 zeolites with different Si/Al ratios (i.e. 11, 25, and 50) have been

prepared and employed for the following passivation treatments. To challenge the technique, a ZSM-5 with a low Si/Al ratio (equal to 11) was employed in acidic form as the core for the following coating with Silicalite-1. Then, the passivation technique has been improved and the idea of coating a ZSM-5 zeolite (with a Si/Al ratio equal to 25) both in as-made form and in H^+-form has been pursued; in the literature, zeolites are commonly coated with empty pores and the decision to change this aspect has been made to set the effect of the presence of structure directing agent (SDA) on the properties of the obtained ZSM-5@Silicalite-1 samples trying to avoid the blockage of the pores of the starting core due to the growth of Silicalite-1 crystals. To study the effect of the acid sites distribution of the starting-to-be-covered zeolite on the success of passivation treatment, a ZSM-5 zeolite with a Si/Al ratio equal to 50 was also employed and coated with Silicalite-1. Chemical vapour deposition of TEOS was also performed on ZSM-5 zeolites (with Si/Al ratio equal to 11 and 25) to highlight specific features of different passivation techniques. Finally, BEA@Silicalite-1 composite materials have been synthesized employing an innovative steam-assisted crystallization technique (SAC). All of the investigated catalysts were characterized by XRD, SEM-EDX, TEM, TG/DTA, chemical analysis by atomic absorption, textural analyses (B.E.T surface area, micropore volume) by nitrogen adsorption isotherm, and acidity analyses by NH_3-TPD (acid sites concentration, distribution and strength) and FT-IR (Brønsted and Lewis acid sites).

XRD patterns demonstrated the high crystallinity and purity of catalysts also after the passivation treatments. In the case of BEA@Silicalite-1 XRD analysis highlighted the presence of both BEA and MFI frameworks. EDX measurement conducted at 5kV allowed us to obtain an estimation of the superficial Si/Al ratio of samples before and after the coating with Silicalite-1. Particularly, EDX measurements proved the growth of Silicalite-1 over the surface of the starting zeolites showing a decrease of aluminium content on the surface of coated catalysts. Moreover, TEM micrography showed the presence of an ordered microporous layer of Silicalite-1 over the surface of the starting zeolite. A particular discussion was dedicated to the physical properties of catalysts calculated through the analysis of N_2 adsorption/desorption isotherms. Results obtained, in terms of BET surface

area, micropore area, and volume, revealed that coating a core with the structure directing agent still inside the pores allowed to preserve of the properties of the starting zeolite without blocking the pores. Porosimetric data obtained for ZSM-5 zeolites passivated via CLD of TEOS showed a slight decrease of BET surface area and micropore volume probably due to a partial blockage of the pores due to the deposition of a thin amorphous silica layer during the silylation. NH_3-TPD and FT-IR analyses were employed to study the effect of passivation treatments over the number, strength, and distribution of acid sites. NH_3-TPD results revealed that the coating with Silicalite-1 allowed to decrease in the total number of acid sites not influencing their strength. FT-IR analyses conducted employing d_3-acetonitrile as a probe demonstrated that the epitaxial growth of Silicalite-1 over the surface of ZSM-5 zeolites caused a preferential decrease of Lewis acid sites especially when the core was coated in as-made form. On the contrary, ZSM-5 zeolite passivated via CLD of TEOS exhibited a strong reduction of both Bronsted and Lewis acid sites probably caused by a partial occlusion of the pores with prevented the probe from reaching all the acidic sites. A decrease of both Bronsted and Lewis acid sites was detected for BEA@Silicalite-1 samples if compared with the nude core of BEA zeolite.

ZSM-5@Slicalite-1 and parent ZSM-5 zeolites were tested as catalysts in the reaction of methanol dehydration to DME. The sample obtained coating ZSM-5 core (Z11) with a Silicalite-1 layer (H-Z11_X) exhibited the worst catalytic performances resulting in decreased methanol conversion, DME selectivity, and increased coke deposition compared to the uncoated ZSM-5. The drop in performance was linked to the formation of an amorphous layer from the first Silicalite-1 coating. However, adding a second Silicalite-1 layer (H-Z11_XX) improved selectivity for DME and reduced coke formation. Also, ZSM-5 zeolite with a Si/Al ratio equal to 25 (Z25) and passivated samples obtained coating the parent zeolite both in as-made (AS-Z25) and acidic form (H-Z25) have been tested. Catalytic tests results showed that the AS-Z25 samples performed similarly to the parent zeolite in terms of methanol conversion and DME selectivity, but with less coke formation and slower deactivation. The H-Z25_X sample (obtained coating once the core in acidic form) exhibited the worst performance due to its textural properties, while the H-Z25_XX (obtained coating

twice the core in acidic form) sample performed similarly to the AS-Z25 catalysts, indicating the effectiveness of the novel passivation technique, enhancing catalyst stability and performance.

The influence of acidity and the effect of surface passivation treatments on the conversion of DME to olefins have also been assessed employing ZSM-5 zeolites with Si/Al ratios equal to 25 (Z25) and 50 (Z50) and the passivated samples obtained via epitaxial growth technique of one or two layers of Silicalite-1. The catalysts were evaluated for DME to olefins conversion over 14 hours in a temperature range of 300°C-375°C. Results showed high selectivity (>60%) for light olefins (ethylene, propylene, and butenes) across all temperatures. Methanol, a byproduct of DME hydration, was also detected, especially at lower temperatures and as the catalysts began to deactivate. Propylene was consistently the most produced olefin, supporting the theory that the alkene-based cycle predominates in MFI zeolite-catalysed MTO or DTO processes. The synthesized ZSM-5 zeolites demonstrated higher DME conversion rates than other catalysts, like SAPO-34. Coating the ZSM-5 zeolite (Si/Al=25) with Silicalite-1 improved its stability at higher temperatures and reduced coke formation at 375°C compared to the uncoated Z25. This suggests that deactivation at high temperatures is mainly due to heavy coke formation blocking zeolite pores. The Z50 sample, with lower acidity, showed greater stability at high temperatures but lower initial activity and higher methanol production, particularly at 300°C and 325°C. The passivation did not enhance the catalytic performance of the Z50 in terms of stability and coke formation, unlike its effects on the Z25 zeolite.

As a final application of the passivation technique, BEA parent zeolite and BEA@Silicalite-1 composite materials were used as bases for synthesizing Zeolite Templated Carbons (ZTCs). The study particularly focused on investigating the "gate effect" created by the Silicalite-1 layer's narrower pores on the properties of the ZTCs. FT-IR analysis showed that ZTCs made from BEA@Silicalite-1 composites had fewer C=O (carbonyl) groups than those derived directly from BEA zeolite, indicating a chemical composition difference. Raman spectroscopy results indicated that ZTCs developed from BEA@Silicalite-1 had a higher structural order and contained less amorphous phase compared to ZTCs synthesized from

BEA zeolite alone. Despite these differences in chemical composition and structural order, no significant differences were observed in the CO_2 adsorption performance of the ZTCs. However, the adsorption enthalpy for ZTCs obtained from BEA@Silicalite-1 matrices was notably higher than that of the ZTC parent sample, suggesting their better affinity for carbon dioxide.

As a summary, the results discussed in this PhD thesis show how surface passivation is an effective way to improve the performance of zeolitic catalysts in different applications. Particularly, the growth of a layer of Silicalite-1 on the external surface of a starting core is a method that has proven effective not only for neutralizing the external acidic sites but also for preserving the properties of the starting zeolite. This technique, which still attracts a lot of attention from researchers, can be even more deeply studied and employed in numerous different applications. The effect of the ratio between the Silicalite-1 layer and the starting core could be extensively investigated as well as the effect of the crystallization time used for the growth of Silicalite-1 crystals. Moreover, a layer of Silicalite-1 could be useful in the synthesis of hybrid catalysts to separate the two catalytic functions and overcome problems due to the interaction between metallic and acidic phases which represents one of the most frequent catalyst deactivation causes.

Future perspectives

The passivation of the external acidity of zeolites and, more generally, the synthesis of composite zeolitic materials opens the way towards challenging and interesting study opportunities for those aspects which are still to be deeply covered:

- First of all, several aspects regarding the deposition of the Silicalite-1 layer can still be investigated, including the crystallization time employed for hydrothermal synthesis. Besides, the effect of the ratio between the amount of zeolite to be coated and the Silicalite-1 gel used needs to be further examined. But also the synthesis of composite zeolitic materials composed of a core and a shell with different frameworks (for example MFI and BEA or FER and MFI) could open a new application field. Steam-assisted crystallization (SAC) could also be used for the synthesis of ZSM-5@Silicalite-1 catalysts and results reached in terms of properties compared with samples obtained by epitaxial growth of Silicalite-1.
- Catalysts treated via chemical liquid deposition of TEOS need to be tested in catalytic applications such as methanol dehydration to DME or DME to olefins to highlight differences between the catalytic behaviour of passivated samples obtained employing different techniques.
- Further acidity investigations are needed to be employed to fully characterise passivated catalysts. FT-IR measurements with different probes having proper kinetic diameter must be used to quantify external acidity and to better assess the effect of passivation treatments in terms of BAS and LAS distribution.
- Finally, following the examples of metal supporting-core passivation, the growth of Silicalite-1 could be employed in the synthesis of hybrid catalysts for CO_2 directly hydrogenation to DME. Particularly, research activities have been started for the synthesis of an innovative hybrid catalyst characterized by a metallic Cu-based core and an acidic zeolitic shell separated by a layer of Silicalite-1. Moreover, hybrid catalysts will also be synthesised employing mesoporous supports (such as MSM-41)

containing the metallic phase coated with Silicalite-1 and subsequently employed as the core for the growth of the zeolitic ZSM-5 phase.

References

[1] N. Masoumifard, R. Guillet-Nicolas, F. Kleitz, Synthesis of Engineered Zeolitic Materials: From Classical Zeolites to Hierarchical Core–Shell Materials, Advanced Materials 30 (2018) 1–40. https://doi.org/10.1002/adma.201704439.

[2] I.K. J. B. Nagy, P. Bodart, I. Hannus, Synthesis, characterization and use of zeolitic microporous materials, DecaGen Ltd., 1998.

[3] K.E. Hamilton, E.N. Coker, A. Sacco, A.G. Dixon, R.W. Thompson, The effects of the silica source on the crystallization of zeolite NaX, Zeolites 13 (1993) 645–653. https://doi.org/10.1016/0144-2449(93)90137-R.

[4] F. Testa, L. Pasqua, F. Crea, R. Aiello, K. Lázár, P. Fejes, P. Lentz, J.B. Nagy, Synthesis of Fe-MFI zeolites in fluoride-containing media, Microporous and Mesoporous Materials 57 (2003) 57–72. https://doi.org/10.1016/S1387-1811(02)00480-8.

[5] Z. Gabelica, N. Blom, E.G. Derouane, Synthesis and characterization of zsm-5 type zeolites III. A critical evaluation of the role of alkali and ammonium cations, Appl Catal 5 (1983) 227–248. https://doi.org/10.1016/0166-9834(83)80135-3.

[6] V. Valtchev, L. Tosheva, Porous Nanosized Particles: Preparation, Properties, and Applications, Chemical Reviews (2013) 6734–6760. https://doi.org/10.1021/cr300439k.

[7] G.T. Kokotailo, S.L. Lawton, D.H. Olson, W.M. Meier, Structure of synthetic zeolite ZSM-5, Nature 272 (1978) 437–438. https://doi.org/10.1038/272437a0.

[8] B. Bensafi, N. Chouat, F. Djafri, The universal zeolite ZSM-5: Structure and synthesis strategies. A review, Coord Chem Rev 496 (2023). https://doi.org/10.1016/j.ccr.2023.215397.

[9] J. Wan, Y. Wei, Z. Liu, B. Li, Y. Qi, M. Li, P. Xie, S. Meng, Y. He, F. Chang, A ZSM-5-based catalyst for efficient production of light olefins and aromatics from fluidized-bed naphtha catalytic cracking, Catal Letters 124 (2008) 150–156. https://doi.org/10.1007/s10562-008-9445-1.

[10] D.J. Collins, B.H. Davis, Xylene isomerization, Zeolites 8 (1988) 341. https://doi.org/10.1016/s0144-2449(88)80145-3.

[11] N. Viswanadham, A.R. Pradhan, N. Ray, S.C. Vishnoi, U. Shanker, T.S.R. Prasada Rao, Reaction pathways for the aromatization of paraffins in the presence of H-ZSM-5 and Zn/H-ZSM-5, Appl Catal A Gen 137 (1996) 225–233. https://doi.org/10.1016/0926-860X(95)00287-1.

[12] M. Zhang, S. Xu, Y. Wei, J. Li, J. Wang, W. Zhang, S. Gao, Z. Liu, Changing the balance of the MTO reaction dual-cycle mechanism: Reactions over ZSM-5 with varying contact times, Cuihua Xuebao/Chinese Journal of Catalysis 37 (2016) 1413–1422. https://doi.org/10.1016/S1872-2067(16)62466-X.

[13] S.K. Matam, A.J. O'Malley, C.R.A. Catlow, Suwardiyanto, P. Collier, A.P. Hawkins, A. Zachariou, D. Lennon, I. Silverwood, S.F. Parker, R.F. Howe, The effects of MTG catalysis on

methanol mobility in ZSM-5, Catal Sci Technol 8 (2018) 3304–3312. https://doi.org/10.1039/c8cy00422f.

[14] M. Tong, D. Zhang, L. Zhu, J. Xu, F. Deng, R. Xu, W. Yan, An elaborate structure investigation of the chiral polymorph A-enriched zeolite beta, CrystEngComm 18 (2016) 1782–1789. https://doi.org/10.1039/c6ce00043f.

[15] T. Lu, W. Yan, R. Xu, Chiral zeolite beta: Structure, synthesis, and application, Inorg Chem Front 6 (2019) 1938–1951. https://doi.org/10.1039/c9qi00574a.

[16] L. Hong, J. Zang, B. Li, G. Liu, Y. Wang, L. Wu, Research Progress on the Synthesis of Nanosized and Hierarchical Beta Zeolites, Inorganics (Basel) 11 (2023). https://doi.org/10.3390/inorganics11050214.

[17] G.S. Nivarthy, K. Seshan, J.A. Lercher, The influence of acidity on zeolite H-BEA catalyzed isobutane/n-butene alkylation, Microporous and Mesoporous Materials 22 (1998) 379–388. https://doi.org/10.1016/S1387-1811(98)00092-4.

[18] S.F. Rastegar, G. Sadovska, R. Pilar, J. Moravkova, D. Kaucky, L. Brabec, J. Pastvova, P. Sazama, Analysis of decisive structural parameters of zeolites for alkylation of benzene with ethylene, Appl Catal A Gen 591 (2020) 117379. https://doi.org/10.1016/j.apcata.2019.117379.

[19] R. Nakao, Y. Kubota, N. Katada, N. Nishiyama, K. Kunimori, K. Tomishige, Performance and characterization of BEA catalysts for catalytic cracking, Appl Catal A Gen 273 (2004) 63–73. https://doi.org/10.1016/j.apcata.2004.06.013.

[20] M. Jendrlin, J. Grand, L. Lakiss, F. Dubray, P. Bazin, J. El Fallah, S. Mintova, V. Zholobenko, Environmental Applications of Zeolites: Hydrophobic Sn-BEA as a Selective Gas Sensor for Exhaust Fumes, Chemistry (Switzerland) 5 (2023) 334–347. https://doi.org/10.3390/chemistry5010025.

[21] B.N. Vasiljević, M. Obradović, D. Bajuk-Bogdanović, M. Milojević-Rakić, Z. Jovanović, N. Gavrilov, I. Holclajtner-Antunović, In situ synthesis of potassium tungstophosphate supported on BEA zeolite and perspective application for pesticide removal, J Environ Sci (China) 81 (2019) 136–147. https://doi.org/10.1016/j.jes.2019.01.018.

[22] Z. Yang, L. Zhang, Y. Zhou, H. Wang, L. Wen, E. Kianfar, Investigation of effective parameters on SAPO-34 nanocatalyst in the methanol-to-olefin conversion process: A review, Reviews in Inorganic Chemistry 40 (2020) 91–105. https://doi.org/10.1515/revic-2020-0003.

[23] T.C. Tsai, S. Bin Liu, I. Wang, Disproportionation and transalkylation of alkylbenzenes over zeolite catalysts, Appl Catal A Gen 181 (1999) 355–398. https://doi.org/10.1016/S0926-860X(98)00396-2.

[24] S.M. Csicsery, The cause of shape selectivity of transalkylation in mordenite, J Catal 23 (1971) 124–130. https://doi.org/10.1016/0021-9517(71)90032-7.

[25] R.C. Deka, Acidity in zeolites and their characterization by different spectroscopic methods, Indian Journal of Chemical Technology 5 (1998) 109–123.

[26] M. Boronat, A. Corma, Factors Controlling the Acidity of Zeolites, Catal Letters 145 (2015) 162–172. https://doi.org/10.1007/s10562-014-1438-7.

[27] E. Catizzone, G. Ferrarelli, P. Bruno, G. Giordano, M. Migliori, Simultaneous catalytic dehydration of methanol and ethanol: How ZSM-5 acidity addresses conversion and products distribution, Catal Today 427 (2024). https://doi.org/10.1016/j.cattod.2023.114436.

[28] E.G. Derouane, J.C. Védrine, R. Ramos Pinto, P.M. Borges, L. Costa, M.A.N.D.A. Lemos, F. Lemos, F. Ramôa Ribeiro, The acidity of zeolites: Concepts, measurements and relation to catalysis: A review on experimental and theoretical methods for the study of zeolite acidity, Catal Rev Sci Eng 55 (2013) 454–515. https://doi.org/10.1080/01614940.2013.822266.

[29] M. Ravi, V.L. Sushkevich, J.A. van Bokhoven, Towards a better understanding of Lewis acidic aluminium in zeolites, Nat Mater 19 (2020) 1047–1056. https://doi.org/10.1038/s41563-020-0751-3.

[30] N.O. Gonzales, A.T. Bell, A.K. Chakraborty, Density functional theory calculations of the effects of local composition and defect structure on the proton affinity of H-ZSM-5, Journal of Physical Chemistry B 101 (1997) 10058–10064. https://doi.org/10.1021/jp971449q.

[31] T. Montanari, M. Bevilacqua, G. Busca, Use of nitriles as probe molecules for the accessibility of the active sites and the detection of complex interactions in zeolites through IR spectroscopy, Appl Catal A Gen 307 (2006) 21–29. https://doi.org/10.1016/j.apcata.2006.03.003.

[32] T.K. Phung, G. Busca, On the Lewis acidity of protonic zeolites, Appl Catal A Gen 504 (2015) 151–157. https://doi.org/10.1016/j.apcata.2014.11.031.

[33] B. Wichterlová, N. Žilkova, E. Uvarova, J. Čejka, P. Sarv, C. Paganini, J.A. Lercher, Effect of Broensted and Lewis sites in ferrierites on skeletal isomerization of n-butenes, Appl Catal A Gen 182 (1999) 297–308. https://doi.org/10.1016/S0926-860X(99)00022-8.

[34] T. Ma, L. Zhang, Y. Song, Y. Shang, Y. Zhai, Y. Gong, A comparative synthesis of ZSM-5 with ethanol or TPABr template: Distinction of Brønsted/Lewis acidity ratio and its impact on: N -hexane cracking, Catal Sci Technol 8 (2018) 1923–1935. https://doi.org/10.1039/c7cy02418e.

[35] M. Elanany, M. Koyama, M. Kubo, E. Broclawik, A. Miyamoto, Periodic density functional investigation of Lewis acid sites in zeolites: Relative strength order as revealed from NH 3 adsorption, Appl Surf Sci 246 (2005) 96–101. https://doi.org/10.1016/j.apsusc.2004.10.052.

[36] E. Kusrini, N.M. Mualim, A. Rahman, A. Usman, Application of activated Na-zeolite a as a water softening agent to remove Ca2+and Mg2+ions from water, AIP Conf Proc 2255 (2020). https://doi.org/10.1063/5.0014314.

[37] Z. Zhang, Y. Sun, H. Zhang, L. Wei, Synthesis, Types, and Applications of Zeolite Capsule Catalysts, Crystal Research and Technology 58 (2023) 1–19. https://doi.org/10.1002/crat.202200287.

[38] A. Aloise, A. Marino, F. Dalena, G. Giorgianni, M. Migliori, L. Frusteri, C. Cannilla, G. Bonura, F. Frusteri, G. Giordano, Desilicated ZSM-5 zeolite: Catalytic performances assessment in methanol to DME dehydration, Microporous and Mesoporous Materials 302 (2020) 110198. https://doi.org/10.1016/j.micromeso.2020.110198.

[39] M. Migliori, A. Aloise, G. Giordano, Methanol to dimethylether on H-MFI catalyst: The influence of the Si/Al ratio on kinetic parameters, Catal Today 227 (2014) 138–143. https://doi.org/10.1016/j.cattod.2013.09.033.

[40] G. Giordano, M. Migliori, G. Ferrarelli, G. Giorgianni, F. Dalena, P. Peng, M. Debost, P. Boullay, Z. Liu, H. Guo, Z.F. Yan, S. Mintova, Passivated Surface of High Aluminum Containing ZSM-5 by Silicalite-1: Synthesis and Application in Dehydration Reaction, ACS Sustain Chem Eng 10 (2022) 4839–4848. https://doi.org/10.1021/acssuschemeng.1c07198.

[41] T.K. Phung, G. Busca, On the Lewis acidity of protonic zeolites, Appl Catal A Gen 504 (2015) 151–157. https://doi.org/10.1016/j.apcata.2014.11.031.

[42] T. Armaroli, M. Trombetta, A. Gutièrrez Alejandre, J.R. Solis, G. Busca, FTIR study of the interaction of some branched aliphatic molecules with the external and internal sites of H-ZSM5 zeolite, Physical Chemistry Chemical Physics 2 (2000) 3341–3348. https://doi.org/10.1039/b001807o.

[43] T. Armaroli, M. Bevilacqua, M. Trombetta, F. Milella, A.` Ida Gutiérrez Alejandre, J. Ramírez, B. Notari, R.J. Willey, G. Busca, A study of the external and internal sites of MFI-type zeolitic materials through the FT-IR investigation of the adsorption of nitriles, 2001.

[44] W. Wang, L. He, Q. Luo, L. Wang, J. Wang, H. Chen, Z. Miao, Q. Yao, M. Sun, Synthesis and application of core-shell, hollow, yolk-shell multifunctional structure zeolites, Microporous and Mesoporous Materials 362 (2023) 112766. https://doi.org/10.1016/j.micromeso.2023.112766.

[45] N. Masoumifard, R. Guillet-Nicolas, F. Kleitz, Synthesis of Engineered Zeolitic Materials: From Classical Zeolites to Hierarchical Core–Shell Materials, Advanced Materials 30 (2018) 1–40. https://doi.org/10.1002/adma.201704439.

[46] H. Li, P. Zhang, L. Guo, Y. He, Y. Zeng, M. Thongkam, J. Natakaranakul, T. Kojima, P. Reubroycharoen, T. Vitidsant, G. Yang, N. Tsubaki, A Well-Defined Core–Shell-Structured Capsule Catalyst for Direct Conversion of CO2 into Liquefied Petroleum Gas, ChemSusChem 13 (2020) 2060–2065. https://doi.org/10.1002/cssc.201903576.

[47] Y. Sun, X. Han, Z. Zhao, Direct coating copper-zinc-aluminum oxalate with H-ZSM-5 to fabricate a highly efficient capsule-structured bifunctional catalyst for dimethyl ether production from syngas, Catal Sci Technol 9 (2019) 3763–3770. https://doi.org/10.1039/c9cy00980a.

[48] C. Hu, H. Zhang, R. Xiao, Catalytic fast pyrolysis of biomass over core-shell HZSM-5@silicalite-1 in a bench-scale two-stage fluidized-bed/fixed-bed reactor, J Anal Appl Pyrolysis 136 (2018) 27–34. https://doi.org/10.1016/j.jaap.2018.11.005.

[49] G. Ferrarelli, G. Giordano, M. Migliori, ZSM-5@Sil-1 core shell: Effect of synthesis method over textural and catalytic properties, Catal Today 390–391 (2022) 176–184. https://doi.org/10.1016/j.cattod.2021.11.036.

[50] D. Van Vu, M. Miyamoto, N. Nishiyama, Y. Egashira, K. Ueyama, Morphology control of silicalite/HZSM-5 composite catalysts for the formation of para-xylene, Catal Letters 127 (2009) 233–238. https://doi.org/10.1007/s10562-008-9676-1.

[51] D. Van Vu, M. Miyamoto, N. Nishiyama, Y. Egashira, K. Ueyama, Selective formation of para-xylene over H-ZSM-5 coated with polycrystalline silicalite crystals, J Catal 243 (2006) 389–394. https://doi.org/10.1016/j.jcat.2006.07.028.

[52] D. Van Vu, M. Miyamoto, N. Nishiyama, S. Ichikawa, Y. Egashira, K. Ueyama, Catalytic activities and structures of silicalite-1/H-ZSM-5 zeolite composites, Microporous and Mesoporous Materials 115 (2008) 106–112. https://doi.org/10.1016/j.micromeso.2007.12.034.

[53] J. Zhang, L. Wang, B. Zhang, H. Zhao, U. Kolb, Y. Zhu, L. Liu, Y. Han, G. Wang, C. Wang, D.S. Su, B.C. Gates, F.S. Xiao, Sinter-resistant metal nanoparticle catalysts achieved by immobilization within zeolite crystals via seed-directed growth, Nat Catal 1 (2018) 540–546. https://doi.org/10.1038/s41929-018-0098-1.

[54] M. Javed, S. Cheng, G. Zhang, P. Dai, Y. Cao, C. Lu, R. Yang, C. Xing, S. Shan, Complete encapsulation of zeolite supported Co based core with silicalite-1 shell to achieve high gasoline selectivity in Fischer-Tropsch synthesis, Fuel 215 (2018) 226–231. https://doi.org/10.1016/j.fuel.2017.10.042.

[55] Z. Tian, C. Wang, Z. Si, Y. Wang, L. Chen, Q. Liu, Q. Zhang, Y. Xu, L. Ma, Product Distributions of Fischer-Tropsch Synthesis over Core-Shell Catalysts: The Effects of Diverse Shell Thickness, ChemistrySelect 3 (2018) 12415–12423. https://doi.org/10.1002/slct.201801515.

[56] G. Xu, X. Zhu, A core-shell structured Zn/SiO2@ZSM-5 catalyst: Preparation and enhanced catalytic properties in methane co-aromatization with propane, Appl Catal B 293 (2021) 120241. https://doi.org/10.1016/j.apcatb.2021.120241.

[57] P. Lu, Q. Chen, G. Yang, L. Tan, X. Feng, J. Yao, Y. Yoneyama, N. Tsubaki, Space-Confined Self-Regulation Mechanism from a Capsule Catalyst to Realize an Ethanol Direct Synthesis Strategy, ACS Catal 10 (2020) 1366–1374. https://doi.org/10.1021/acscatal.9b02891.

[58] Z. Zhang, Y. Sun, H. Zhang, L. Wei, Synthesis, Types, and Applications of Zeolite Capsule Catalysts, Crystal Research and Technology 58 (2023) 1–19. https://doi.org/10.1002/crat.202200287.

[59] K. Miyake, Y. Hirota, K. Ono, Y. Uchida, N. Nishiyama, Selective Production of Benzene, Toluene and p-Xylene (BTpX) from Various C1-3 Feedstocks over ZSM-5/Silicalite-1 Core-Shell Zeolite Catalyst, ChemistrySelect 1 (2016) 967–969. https://doi.org/10.1002/slct.201600172.

[60] B. Zhang, X. Liu, Catalytic performance of MFI/MFI core-shell zeolites in Benzene methylation, China Petroleum Processing and Petrochemical Technology 16 (2014) 94–99.

[61] T. Wang, Y. Xu, C. Shi, F. Jiang, B. Liu, X. Liu, Direct production of aromatics from syngas over a hybrid FeMn Fischer-Tropsch catalyst and HZSM-5 zeolite: Local environment effect and mechanism-directed tuning of the aromatic selectivity, Catal Sci Technol 9 (2019) 3933–3946. https://doi.org/10.1039/c9cy00750d.

[62] Z. Jin, S. Liu, L. Qin, Z. Liu, Y. Wang, Z. Xie, X. Wang, Methane dehydroaromatization by Mo-supported MFI-type zeolite with core-shell structure, Appl Catal A Gen 453 (2013) 295–301. https://doi.org/10.1016/j.apcata.2012.12.043.

[63] M. Miyamoto, K. Mabuchi, J. Kamada, Y. Hirota, Y. Oumi, N. Nishiyama, S. Uemiya, para-Selectivity of silicalite-1 coated MFI type galloaluminosilicate in aromatization of light alkanes, Journal of Porous Materials 22 (2015) 769–778. https://doi.org/10.1007/s10934-015-9950-8.

[64] Y.Q. Deng, W.F. Zhou, H.M. Lv, Y.Y. Zhang, C.T. Au, S.F. Yin, Synthesis of HZSM-5@silicalite-1 core-shell composite and its catalytic application in the generation of p-xylene by methylation of toluene with methyl bromide, RSC Adv 4 (2014) 37296–37301. https://doi.org/10.1039/c4ra04126g.

[65] F. Goodarzi, I.P. Herrero, G.N. Kalantzopoulos, S. Svelle, A. Lazzarini, P. Beato, U. Olsbye, S. Kegnæs, Synthesis of mesoporous ZSM-5 zeolite encapsulated in an ultrathin protective shell of silicalite-1 for MTH conversion, Microporous and Mesoporous Materials 292 (2020) 109730. https://doi.org/10.1016/j.micromeso.2019.109730.

[66] M. Kustova, M.S. Holm, C.H. Christensen, Y.H. Pan, P. Beato, T.V.W. Janssens, F. Joensen, J. Nerlov, Synthesis and characterization of mesoporous ZSM-5 core-shell particles for improved catalytic properties, Elsevier B.V., 2008. https://doi.org/10.1016/S0167-2991(08)80161-9.

[67] D. Chen, J. Wang, X. Ren, H. Teng, H. Gu, Silicalite-1 shell synthesized onto cylinder-shaped ZSM-5 extrudate for disproportionation of toluene into para-xylene, Catal Letters 136 (2010) 65–70. https://doi.org/10.1007/s10562-010-0309-0.

[68] C. Peng, Z. Liu, Y. Yonezawa, Y. Yanaba, N. Katada, I. Murayama, S. Segoshi, T. Okubo, T. Wakihara, Ultrafast post-synthesis treatment to prepare ZSM-5@Silicalite-1 as a core-shell structured zeolite catalyst, Microporous and Mesoporous Materials 277 (2019) 197–202. https://doi.org/10.1016/j.micromeso.2018.10.036.

[69] T. Du, H. Qu, Q. Liu, Q. Zhong, W. Ma, Synthesis, activity and hydrophobicity of Fe-ZSM-5 at silicalite-1 for NH3-SCR, Chemical Engineering Journal 262 (2015) 1199–1207. https://doi.org/10.1016/j.cej.2014.09.119.

[70] K. Miyake, R. Inoue, T. Miura, M. Nakai, H. Al-Jabri, Y. Hirota, Y. Uchida, S. Tanaka, M. Miyamoto, S. Inagaki, Y. Kubota, C.Y. Kong, N. Nishiyama, Improving hydrothermal stability of acid sites in MFI type aluminosilicate zeolite (ZSM-5) by coating MFI type all silica zeolite (silicalite-1) shell layer, Microporous and Mesoporous Materials 288 (2019) 109523. https://doi.org/10.1016/j.micromeso.2019.05.048.

[71] M. Okamoto, Y. Osafune, MFI-type zeolite with a core-shell structure with minimal defects synthesized by crystal overgrowth of aluminum-free MFI-type zeolite on aluminum-containing zeolite and its catalytic performance, Microporous and Mesoporous Materials 143 (2011) 413–418. https://doi.org/10.1016/j.micromeso.2011.03.032.

[72] C.J. Baranowski, A.M. Bahmanpour, F. Héroguel, J.S. Luterbacher, O. Kröcher, Prominent role of mesopore surface area and external acid sites for the synthesis of polyoxymethylene dimethyl ethers (OME) on a hierarchical H-ZSM-5 zeolite, Catal Sci Technol 9 (2019) 366–376. https://doi.org/10.1039/c8cy02194e.

[73] J. Zheng, X. Sun, Y. Du, B. Qin, Y. Zhang, H. Zhang, M. Pan, R. Li, Structural features of core–shell zeolite–zeolite composite and its performance for methanol conversion into gasoline and diesel, J Mater Res 31 (2016) 2302–2316. https://doi.org/10.1557/jmr.2016.208.

[74] C. Liu, Y. Long, Z. Wang, Optimization of conditions for preparation of ZSM-5@silicalite-1 core–shell catalysts via hydrothermal synthesis, Chin J Chem Eng 26 (2018) 2070–2076. https://doi.org/10.1016/j.cjche.2018.03.030.

[75] M. Miyamoto, T. Kamei, N. Nishiyama, Y. Egashira, K. Ueyama, Single crystals of ZSM-5/silicalite composites, Advanced Materials 17 (2005) 1985–1988. https://doi.org/10.1002/adma.200500522.

[76] M. Miyamoto, S. Ono, K. Kusukami, Y. Oumi, S. Uemiya, High Water Tolerance of a Core–Shell-Structured Zeolite for CO2 Adsorptive Separation under Wet Conditions, ChemSusChem 11 (2018) 1756–1760. https://doi.org/10.1002/cssc.201800063.

[77] D. Yi, X. Xu, X. Meng, N. Liu, L. Shi, Synthesis of core–shell ZSM-5 zeolite with passivated external surface acidity by b-oriented thin silicalite-1 shell using a self-assembly process, Journal of Porous Materials 26 (2019) 1767–1779. https://doi.org/10.1007/s10934-019-00776-0.

[78] H. Shen, M. Liu, J. Li, X. Li, S. Xie, F. Chen, L. Xu, X. Guo, C. Song, X. Zhu, Promising Strategy to Synthesize ZSM-5@Silicalite-1 with Superior Catalytic Performance for Catalytic Cracking Reactions, Ind Eng Chem Res 60 (2021) 9098–9106. https://doi.org/10.1021/acs.iecr.1c01043.

[79] J. Zheng, X. Sun, Y. Du, B. Qin, Y. Zhang, H. Zhang, M. Pan, R. Li, Structural features of core–shell zeolite–zeolite composite and its performance for methanol conversion into gasoline and diesel, J Mater Res 31 (2016) 2302–2316. https://doi.org/10.1557/jmr.2016.208.

[80] S. Zheng, H.R. Heydenrych, H.P. Röger, A. Jentys, J.A. Lercher, On the enhanced selectivity of HZSM-5 modified by chemical liquid deposition, Top Catal 22 (2003) 101–106. https://doi.org/10.1023/A:1021476014917.

[81] G. Li, C. Wu, P. Dong, D. Ji, Y. Zhang, Core–Shell HZSM-5@silicalite-1 Composite: Controllable Synthesis and Catalytic Performance in Alkylation of Toluene with Methanol, Catal Letters 150 (2020) 1923–1931. https://doi.org/10.1007/s10562-019-03085-y.

[82] X. Pan, X. Huang, R. Wang, H. Zhang, H. Wei, J. Chen, S. Liu, L. Sun, D. Xu, Y. Liu, Effects of Silicalite-1 Coating on the p-Xylene Selectivity and Catalytic Stability of HZSM-5 in Toluene Methylation with Methanol, Catalysts 12 (2022). https://doi.org/10.3390/catal12121538.

[83] J. Li, H. Xiang, M. Liu, Q. Wang, Z. Zhu, Z. Hu, The deactivation mechanism of two typical shape-selective HZSM-5 catalysts for alkylation of toluene with methanol, Catal Sci Technol 4 (2014) 2639–2649. https://doi.org/10.1039/c4cy00095a.

[84] J. Zhu, F. Yang, S. Yan, H. Wu, X. Zhu, Fabrication and characterization of ZSM-5@Silicalite-1 core-shell composites and their application in hexane catalytic cracking, ChemistrySelect 8 (2023). https://doi.org/10.1002/slct.202302769.

[85] X. Zou, K.L. Wong, S. Thomas, T.H. Metzger, V. Valtchev, S. Mintova, Platinum clusters confined in FAU-LTA hierarchical porous composite with a core-shell structure, Catal Today 168 (2011) 140–146. https://doi.org/10.1016/j.cattod.2010.12.034.

[86] Y. Bouizi, L. Rouleau, V.P. Valtchev, Factors controlling the formation of core-shell zeolite-zeolite composites, Chemistry of Materials 18 (2006) 4959–4966. https://doi.org/10.1021/cm0611744.

[87] Y. Bouizi, L. Rouleau, V.P. Valtchev, Bi-phase MOR/MFI-type zeolite core-shell composite, Microporous and Mesoporous Materials 91 (2006) 70–77. https://doi.org/10.1016/j.micromeso.2005.11.016.

[88] L. Xu, Y. Yuan, J. Zhang, Y. Zhang, X. Zhang, L. Chen, L. Xu, In situ fabrication of core-shell-structured Beta@Silicalite-1 catalysts by a novel steam-assisted crystallization strategy, CrystEngComm 22 (2020) 945–954. https://doi.org/10.1039/c9ce01624d.

[89] P. Losch, M. Boltz, C. Bernardon, B. Louis, A. Palčić, V. Valtchev, Impact of external surface passivation of nano-ZSM-5 zeolites in the methanol-to-olefins reaction, Appl Catal A Gen 509 (2016) 30–37. https://doi.org/10.1016/j.apcata.2015.09.037.

[90] S. Zheng, H.R. Heydenrych, A. Jentys, J.A. Lercher, Influence of surface modification on the acid site distribution of HZSM-5, Journal of Physical Chemistry B 106 (2002) 9552–9558. https://doi.org/10.1021/jp014091d.

[91] S. Inagaki, S. Shinoda, Y. Kaneko, K. Takechi, R. Komatsu, Y. Tsuboi, H. Yamazaki, J.N. Kondo, Y. Kubota, Facile fabrication of ZSM-5 zeolite catalyst with high durability to coke formation during catalytic cracking of paraffins, ACS Catal 3 (2013) 74–78. https://doi.org/10.1021/cs300426k.

[92] B. Zhang, Z. Zhong, Q. Xie, P. Chen, R. Ruan, Reducing coke formation in the catalytic fast pyrolysis of bio-derived furan with surface modified HZSM-5 catalysts, RSC Adv 5 (2015) 56286–56292. https://doi.org/10.1039/c5ra08827e.

[93] D. Yi, X. Meng, X. Xu, N. Liu, L. Shi, Catalytic performance of modified ZSM-5 designed with selectively passivated external surface acidity by phosphorus, Ind Eng Chem Res 58 (2019) 10154–10163. https://doi.org/10.1021/acs.iecr.9b00629.

[94] J. Lyu, H. Hu, C. Tait, J. Rui, C. Lou, Q. Wang, W. Han, Q. Zhang, Z. Pan, X. Li, Benzene alkylation with methanol over phosphate modified hierarchical porous ZSM-5 with tailored acidity, Chin J Chem Eng 25 (2017) 1187–1194. https://doi.org/10.1016/j.cjche.2016.12.005.

[95] S. Zheng, A. Jentys, J.A. Lercher, On the enhanced para-selectivity of HZSM-5 modified by antimony oxide, J Catal 219 (2003) 310–319. https://doi.org/10.1016/S0021-9517(03)00234-3.

[96] J. Lv, Z. Hua, J. Zhou, Z. Liu, H. Guo, J. Shi, Surface-Passivated Hierarchically Structured ZSM5 Zeolites: High-Performance Shape-Selective Catalysts for para-Xylene Production, ChemCatChem 10 (2018) 2278–2284. https://doi.org/10.1002/cctc.201800044.

[97] C. Cheng, G. Li, D. Ji, Y. Zhao, J. Shen, Regulating hierarchical structure and acidity of HZSM-5 for methanol to aromatics via protective desiliconization and external surface modification,

Microporous and Mesoporous Materials 312 (2021) 110784. https://doi.org/10.1016/j.micromeso.2020.110784.

[98] T. Zhu, H. Liang, B. Zhang, Y. Tian, G. Liu, Controllably tailoring external surface sites of nanosheet HZSM-5 for maximizing light olefins in catalytic cracking of n-decane, Chin J Chem Eng 38 (2021) 276–285. https://doi.org/10.1016/j.cjche.2021.04.015.

[99] G. Wu, Y. Hu, Q. Bao, J. Zhang, J. Ge, Improved Catalytic Performances of the NaOH-Treated ZSM-22 Zeolite in the 1-Butene Skeletal Isomerization Reaction: Effect of External Acid Sites, ACS Omega 8 (2023) 14349–14364. https://doi.org/10.1021/acsomega.2c05478.

[100] X. Cao, K. Wang, L. Kong, Z. Gu, F. Wang, Comparison of surface passivation modification of two mordenite zeolites and their application on the isomerisation of o-ethyltoluene, RSC Adv 12 (2022) 31326–31337. https://doi.org/10.1039/d2ra05390j.

[101] P. Tynjälä, T.T. Pakkanen, Shape selectivity of ZSM-5 zeolite modified with chemical vapor deposition of silicon and germanium alkoxides, J Mol Catal A Chem 122 (1997) 159–168. https://doi.org/10.1016/S1381-1169(97)00020-4.

[102] P.J. Kunkeler, D. Moeskops, H. Van Bekkum, Zeolite Beta: Characterization and passivation of the external surface acidity, Microporous Materials 11 (1997) 313–323. https://doi.org/10.1016/S0927-6513(97)00053-9.

[103] K. Tominaga, S. Maruoka, M. Gotoh, N. Katada, M. Niwa, HZSM-5 modified by silica CVD for shape-selective production of p-xylene: Influence of in situ and ex situ preparation conditions of the zeolite, Microporous and Mesoporous Materials 117 (2009) 523–529. https://doi.org/10.1016/j.micromeso.2008.07.033.

[104] J.-W. Kim, T.-W. Kim, S. Lee, N. Kim, K.-E. Jeong, S.-Y. Jeong, C.-U. Kim, Effects of Steaming and SiO 2 Surface Passivation on SSZ-13 Zeolites in the Ethylene to Propylene Reaction , J Nanosci Nanotechnol 20 (2020) 5783–5786. https://doi.org/10.1166/jnn.2020.17644.

[105] Z. Zhu, Q. Chen, Z. Xie, W. Yang, D. Kong, C. Li, Shape-selective disproportionation of ethylbenzene to para-diethylbenzene over ZSM-5 modified by chemical liquid deposition and MgO, J Mol Catal A Chem 248 (2006) 152–158. https://doi.org/10.1016/j.molcata.2005.10.023.

[106] Z. Jin, S. Liu, L. Qin, Z. Liu, Y. Wang, Z. Xie, X. Wang, Methane dehydroaromatization by Mo-supported MFI-type zeolite with core-shell structure, Appl Catal A Gen 453 (2013) 295–301. https://doi.org/10.1016/j.apcata.2012.12.043.

[107] M.A. Ali, B. Brisdon, W.J. Thomas, Synthesis, characterization and catalytic activity of ZSM-5 zeolites having variable silicon-to-aluminum ratios, Appl Catal A Gen 252 (2003) 149–162. https://doi.org/10.1016/S0926-860X(03)00413-7.

[108] C.G. Pope, X-ray diffraction and the bragg equation, J Chem Educ 74 (1997) 129–131. https://doi.org/10.1021/ed074p129.

[109] G. Leofanti, M. Padovan, G. Tozzola, B. Venturelli, Surface area and pore texture of catalysts, Catal Today 41 (1998) 207–219. https://doi.org/10.1016/S0920-5861(98)00050-9.

[110] I. Miletto, E. Catizzone, G. Bonura, C. Ivaldi, M. Migliori, E. Gianotti, L. Marchese, F. Frusteri, G. Giordano, In situ FT-IR characterization of CuZnZr/ferrierite hybrid catalysts for one-pot CO2-to-DME conversion, Materials 11 (2018). https://doi.org/10.3390/ma11112275.

[111] Q. Li, B. Mihailova, D. Creaser, J. Sterte, The nucleation period for crystallization of colloidal TPA-silicalite-1 with varying silica source, n.d. www.elsevier.nl/locate/micromeso.

[112] G.P. Babu, S.G. Hegde, S.B. Kulkarni, P. Ratnasamy~, Active Centres over HZSMS Zeolites I. Xylene Isomerizationl, 1983.

[113] M. Thommes, K. Kaneko, A. V. Neimark, J.P. Olivier, F. Rodriguez-Reinoso, J. Rouquerol, K.S.W. Sing, Physisorption of gases, with special reference to the evaluation of surface area and pore size distribution (IUPAC Technical Report), Pure and Applied Chemistry 87 (2015) 1051–1069. https://doi.org/10.1515/pac-2014-1117.

[114] E. Catizzone, A. Aloise, M. Migliori, G. Giordano, Dimethyl ether synthesis via methanol dehydration: Effect of zeolite structure, Appl Catal A Gen 502 (2015) 215–220. https://doi.org/10.1016/j.apcata.2015.06.017.

[115] E. Catizzone, A. Aloise, E. Giglio, G. Ferrarelli, M. Bianco, M. Migliori, G. Giordano, MFI vs. FER zeolite during methanol dehydration to dimethyl ether: The crystal size plays a key role, Catal Commun 149 (2021) 106214. https://doi.org/10.1016/j.catcom.2020.106214.

[116] G.L. Woolery, G.H. Kuehl, H.C. Timken, A.W. Chester, J.C.V. Brarnsted, On the nature of framework Lewis acid sites in ZSM-5, n.d.

[117] Auroux Aline, Acidity characterization by microcalorimetry and relationship with reactivity, Topics in Catalysis 4 (1997) 71–89.

[118] K. Barbera, F. Bonino, S. Bordiga, T.V.W. Janssens, P. Beato, Structure-deactivation relationship for ZSM-5 catalysts governed by framework defects, J Catal 280 (2011) 196–205. https://doi.org/10.1016/j.jcat.2011.03.016.

[119] D. Mores, J. Kornatowski, U. Olsbye, B.M. Weckhuysen, Coke formation during the methanol-to-olefin conversion: In situ microspectroscopy on individual H-ZSM-5 crystals with different brønsted acidity, Chemistry - A European Journal 17 (2011) 2874–2884. https://doi.org/10.1002/chem.201002624.

[120] E. Catizzone, A. Aloise, M. Migliori, G. Giordano, From 1-D to 3-D zeolite structures: performance assessment in catalysis of vapour-phase methanol dehydration to DME, Microporous and Mesoporous Materials 243 (2017) 102–111. https://doi.org/10.1016/j.micromeso.2017.02.022.

[121] J.G.J. and P.J.A.H.W. Olivier, Trends in Global Co2 and Total Greenhouse Gas Emissions, PBL Netherlands Environmental Assessment Agency (2020) 1–85.

[122] International Energy Agency, Global CO2 emissions from energy combustion and industrial processes, 1900-2022, CO2 Emissions in 2022 (2023) 2022–2024. https://www.iea.org/data-and-statistics/charts/global-co2-emissions-from-energy-combustion-and-industrial-processes-1900-2022.

[123] World Energy & Climate Statistics: Yearbook 2023, (n.d.). https://yearbook.enerdata.net/total-energy/world-consumption-statistics.html.

[124] Statista. Energy consumption worldwide from 2000 to 2019, with a forecast until 2050, by energy source, (n.d.). https://www.statista.com/statistics/222066/projected-global-energy-consumption-by-source/.

[125] A. Lotfollahzade Moghaddam, M.J. Hazlett, Methanol dehydration catalysts in direct and indirect dimethyl ether (DME) production and the beneficial role of DME in energy supply and environmental pollution, J Environ Chem Eng 11 (2023) 110307. https://doi.org/10.1016/j.jece.2023.110307.

[126] T.A. Semelsberger, R.L. Borup, H.L. Greene, Dimethyl ether (DME) as an alternative fuel, J Power Sources 156 (2006) 497–511. https://doi.org/10.1016/j.jpowsour.2005.05.082.

[127] S.H. Park, C.S. Lee, Combustion performance and emission reduction characteristics of automotive DME engine system, Prog Energy Combust Sci 39 (2013) 147–168. https://doi.org/10.1016/j.pecs.2012.10.002.

[128] S. Sidhu, J. Graham, R. Striebich, Semi-volatile and particulate emissions from the combustion of alternative diesel fuels, Chemosphere 42 (2001) 681–690. https://doi.org/10.1016/S0045-6535(00)00242-3.

[129] J. Zhong, J. Han, Y. Wei, P. Tian, X. Guo, C. Song, Z. Liu, Recent advances of the nano-hierarchical SAPO-34 in the methanol-to-olefin (MTO) reaction and other applications, Catal Sci Technol 7 (2017) 4905–4923. https://doi.org/10.1039/c7cy01466j.

[130] A. Haryanto, S. Fernando, N. Murali, S. Adhikari, Current status of hydrogen production techniques by steam reforming of ethanol: A review, Energy and Fuels 19 (2005) 2098–2106. https://doi.org/10.1021/ef0500538.

[131] A.F. Ghenciu, Review of fuel processing catalysts for hydrogen production in PEM fuel cell systems, Curr Opin Solid State Mater Sci 6 (2002) 389–399. https://doi.org/10.1016/S1359-0286(02)00108-0.

[132] D. Kim, G. Park, B. Choi, Y.B. Kim, Reaction characteristics of dimethyl ether (DME) steam reforming catalysts for hydrogen production, Int J Hydrogen Energy 42 (2017) 29210–29221. https://doi.org/10.1016/j.ijhydene.2017.10.020.

[133] K. Faungnawakij, Y. Tanaka, N. Shimoda, T. Fukunaga, R. Kikuchi, K. Eguchi, Hydrogen production from dimethyl ether steam reforming over composite catalysts of copper ferrite spinel and alumina, Appl Catal B 74 (2007) 144–151. https://doi.org/10.1016/j.apcatb.2007.02.010.

[134] K.K. Gupta, A. Rehman, R.M. Sarviya, Bio-fuels for the gas turbine: A review, Renewable and Sustainable Energy Reviews 14 (2010) 2946–2955. https://doi.org/10.1016/j.rser.2010.07.025.

[135] Z. Azizi, M. Rezaeimanesh, T. Tohidian, M.R. Rahimpour, Dimethyl ether: A review of technologies and production challenges, Chemical Engineering and Processing: Process Intensification 82 (2014) 150–172. https://doi.org/10.1016/j.cep.2014.06.007.

[136] C. Peinado, D. Liuzzi, S.N. Sluijter, G. Skorikova, J. Boon, S. Guffanti, G. Groppi, S. Rojas, Review and perspective: Next generation DME synthesis technologies for the energy transition, Chemical Engineering Journal 479 (2024) 147494. https://doi.org/10.1016/j.cej.2023.147494.

[137] L.R. Clausen, B. Elmegaard, N. Houbak, Technoeconomic analysis of a low CO2 emission dimethyl ether (DME) plant based on gasification of torrefied biomass, Energy 35 (2010) 4831–4842. https://doi.org/10.1016/j.energy.2010.09.004.

[138] M. Higo, K. Dowaki, A Life Cycle Analysis on a Bio-DME production system considering the species of biomass feedstock in Japan and Papua New Guinea, Appl Energy 87 (2010) 58–67. https://doi.org/10.1016/j.apenergy.2009.08.030.

[139] F. Studt, M. Behrens, E.L. Kunkes, N. Thomas, S. Zander, A. Tarasov, J. Schumann, E. Frei, J.B. Varley, F. Abild-Pedersen, J.K. Nørskov, R. Schlögl, The Mechanism of CO and CO2 Hydrogenation to Methanol over Cu-Based Catalysts, ChemCatChem 7 (2015) 1105–1111. https://doi.org/10.1002/cctc.201500123.

[140] J. Liu, J. Shi, D. He, Q. Zhang, X. Wu, Y. Liang, Q. Zhu, Surface active structure of ultra-fine Cu/ZrO2 catalysts used for the CO2+H2 to methanol reaction, Appl Catal A Gen 218 (2001) 113–119. https://doi.org/10.1016/S0926-860X(01)00625-1.

[141] X. Guo, D. Mao, G. Lu, S. Wang, G. Wu, CO2 hydrogenation to methanol over Cu/ZnO/ZrO2 catalysts prepared via a route of solid-state reaction, Catal Commun 12 (2011) 1095–1098. https://doi.org/10.1016/j.catcom.2011.03.033.

[142] J. Słoczyński, R. Grabowski, A. Kozłowska, P. Olszewski, M. Lachowska, J. Skrzypek, J. Stoch, Effect of Mg and Mn oxide additions on structural and adsorptive properties of Cu/ZnO/ZrO2 catalysts for the methanol synthesis from CO2, Appl Catal A Gen 249 (2003) 129–138. https://doi.org/10.1016/S0926-860X(03)00191-1.

[143] C. Yang, Z. Ma, N. Zhao, W. Wei, T. Hu, Y. Sun, Methanol synthesis from CO2-rich syngas over a ZrO2 doped CuZnO catalyst, Catal Today 115 (2006) 222–227. https://doi.org/10.1016/j.cattod.2006.02.077.

[144] J.L.G. Fierro, I. Melián-Cabrera, M. López Granados, Pd-modified Cu-Zn catalysts for methanol synthesis from CO2/H2 mixtures: Catalytic structures and performance, J Catal 210 (2002) 285–294. https://doi.org/10.1006/jcat.2002.3677.

[145] Y. Tavan, S.H. Hosseini, M. Ghavipour, M.R.K. Nikou, A. Shariati, From laboratory experiments to simulation studies of methanol dehydration to produce dimethyl ether - Part I: Reaction kinetic study, Chemical Engineering and Processing: Process Intensification 73 (2013) 144–150. https://doi.org/10.1016/j.cep.2013.06.006.

[146] V. Vishwanathan, K.W. Jun, J.W. Kim, H.S. Roh, Vapour phase dehydration of crude methanol to dimethyl ether over Na-modified H-ZSM-5 catalysts, Appl Catal A Gen 276 (2004) 251–255. https://doi.org/10.1016/j.apcata.2004.08.011.

[147] c and S.-E.P. Shan Jiang, a, b Jin-Soo Hwang, 저,* Taihuan Jin, 거 Tianxi Cai, b Wonihl Cho, c Young soon Baek, Dehydration of Methanol to Dimethyl Ether over ZSM-5 Zeolite, 25 (2004) 185–189.

[148] Z. Azizi, M. Rezaeimanesh, T. Tohidian, M.R. Rahimpour, Dimethyl ether: A review of technologies and production challenges, Chemical Engineering and Processing: Process Intensification 82 (2014) 150–172. https://doi.org/10.1016/j.cep.2014.06.007.

[149] T. Ogawa, N. Inoue, T. Shikada, Y. Ohno, Direct Dimethyl Ether Synthesis, Journal of Natural Gas Chemistry (2003).

[150] S.C. Baek, S.H. Kang, J.W. Bae, Y.J. Lee, K.W. Jun, D.H. Lee, K.Y. Lee, Effect of copper precursors to the activity for dimethyl ether synthesis from syngas over Cu-ZnO/γ-Al2O3 bifunctional catalysts, Energy and Fuels 25 (2011) 3865. https://doi.org/10.1021/ef200939b.

[151] X. Zhang, L. Zhong, Q. Guo, H. Fan, H. Zheng, K. Xie, Influence of the calcination on the activity and stability of the Cu/ZnO/Al2O3 catalyst in liquid phase methanol synthesis, Fuel 89 (2010) 1348–1352. https://doi.org/10.1016/j.fuel.2009.06.011.

[152] V. V. Ordomsky, M. Cai, V. Sushkevich, S. Moldovan, O. Ersen, C. Lancelot, V. Valtchev, A.Y. Khodakov, The role of external acid sites of ZSM-5 in deactivation of hybrid CuZnAl/ZSM-5 catalyst for direct dimethyl ether synthesis from syngas, Appl Catal A Gen 486 (2014) 266–275. https://doi.org/10.1016/j.apcata.2014.08.030.

[153] M. Sánchez-Contador, A. Ateka, A.T. Aguayo, J. Bilbao, Direct synthesis of dimethyl ether from CO and CO2 over a core-shell structured CuO-ZnO-ZrO2@SAPO-11 catalyst, Fuel Processing Technology 179 (2018) 258–268. https://doi.org/10.1016/j.fuproc.2018.07.009.

[154] G. Yang, M. Thongkam, T. Vitidsant, Y. Yoneyama, Y. Tan, N. Tsubaki, A double-shell capsule catalyst with core-shell-like structure for one-step exactly controlled synthesis of dimethyl ether from CO2 containing syngas, Catal Today 171 (2011) 229–235. https://doi.org/10.1016/j.cattod.2011.02.021.

[155] R. Phienluphon, K. Pinkaew, G. Yang, J. Li, Q. Wei, Y. Yoneyama, T. Vitidsant, N. Tsubaki, Designing core (Cu/ZnO/Al2O3)-shell (SAPO-11) zeolite capsule catalyst with a facile physical way for dimethyl ether direct synthesis from syngas, Chemical Engineering Journal 270 (2015) 605–611. https://doi.org/10.1016/j.cej.2015.02.071.

[156] J.J. Spivey, Review: Dehydration catalysts for the methanol/dimethyl ether reaction, Chem Eng Commun 110 (1991) 123–142. https://doi.org/10.1080/00986449108939946.

[157] U. Olsbye, S. Svelle, K.P. Lillerud, Z.H. Wei, Y.Y. Chen, J.F. Li, J.G. Wang, W.B. Fan, The formation and degradation of active species during methanol conversion over protonated zeotype catalysts, Chem Soc Rev 44 (2015) 7155–7176. https://doi.org/10.1039/c5cs00304k.

[158] M. Guisnet, P. Magnoux, Deactivation by coking of zeolite catalysts. Prevention of deactivation. Optimal conditions for regeneration, Catal Today 36 (1997) 477–483. https://doi.org/10.1016/S0920-5861(96)00238-6.

[159] U. Olsbye, S. Svelle, M. Bjrgen, P. Beato, T.V.W. Janssens, F. Joensen, S. Bordiga, K.P. Lillerud, Conversion of methanol to hydrocarbons: How zeolite cavity and pore size controls product selectivity, Angewandte Chemie - International Edition 51 (2012) 5810–5831. https://doi.org/10.1002/anie.201103657.

[160] M. Migliori, E. Catizzone, A. Aloise, G. Bonura, L. Gómez-Hortigüela, L. Frusteri, C. Cannilla, F. Frusteri, G. Giordano, New insights about coke deposition in methanol-to-DME reaction over MOR-, MFI- and FER-type zeolites, Journal of Industrial and Engineering Chemistry 68 (2018). https://doi.org/10.1016/j.jiec.2018.07.046.

[161] S.A. Chernyak, M. Corda, J.P. Dath, V. V. Ordomsky, A.Y. Khodakov, Light olefin synthesis from a diversity of renewable and fossil feedstocks: state-of the-art and outlook, Chem Soc Rev 51 (2022) 7994–8044. https://doi.org/10.1039/d1cs01036k.

[162] M. Salimi, A Review on the Production of Light Olefins from Hydrocarbons Cracking and Methanol Conversion, n.d. https://www.researchgate.net/publication/336680370.

[163] Statista. Ethylene demand and production capacity worldwide from 2015 to 2022 (last access: 3rd November 2022). , (n.d.).

[164] Statista. Propylene demand and capacity worldwide from 2015 to 2022 (last access: 3rd November 2022)., (n.d.).

[165] IEA. Key World Energy Statistics. 2021, (n.d.).

[166] Z. Ma, M.D. Porosoff, Development of tandem catalysts for CO 2 hydrogenation to olefins, 2019. http://pubs.acs.org.

[167] J. Li, Y. Wei, G. Liu, Y. Qi, P. Tian, B. Li, Y. He, Z. Liu, Comparative study of MTO conversion over SAPO-34, H-ZSM-5 and H-ZSM-22: Correlating catalytic performance and reaction mechanism to zeolite topology, in: Catal Today, 2011: pp. 221–228. https://doi.org/10.1016/j.cattod.2011.02.027.

[168] J. Valecillos, E. Epelde, J. Albo, A.T. Aguayo, J. Bilbao, P. Castaño, Slowing down the deactivation of H-ZSM-5 zeolite catalyst in the methanol-to-olefin (MTO) reaction by P or Zn modifications, Catal Today 348 (2020) 243–256. https://doi.org/10.1016/j.cattod.2019.07.059.

[169] J. Li, Y. Wei, G. Liu, Y. Qi, P. Tian, B. Li, Y. He, Z. Liu, Comparative study of MTO conversion over SAPO-34, H-ZSM-5 and H-ZSM-22: Correlating catalytic performance and reaction mechanism to zeolite topology, in: Catal Today, 2011: pp. 221–228. https://doi.org/10.1016/j.cattod.2011.02.027.

[170] T. Cordero-Lanzac, A.T. Aguayo, J. Bilbao, Reactor-regenerator system for the dimethyl ether-to-olefins process over HZSM-5 catalysts: Conceptual development and analysis of the process variables, Ind Eng Chem Res 59 (2020) 14689–14702. https://doi.org/10.1021/acs.iecr.0c02276.

[171] P. Pérez-Uriarte, A. Ateka, A.T. Aguayo, A.G. Gayubo, J. Bilbao, Kinetic model for the reaction of DME to olefins over a HZSM-5 zeolite catalyst, Chemical Engineering Journal 302 (2016) 801–810. https://doi.org/10.1016/j.cej.2016.05.096.

[172] Y. Hirota, K. Murata, M. Miyamoto, Y. Egashira, N. Nishiyama, Light olefins synthesis from methanol and dimethylether over SAPO-34 nanocrystals, Catal Letters 140 (2010) 22–26. https://doi.org/10.1007/s10562-010-0421-1.

[173] Y. Cui, Q. Zhang, J. He, Y. Wang, F. Wei, Pore-structure-mediated hierarchical SAPO-34: Facile synthesis, tunable nanostructure, and catalysis applications for the conversion of dimethyl ether into olefins, Particuology 11 (2013) 468–474. https://doi.org/10.1016/j.partic.2012.12.009.

[174] S.G. Lee, H.S. Kim, Y.H. Kim, E.J. Kang, D.H. Lee, C.S. Park, Dimethyl ether conversion to light olefins over the SAPO-34/ZrO2 composite catalysts with high lifetime, Journal of Industrial and Engineering Chemistry 20 (2014) 61–67. https://doi.org/10.1016/j.jiec.2013.04.026.

[175] Y. Gao, S.L. Chen, Y. Wei, Y. Wang, W. Sun, Y. Cao, P. Zeng, Kinetics of coke formation in the dimethyl ether-to-olefins process over SAPO-34 catalyst, Chemical Engineering Journal 326 (2017) 528–539. https://doi.org/10.1016/j.cej.2017.05.158.

[176] D. Zhao, Y. Zhang, Z. Li, Y. Wang, J. Yu, Synthesis of AEI/CHA intergrowth zeolites by dual templates and their catalytic performance for dimethyl ether to olefins, Chemical Engineering Journal 323 (2017) 295–303. https://doi.org/10.1016/j.cej.2017.04.109.

[177] Y. Zhang, H. Ding, L. Li, K. Zhu, J. Liu, Generating nanocrystalline SAPO-34 through bead-milling and porogen-assisted recrystallization: Structural evolution and catalytic consequence in dimethyl ether-to-olefin conversion, Appl Catal A Gen 632 (2022). https://doi.org/10.1016/j.apcata.2022.118483.

[178] T. Cordero-Lanzac, A. Ateka, P. Pérez-Uriarte, P. Castaño, A.T. Aguayo, J. Bilbao, Insight into the Deactivation and Regeneration of HZSM-5 Zeolite Catalysts in the Conversion of Dimethyl Ether to Olefins, Ind Eng Chem Res 57 (2018) 13689–13702. https://doi.org/10.1021/acs.iecr.8b03308.

[179] P. Pérez-Uriarte, A. Ateka, A.T. Aguayo, J. Bilbao, Comparison of HZSM-5 Zeolite and SAPO (-18 and -34) Based Catalysts for the Production of Light Olefins from DME, Catal Letters 146 (2016) 1892–1902. https://doi.org/10.1007/s10562-016-1829-z.

[180] P. Pérez-Uriarte, M. Gamero, A. Ateka, M. Díaz, A.T. Aguayo, J. Bilbao, Effect of the Acidity of HZSM-5 Zeolite and the Binder in the DME Transformation to Olefins, Ind Eng Chem Res 55 (2016) 1513–1521. https://doi.org/10.1021/acs.iecr.5b04477.

[181] P. Pérez-Uriarte, A. Ateka, A.G. Gayubo, T. Cordero-Lanzac, A.T. Aguayo, J. Bilbao, Deactivation kinetics for the conversion of dimethyl ether to olefins over a HZSM-5 zeolite catalyst, Chemical Engineering Journal 311 (2017) 367–377. https://doi.org/10.1016/j.cej.2016.11.104.

[182] Z. Chen, Z. Li, Y. Zhang, D. Chevella, G. Li, Y. Chen, X. Guo, J. Liu, J. Yu, A green route for the synthesis of nano-sized hierarchical ZSM-5 zeolite with excellent DTO catalytic performance, Chemical Engineering Journal 388 (2020). https://doi.org/10.1016/j.cej.2020.124322.

[183] I.A. Bakare, O. Muraza, M.A. Sanhoob, K. Miyake, Y. Hirota, Z.H. Yamani, N. Nishiyama, Dimethyl ether-to-olefins over aluminum rich ZSM-5: The role of Ca and La as modifiers, Fuel 211 (2018) 18–26. https://doi.org/10.1016/j.fuel.2017.08.117.

[184] N. V. Kolesnichenko, N. Khivrich, T.K. Obukhova, I. Batova, G.N. Bondarenko, Effect of magnesium on the catalytic properties of polymetallic zeolite catalysts for conversion of dimethyl ether to light olefins, Microporous and Mesoporous Materials 298 (2020). https://doi.org/10.1016/j.micromeso.2020.110087.

[185] S. Park, Y. Watanabe, Y. Nishita, T. Fukuoka, S. Inagaki, Y. Kubota, Catalytic conversion of dimethyl ether into propylene over MCM-68 zeolite, J Catal 319 (2014) 265–273. https://doi.org/10.1016/j.jcat.2014.09.002.

[186] G. Nasser, T. Kurniawan, K. Miyake, A. Galadima, Y. Hirota, N. Nishiyama, O. Muraza, Dimethyl ether to olefins over dealuminated mordenite (MOR) zeolites derived from natural minerals, J Nat Gas Sci Eng 28 (2016) 566–571. https://doi.org/10.1016/j.jngse.2015.12.032.

[187] T. Kurniawan, O. Muraza, K. Miyake, A.S. Hakeem, Y. Hirota, A.M. Al-Amer, N. Nishiyama, Conversion of Dimethyl Ether to Olefins over Nanosized Mordenite Fabricated by a Combined High-Energy Ball Milling with Recrystallization, Ind Eng Chem Res 56 (2017) 4258–4266. https://doi.org/10.1021/acs.iecr.6b04834.

[188] M.H.M. Ahmed, O. Muraza, A.M. Al Amer, Y. Sugiura, N. Nishiyama, Development of desilicated EU-1 zeolite and its application in conversion of dimethyl ether to olefins, Microporous and Mesoporous Materials 207 (2015) 9–16. https://doi.org/10.1016/j.micromeso.2015.01.006.

[189] M.H.M. Ahmed, O. Muraza, K. Miyake, Y. Hirota, N. Nishiyama, Orchestrating fluoride effect, secondary growth and microwave irradiation in the synthesis of EU-1/ZSM-48 intergrowth crystals for the conversion of dimethyl ether to olefins, Microporous and Mesoporous Materials 267 (2018) 115–123. https://doi.org/10.1016/j.micromeso.2018.02.047.

[190] M.H.M. Ahmed, O. Muraza, A.M. Al-Amer, K. Miyake, N. Nishiyama, Development of hierarchical EU-1 zeolite by sequential alkaline and acid treatments for selective dimethyl ether to propylene (DTP), Appl Catal A Gen 497 (2015) 127–134. https://doi.org/10.1016/j.apcata.2015.03.011.

[191] M. Guisnet, L. Costa, F.R. Ribeiro, Prevention of zeolite deactivation by coking, J Mol Catal A Chem 305 (2009) 69–83. https://doi.org/10.1016/j.molcata.2008.11.012.

[192] M. Bjørgen, S. Svelle, F. Joensen, J. Nerlov, S. Kolboe, F. Bonino, L. Palumbo, S. Bordiga, U. Olsbye, Conversion of methanol to hydrocarbons over zeolite H-ZSM-5: On the origin of the olefinic species, J Catal 249 (2007) 195–207. https://doi.org/10.1016/j.jcat.2007.04.006.

[193] S. Ilias, A. Bhan, Mechanism of the catalytic conversion of methanol to hydrocarbons, ACS Catal 3 (2013) 18–31. https://doi.org/10.1021/cs3006583.

[194] P. Tian, Y. Wei, M. Ye, Z. Liu, Methanol to olefins (MTO): From fundamentals to commercialization, ACS Catal 5 (2015) 1922–1938. https://doi.org/10.1021/acscatal.5b00007.

[195] P. Pérez-Uriarte, A. Ateka, M. Gamero, A.T. Aguayo, J. Bilbao, Effect of the Operating Conditions in the Transformation of DME to olefins over a HZSM-5 Zeolite Catalyst, Ind Eng Chem Res 55 (2016) 6569–6578. https://doi.org/10.1021/acs.iecr.6b00627.

[196] P. Pérez-Uriarte, A. Ateka, A.T. Aguayo, J. Bilbao, Comparison of HZSM-5 Zeolite and SAPO (-18 and -34) Based Catalysts for the Production of Light Olefins from DME, Catal Letters 146 (2016) 1892–1902. https://doi.org/10.1007/s10562-016-1829-z.

[197] P. Pérez-Uriarte, M. Gamero, A. Ateka, M. Díaz, A.T. Aguayo, J. Bilbao, Effect of the Acidity of HZSM-5 Zeolite and the Binder in the DME Transformation to Olefins, Ind Eng Chem Res 55 (2016) 1513–1521. https://doi.org/10.1021/acs.iecr.5b04477.

[198] Z. Yang, Y. Xia, X. Sun, R. Mokaya, Preparation and hydrogen storage properties of zeolite-templated carbon materials nanocast via chemical vapor deposition: Effect of the zeolite template and nitrogen doping, Journal of Physical Chemistry B 110 (2006) 18424–18431. https://doi.org/10.1021/jp0639849.

[199] H. Nishihara, T. Kyotani, Zeolite-templated carbons-three-dimensional microporous graphene frameworks, Chemical Communications 54 (2018) 5648–5673. https://doi.org/10.1039/c8cc01932k.

[200] F. Su, J. Zeng, Y. Yu, L. Lv, J.Y. Lee, X.S. Zhao, Template synthesis of microporous carbon for direct methanol fuel cell application, Carbon N Y 43 (2005) 2366–2373. https://doi.org/10.1016/j.carbon.2005.04.018.

[201] M. Yabushita, K. Techikawara, H. Kobayashi, A. Fukuoka, A. Katz, Zeolite-Templated Carbon Catalysts for Adsorption and Hydrolysis of Cellulose-Derived Long-Chain Glucans: Effect of Post-Synthetic Surface Functionalization, ACS Sustain Chem Eng 4 (2016) 6844–6851. https://doi.org/10.1021/acssuschemeng.6b01796.

[202] N.P. Stadie, S. Wang, K. V. Kravchyk, M. V. Kovalenko, Zeolite-Templated Carbon as an Ordered Microporous Electrode for Aluminum Batteries, ACS Nano 11 (2017) 1911–1919. https://doi.org/10.1021/acsnano.6b07995.

[203] J. Shi, W. Li, D. Li, Rapidly reversible adsorption of methane with a high storage capacity on the zeolite templated carbons with glucose as carbon precursors, Colloids Surf A Physicochem Eng Asp 485 (2015) 11–17. https://doi.org/10.1016/j.colsurfa.2015.08.026.

[204] N.M. Musyoka, K.M. Rambau, N. Manyala, J. Ren, H.W. Langmi, M.K. Mathe, Utilization of waste tyres pyrolysis oil vapour in the synthesis of Zeolite Templated Carbons (ZTCs) for hydrogen storage application, J Environ Sci Health A Tox Hazard Subst Environ Eng 53 (2018) 1022–1028. https://doi.org/10.1080/10934529.2018.1471099.

[205] K. Kim, M. Choi, R. Ryoo, Ethanol-based synthesis of hierarchically porous carbon using nanocrystalline beta zeolite template for high-rate electrical double layer capacitor, Carbon N Y 60 (2013) 175–185. https://doi.org/10.1016/j.carbon.2013.04.011.

[206] S. Builes, T. Roussel, C.M. Ghimbeu, J. Parmentier, R. Gadiou, C. Vix-Guterl, L.F. Vega, Microporous carbon adsorbents with high CO2 capacities for industrial applications, Physical Chemistry Chemical Physics 13 (2011) 16063–16070. https://doi.org/10.1039/c1cp21673b.

[207] A.Y. Lo, C. Te Hung, N. Yu, C.T. Kuo, S. Bin Liu, Syntheses of carbon porous materials with varied pore sizes and their performances as catalyst supports during methanol oxidation reaction, Appl Energy 100 (2012) 66–74. https://doi.org/10.1016/j.apenergy.2012.05.043.

[208] C.H. Choi, M. Kim, H.C. Kwon, S.J. Cho, S. Yun, H.T. Kim, K.J.J. Mayrhofer, H. Kim, M. Choi, Tuning selectivity of electrochemical reactions by atomically dispersed platinum catalyst, Nat Commun 7 (2016) 1–9. https://doi.org/10.1038/ncomms10922.

[209] H. Wang, Q. Gao, J. Hu, Z. Chen, High performance of nanoporous carbon in cryogenic hydrogen storage and electrochemical capacitance, Carbon N Y 47 (2009) 2259–2268. https://doi.org/10.1016/j.carbon.2009.04.021.

[210] G. Papanikolaou, P. Lanzafame, S. Perathoner, G. Centi, D. Cozza, G. Giorgianni, M. Migliori, G. Giordano, High performance of Au/ZTC based catalysts for the selective oxidation of bio-derivative furfural to 2-furoic acid 1, Catal Commun 149 (2021) 106234. https://doi.org/10.1016/j.catcom.2020.106234.

[211] Z. Yang, Y. Xia, R. Mokaya, Enhanced hydrogen storage capacity of high surface area zeolite-like carbon materials, J Am Chem Soc 129 (2007) 1673–1679. https://doi.org/10.1021/ja067149g.

[212] T. Kyotani, Z. Ma, A. Tomita, Template synthesis of novel porous carbons using various types of zeolites, Carbon N Y 41 (2003) 1451–1459. https://doi.org/10.1016/S0008-6223(03)00090-3.

[213] M. Vujković, D. Bajuk-Bogdanović, L. Matović, M. Stojmenović, S. Mentus, Mild electrochemical oxidation of zeolite templated carbon in acidic solutions, as a way to boost its charge storage properties in alkaline solutions, Carbon N Y 138 (2018) 369–378. https://doi.org/10.1016/j.carbon.2018.07.053.

[214] Z. Yang, Y. Xia, R. Mokaya, Enhanced hydrogen storage capacity of high surface area zeolite-like carbon materials, J Am Chem Soc 129 (2007) 1673–1679. https://doi.org/10.1021/ja067149g.

[215] H. Nishihara, Q.H. Yang, P.X. Hou, M. Unno, S. Yamauchi, R. Saito, J.I. Paredes, A. Martínez-Alonso, J.M.D. Tascón, Y. Sato, M. Terauchi, T. Kyotani, A possible buckybowl-like structure of zeolite templated carbon, Carbon N Y 47 (2009) 1220–1230. https://doi.org/10.1016/j.carbon.2008.12.040.

[216] TUINSTRA F, KOENIG JL, Raman Spectrum of Graphite, Journal of Chemical Physics 53 (1970) 1126–1130. https://doi.org/10.1063/1.1674108.

[217] Y. Wang, D.C. Alsmeyer, R.L. McCreery, Raman Spectroscopy of Carbon Materials: Structural Basis of Observed Spectra, Chemistry of Materials 2 (1990) 557–563. https://doi.org/10.1021/cm00011a018.

[218] A.Y. Lee, K. Yang, N.D. Anh, C. Park, S.M. Lee, T.G. Lee, M.S. Jeong, Raman study of D* band in graphene oxide and its correlation with reduction, Appl Surf Sci 536 (2021) 147990. https://doi.org/10.1016/j.apsusc.2020.147990.

[219] E. Groppo, F. Bonino, F. Cesano, A. Damin, M. Manzoli, CHAPTER 4. Raman, IR and INS characterization of functionalized carbon materials, ROYAL SOCIETY OF CHEMISTRY, 2018. https://doi.org/https://dx.doi.org/10.1039/9781788013116-00103.

[220] M. Kwiatkowski, A. Policicchio, M. Seredych, T.J. Bandosz, Evaluation of CO2 interactions with S-doped nanoporous carbon and its composites with a reduced GO: Effect of surface features on an apparent physical adsorption mechanism, Carbon N Y 98 (2016) 250–258. https://doi.org/10.1016/j.carbon.2015.11.019.

APPENDIX A: Textural properties of investigated samples.

APPENDIX A: Textural properties of investigated samples.

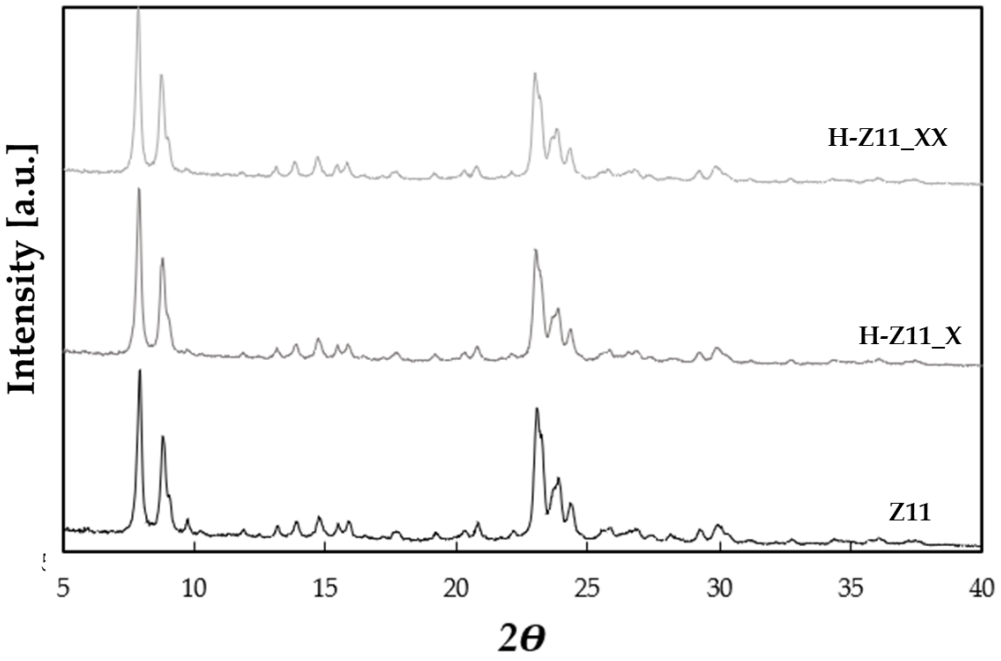

Figure A 1: XRD spectra of Z11, H-Z11_X and H-Z11_XX samples

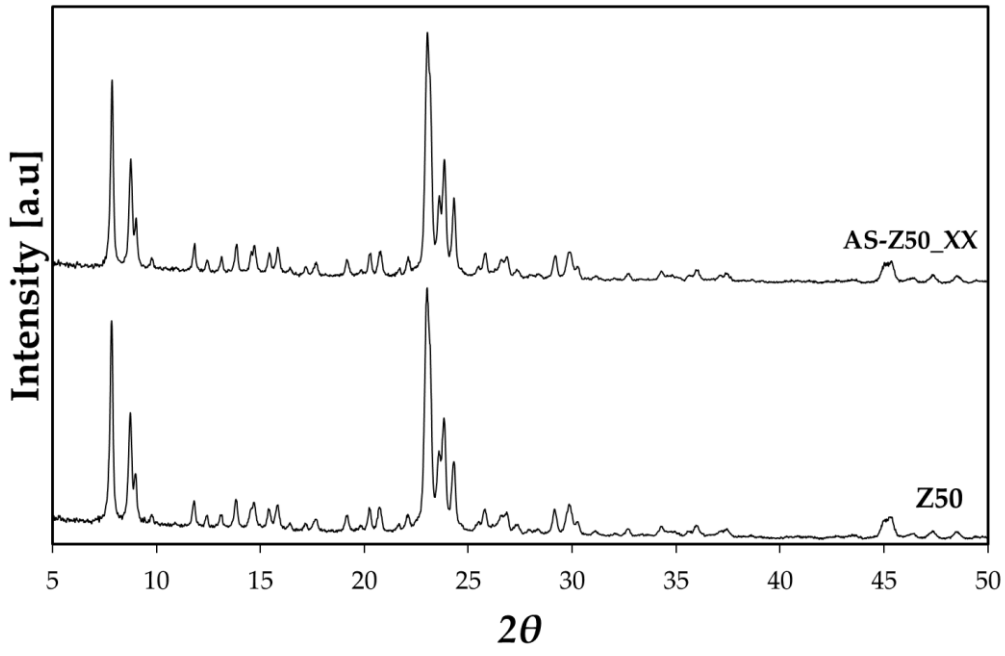

Figure A 2: XRD patterns of Z50 and passivated AS-Z50_XX samples.

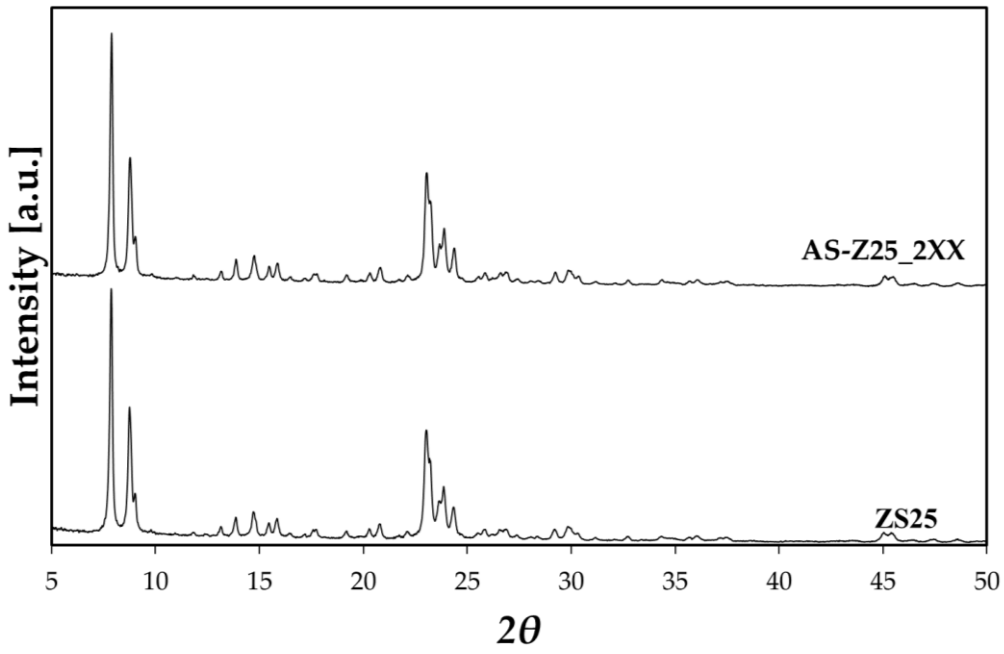

Figure A 3: XRD patterns of Z25 and passivated AS-Z25_2XX samples.

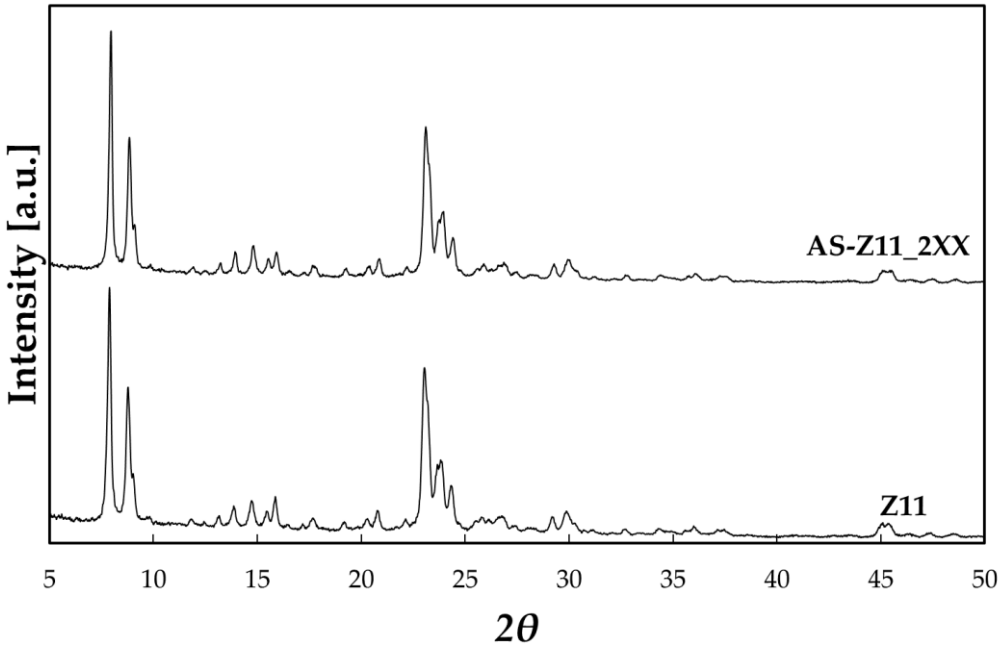

Figure A 4: XRD patterns of Z11 and passivated AS-Z11_2XX samples.

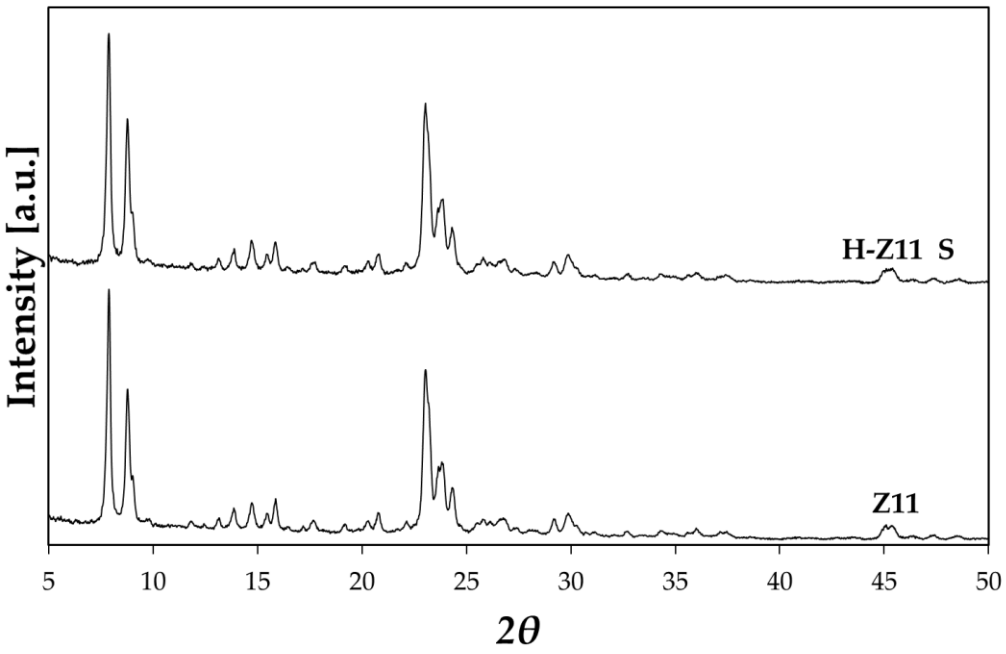

Figure A 5: XRD patterns of Z11 and passivated H-Z11_S obtained via CLD of TEOS.

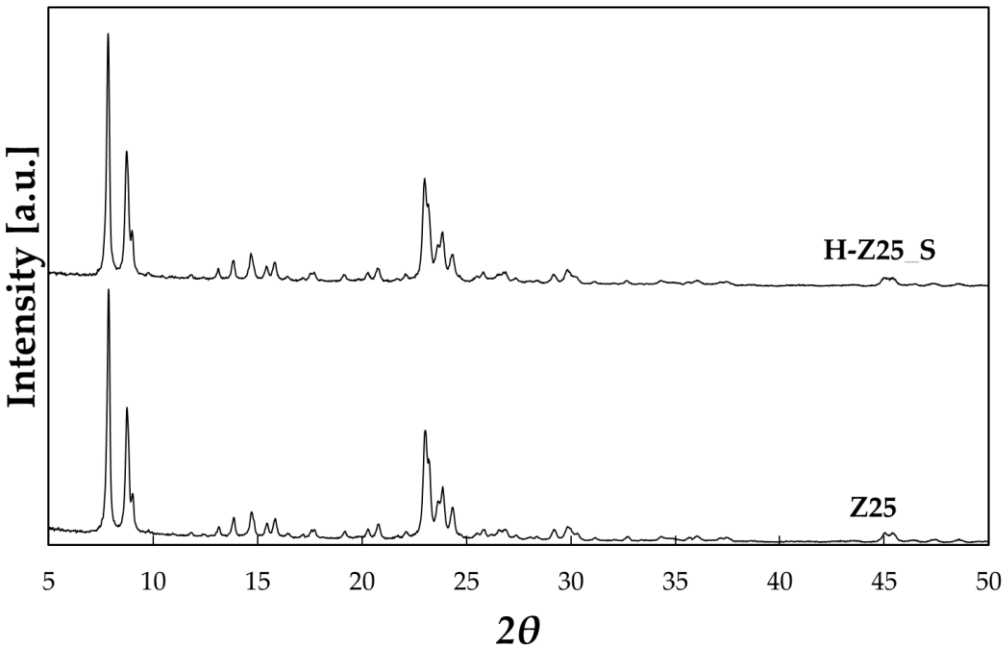

Figure A 6: XRD patterns of Z11 and passivated H-Z11_S obtained via CLD of TEOS.

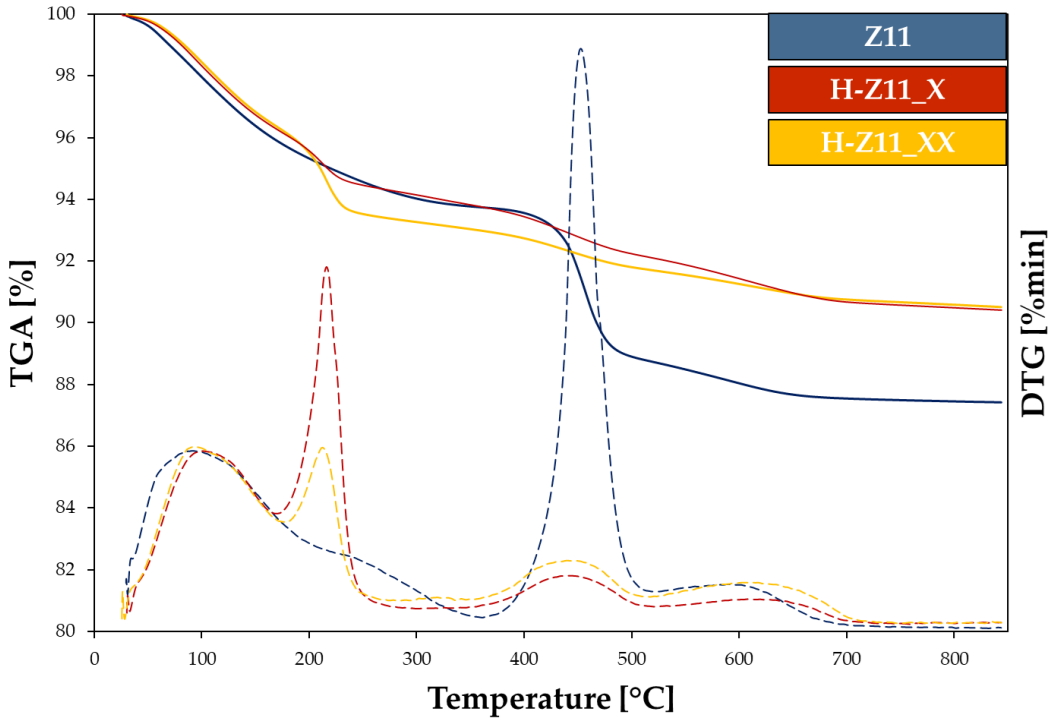

Figure A 7: TGA-DTG results of Z11, H-Z11_X and H-Z11_XX samples.

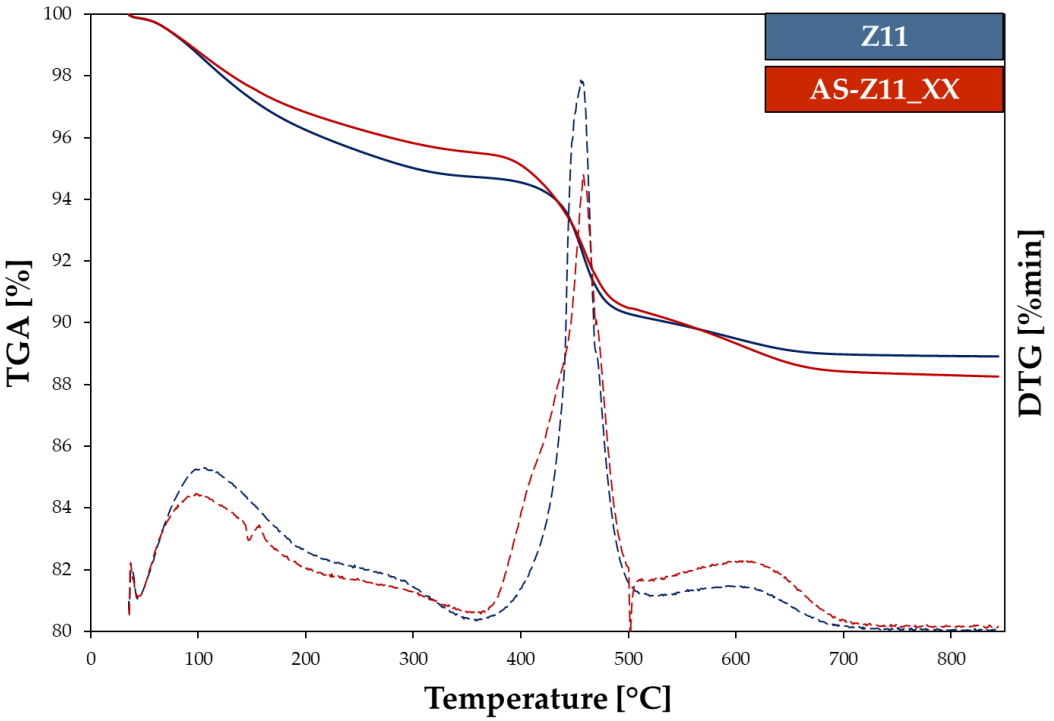

Figure A 8: TGA-DTG results of Z11, and AS-Z11_XX samples.

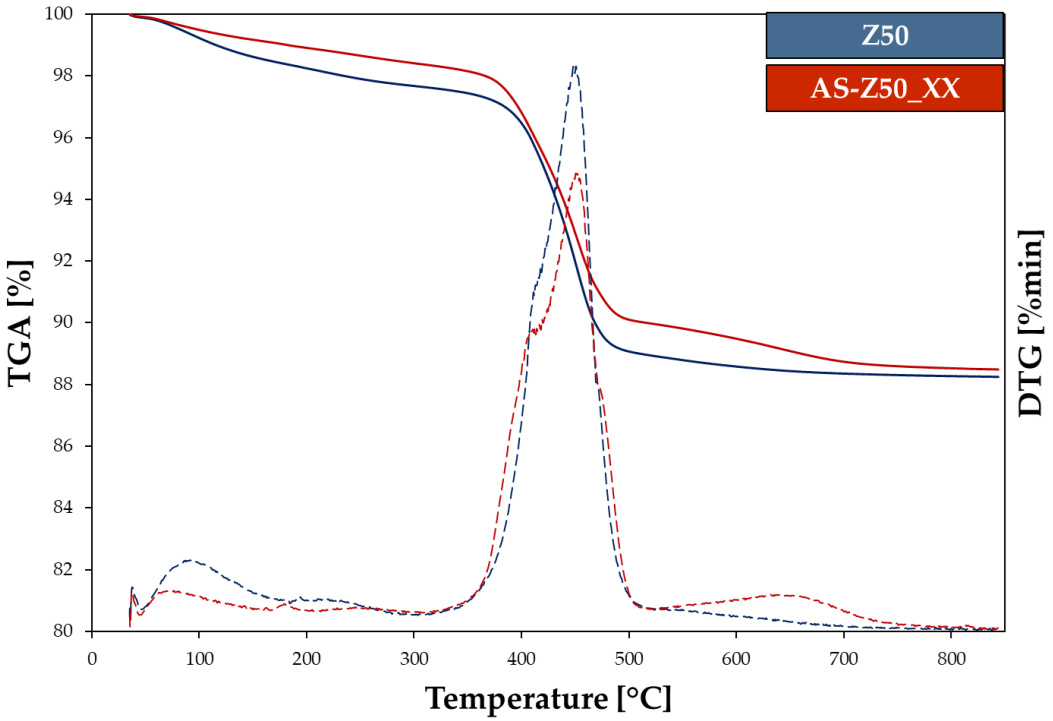

Figure A 9: TGA-DTG results of Z50, and AS-Z50_XX samples.

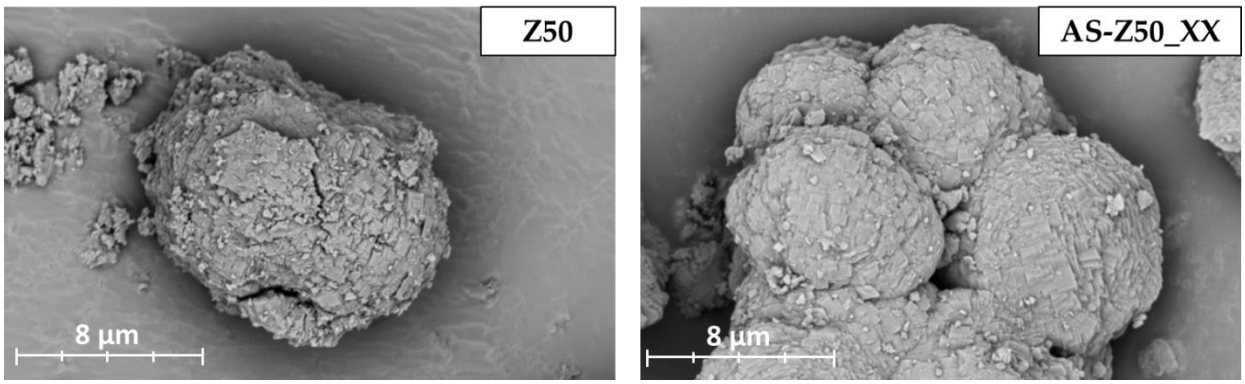

Figure A 10: SEM micrographs obtained at 5kV for Z50 and AS-Z50_XX samples.

APPENDIX A: Textural properties of investigated samples.

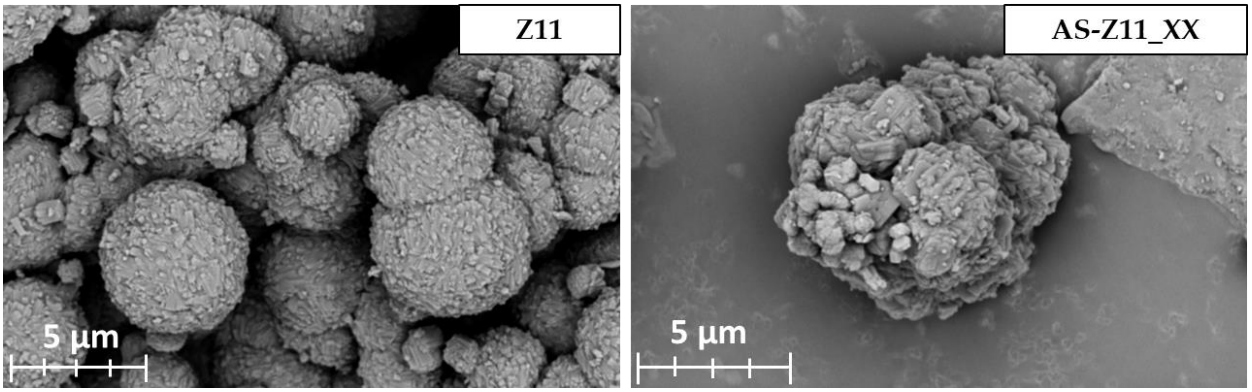

Figure A 11: SEM micrographs obtained at 5kV for Z11 and AS-Z11_XX samples.

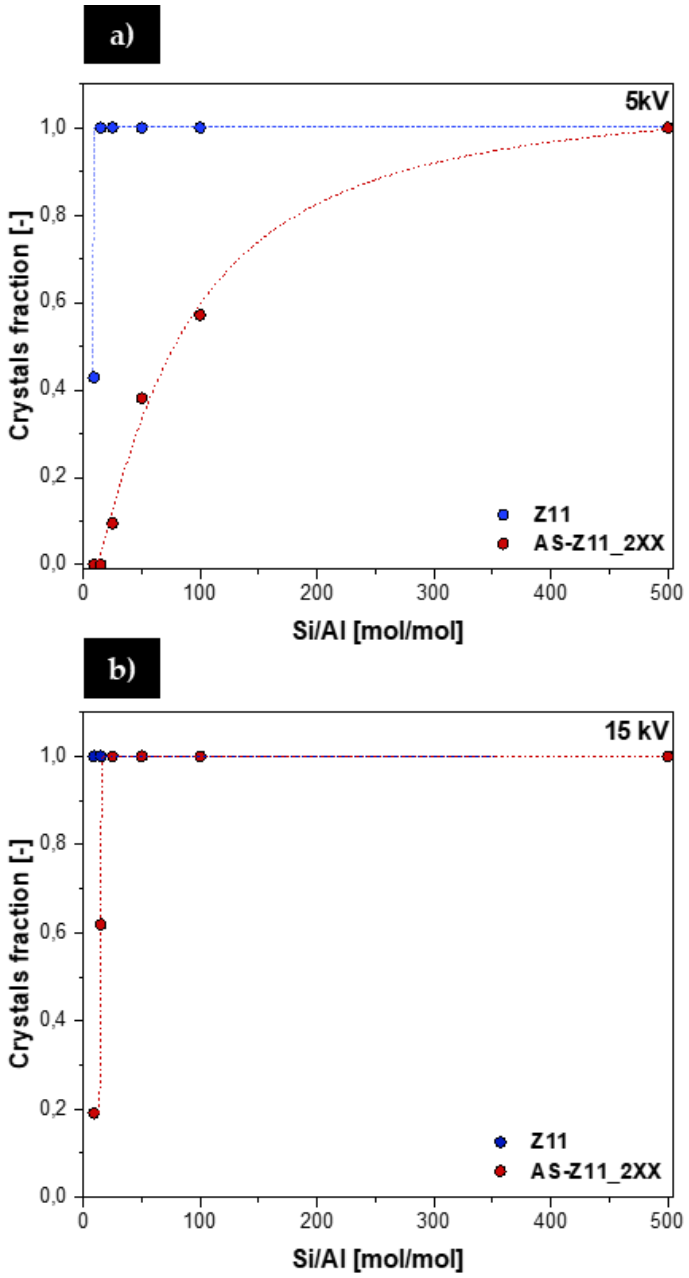

Figure A 12: Cumulative functions of Z11 and AS-Z11_2XX samples obtained via EDX measurements at 5 kV (a) and 15kV (b).

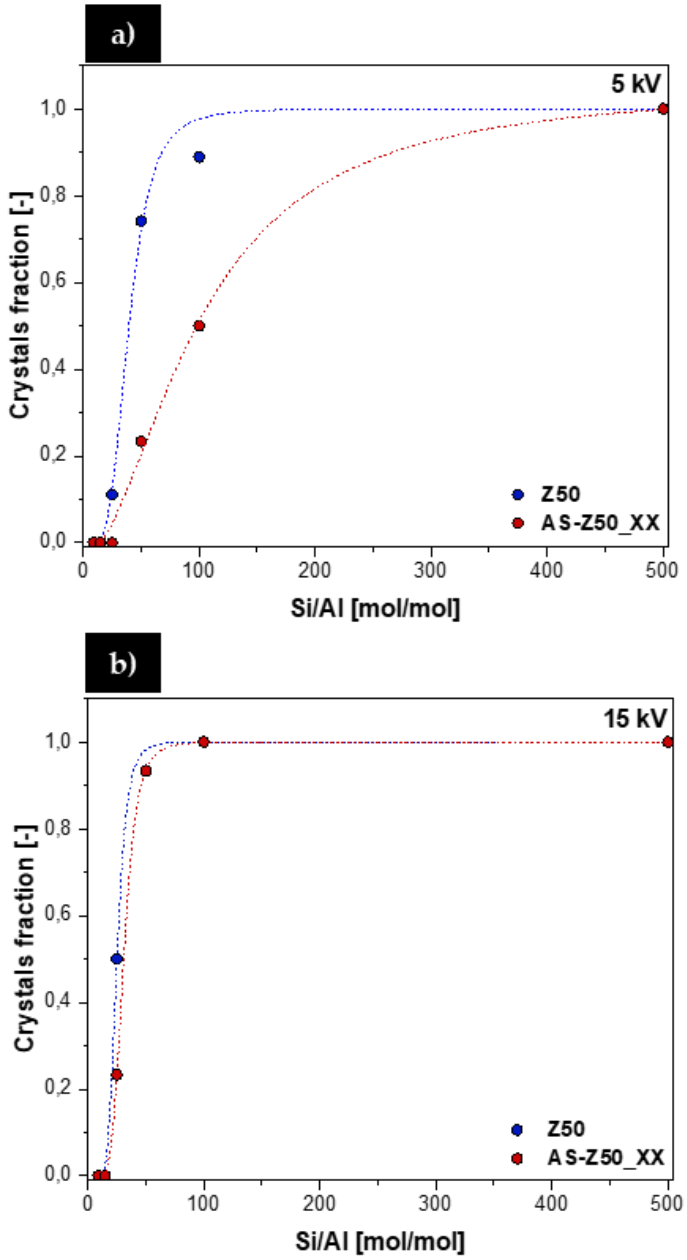

Figure A 13: Cumulative functions of Z50 and AS-Z50_XX samples obtained via EDX measurements at 5 kV (a) and 15kV (b).

APPENDIX A: Textural properties of investigated samples.

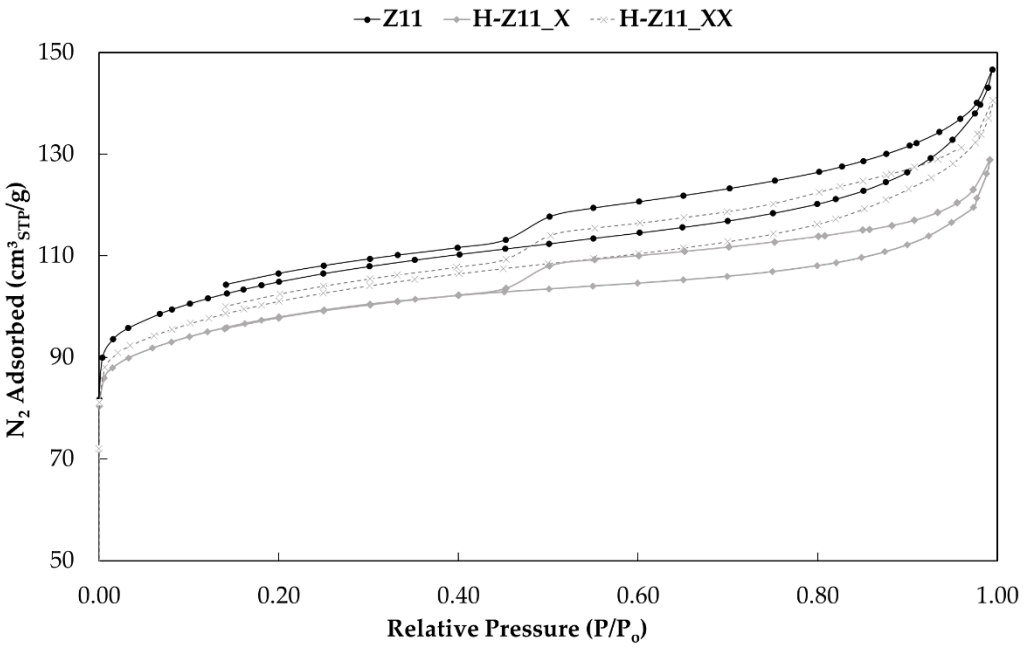

Figure A 14: N_2 sorption isotherms of parent (Z11) and passivated H-Z11_X and H-Z11_XX samples.

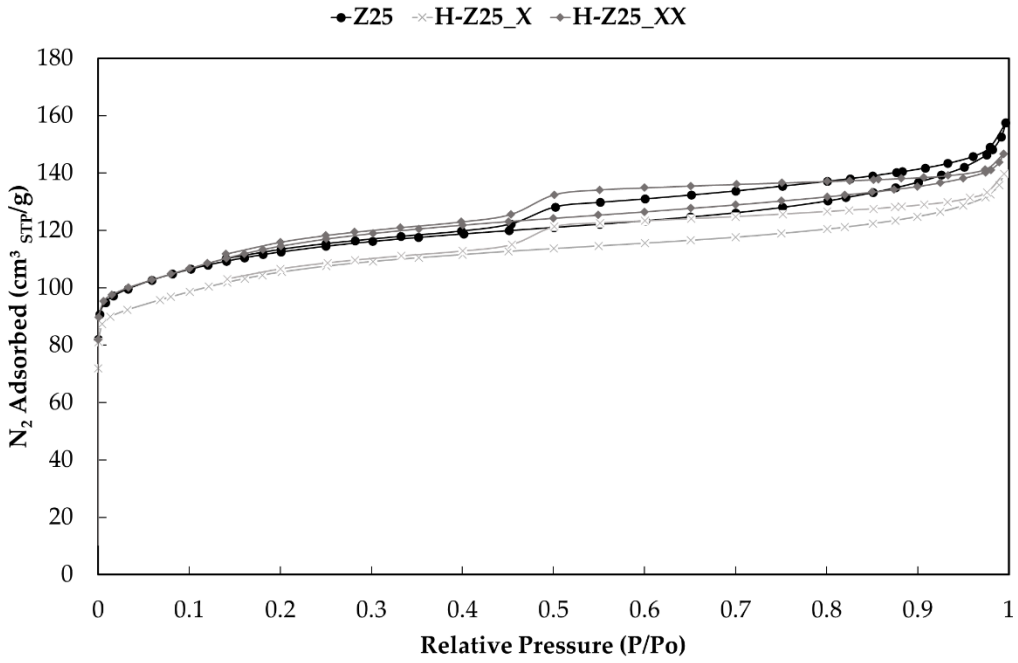

Figure A 15: N_2 sorption isotherms of parent (Z25) and passivated H-Z25_X and H-Z25_XX samples.

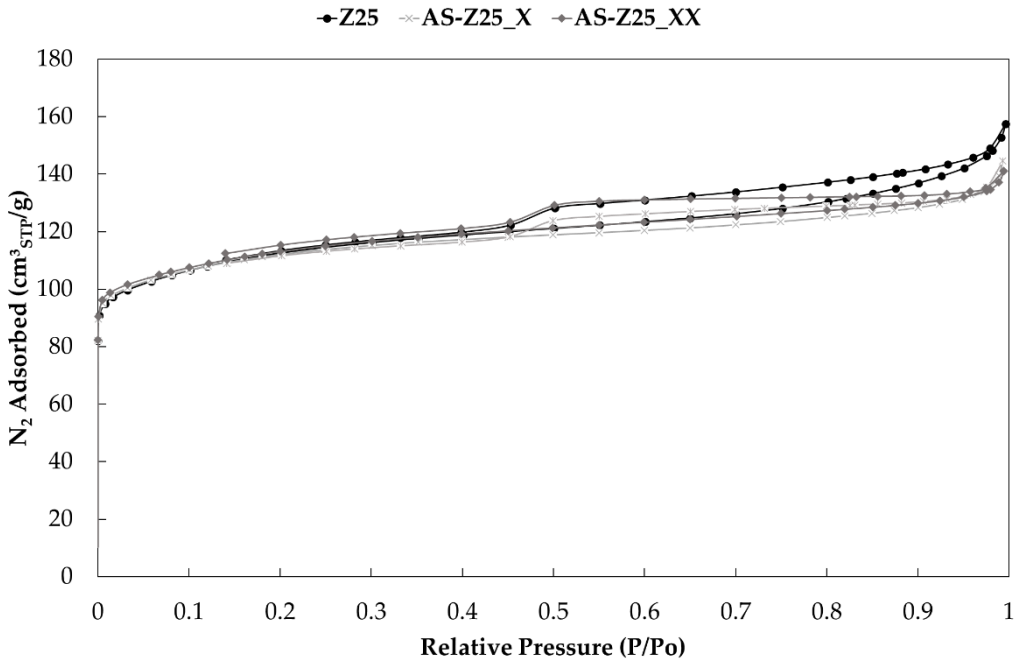

Figure A 16: N_2 sorption isotherms of parent (Z25) and passivated AS-Z25_X and AS-Z25_XX samples.

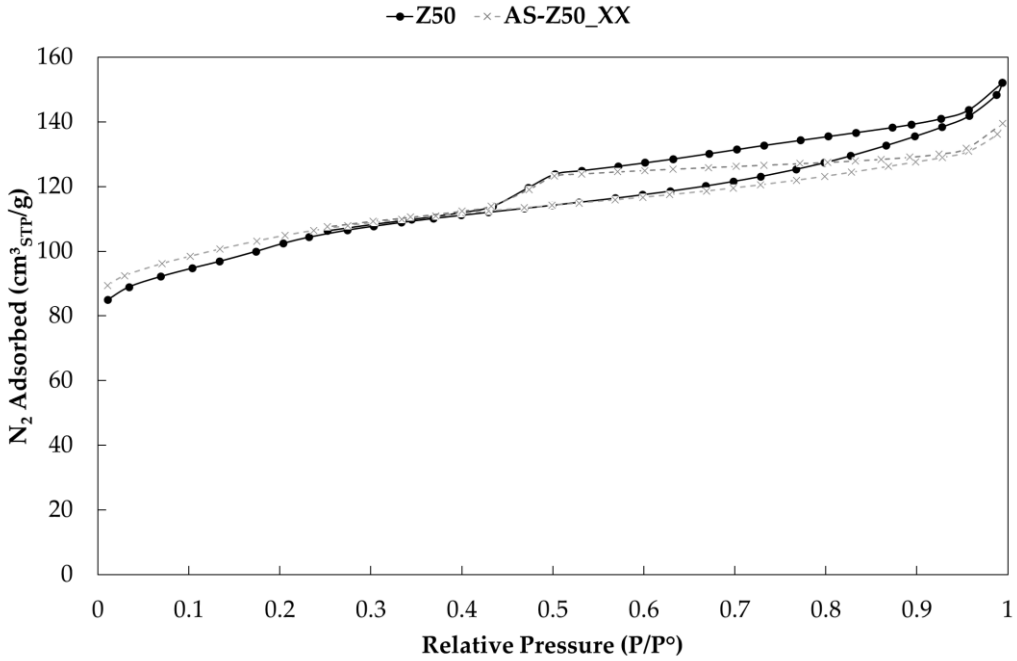

Figure A 17: N_2 sorption isotherms of parent (Z50) and passivated AS-Z50_XX sample.

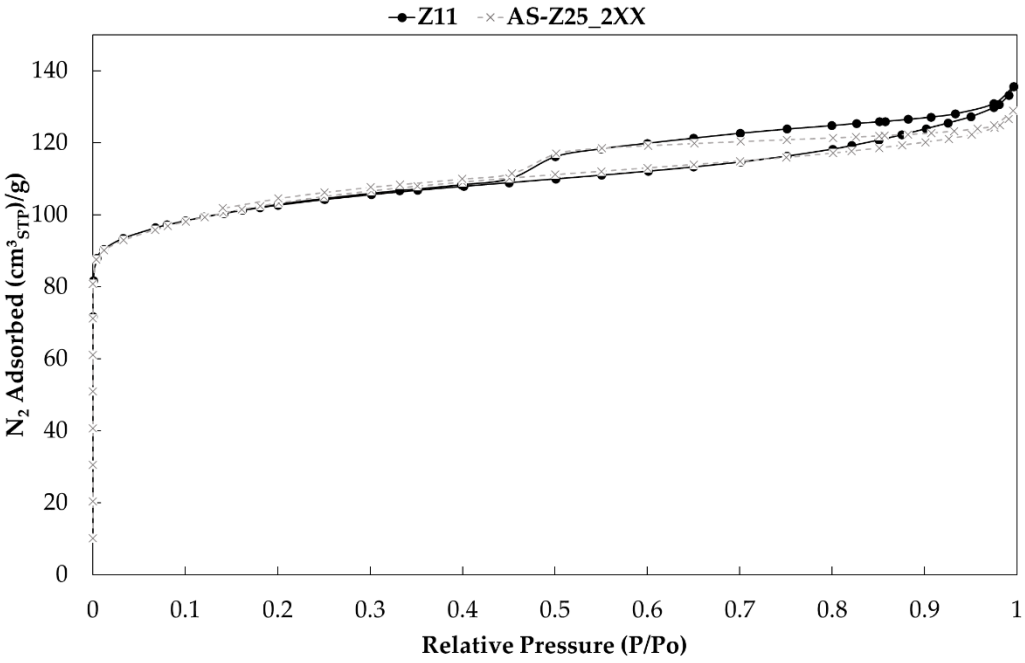

Figure A 18: N2 sorption isotherms of parent (Z11) and passivated AS-Z11_2XX sample.

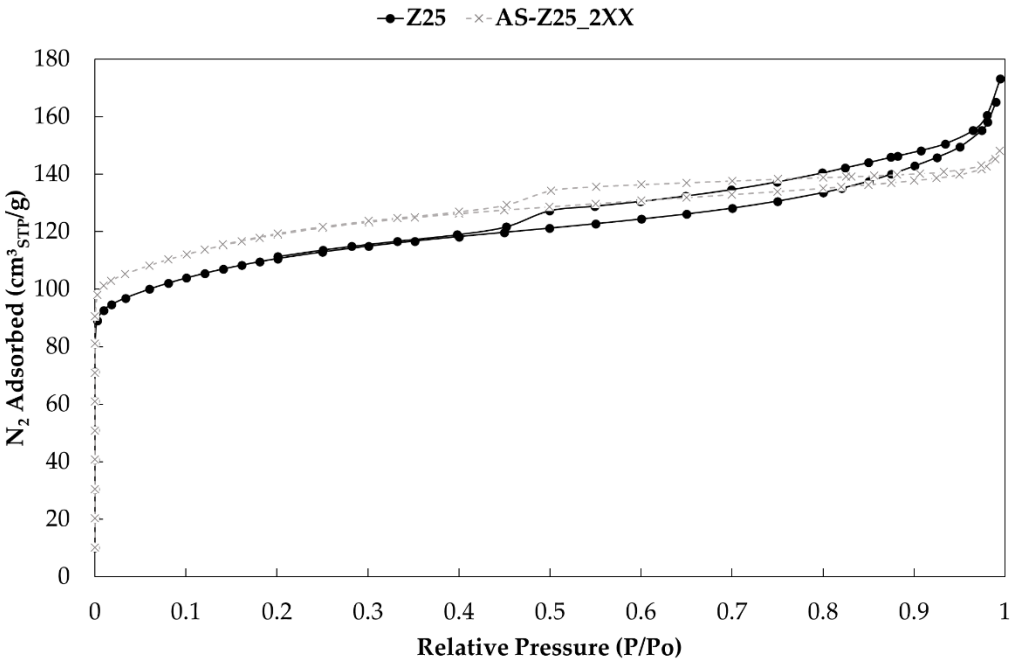

Figure A 19: N_2 sorption isotherms of parent (Z25) and passivated AS-Z25_2XX sample.

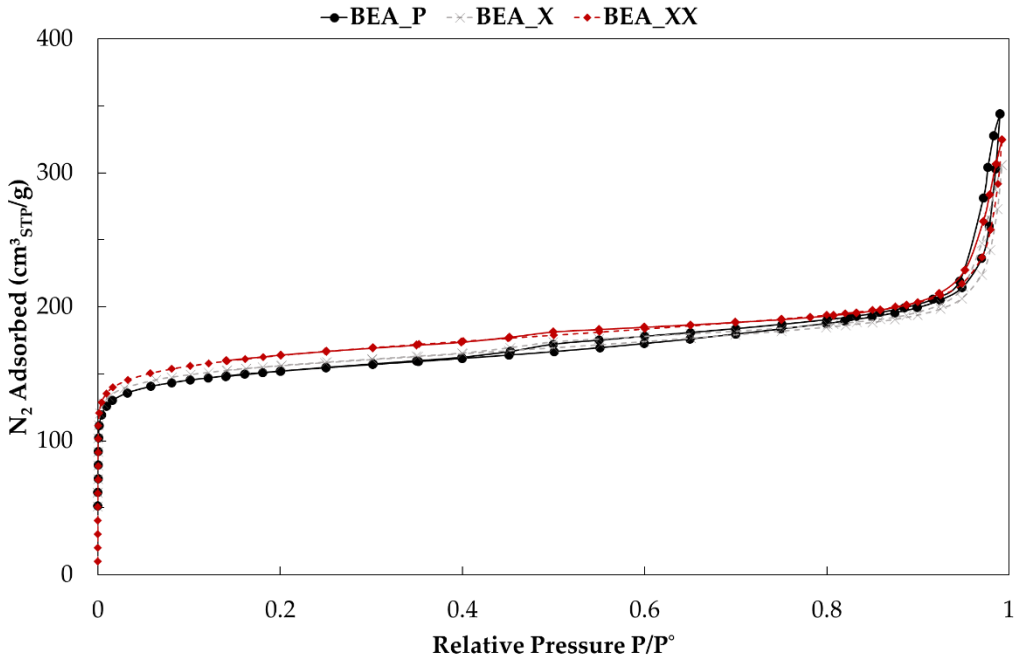

Figure A 20: N_2 sorption isotherms of parent (BEA) and coated BEA_X and BEA_XX samples.

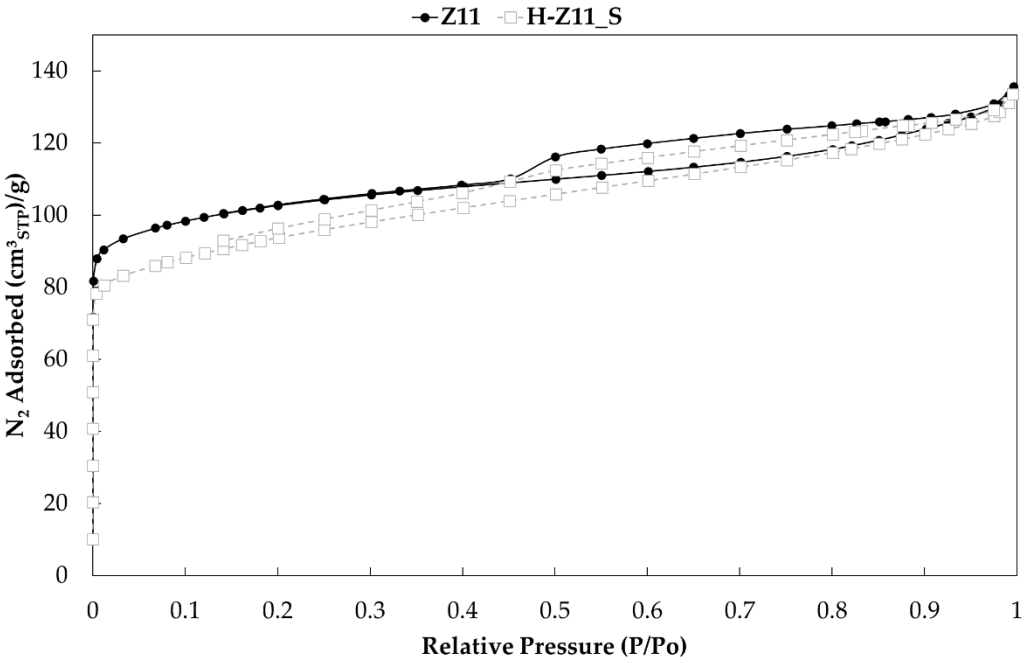

Figure A 21: N_2 sorption isotherms of parent (Z11) and passivated (H-Z11_S) samples.

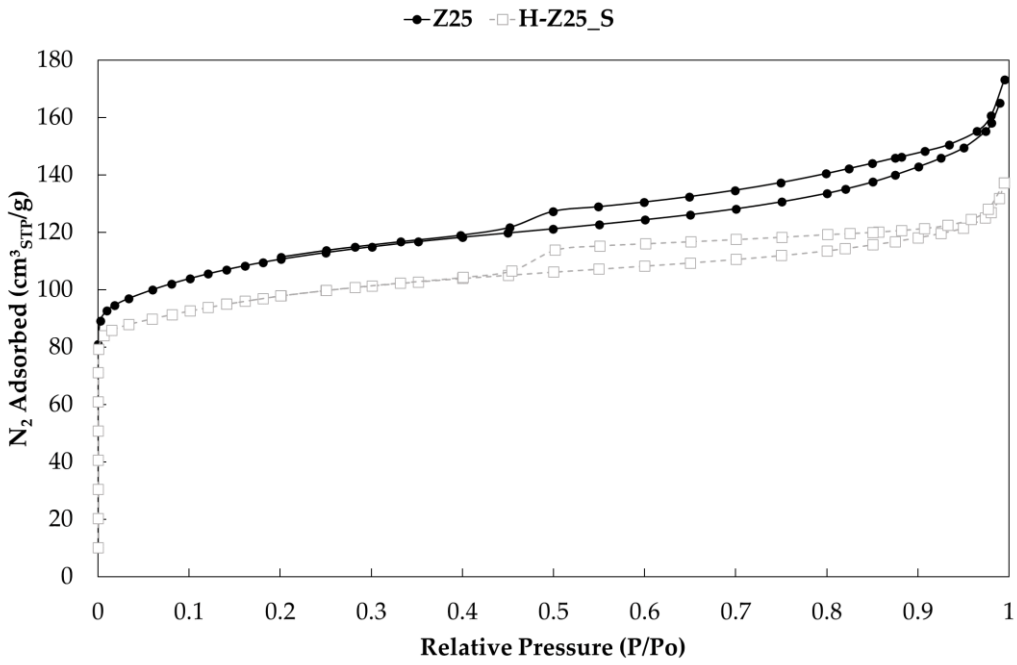

Figure A 22: N_2 sorption isotherms of parent (Z25) and passivated (H-Z25_S) samples.

APPENDIX B: Acidity properties of investigated samples.

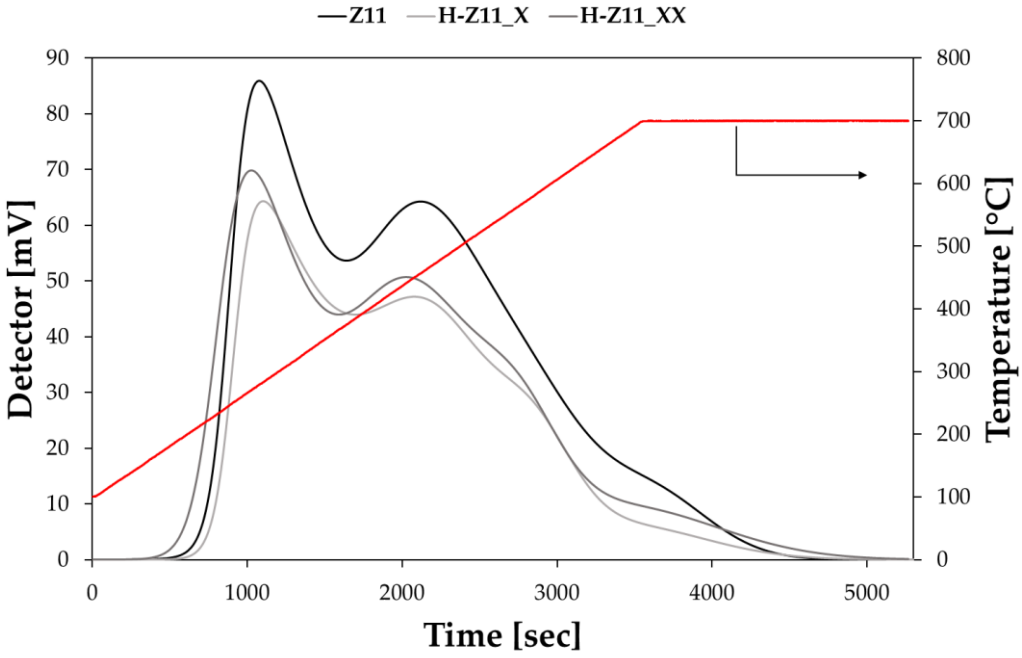

Figure B 1: NH_3-TPD profiles of Z11, H-Z11_X and H-Z11_XX samples.

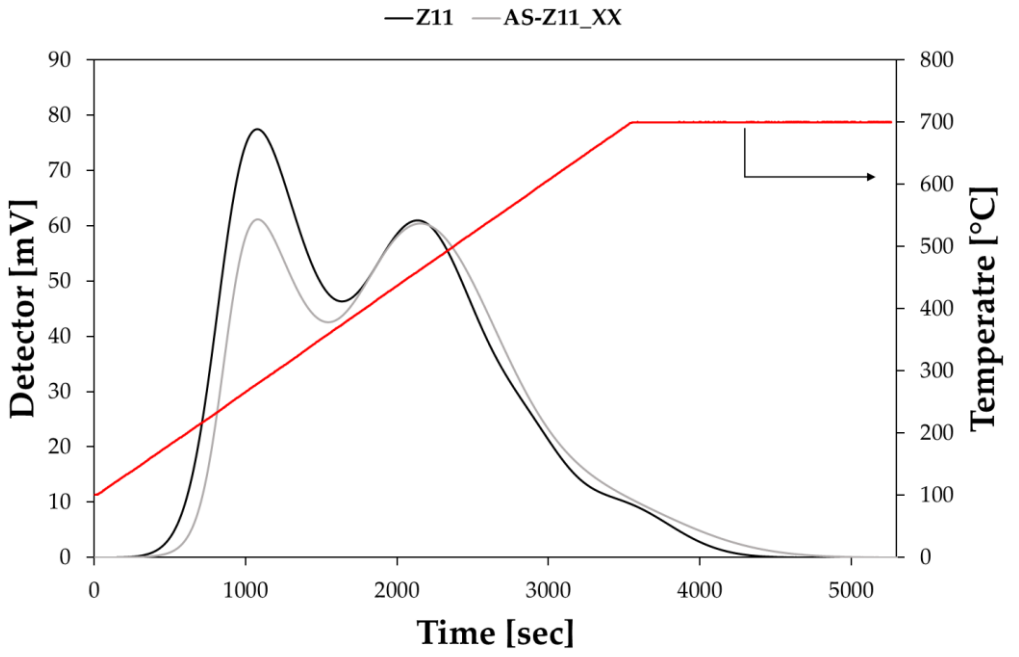

Figure B 2: NH_3-TPD profiles of Z11 and AS-Z11_XX samples.

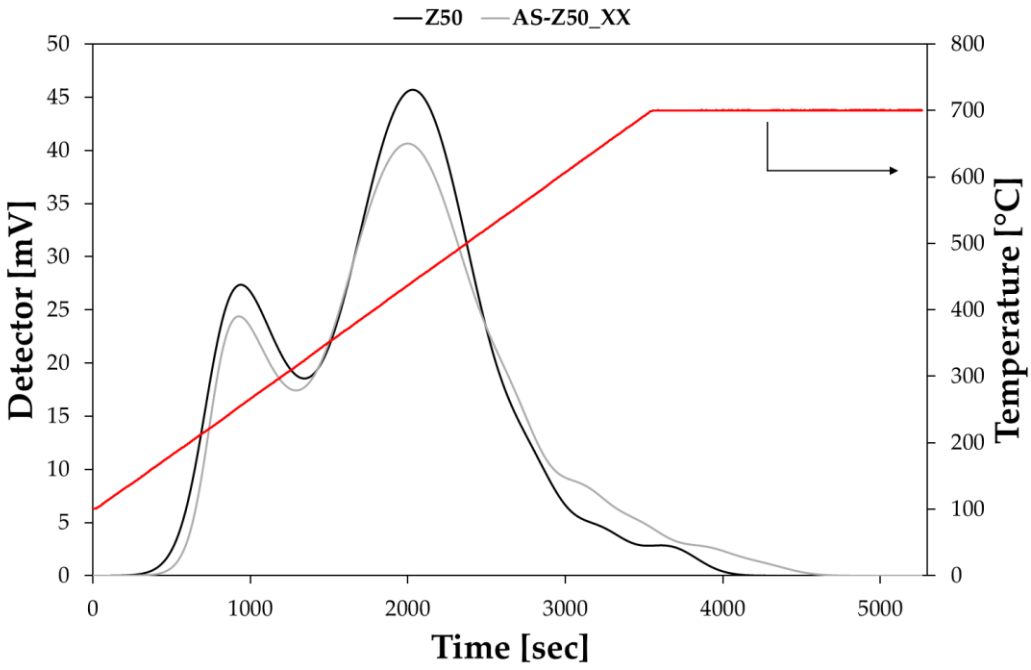

Figure B 3: NH_3-TPD profiles of Z50 and H-Z50_XX samples.

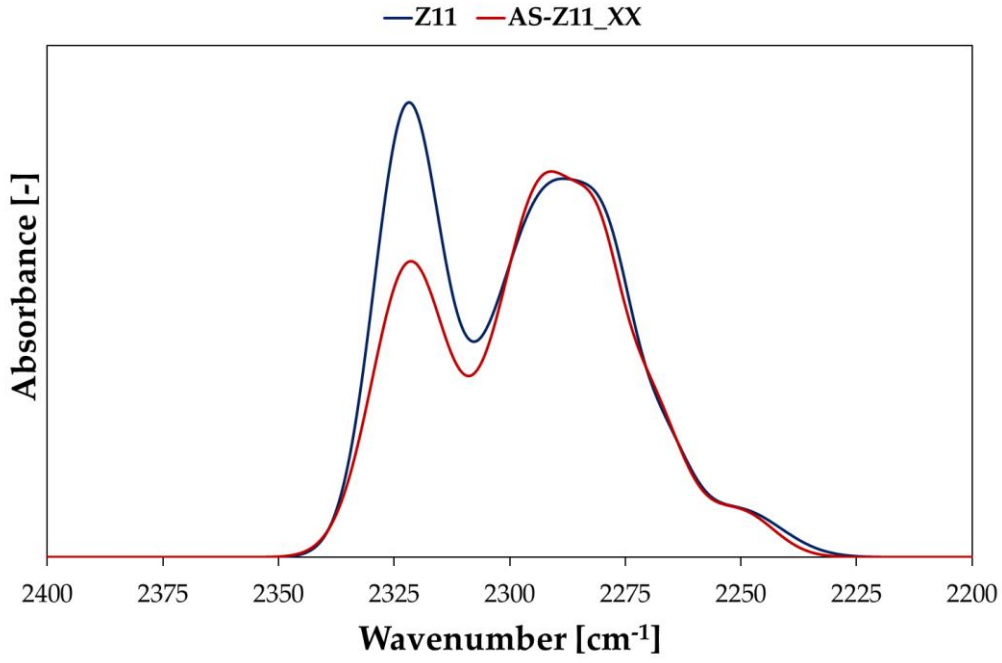

Figure B 4: FT-IR spectra of Z25 and AS-Z11_XX samples after d_3-acetonitrile adsorption.

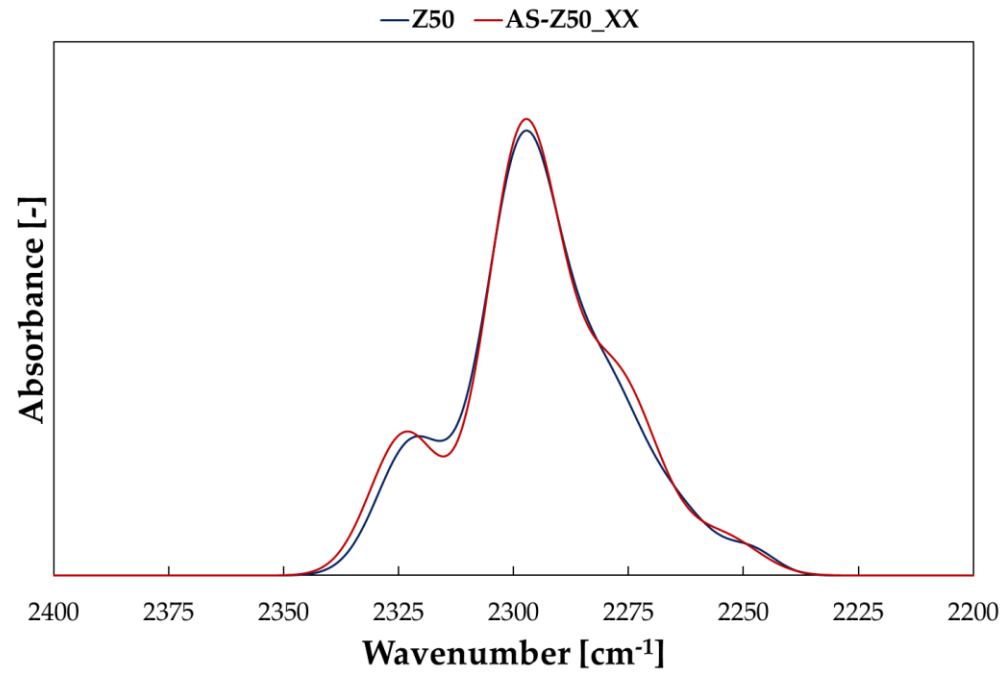

Figure B 5: FT-IR spectra of Z50 and AS-Z50_XX samples after d_3-acetonitrile adsorption.

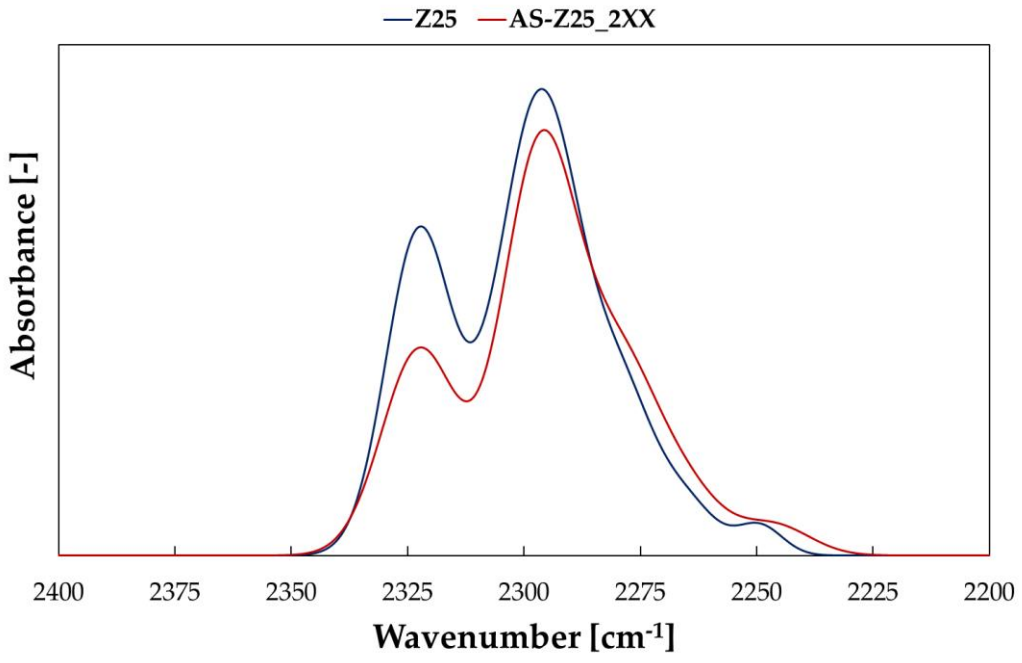

Figure B 6: FT-IR spectra of Z25 and AS-Z25_2XX samples after d_3-acetonitrile adsorption.

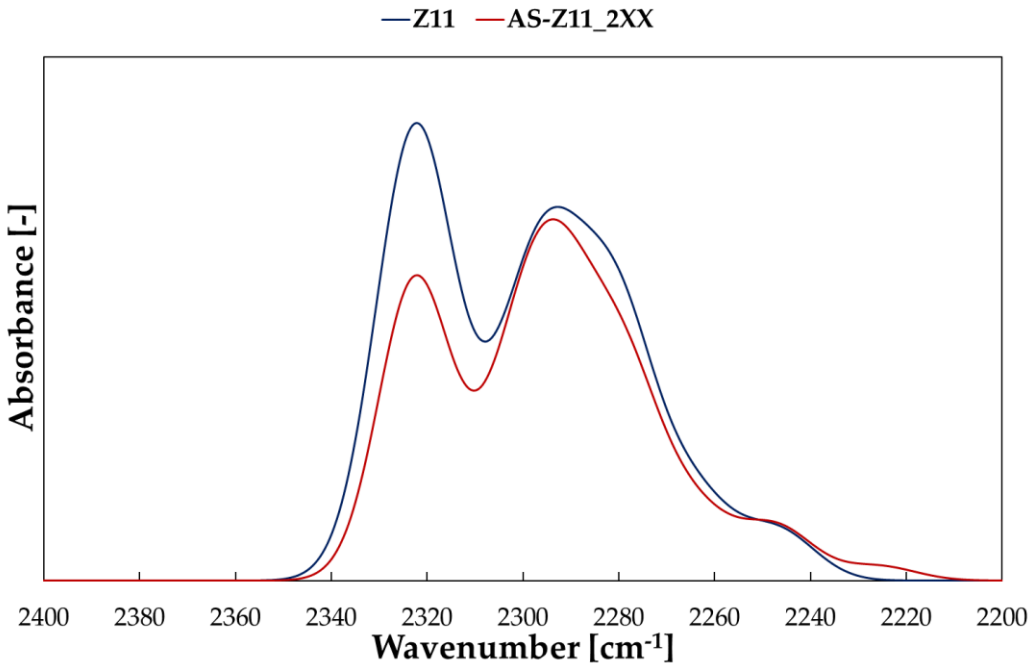

Figure B 7: FT-IR spectra of Z11 and AS-Z11_2XX samples after d_3-acetonitrile adsorption.

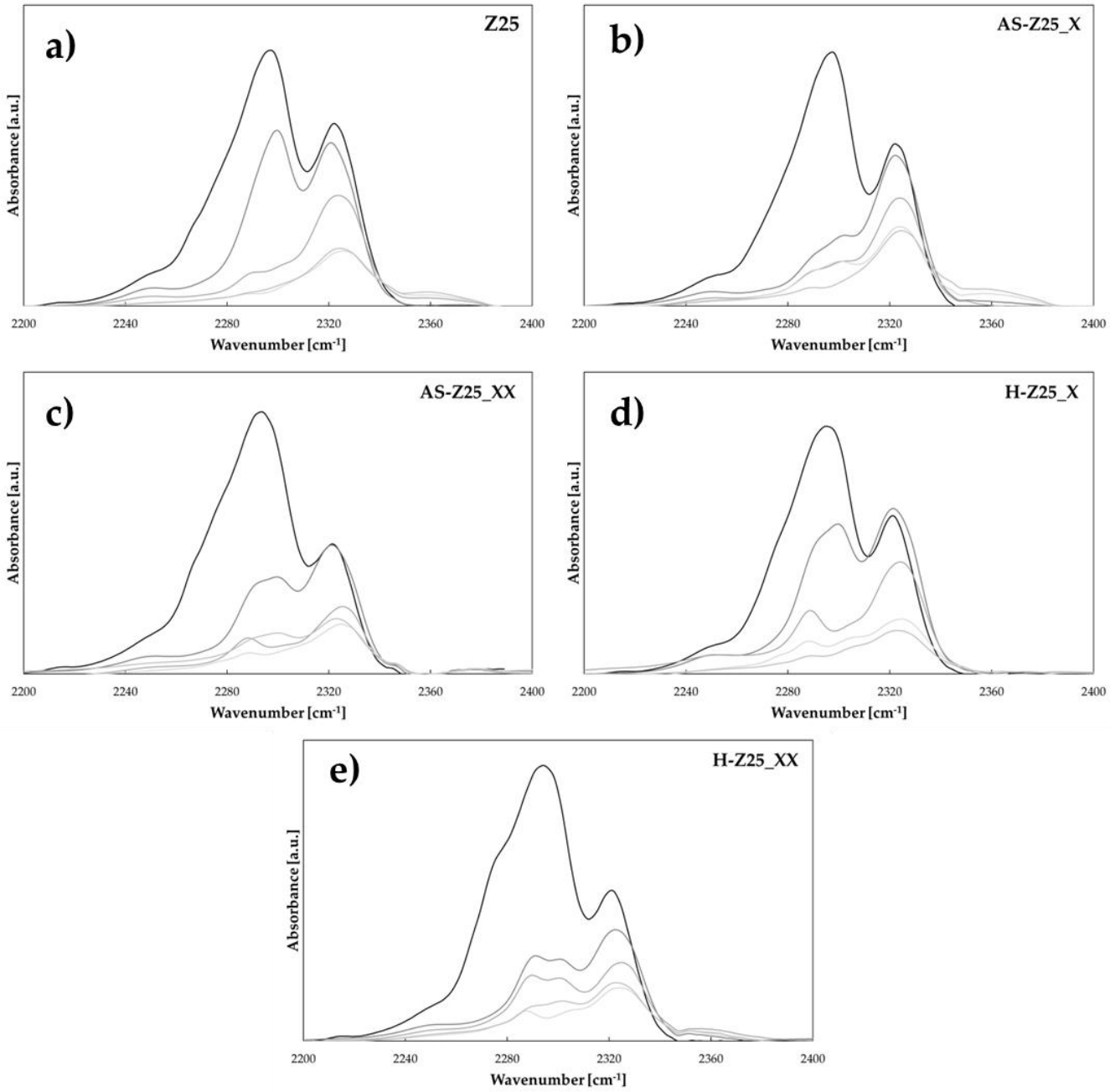

Figure B 8: FT-IR spectra in LAS/BAS region at room temperature and after the desorption of d3-acetonitrile at 150°C, 200°C, 300°C and 400°C for Z25 parent zeolite and passivated H-Z25 and AS-Z25 samples.

List of figures

List of tables

Related Publications

I. **G. Ferrarelli**, G. Giordano, M. Migliori, ZSM-5@Sil-1 core shell: *Effect of synthesis method over textural and catalytic properties*, Catal Today 390–391 (2022) 176–184. https://doi.org/10.1016/j.cattod.2021.11.036.

II. G. Giordano, M. Migliori**, G. Ferrarelli**, G. Giorgianni, F. Dalena, P. Peng, M. Debost, P. Boullay, Z. Liu, H. Guo, Z.F. Yan, S. Mintova, *Passivated Surface of High Aluminum Containing ZSM-5 by Silicalite-1: Synthesis and Application in Dehydration Reaction*, ACS Sustain Chem Eng 10 (2022) 4839–4848. https://doi.org/10.1021/acssuschemeng.1c07198.

III. E. Catizzone, **G. Ferrarelli**, P. Bruno, G. Giordano, M. Migliori, Simultaneous catalytic dehydration of methanol and ethanol: How ZSM-5 acidity addresses conversion and products distribution, Catal Today 427 (2024). https://doi.org/10.1016/j.cattod.2023.114436.

IV. E. Giglio, **G. Ferrarelli**, F. Salomone, E. Corrao, M. Migliori, S. Bensaid, R. Pirone, G. Giordano, *Tailoring the acidity of ZSM-5 via surface passivation: Catalytic assessment on dimethyl ether to olefins (DTO) process*, Fuel 362 (2024) 130559. https://doi.org/10.1016/j.fuel.2023.130559.

V. F. Dalena; E. Dib; B. Onida; **G. Ferrarelli**; M. Daturi; G. Giordano; M. Migliori; S. Mintova, *Evaluation of zeolite composites by IR and NMR spectroscopy*, **submitted to ChemPlusChem, 2024.**

Off Topic Publications

I. E. Catizzone, A. Aloise, E. Giglio, **G. Ferrarelli**, M. Bianco, M. Migliori, G. Giordano, *MFI vs. FER zeolite during methanol dehydration to dimethyl ether: The crystal size plays a key role*, Catal Commun 149 (2021) 106214. https://doi.org/10.1016/j.catcom.2020.106214.

II. A. Marino, E. Catizzone, M. Migliori, **G. Ferrarelli**, A. Aloise, D. Chillè, G. Papanikolaou, P. Lanzafame, S. Perathoner, G. Centi, G. Giordano, *Hydrothermal Synthesis and Catalytic Assessment of High-Silica (B,Fe)-beta Zeolites*, Cryst Growth Des 23 (2023) 2988–3001. https://doi.org/10.1021/acs.cgd.3c00085.

III. T. Battiston, D. Comboni, P. Lotti, **G. Ferrarelli**, M. Migliori, G. Giordano, M. Hanfland, G. Garbarino, H.-P. Liermann, G.D. Gatta, *High-pressure adsorption phenomena in natural and synthetic zeolites with EAB topology*, Microporous and Mesoporous Materials 365 (2024) 112873. https://doi.org/10.1016/j.micromeso.2023.112873.

Conference Contributions

I. *Light Gas adsorption on BEA@Sil-1 zeolite templated carbons,* P. Bruno, G. Ferrarelli, D. Cozza, A. Policicchio, G. Conte, R. G. Agostino, E. Catizzone, G. Giordano, M. Migliori, 5th Euro Asia Zeolite Conference, January 31- February 3, 2023, Busan (Korea), Oral Communication.

II. *Tailoring of surface properties of ZSM-5 zeolites and catalytic application in alcohol dehydration reactions*, G. Ferrarelli, P. Bruno, E. Catizzone, M. Migliori, G. Giordano, 5th Euro Asia Zeolite Conference, January 31- February 3, 2023, Busan (Korea), Oral Communication.

III. *New insights about the effect of acidity of ZSM-5 zeolite on dehydration of methanol and ethanol,* G. Ferrarelli, P. Bruno, E. Catizzone, M. Migliori, G. Giordano, XVI Italian

Congress of Zeolites Science and Technology, September 21 – 23, 2023, Salerno (Italy), Oral Communication.

IV. *High-silica (B, Fe)-BEA zeolite synthesis and application in HMF etherification*. A. Marino, E. Catizzone, A. Aloise, G. Ferrarelli, D. Cozza, G. Giordano, G. Papanikolaou, P. Lanzafame, S. Perathoner, G. Centi, M. Migliori, 9th Conference of the Federation of the European Zeolite Associations (FEZA2023), July 2-6, 2023, Portorož-Portorose (Slovenia). Oral Communication.

V. *Novel ZTC materials for the electrocatalytic upgrading of furfural to high added value products.* G. Papanikolaou, P. Squillaci, D. Chillè, G. Centi, S. Perathoner, P. Bruno, G. Ferrarelli, D. Cozza, E. Catizzone, G. Giordano, M. Migliori, P. Lanzafame, 9th Conference of the Federation of the European Zeolite Associations (FEZA2023), July 2-6, 2023, Portorož-Portorose, Slovenia. Oral Communication.

VI. *Induced crystal fluid interaction in 6 membered ring zeolites the case of ERI off and EAB topologies,* T. Battiston, D. Comboni, G. Ferrarelli, P. Lotti, M. Migliori, G. Giordano, G. D. Gatta, 9th Conference of the Federation of the European Zeolite Associations (FEZA2023), July 2-6, 2023, Portorož-Portorose, Slovenia Oral Communication.

VII. *Light olefins through dimethyl ether conversion over MFI type zeolites effect of superficial passivation on catalytic performance and stability,* E. Giglio, G. Ferrarelli, F. Salomone, E. Corrao, M. Migliori, S. Bensaid, R. Pirone, G. Giordano, 9th Conference of the Federation of the European Zeolite Associations (FEZA2023), July 2-6, 2023, Portorož-Portorose, Slovenia. Oral Communication.

VIII. *Olefins production from Dimethyl Ether over zeolites: material properties, products selectivity, and catalysts stability*, E. Giglio, E. Corrao, G. Ferrarelli, F. Salomone, M. Migliori, S. Bensaid, R. Pirone and G. Giordano, The 28th North American Catalysis Society Meeting (NAM2023), June 18-23, 2023, Providence (Rhode Island), Oral Communication.

IX. *New insights about the effect of acidity of ZSM-5 zeolite on dehydration of methanol and ethanol*, G. Ferrarelli, E. Catizzone, M. Migliori, G. Giordano, 9th Czech – Italian – Spanish Conference on Molecular Sieves and Catalysis, June 4-7, 2023, Toledo (Spain), Oral Communication.

X. *Hierarchical zeolites for dimethyl ether conversion into light olefins (DTO): synthesis, characterization, and catalytic performance,* E. Giglio, **G. Ferrarelli**, F. Salomone, E. Corrao, M. Migliori, S. Bensaid, R. Pirone, G. Giordano, 9th Czech – Italian – Spanish Conference on Molecular Sieves and Catalysis, June 4-7, 2023, Toledo (Spain), **Oral Communication.**

XI. *ZSM-5 surface modification via secondary sil-1 synthesis and chemical etching*, G. Ferrarelli, E. Catizzone, M. Migliori, G. Giordano, AIZ Days 2022 Workshop on Zeolites Science and Technology, 24 – 25 November, 2022, Torino (Italy), Oral Communication.

XII. *Study on the oxygen content of BEA and BEA@Sil-1 zeolite templated carbon*, P. Bruno, G. Ferrarelli, D. Cozza, E. Catizzone, M. Migliori, G. Giordano, AIZ Days 2022 Workshop on Zeolites Science and Technology, 24 – 25 November, 2022, Torino (Italy), Oral Communication.

XIII. *Synthesis and characterization of composite BETA@Sil-1 zeolites: catalytic application in methanol dehydration*, G. Ferrarelli, D. Cozza, G. Giordano, M. Migliori, 12th International Conference on Environmental Catalysis (ICEC2022), July 30-August 2, 2022, Osaka (Japan), Oral Communication.

XIV. *Light olefins production via dimethyl ether dehydration over zeolites: material properties, products selectivity, and catalysts stability* E. Giglio, F. Salomone, G. Ferrarelli, E. Corrao, M. Migliori, S. Bensaid, R. Pirone, G. Giordano, 20th International Zeolite Conference (IZC2022), July 3-8, 2022, Valencia (Spain), Poster Communication.

XV. *Olefins production from Dimethyl Ether over zeolites: material properties, products selectivity, and catalysts stability*, E. Giglio, E. Corrao, G. Ferrarelli, F. Salomone, M. Migliori, S. Bensaid, R. Pirone and G. Giordano, 27th North American Catalysis Society Meeting (NAM2022), May 22-27, 2022, New York City (New York), Oral Communication.

XVI. *ZSM-5 surface modification via secondary sil-1 synthesis*, **G. Ferrarelli**, D. Cozza, G. Giordano, M. Migliori, F. Dalena, E. Dib, S. Mintova, V. Valtchev, AIZ 2021 XV Italian Congress of Zeolites Science and Technology, December 9-11, 2021, Napoli (Italy), **Oral Communication as winner of "G. Gottardi Award 2021".**

XVII. *Sil-1@ZSM-5 core shell: effect of synthesis method over textural properties*, **G. Ferrarelli**, E. Giglio, G. Giordano, M. Migliori, Young Researchers CIS 2021-. September 6-8, 2021, On-line Conference, **Oral Communication**.

XVIII. *Core-shell ZSM5/Sil-1 composites: application in dehydration reactions*, **G. Ferrarelli**, A. Aloise, F. Dalena, G. Giorgianni, G. Giordano, M. Migliori, 8th Conference of the Federation of the European Zeolite Associations (FEZA2021), July 5-9, 2021, On-line Conference, Poster Communication.